RCA Victor

Proj.: 3457 - F

S.O. : 94260250

GROUND ANTENNA PARAMETERS

EFFECTING THE RANGE OF A

SPACE COMMUNICATION SYSTEM

Submitted

to

JET PROPULSION LABORATORIES

Pasadena

under NAS 7-100 or

NASw-6.

by

Technical Products Division

RCA VICTOR COMPANY, LTD.

1001 Lenoir St.,

Montreal.

August 26, 1960.

Prepared by Peter Folder
Acting Supervisor

Approved by _____
Manager of the Ant. Group

Approved by _____
Manager, Engrg. Dept.

TABLE OF CONTENTS

		Page
1.	INTRODUCTION	2
2.	FACTORS AFFECTING THE RANGE EQUATION OF A GIVEN ANTENNA SYSTEM	3
2.1	External Noise Sources	4
2.2	Internal Noise Sources	10
3.	THE BACK RADIATION OF REFLECTOR TYPE ANTENNAS	17
3.1	Sources of Back Radiation	17
3.2	Analysis of a Diffracted Field around a Metallic Reflector	19
3.2.1	Diffraction Field in the Presence of a Circularly Cylindrical Reflector	19
3.2.2	Diffraction Field in the Presence of a Spherical Cup Reflector	28
4.	THERMAL RADIATION OF WIRE GRATINGS	51
5.	SOME APPLICATIONS OF THE PREVIOUS RESULTS TO THE OPTIMUM GROUND ANTENNA PROBLEM	57
5.1	Feed System Problem	57
5.2	Radiation through a Wire Gratings Reflector	61
5.3	Edge Currents	63
5.4	Determination of the Optimum Antenna Parameters for a Given Aperture Size	66
6.	CONCLUSIONS	69
	LIST OF SYMBOLS	71
	REFERENCES	75

GROUND ANTENNA PARAMETERS

EFFECTING THE RANGE

OF A

SPACE COMMUNICATION SYSTEM

SUMMARY

The available optimum range of a space to ground communication system is analized from the standpoint of the ground antenna. The range or signal to noise ratio of a system is influenced by the aperture efficiency and noise temperature of the antenna. Simultaneous with the increase of the aperture efficiency, the noise temperature can be decreased by the application of a special feed pattern, f (ψ). It is shown that the ideal feed pattern f (ψ) is a "square wave" as a function of ψ, being unity up to the ψ_{ap} aperture angle of the secondary reflector (paraboloid) and is zero for $\psi_{ap} < \psi \leq \pi$.

The ideal feed pattern can be very well approximated to Cassagrain type primary reflector if the aperture size of the secondary reflector is large. Several design curves are prepared which provide a means of determining the basic dimensions of an "optimum" antenna.

1. INTRODUCTION

The optimum selection of the system parameters of a deep space communication system is extremely important because of the large costs involved and the difficulty in changing a fixed system parameter. In the present discussion, the characteristics of the ground antenna will be analyzed from the standpoint of maximum range.

It had been assumed in the past, that the maximum range of an antenna is determined by its gain. The gain is limited by the aperture distribution (reflector) accuracy.[1] However, with the advent of extremely low noise receivers (masers)[2,3], it has become evident that the range of a space communication system might be limited by the antenna noise rather than by the accuracy of the aperture distribution.

In the following study, first the general relationship between the system range and the antenna characteristics will be established. It will then be shown that one of the most important characteristics of a high gain, ground based, space communication antenna is the antenna radiation toward the ground. A concept, the "radiation suppression" can be introduced to characterize this effect.

In the second part of the study, the design parameters effecting the radiation suppression toward the ground will be investigated in more detail. A reflector type ground antenna will be assumed in the analysis because, at the present state of the art, this type of antenna promises the optimum overall performance at economical cost. Furthermore, to simplify the mathematical calculations of the back radiation of the antenna, circularly

cylindrical or spherical reflector shapes will be assumed.

2. FACTORS EFFECTING THE RANGE EQUATION OF A GIVEN ANTENNA SYSTEM.

The range equation of a one way, space communication system can be expressed as

$$R^2 = C \frac{\eta D_\lambda^2}{P_R} \quad , \qquad (1)$$

where

R = the distance between the ground antenna and the space station,

$D_\lambda = \frac{D}{\lambda}$ = the diameter of the ground antenna aperture expressed in wavelengths,

η = aperture efficiency of the ground antenna,

P_R = the specified receiver power for acceptable communication,

$C = \frac{\pi}{4} P_T A_T$, where P_T and A_T are the transmitter power and effective antenna area of the space station respectively.

(1) neglects the ionospheric and atmospheric attenuation. This is a good approximation in the 50-3000 Mc/s frequency band. In the following discussion, only the problems of the ground antenna will be analyzed. Therefore, C = constant will be assumed.

According to (1), the range of the communication system is proportional to the size of the aperture diameter. However, in (1), η is a function of D_λ and as D_λ increases, the absolute accuracy of the reflector (expressed in wavelength) can not be maintained. Therefore, an optimum aperture size exists beyond which η decreases rapidly. For the present purpose, the aperture

efficiency can be expressed [1] as

$$\eta = \eta_o e^{-16\pi^2 m^2 D_\lambda^2} \tag{2}$$

where

η_o = the aperture efficiency of the perfect paraboloid,

m = $\frac{t}{D}$,

t = root mean square deviation of the reflector from the exact parabolic shape.

The received power can be expressed as

$$P_R = M P_N = Mk \Delta f \; T_T , \tag{3}$$

where

M = the specified signal to noise ratio,

P_N = total noise power in the receiving system, w,

k = Boltzman constant = $1.38.10^{-23}$ ws/°K,

Δf = receiver bandwidth, c/s,

T_T = total apparent noise temperature of the receiving system, °K.

The T_T total noise temperature can be written as

$$T_T = T_{Rec} + T_{Aint} + T_{Aext} \tag{4}$$

where T_{Rec} is the receiver noise temperature and T_{Aint} and T_{Aext} are the internal and external noise temperatures of the antenna system respectively.

External Noise Sources

It is not difficult to calculate the approximate relationship between the T_{Aext} antenna temperature and the more familiar

antenna parameters. It can be assumed for this calculation, that the antenna is within a "gray body cavity" and the distance from the antenna to the walls of the cavity is large relative to either the antenna dimensions or the wavelength. According to the Rayleigh - Jeans expression for the radiant flux, the total bipolarized radiated power of a dA_1 surface element toward a dA receiver antenna surface (see Fig. 1)[4, 5, 6]

$$d^2(P) = \frac{2ck\epsilon T}{\lambda^3} \left|\frac{\Delta\lambda}{\lambda}\right| F_o(\psi, \varphi)\, dA \, \frac{dA_1 \cos\alpha_1}{r^2} , \tag{5}$$

where

c = velocity of light,

ϵ = emissivity of the gray body,

T = absolute temperature of the radiating surface,

$\left|\frac{\Delta\lambda}{\lambda}\right| = \left|\frac{\Delta f}{f}\right| = \delta$ = relative bandwidth of the receiver,

$F_o(\psi, \varphi)$ = power directional pattern of the elementary receiver antenna,

α_1 = angle between the normal of the radiating surface dA_1 and the direction of the receiving antenna,

r = distance between the two elements.

Integrating (5) over the aperture of the receiver antenna and assuming that the receiver antenna is unipolarized, the received thermal power from the element dA_1

$$dP = \frac{ck\epsilon T\delta\eta A}{\lambda^3} F(\psi, \varphi) \frac{dA_1 \cos\alpha_1}{r^2}$$

$$= \frac{k\,\Delta f\,\eta A}{\lambda^2} \epsilon T F(\psi, \varphi)\, d\Omega , \tag{6}$$

where $F(\psi, \varphi)$ is the power radiation pattern of the receiver antenna, $d\Omega$ is the elementary solid angle and $\eta A = A_{eff}$ is the effective receiving antenna area in the direction where $F(\psi_0, \varphi_0) = 1$.

The total received power

$$P = \frac{\pi}{4} k \, \Delta f \, \eta \, D_\lambda^2 \iint (T\epsilon) \, F(\psi, \varphi) \, d\Omega \, . \tag{7}$$

(7) shows that the received, thermal noise power is a function of the antenna position because the radiating surfaces around the antenna are generally inhomogenous. Most authors define the antenna noise temperature of a directive antenna in a position when the antenna beam is pointed vertically toward a "cool" point of the sky [7]. (See Fig. 2). In this case, it is convenient to calculate the integral of (7) separately over the upper and lower hemisphere. For the upper hemisphere

$$\iint_{\Omega_{up}} = T_s \Omega_B = T_s \frac{1}{\eta D_\lambda^2} \, , \tag{8}$$

where T_s is the apparent sky temperature toward the direction of the main beam and $\Omega_B = 1/\eta D_\lambda^2$ is the equivalent beam cross section of the antenna [8]. According to observations made during recent years [9, 10, 11], the largest component of celestial noise

in the 50-3000 Mc/s band is galactic radiation. The power distribution of this noise shows a rapidly decreasing character with frequency (See Fig. 3) and its space distribution shows a minimum in the plane of the celestial equator. However, the angular variation of this noise is small. Therefore $T_s =$ const. can be assumed within the main antenna beam.

The precise integration of (7) for the lower hemisphere is more difficult because all factors in the integral are usually complicated functions of angles.

For some flat, ground surfaces, the apparent ground temperature ϵT was calculated by E. Weger [12] in the range of 10 kmc/s. At lower frequencies, the effect of atmospheric attenuation and scattering is negligible. On the other hand, the noise power of the sky, which is reflected from the ground, becomes more important. Therefore, $(T\epsilon)$ in (7) should be generalized as

$$(T\epsilon)_G = T_{AG} = \epsilon_G T_G + \Gamma_G T_s \quad , \tag{9}$$

where T_{AG} and T_G are the apparent and the thermodynamical temperatures of the ground respectively, while ϵ_G is the emissivity and Γ_G is the reflection coefficient of the surface. From (7) and (9), the integral for the lower hemisphere becomes

$$\iint_{\Omega_L} = \iint (\epsilon_G T_G + \Gamma_G T_s) F \, d\Omega \approx T_{AG} \iint_{\Omega_L} F \, d\Omega \quad , \tag{10}$$

where in the last approximation the angular dependence of ϵ_G and Γ_G is neglected. This approximation is obviously only applicable toward the lower frequencies of the band. Fig. 4 indicates the frequency dependency of the apparent ground temperature for normal incidence.

It is convenient to introduce the radiation suppression of the antenna, or briefly suppression S, into a solid angle Ω_1, by the definition

$$S = \frac{\text{Average radiation into } \Omega_1}{\text{Average radiation into } \Omega = 4\pi}$$

$$= \frac{\frac{1}{\Omega_1}\iint_{\Omega_1} F(\psi,\varphi)\, d\Omega}{\frac{1}{4\pi}\iint_{\Omega} F(\psi,\varphi)\, d\Omega} = G F_{av\Omega_1} \quad , \tag{11}$$

where

$$G = \frac{F_{Max}}{\frac{1}{4\pi}\iint_{\Omega} F\, d\Omega} \quad , \quad F_{av\Omega_1} = \frac{1}{\Omega_1}\iint_{\Omega_1} F\, d\Omega \; .$$

From here on, Ω_1 will always refer to the lower hemisphere. Then, using (10) and (11)

$$\iint_{\Omega_1} \approx 2\pi\, T_{AG} \frac{S}{G} = \frac{2\, T_{AG}\, S}{\pi \eta D_\lambda^2} \; . \tag{12}$$

Inserting (8) and (12) into (7)

$$P = k\, \Delta f\, \frac{\pi}{4}\left[T_s + \frac{2}{\pi} T_{AG} S\right] \; . \tag{13}$$

The noise power of a receiving system in which only external sources are introducing noise

$$P = k \, \Delta f \, T_{A_{ext}} \quad . \tag{14}$$

Comparing (13) and (14)

$$T_{A_{ext}} = \frac{\pi}{4}\left[T_s + \frac{2}{\pi} T_{AG} S\right]$$

$$= \frac{\pi}{4}\left[T_s + 2\pi D_\lambda^2 F_{avG} T_{AG}\right] \tag{15}$$

(15) indicates that the external noise of the antenna is determined by the sky and ground temperatures and the radiation suppression toward the ground. At low frequencies, T_S is inherently high while, on the other hand, S can be a small quantity because the gain of the antenna is usually small at low frequencies.

Toward the upper part of the frequency range, T_S becomes small. Nevertheless, the feasibility of building high gain antennas may bring the value of S closer to unity.

Fig. 5 indicates the apparent external noise temperature T_{aext} as a function of frequency, for D = 100'. It can be seen that T_{aext} decreases rapidly as the average radiation toward the ground decreases. For a fixed aperture diameter and level of backradiation T_{aext} has a minimum. Thus Fig. 5 can be used to select the optimum operating frequency of the system. This can be determined from the cross section of the $F_{avG} = \text{const}$ curves and the "line of optimum" frequency. In turn, once the

operating frequency is selected, the required value of F_{avG} can be specified by the use of Fig. 5.

Furthermore, it can be concluded from Fig. 5, that the importance of the whole antenna noise problem is a direct function of the T_{Rec} noise (See eg. 4). Maser receivers already are able to produce 5-10°K noise temperatures. Thus, it can be expected that, in the future, the operating frequency of space communication systems will be increased, probably up to 2000 mc/s, and $F_{avG} \cong$ 80 db will be needed. The latter requirement will present an ever-increasing refinement in the antenna technique.

The thermal radiation of the ground can be decreased by either decreasing T_{AG} or S. According to (9) and Fig. 3, $T_{AG} \approx \epsilon_G T_G$ at higher frequencies. The emissivity of the ground can be decreased by covering the ground with a metallic screen. However, this method is very expensive if the center of the antenna is high above the ground, which is the case in large antenna systems. A more convenient solution of this problem is to provide large suppression toward the ground.

Internal Noise Sources

Fig. 6 indicates how rapidly the apparent external antenna noise temperature increases for large antenna systems as S increases. This far, only the external noise sources have been considered. However, the internal thermal power of a large antenna and waveguide system is not negligible and at least the former should be taken into account [13, 14, 15].

A simple calculation can be made assuming an axially symmetrical, solid reflector surface in free space, which has a receiver antenna in its focal point. According to (7), the received thermal power at the feed point

$$P_R = k\,\Delta f\,\epsilon_R T_R\,\eta_F \frac{A_F}{\lambda^2}\,H^s \quad , \tag{16}$$

where

ϵ_R = emissivity of the reflector,

T_R = absolute temperature of the reflector,

η_F = aperture efficiency of the feed horn,

A_F = geometrical aperture of the feed horn,

H^s = geometrical factor of the solid reflector with an aperture angle ψ_a

$$H^s = \int_0^{2\pi}\int_0^{\psi_a} F_F(\psi,\varphi)\sin\psi\,\cos\alpha_2(\psi)\,d\psi\,d\varphi \; . \tag{17}$$

In (17), $F_F(\psi,\varphi)$ is the power pattern of the feed system. Fig. 7 indicates H^s for spherical (H^s_{sp}) and parabolic (H^s_p) reflectors as a function of ψ_a , assuming $F_F(\psi) = \cos^2\psi$. From (16), the apparent noise temperature component introduced by the reflector

$$T_{AR} = \epsilon_R\,\eta_F \frac{A_F}{\lambda^2}\,H^s T_R = \frac{1}{4\pi}\,\epsilon_R G_F H^s T_R \; . \tag{18}$$

Usually in (18), $T_R \cong 300\,°K$, $G_F \cong 5 \sim 10$ and the material of the reflector is almost always aluminum, ($\epsilon_R \approx 2\%$). (Table 1 indicates the emissivities of some materials. More complete data can be found in the literature [16, 17]). For the usual $\psi_a = 60\text{-}80°$ aperture angles, $G_F H^s = 4\pi$ can be assumed and then, the apparent reflector temperature is 6^oK. This is a relatively high value. It should be noted however, that the available thermal noise power of a surface is proportional to its projected area. Thus, in the case of a wire gratings reflector, the noise radiation can be considerably reduced. This reduction can be expressed by the transparency ratio

$$\kappa = \frac{H^g}{H^s} , \tag{19}$$

where H^g is the geometrical factor of the wire gratings reflector. κ can be determined from (17) by integrating only over the metallic part of the reflector. The noise radiation characteristics of a single wire was calculated by C. M. Rytov [13]) and it is easy to extend his calculations to a set of parallel wires. It will be shown later that, at optical frequencies, $\kappa \approx \frac{A^g}{A^s}$ where A^g and A^s are the projected geometrical areas of the wire and solid reflector respectively, assuming that the wires have circular cross-sections and are parallel with the polarization of the receiver antenna.

TABLE 1

THERMAL EMISSIVITY OF DIFFERENT MATERIALS

Material	Temperature	Condition	Emissivity %
Aluminum	25°C	Unoxidised, $\lambda = .65$	2.2
	100°C	"	2.8
	500°C	" "	6.0
Copper	100°C	" "	2.0
Silver	100°C	" "	2.0
Steel	100°C	" "	8.0
Asbestos		$\lambda = .65$	96
Brick		"	93
Plaster		"	95
Snow-white enamel on rough iron plate		"	90
Water		"	91

		Horizontal Polarization	Vertical Polarization
Water	$\lambda = 3$ cm	41	50
Grass	"	98	98
Concrete	"	88	88
Asphalt	"	89	89

For microwave frequencies, the optical approximation is acceptable until the skin depth is negligible relative to the wire diameter. With the above considerations, the generalized form of (18)

$$T_{AR} = \frac{1}{4\pi} \epsilon_R \kappa H^s G_F T_R \quad . \tag{20}$$

In practice κ can not be very small because the reflector is not in free space and the thermal radiation of the ground through the reflector becomes noticeable. This problem will be discussed later in this paper. From the latter considerations, it follows that κ can be made small enough to reduce the thermal noise of the reflector before the transmission of ground noise through the mesh becomes noticeable.

In the given example, an aluminum surface was assumed. Unfortunately, the reflector can support precipitation in rainy weather, or ice during winter conditions. Under these circumstances, the emissivity of the reflector might be 10-20 times larger than for the ideal metallic surface.

Besides the thermal radiation of the reflector, there is another internal noise source in the antenna system, the loss resistance of the antenna. Assuming that the radiation resistance R_R and loss resistance R_L of the antenna can be represented as a series network, the time average of the square of the noise voltages on these resistances will be in a Δf frequency band,

$$V_R^2 = 4kT_A R_R \Delta f \quad , \qquad V_L^2 = 4kT R_L \Delta f \quad , \tag{21}$$

where T_A is the apparent and T the thermodynamical temperature of the antenna system respectively. The noise power ratio of

the lossy to the loss-less antenna

$$\frac{P_{NL}}{P_{No}} \equiv \tau = \frac{V_R^2 + V_L^2}{V_R^2} = 1 + \frac{R_L T}{R_R T_A} = 1 + \frac{P_L T}{P_R T_A} \quad , \tag{22}$$

where P_R and P_L are the radiated and loss powers of the antenna. But

$$P_{NL} = P_{No}\tau = k\,\Delta f\, T_A \tau = k\,\Delta f\, T_{AL} \quad , \tag{23}$$

$$T_{AL} = T_A \tau = T_A + \frac{P_L}{P_R} T \quad , \tag{24}$$

where T_{AL} is the apparent temperature of the lossy antenna. According to (24), 1% power loss is already equivalent to $3^{\circ}K$ additional noise temperature assuming $T = 300^{\circ}K$.

Collecting the various noise temperature components from (15), (20) and (24), the total apparent noise temperature of the receiving system

$$T_T = T_{Rec} + \frac{P_L}{P_R} T + \frac{\epsilon_R K H^5 G_F T_R}{4\pi} + \frac{1}{2} S T_{AG} + \frac{\pi}{4} T_s \, . \tag{25}$$

Using (2), (3), (4) and (25), the range equation

$$R^2 = \frac{C}{M k \Delta f} \frac{\eta_0 D_A^2 e^{-16\pi^2 m^2 D_A^2}}{T_{Rec} + \frac{P_L}{P_R} T + \frac{\epsilon_R K H^5 G_F T_R}{4\pi} + \frac{1}{2} S T_{AG} + \frac{\pi}{4} T_s} \, . \tag{26}$$

In (26), the second factor of the right side contains the antenna design parameters. If the noise temperature of the sky is high (at low frequency) or the noise temperature of the receiver is large (conventional receiver), the antenna design does not affect the overall noise temperature of the system, and the reflector size, accuracy and aperture efficiency are only the controlling parameters.

However, if the sum of the receiver and sky noise temperature is in the order of $10^{o}K$ or less, the resistive, reflector and ground noise becomes increasingly important and their value should be maintained as small as possible by proper design. The reflector noise can be controlled by κ, while the noise caused by the antenna loss can be decreased by the elimination of the feeder line, i.e., placing the receiver directly to the feed point. However, the noise caused by thermal radiation from the ground still remains and may become the largest single component.

Fig. 8 shows the range variation with D_λ for various levels of backradiation. The range increases with decreasing backradiation and has an optimum value determined by the reflector accuracy. If the level of backradiation is large, the range is seriously limited by the noise, long before the reflector accuracy affects the operation.

3. THE BACK RADIATION OF REFLECTOR TYPE ANTENNAS

3.1 Sources of back radiation

Fig. 2 indicates schematically, the possible sources of back radiation.

According to this figure, the back radiation of an antenna may be generated by :

A) Spill over radiation of the feed.

B) Radiations caused by the currents on the rear side of the reflector.

C) Transmission through the reflector if it is not solid.

A) In many cases, the spillover radiation produces the largest contribution. Obviously, this radiation can be decreased :

a) by increasing the aperture angle ψ_a , or

b) by increasing the directivity of the feed system.

However, the first approach increases the surface of the paraboloid relative to the aperture area (see Fig. 9) which increases the weight, wind load and constructional difficulty of the antenna system. The second approach reduces the aperture efficiency. Thus, both methods increase the cost of the antenna per unit gain. Instead of these non-economical approaches, the feed pattern can be specified according to Fig. 10. This pattern produces constant illumination for the reflector within the $\delta\psi_a$ angle, where δ is close to unity, and radiates little power

into the spill over region. The radiation into this second region can be characterized by $\sigma = \frac{F_F(\psi > \psi_a)}{F_F(0)} < 1$. It would appear from Fig. 10 that for σ = const, η_0 is maximum if $\delta = 1$. However, as δ approaches unity, the size of the feed system increases and screens the center of the aperture. This latter fact tends to decrease the aperture efficiency which, therefore, has a maximum when $\delta < 1$.

One possible realization of the feed pattern indicated on Fig. 10 was suggested by S. A. Schelkunoff [18] using a linear array. A solution applicable for microwave frequencies was described in the literature and was successfully used to obtain high front to back ratio.[19]

B) In the theoretical case of $\sigma = 0$, the feed does not directly radiate power in the rear hemisphere. However, the feed radiation induces currents on the inner part of the reflector, which may flow towards the rear side of the surface. These currents were analized by E. B. Moullin[20] for the case when a cylindrical wave hits a semi-infinite plane reflector. According to his calculations, the rear current density has its maximum at the edge and decreases rapidly with the distance from the edge. The nature of these currents will not be analyzed in this study, but a method will be outlined to localize these currents at the edge region of the reflector and then compensate their radiation toward the rear hemisphere.

C) The transmission through a plane wire gratings was analyzed by several authors and the attenuation was calculated as a function of the wire radius ρ and separation ℓ expressed in wavelengths.[21, 22] In the following, only two aspects of this problem will be discussed:

a) the effect of the reflector shape on the transmitted field through the wire gratings and

b) the optimum selection of the ρ/ℓ ratio, which produces low thermal noise radiation with satisfactory attenuation through the reflector.

3.2 Analysis of the Diffracted Field around a Metallic Reflector

Two reflector shapes will be discussed in this paragraph:

1. An axially infinite, cylindrical shell reflector which is illuminated by an infinitely long line source.
2. A spherical cup reflector illuminated by a point source.

3.2.1 Diffraction Field in the presence of a Circularly Cylindrical Reflector

Fig. 11 indicates the cross section of an axially infinite, circular cylinder. The geometry of the circular arc is determined by the radius ρ and the aperture angle ψ_a. If an arbitrary polarized field exists along the axis of the cylinder, the field, along the circular aperture, can be synthetized by an axial and a circumferential component.

The radiation pattern of the elementary Huygens source in the aperture at $\pm\psi$ angle

$$f_{H\pm} = \begin{cases} 1 + \cos(\psi \mp \Theta) & \text{for circumferential polarization} \\ 1 & \text{for axial polarization.} \end{cases} \tag{27}$$

Only the first case should be calculated, becuase it contains the solution of the second case. The normalized far field component for the circumferential polarization

$$dE = \left(f_{H+} e^{j\varphi_+} + f_{H-} e^{j\varphi_-}\right) \rho \, d\psi \tag{28}$$

where

$$\varphi_\pm = -\frac{2\pi}{\lambda} \rho \cos(\psi \mp \Theta) = -r\cos(\psi \mp \Theta) \tag{29}$$

Introducing

$$f_1 = \cos\psi \cos\Theta \quad , \quad f_2 = \sin\psi \sin\Theta \quad ,$$

$$f_{H+} = 1 + \cos\psi\cos\Theta + \sin\psi\sin\Theta = 1 + f_1 + f_2$$

$$f_{H-} = 1 + \cos\psi\cos\Theta - \sin\psi\sin\Theta = 1 + f_1 - f_2$$

$$\varphi_+ = -rf_1 - rf_2 \quad , \quad \varphi_- = -rf_1 + rf_2 \, ,$$

then

$$\frac{dE}{2} = \left[\cos rf_1 - j\sin rf_2\right]\left[(1+f_1)\cos rf_2 - jf_2 \sin rf_2\right]\rho \, . \tag{30}$$

With

$$\alpha = rf_1 \quad , \quad \beta = rf_2 \quad , \quad A = 1 + f_1 \quad , \quad B = f_2 \quad , \tag{31}$$

$$\frac{E}{2} = T_1 + T_2 - j(T_3 + T_4) \quad , \tag{32}$$

where

$$T_1 = \int_0^{\psi_a} A\rho \cos\alpha \cos\beta \, d\psi \quad , \tag{33}$$

$$T_2 = \int_0^{\psi_a} B\rho \sin\alpha \sin\beta \, d\psi \quad , \tag{34}$$

$$T_3 = \int_0^{\psi_a} A\rho \sin\alpha \cos\beta \, d\psi \quad , \tag{35}$$

$$T_4 = \int_0^{\psi_a} B\rho \cos\alpha \sin\beta \, d\psi \quad . \tag{36}$$

(33-36) are valid for any arbitrarily cylinder which has a symmetry plane. However, in the general case, the integration can be carried out only numerically. (For instance, for a parabolic shape, where $\rho = \cos^{-2}\frac{\psi}{2}$). If $\rho = \text{constant}$, the integration is straightforward but still quite tedious. Omitting the details, (32) can be expressed as

$$\frac{E}{\rho} = (-\theta, cc) + (\theta, cc) + \cos 2\theta(-\theta, ccc) - \sin 2\theta(-\theta, scc) + \cos 2\theta(\theta, ccc)$$
$$+ \sin 2\theta(\theta, scc) - j\left\{(-\theta, sc) + (\theta, sc) + \cos 2\theta(-\theta, csc) - \sin 2\theta(-\theta, csc)\right\} \tag{37}$$

where the symbols represent the following integrals

$$(\Theta, cc) = \int_{\Theta}^{\psi_a + \Theta} \cos[r\cos\psi]\, d\psi \quad , \tag{38}$$

$$(\Theta, sc) = \int_{\Theta}^{\psi_a + \Theta} \sin[r\cos\psi]\, d\psi \, , \tag{39}$$

$$(\Theta, ccc) = \int_{\Theta}^{\psi_a + \Theta} \cos\psi \cos[r\cos\psi]\, d\psi \quad , \tag{40}$$

$$(\Theta, scc) = \int_{\Theta}^{\psi_a + \Theta} \sin\psi \cos[r\cos\psi]\, d\psi \quad , \tag{41}$$

$$(\Theta, csc) = \int_{\Theta}^{\psi_a + \Theta} \cos\psi \sin[r\cos\psi]\, d\psi \quad . \tag{42}$$

If the polarization is parallel with the axis of the cylinder, then from (27), (28) and (29) only (38) and (39) are different from zero. The far field

$$\frac{E}{\rho} = (-\Theta, cc) + (\Theta, cc) - j\left[(-\Theta, sc) + (\Theta, sc)\right] \quad , \tag{43}$$

where

$$(\Theta, cc) = J_0(r)\psi_a + 2\sum_{n=1}^{\infty} (-1)^n J_{2n}(r) \int_{\Theta}^{\psi_a + \Theta} \cos 2n\psi \, d\psi \tag{44}$$

$$(\theta, sc) = 2\sum_{n=0}^{\infty}(-1)^n \mathfrak{J}_{2n+1}(r)\int_{\theta}^{\psi_a+\theta}\cos(2n+1)\psi\, d\psi \quad . \tag{45}$$

From (43), (44) and (45)

$$\frac{E}{\rho} = f(\theta) = \mathfrak{J}_0(r)\psi_a + 2\sum_{1}^{\infty}(-1)^n \frac{\mathfrak{J}_{2n}(r)\sin 2n\psi_a}{2n}\cos 2n\theta$$

$$-j2\sum_{0}^{\infty}(-1)^n \frac{\mathfrak{J}_{2n+1}(r)\sin(2n+1)\psi_a}{2n+1}\cos(2n+1)\theta \quad . \tag{46}$$

Fig. 12 shows the variation of the $|f(\theta)|$ field pattern for $\psi_a = 45°, 60°, 72°$ and $\rho_\lambda = 1.52\ ,\ 3.02\ ,\ 6.04.\ \left(\rho_\lambda \equiv \frac{r}{2\pi}\right)$

If $r \gg 1$ (geometrical optics)

$$\mathfrak{J}_{2n}\left(r+\frac{\pi}{4}\right) \cong \frac{\cos(r-\pi n)}{\left[\frac{\pi}{2}\left(r+\frac{\pi}{4}\right)\right]^{\frac{1}{2}}} \cong (-1)^n \frac{\cos r}{\left(\frac{\pi}{2}r\right)^{\frac{1}{2}}} \quad , \tag{47}$$

$$\mathfrak{J}_{2n+1}\left(r+\frac{\pi}{4}\right) \cong (-1)^n \frac{\sin r}{\left(\frac{\pi}{2}r\right)^{\frac{1}{2}}} \quad . \tag{48}$$

$$\frac{E}{4\rho}\left(\frac{\pi}{2}r\right)^{\frac{1}{2}}\frac{1}{\psi_a} = \cos r\left[\frac{1}{2} + \sum_{1}^{\infty}\frac{\sin 2n\psi_a}{2n\psi_a}\cos 2n\theta\right]$$

$$-j\sin r\left[\sum_{0}^{\infty}\frac{\sin(2n+1)\psi_a}{(2n+1)\psi_a}\cos(2n+1)\theta\right] \quad . \tag{49}$$

Selecting $\cos r = 1$, the far field pattern

$$f(\theta) = \frac{1}{2} + \sum_{1}^{\infty} \frac{\sin 2n\psi_a}{2n\psi_a} \cos 2n\theta$$

$$\cong \frac{2}{\pi} \int_0^{\infty} \frac{\sin u}{u} \cos \frac{\theta}{\psi_a} u \, du = \begin{cases} 1 & \text{if } 0 \leq \theta < \psi_a \\ \frac{1}{2} & \text{if } \theta = \psi_a \\ 0 & \text{if } \psi_a < \theta \leq \pi \end{cases} \tag{50}$$

which is the familiar expression of the geometrical optical field, where $f(\theta)$ is a "square wave" with a period of π and a width of ψ_a .

In the previous discussions, the range of ψ_a was not restricted. This is the case when the circular arc in Fig. 11 represents an "open" aperture, i.e. when a cylindrical wave hits a $2\rho \sin \psi_a$ wide slot (See Fig. 13a). In the case of a closed aperture, the elementary Huygens source can not radiate without obstruction into every direction because it is obstructed by the aperture itself. This physical arrangement occurs when a cylindrical wavefront exist on the rear surface of a cylindrical wire gratings reflector.

In the latter case, the validity of (37) and (43) should be restricted for $0 \leq \psi_a \leq \frac{\pi}{4}$ and $0 \leq \theta \leq \frac{\pi}{2} - \psi_a$.

The more general form of (37)

$$\frac{E}{\rho} = \int_0^{\psi_a} e^{-r\cos(\psi - \theta)} d\psi + \int_0^{\psi_a} e^{-r\cos(\psi + \theta)} d\psi$$

$$= (-\theta, cc) - j(-\theta, sc) + \int_0^{k} e^{-r\cos(\psi + \theta)} d\psi \tag{51}$$

where

$$k = \begin{cases} \psi_a & \text{if} \quad 0 < \Theta \leq \frac{\pi}{2} - \psi_a \\ \frac{\pi}{2} - \Theta & \text{if} \quad \frac{\pi}{2} - \psi_a \leq \Theta \leq \frac{\pi}{2} \end{cases} \tag{52}$$

The result for $k = \psi_a$ was given by (46). For $\frac{\pi}{2} - \psi_a \leq \theta \leq \frac{\pi}{2}$

$$\begin{aligned} \frac{E}{\rho} = J_0(r)\frac{\pi}{2} + 2\sum_1^\infty (-1)^n \frac{J_{2n}(r)}{2n}\Big[&\sin 2n\psi_a \cos 2n\Theta \\ &- \cos 2n\psi_a \sin 2n\Theta\Big] \\ -j2\sum_0^\infty (-1)^n \frac{J_{2n+1}(r)}{2n+1}\Big[&\sin(2n+1)\psi_a \cos(2n+1)\Theta \\ &- \cos(2n+1)\psi_a \sin(2n+1)\Theta + (-1)^n\Big] \end{aligned} \tag{53}$$

If $r \gg 1$ and $\cos r = 1$, the far field pattern

$$f(\theta) = \frac{\pi}{4} + \sum_1^\infty \frac{1}{2n}\left[\sin 2n\psi_a \cos 2n\Theta - \cos 2n\psi_a \sin 2n\Theta\right] \tag{54}$$

(46) and (53) describe the far field pattern if a uniform field exists along the circular cylinder between $0 \leq \psi \leq \psi_a$ and is zero along the rest of this circle. This model can be used to analyze the radiation of a wire gratings reflector in the rear hemisphere, if the feed pattern agrees with Fig. 10. However, an equally important case occurs in practice, when the

field is zero along the aperture arc for $0 \leq |\psi| \leq \psi_a$ and is unity along the rest of the circle. This model can be used to analyze the screening effect of a solid reflector if the feed pattern is omnidirectional. According to the Babinet principle[23], the superimposed radiation of the two complementary (a and b) cases on Fig. 14 produces case c, which is the field of the unobstructed cylindrical line source. Mathematically, if $f_a(\theta)$ and $f_b(\theta)$ are normalized to unity

$$f_a(\theta) + f_b(\theta) = 1 \quad . \tag{55}$$

For instance, the diffracted field around the circular reflector from (46) and (55)

$$f_a = 1 - f_b = 1 - J_0(r)\psi_a - 2\sum_1^{\infty}(-1)^n \frac{J_{2n}(r)\sin 2n\psi_a}{2n}\cos 2n\theta$$

$$+ j2\sum_0^{\infty}(-1)^n \frac{J_{2n+1}(r)\sin(2n+1)\psi_a}{(2n+1)}\cos(2n+1)\theta \quad . \tag{56}$$

Rigorously, (56) is valid only for $0 \leq \psi_a \leq \frac{\pi}{4}$ and $0 \leq \theta \leq \frac{\pi}{2} - \psi_a$. However, the approximation is quite good if θ exceeds ψ_a by a small amount. Thus (56) can be used to study the field of the transition range at the circular reflector.

The geometrical optical form of (56) ($r >> 1$, $\cos r = 1$) after normalization

$$f_a = \frac{1}{2} - \sum_1^{\infty} \frac{\sin 2n\psi_a}{2n\psi_a}\cos 2n\theta \quad . \tag{57}$$

If (57) describes the pattern of an antenna system for all Θ, then the antenna suppression of this antenna system for the rear hemisphere

$$S_o = \frac{\frac{2}{\pi}\int_{\psi_a}^{\pi/2} f_a^2(\theta)\sin\Theta\, d\Theta}{\frac{1}{\pi}\int_0^{\pi} f_a^2(\theta)\sin\theta\, d\Theta} = \frac{2\int_{\psi_a}^{\pi/2}\sin\Theta\, d\Theta}{\int_0^{\pi}\sin\Theta\, d\Theta} = \cos\psi_a \tag{58}$$

(58) shows that, for an isotropic feed source, the antenna suppression decreases slowly with ψ_a unless the aperture angle is close to $\pi/2$. However, the suppression for the feed pattern given on Fig. 10.

$$S = \frac{2\sigma\int_{\psi_a}^{\pi/2}\sin\Theta\, d\Theta}{\int_0^{\delta\psi_a}\sin\theta\, d\Theta + \sqrt{\sigma}(1-\delta)\psi_a\sin\frac{1+\delta}{2}\psi_a + \sigma\int_{\psi_a}^{\pi}\sin\theta\, d\theta}$$

$$= \frac{2\sigma\cos\psi_a}{\left[1-\cos\delta\psi_a\right] + \sqrt{\sigma}(1-\delta)\psi_a\sin\frac{1+\delta}{2}\psi_a + \sigma\left[1+\cos\psi_a\right]} \tag{59}$$

Although σ cannot be decreased arbitrarily without affecting the aperture efficiency, (59) clearly shows that the control of σ is a more effective method of decreasing S than increasing the aperture angle. It should be emphasized however, that the range of the communication system is determined both by the gain

and the suppression at the antenna. The optimum combination determines a single σ for each ψ_a angle. Assuming the discussed feed pattern, then $\eta_0 \rightarrow 1$ as $\psi_a \rightarrow 0$ while $S \rightarrow 0$ as $\psi_a \rightarrow \frac{\pi}{2}$.

Thus the absolute maximum of the range always occurs at a $\psi_a < \frac{\pi}{2}$ aperture angle!

The validity of this conclusion is not influenced by the fact that the total noise temperature of the antenna system is also determined by other parameters which are independent of ψ_a.

Fig. 15 indicates the suppression and the apparent ground temperature component for various $\sigma = \frac{F_F(\psi_a)}{F_F(0)}$ as a function of the aperture angle.

$\delta = 0.75$ was assumed throughout this calculation.

3.2.2 Diffraction Field in the presence of a Spherical Cup Reflector

The results obtained in the previous paragraph are not strictly applicable to any practical antenna because the axial length of the cylinder is infinite. The advantage of this simple model is obvious, however, for many practical problems, a more accurate analysis is needed.

In this paragraph, the screening properties of a finite spherical reflector will be analyzed.

This model approximates very closely, the paraboloidal reflector from the standpoint of back radiation.

Fig. 16 indicates the coordinate system suited to this problem. A spherical cup, with a radius of ρ and a symmetry line along

the z coordinate axis extends between $0 \leq \psi \leq \psi_a$. The general current source in the center of the coordinate system can be expressed as a current vector with l_x, l_y, and l_z components. Because the calculations for the two perpendicular current elements are similar, only the field of the l_y and l_z components will be analyzed. The far field of the l_z current element seems to be less interesting because most feed systems have only transversal current elements. However, the field structure at the edge of the reflector is identical for the l_z and l_y component if $\psi_a = \frac{\pi}{4}$. Obviously, the far field of the antenna system is determined by the <u>total</u> aperture distribution along the surface of the aperture sphere. Nevertheless, the similarity between the two far fields in the $\phi = 0$ plane remains quite considerable, if the feed produces a highly directed field towards the reflector and its pattern has practically zero amplitude for $\psi > \psi_a$. On the other hand, the far field expression of the l_z element is much simpler, therefore, it is worth while to include its analysis.

A. <u>Field of the l_z Current Element.</u>

The normalized field of the l_z current element along the $\rho \gg \lambda$ sphere has only ψ component

$$E_\psi = \sin\psi. \tag{60}$$

If the field on the rear side of the spherical cup is zero, the only component of the far field[23)]

$$E_\theta' = \bar{E}_p \bar{\iota}_\theta = \frac{j\beta e^{-j\beta R}}{4\pi R} \int_{\psi_a}^{\pi} \int_0^{2\pi} \left\{ \left[\bar{\rho}_o \times \bar{E} \right] \bar{\iota}_\phi - \left(\frac{\mu}{\epsilon} \right)^{\frac{1}{2}} \left[\bar{\rho}_o \times \bar{H} \right] \right\} e^{j\beta \bar{R}_o \bar{\rho}} \sin\psi \, d\phi \, d\psi \tag{61}$$

or, omitting the constants,

$$\bar{E}_\theta = \int_{\psi_a}^{\pi} \int_0^{2\pi} \left\{ \left[\bar{\rho}_o \times \bar{E} \right] \bar{\iota}_\phi + \bar{E} \bar{\iota}_\theta \right\} e^{jr\cos\alpha} \sin\psi \, d\phi \, d\psi \, . \tag{62}$$

(61) describes the far field of the spherical aperture. If the field is eliminated from the $0 \leq \psi \leq \psi_a$ region of the aperture sphere by a metallic cup, then the aperture is along the outside (rear) surface of this cup. Thus, (61) does not describe the field caused by the inside currents of the reflector.

The components of the various vectors in (62)

	In the			In the	
ρ	ψ	φ	x	y	z
	system			system	

$$\bar{\rho}_o = \left[1 \, , \quad 0 \, , \quad 0 \right] = \left[\sin\psi\cos\varphi \, , \sin\psi\sin\varphi \, , \quad \cos\psi \right] \tag{63}$$

$$\bar{E} = \left[0 \, , \quad \sin\psi \, , \quad 0 \right] = \left[\cos\psi\sin\psi\cos\varphi, \cos\psi\sin\psi\sin\varphi, \; -\sin\psi\cos\psi \right] \tag{64}$$

$$\bar{R}_o = \left[\sin\theta\cos\phi,\ \sin\theta\sin\phi,\ \cos\theta\right] , \tag{65}$$

$$\bar{\iota}_\phi = \left[\sin(\phi-\varphi),\ 0,\ \cos(\phi-\varphi)\right] , \tag{66}$$

$$\bar{\iota}_\theta = \left[\sin(\theta-\psi),\ \cos(\theta-\psi),\ 0\right] , \tag{67}$$

$$r = \frac{2\pi}{\lambda}\rho . \tag{68}$$

The far field is axially symmetrical. Thus, the products of (62) should be calculated only in the $\phi = 0$ plane.

$$(\bar{\rho}_o \times \bar{E})\bar{\iota}_\phi = \sin^2\psi \cos\varphi , \tag{69}$$

$$\bar{E}\bar{\iota}_\theta = \sin\psi \cos(\theta-\psi) , \tag{70}$$

$$\cos\alpha = \sin\psi \sin\theta \cos\varphi + \cos\theta \cos\psi . \tag{71}$$

Introducing

$$P_1 = r\sin\theta \sin\psi , \qquad P_2 = r\cos\theta \cos\psi , \tag{72}$$

$$E_\theta = \int_{\psi_a}^{\pi} e^{jP_2} \sin^3\psi \, K_1(P_1)\, d\psi + \int_{\psi_a}^{\pi} e^{jP_2} \sin^2\psi \cos(\theta-\psi) K_2(P_1)\, d\psi, \tag{73}$$

where

$$K_1 = j \int_0^{2\pi} \cos\varphi \sin(P_1 \cos\varphi)\, d\varphi = j 2\pi J_1(P_1) \tag{74}$$

$$K_2 = \int_0^{2\pi} \cos(P_1 \cos\varphi)\, d\varphi = 2\pi J_0(P_1) \quad . \tag{75}$$

With (74) and (75), (73) can be written as

$$E_\theta = E_{\theta 1} + j E_{\theta 2} \quad , \tag{76}$$

where

$$E_{\theta 1} = 2\pi \int_{\psi_a}^{\pi} \sin^2\psi \cos(\theta - \psi) J_0(r \sin\theta \sin\psi) e^{jr\cos\theta\cos\psi} d\psi \quad , \tag{77}$$

$$E_{\theta 2} = 2\pi \int_{\psi_a}^{\pi} \sin^3\psi \, J_1(r \sin\theta \sin\psi) e^{jr\cos\theta\cos\psi} d\psi \quad . \tag{78}$$

(76) can be easily calculated for two special cases:

a) for $\theta = 0$ (along the z axis) and

b) for $\theta = \frac{\pi}{2}$ (in the xy plane) .

a) $\Theta = 0$. Here

$$E_\Theta(0) = E_{\Theta 1}(0) = 2\pi \int_{\psi_a}^{\pi} \sin^2\psi \cos\psi \, e^{jr\cos\psi} \, d\psi = \epsilon_{11} - \epsilon_{12} + j[\epsilon_{21} - \epsilon_{22}] , \tag{79}$$

where

$$\epsilon_{11} = 2\pi\left[-J_0(r)\sin\psi_a + 2\sum_{n=1}^{\infty}(-1)^n J_{2n}(r)\int_{\psi_a}^{\pi}\cos\psi\cos 2n\psi \, d\psi\right] , \tag{80}$$

$$\epsilon_{12} = 2\pi\left[2\sum_{0}^{\infty}(-1)^n J_{2n+1}(r)\int_{\psi_a}^{\pi}\cos\psi\cos(2n+1)\psi \, d\psi\right] , \tag{81}$$

$$\epsilon_{21} = 2\pi\left[-J_0(r)\left(\sin\psi_a - \tfrac{1}{3}\sin^3\psi_a\right) + 2\sum_{n=1}^{\infty}(-1)^n J_{2n}(r)\int_{\psi_a}^{\pi}\cos^3\psi\cos 2n\psi \, d\psi\right] , \tag{82}$$

$$\epsilon_{22} = 2\pi\left[2\sum_{0}^{\infty}(-1)^n J_{2n+1}(r)\int_{\psi_a}^{\pi}\cos^3\psi\cos(2n+1)\psi \, d\psi\right] , \tag{83}$$

or

$$\epsilon_{11} = 2\pi\left[-J_0(r)\sin\psi_a + 2\sum_{n=1}^{\infty}(-1)^n J_{2n}(r) M_{2n}(\psi_a)\right] , \tag{84}$$

$$\epsilon_{12} = 2\pi\left[\mathcal{J}_1(r)\left(\pi - \psi_a - \frac{1}{2}\sin 2\psi_a\right) + 2\sum_{n=1}^{\infty}(-1)^n \mathcal{J}_{2n+1}(r)\, M_{2n+1}(\psi_a)\right] \tag{85}$$

$$\epsilon_{21} = 2\pi\left\{-\mathcal{J}_0(r)\left(\sin\psi_a - \frac{1}{3}\sin^3\psi_a\right) + 2\sum_{n=1}^{\infty}(-1)^n \mathcal{J}_{2n}(r)\left[\frac{1}{4}N_{2n}(\psi_a) + \frac{3}{4}M_{2n}(\psi_a)\right]\right\} \tag{86}$$

$$\epsilon_{22} = 2\pi\left\{-\frac{\mathcal{J}_1(r)}{4}\left(2\sin 2\psi_a + \frac{1}{4}\sin 4\psi_a + 3\psi_a - 3\pi\right) + \frac{\mathcal{J}_3(r)}{8}\left(\sin 2\psi_a + \frac{\sin 4\psi_a}{2}\right.\right.$$

$$\left. + \sin 6\psi_a\right) + 2\sum_{n=2}^{\infty}(-1)^n \mathcal{J}_{2n+1}(r)\left[\frac{1}{4}N_{2n+1}(\psi_a) + \frac{3}{4}M_{2n}(\psi_a)\right] \quad , \tag{87}$$

where

$$M_k = \int_{\psi_a}^{\pi} \cos\psi \cos k\psi \, d\psi = \begin{cases} \dfrac{\pi - \psi_a}{2} - \dfrac{\sin 2\psi_a}{4} & \text{if } k = 1 \\[2ex] \dfrac{\sin(k-1)\psi_a}{2(1-k)} - \dfrac{\sin(k+1)\psi_a}{2(k+1)} & \text{if } k \neq 1 \end{cases} \tag{88}$$

$$N_k = \int_{\psi_a}^{\pi} \cos 3\psi \cos k\psi \, d\psi = \begin{cases} \dfrac{\pi - \psi_a}{2} - \dfrac{\sin 6\psi_a}{12} & \text{if } k = 3 \\[2ex] \dfrac{\sin(3-k)\psi_a}{2(k-3)} - \dfrac{\sin(3+k)}{2(3+k)} & \text{if } k \neq 3 \end{cases} \tag{89}$$

If $\psi_a \ll 1$, then $\epsilon_{11} \gg \epsilon_{21}$ and $\epsilon_{12} \gg \epsilon_{22}$.

Thus (79) reduces

$$\frac{E_\theta(0)}{2\pi} = \frac{\epsilon_{11}}{2\pi} + j\frac{\epsilon_{12}}{2\pi}$$

$$= -J_0(r)\sin\psi_a - \psi_a\sum_{n=1}^{\infty}(-1)^n J_{2n}(r)\left[\frac{\sin(2n-1)\psi_a}{(2n-1)\psi_a} + \frac{\sin(2n+1)\psi_a}{(2n+1)\psi_a}\right]$$

$$+ j\left\{J_1(r)\left[\pi - \psi_a - \tfrac{1}{2}\sin 2\psi_a\right] - \psi_a\sum_{n=1}^{\infty}(-1)^n J_{2n+1}(r)\left[\frac{\sin 2n\psi_a}{2n\psi_a} + \frac{\sin(2n+2)\psi_a}{(2n+2)\psi_a}\right]\right. \tag{90}$$

The similarity between (90) and (53) is quite obvious. According to (90), no E_θ component exists along the z axis if $\psi_a = 0$. However, the presence of the reflector (finite ψ_a) introduces a field along the axis which varies with ψ_a , even for the axially polarized I_z current element. If r is large, the particular value of r always can be selected so that the imaginary part of (90) is negligible relative to the real part. Furthermore, in this case, the sum can be terminated at $n < r$.

With

$$\frac{\sin(2n-1)\psi_a}{(2n-1)\psi_a} + \frac{\sin(2n+1)\psi_a}{(2n+1)\psi_a} \approx 2\,\frac{\sin 2n\psi_a}{2n\psi_a}\cos\psi_a \tag{91}$$

and if r is selected at a maximum of the even Bessel function,

$$\frac{E_\theta(0)}{2\pi} \cong -J_0(r)\sin\psi_a - 2\psi_a\cos\psi_a \sum_1^r (-1)^n J_{2n}(r)\frac{\sin 2n\psi_a}{2n\psi_a}$$

$$\cong -\frac{\sqrt{2}}{D_\lambda^{\frac{1}{2}}}\sin^{1/2}\psi_a\left(\sin\psi_a + \pi\psi_a\cos\psi_a\right) \tag{92}$$

According to the approximate expression of (92), the axial field has a maximum and a zero determined by

$$\tan\psi_{am} = \frac{1+\pi}{\pi}\,\frac{1}{\psi_{am}} \tag{93}$$

and

$$\tan\psi_{ao} = -\pi\psi_{ao} \tag{94}$$

As Fig. 17 shows, $\psi_{am} < \frac{\pi}{2}$ and $\psi_{ao} > \frac{\pi}{2}$.

Another single observation can be made on the basis of (92). The field of a paraboloidal reflector antenna system along its beam maximum is proportional to D_λ. Thus, from (92), the front to back ratio is proportional to $D_\lambda^{\frac{3}{2}}$. The other factor of proportionality is σ as defined in Fig. 10. Thus, the front to back ratio

$$\frac{F}{B} \cong \frac{D_\lambda^{\frac{3}{2}}}{\sigma} \tag{95}$$

(For isotropic feed source $\sigma = 1$). If $D_\lambda = 50$ and $\sigma = 0.335$, then $F/B = 10^3 = 60$ db.

b) $\Theta = \frac{\pi}{2}$. Here

$$\frac{E_\theta\left(\frac{\pi}{2}\right)}{2\pi} =$$

$$= j\int_{\psi_a}^{\pi} \sin^3\psi\, J_1(r\sin\psi)\,d\psi - \int_{\psi_a}^{\pi} \sin^3\psi\, J_0(r\sin\psi)\,d\psi$$

$$= -\int_{-\psi_a' = -\left(\frac{\pi}{2}-\psi_a\right)}^{\pi/2} \cos^3\psi\, J_0(r\cos\psi)\,d\psi + j\int_{-\psi_a'}^{\pi/2} \cos^3\psi\, J_1(r\cos\psi)\,d\psi$$

$$= -\int_0^{\pi/2} \cos^3\psi\, J_0(r\cos\psi)\,d\psi + j\int_0^{\pi/2} \cos^3\psi\, J_1(r\cos\psi)\,d\psi$$

$$+ \int_0^{\psi_a'} \cos^3\psi\, J_0(r\cos\psi)\,d\psi - j\int_0^{\psi_a'} \cos^3\psi\, J_1(r\cos\psi)\,d\psi \tag{96}$$

The first two integrals can easily be integrated,

$$-\int_0^{\pi/2} \cos^3\psi\, J_0(r\cos\psi)\,d\psi =$$

$$= -\frac{1}{4}\int_0^{\pi/2} \cos 3\psi\, J_0(r\cos\psi)\,d\psi - \frac{3}{4}\int_0^{\pi/2} \cos\psi\, J_0(r\cos\psi)\,d\psi$$

$$= -\frac{\pi}{8} J_{\frac{3}{2}}\left(\frac{r}{2}\right) J_{-\frac{3}{2}}\left(\frac{r}{2}\right) - \frac{3\pi}{8} J_{\frac{1}{2}}\left(\frac{r}{2}\right) J_{-\frac{1}{2}}\left(\frac{r}{2}\right)$$

$$j\int_0^{\pi/2} \cos^3\psi \, J_1(r\cos\psi)\, d\psi =$$

$$= \frac{j}{4}\int_0^{\pi/2} \cos 3\psi \, J_1(r\cos\psi)\, d\psi + j\frac{3}{4}\int_0^{\pi/2} \cos\psi \, J_1(r\cos\psi)\, d\psi$$

$$= j\frac{\pi}{8} J_2\left(\frac{r}{2}\right) J_{-1}\left(\frac{r}{2}\right) + j\frac{3\pi}{8} J_1\left(\frac{r}{2}\right) J_0\left(\frac{r}{2}\right) .$$

In the last two integrals of (96), the assymptotic form of the Bessel functions can be used if $r \gg 1$ and $\psi_a' \ll 1$. This is the practical case.

Then

$$\int_0^{\psi_a'} \cos^3\psi \, J_0(r\cos\psi)\, d\psi \cong$$

$$\cong \left(\frac{2}{\pi r}\right)^{\frac{1}{2}} \int_0^{\psi_a'} \cos^{5/2}\psi \cos(r\cos\psi)\, d\psi \cong \left(\frac{2}{\pi r}\right)^{\frac{1}{2}} \cos^{5/2}\frac{\psi_a'}{3} \int_0^{\psi_a'} \cos(r\cos\psi)\, d\psi$$

$$= \left(\frac{2}{\pi r}\right)^{\frac{1}{2}} \psi_a' \cos^{5/2}\frac{\psi_a'}{3}\left[J_0(r) - 2\sum_{n=1}^{\infty}(-1)^n J_{2n}(r)\frac{\sin 2n\psi_a'}{2n\psi_a'}\right]$$

$$-j\int_0^{\psi_a'} \cos^3\psi \, J_1(r\cos\psi)\, d\psi \cong$$

$$\cong -j\left(\frac{2}{\pi r}\right)^{\frac{1}{2}} 2\psi_a' \cos^{5/2}\frac{\psi_a'}{3} \sum_0^{\infty}(-1)^n J_{2n+1}(r)\frac{\sin(2n+1)\psi_a'}{(2n+1)\psi_a'} .$$

With the last results, the form of (96)

$$\frac{E_\theta\left(\frac{r}{2}\right)}{2\pi} \cong$$

$$\cong -\frac{\pi}{8} J_{\frac{3}{2}}\left(\frac{r}{2}\right) J_{-\frac{3}{2}}\left(\frac{r}{2}\right) - \frac{3\pi}{8} J_{\frac{1}{2}}\left(\frac{r}{2}\right) J_{-\frac{1}{2}}\left(\frac{r}{2}\right)$$

$$+ j\left[\frac{\pi}{8} J_2\left(\frac{r}{2}\right) J_{-1}\left(\frac{r}{2}\right) + \frac{3\pi}{8} J_1\left(\frac{r}{2}\right) J_0\left(\frac{r}{2}\right)\right]$$

$$+\left(\frac{2}{\pi r}\right)^{\frac{1}{2}}\psi_a' \cos^{5/2}\frac{\psi_a'}{3}\left[\mathcal{J}_0(r) - 2\sum_{n=1}^{\infty}(-1)^n \mathcal{J}_{2n}(r)\,\frac{\sin 2n\psi_a'}{2n\psi_a'}\right]$$

$$-\,j\left(\frac{2}{\pi r}\right)^{\frac{1}{2}}\psi_a' \cos^{5/2}\frac{\psi_a'}{3}\; 2\sum_{n=0}^{\infty}(-1)^n \mathcal{J}_{2n+1}(r)\,\frac{\sin(2n+1)\psi_a'}{(2n+1)\psi_a'} \quad . \tag{97}$$

(97) can be used to calculate the field in the $\Theta = \frac{\pi}{2}$ plane, assuming that the "complementary aperture angle" ψ_a' is small. Thus, varying ψ_a', the field in the "transition" zone can be studied without integrating (77) and (78) for arbitrarily Θ (See Fig. 18). In other words, the role of Θ and ψ_a' can be interchanged in the transition range. As ψ_a' increases, the validity of (97) deteriorates, but in that case, $E_\Theta\left(\frac{\pi}{2}\right)$ obviously approaches the far field of the I_z current element itself.

B. <u>Diffracted Field of the I_y Current Element.</u>

If the current element is along the y axis, the geometrical relationship can be studied by means of Fig. 19a and b.

$$|\bar{E}_\gamma| = \sin\gamma$$

$$\bar{E}_{\gamma o} = \frac{\bar{E}_\gamma}{|\bar{E}_\gamma|} = \left[\cos\gamma\sin\pi,\ -\sin\gamma,\ \cos\gamma\cos\pi\right] \tag{98}$$

For further calculations, $\bar{E}_\gamma$ should be expressed in terms of φ, ψ instead of γ and π. The transformations are determined by

$$\bar{E}_{\gamma o}\,\bar{\rho}_o = 0$$

$$\cos\gamma = \bar{\rho}_o\,\bar{\iota}_{yo} \tag{99}$$

where

$$\bar{\rho}_o = [\sin\psi\cos\varphi\,,\ \sin\psi\sin\varphi\,,\ \cos\psi]$$

$$\bar{\iota}_y = [\ 0\ ,\ 1\ ,\ 0\ ] \tag{100}$$

Thus

$$\cos\gamma\sin\pi\cos\varphi - \sin\gamma\sin\psi\sin\varphi + \cos\gamma\cos\pi\cos\psi = 0 \tag{101}$$

$$\cos\gamma = \sin\psi\sin\varphi \tag{102}$$

From (101) and (102)

$$\cos\pi = \frac{\cos\psi}{[1 - \sin^2\psi\sin^2\varphi]^{1/2}} \tag{103}$$

The aperture field from (96), (101) and (102)

$$\bar{E}_\gamma = [e_x\,,\ e_y\,,\ e_z] \tag{104}$$

where

$$e_x = \sin\gamma\cos\gamma\sin\pi = \sin^2\psi\sin\varphi\cos\varphi \tag{105}$$

$$e_y = -\sin^2\gamma = \sin^2\psi\sin^2\varphi - 1 \tag{106}$$

$$e_z = \sin\gamma\cos\gamma\cos\pi = \sin\psi\cos\psi\sin\varphi \tag{107}$$

For $\psi \ll \pi/2$

$$e_x \cong 0 \quad , \quad e_y \cong -1 \quad , \quad e_z \cong \psi\sin\varphi \tag{108}$$

The far field at the point P

$$\bar{E}_p' = -\frac{j\beta e^{-j\beta R}}{4\pi R}\bar{R}_o \times \iint\left[(\bar{\rho}_o \times \bar{E}_\gamma) + (\bar{E}_\gamma \times \bar{R}_o)\right] e^{j\beta\bar{R}_o\bar{\rho}} dA \tag{109}$$

or dropping the constants

$$\bar{E}_p = \bar{R}_o \times \iint(\bar{a} + \bar{b})\, e^{jr\bar{R}_o\bar{\rho}_o}\, dA \tag{110}$$

where

$$\bar{a} = \bar{\rho}_o \times \bar{E}_\gamma \tag{111}$$

$$\bar{b} = \bar{E}_\gamma \times \bar{R}_o \tag{112}$$

$$\bar{\rho}_o = [\rho_x, \rho_y, \rho_z] = [\sin\psi\cos\varphi, \sin\psi\sin\varphi, \cos\psi] \tag{113}$$

$$\bar{R}_o = [R_x, R_y, R_z] = [\sin\Theta\cos\phi, \sin\Theta\sin\phi, \cos\Theta] \tag{114}$$

and in the $\phi = 0$ plane

$$\bar{R}(0) = [\sin\Theta, 0, \cos\Theta] \tag{115}$$

The following calculations will be restricted to the $\phi = 0$ plane.

Here

$$E_\theta(\Theta, 0) = \frac{E_z}{\sin\Theta} \quad \text{and} \quad E_\phi = (\Theta, 0) = E_y \,. \tag{116}$$

<u>Calculation of $E_\theta(\Theta, 0)$</u>

Calculating the products indicated in (110) and taking into account (116), the E_θ component of the field can be expressed as

$$E_\theta(\Theta, 0) = \\ = \int_0^{2\pi}\int_{\psi_a}^{\pi} [A_1 - A_2 + A_3 - A_4]\, e^{jr[\sin\psi\cos\varphi\sin\Theta + \cos\psi\cos\Theta]}\, d\varphi\, d\psi \,, \tag{117}$$

where

$$A_1 = \frac{R_x^2 e_z}{\sin\Theta} = \sin\Theta\sin\psi\cos\psi\sin\varphi = -\frac{j}{2}\sin\Theta\sin\psi\cos\psi\left[e^{j\varphi} - e^{-j\varphi}\right] \,,$$

$$A_2 = \frac{R_x e_z \rho_x}{\sin\Theta} = \frac{1}{2}\sin^2\psi\cos\psi\,\sin 2\varphi \,,$$

$$A_3 = \frac{R_x R_z e_x}{\sin\Theta} = A_2 \,,$$

$$A_4 = \frac{R_x R_z e_x}{\sin\Theta} = \frac{1}{2}\cos\Theta\sin^2\psi\,\sin 2\varphi = -\frac{j}{4}\cos\Theta\sin^2\psi\left[e^{j2\varphi} - e^{-j2\varphi}\right] \,. \tag{118}$$

$$j2E_\theta(\theta,0) =$$

$$= \sin\Theta \int_{\psi_a}^{\pi} \sin\psi \cos\psi \, e^{jr\cos\Theta\cos\psi} \left\{ \int_0^{2\pi} \left[e^{j(\varphi + r\sin\Theta\sin\psi\cos\varphi)} - \right.\right.$$

$$\left.\left. - e^{j(-\varphi + r\sin\Theta\sin\psi\cos\varphi)} \right] d\varphi \right\} d\psi \quad +$$

$$+ \frac{\cos\Theta}{2} \int_{\psi_a}^{\pi} \sin^2\psi \, e^{jr\cos\Theta\cos\psi} \left\{ \int_0^{2\pi} \left[e^{j(2\varphi + r\sin\Theta\sin\psi\cos\varphi)} - \right.\right.$$

$$\left.\left. - e^{j(-2\varphi + r\sin\Theta\sin\psi\cos\varphi)} \right] d\varphi \right\} d\psi$$

$$= j4\pi \sin\Theta \int_{\psi_a}^{\pi} \sin\psi \cos\psi \, e^{jr\cos\Theta\cos\psi} J_1(r\sin\Theta\sin\psi) \, d\psi \; -$$

$$- 2\pi \cos\Theta \int_{\psi_a}^{\pi} \sin^2\psi \, e^{jr\cos\Theta\cos\psi} J_2(r\sin\Theta\sin\psi) \, d\psi \tag{119}$$

The integration of (119) for arbitrary r and Θ is quite complicated. It is more practical to integrate separately for $r\sin\Theta \ll 1$ and for $r\sin\Theta \gg 1$

If $r\sin\Theta \ll 1$

$$J_1(r\sin\Theta\sin\psi) \cong \frac{r}{2}\sin\Theta\sin\psi \quad ,$$

$$J_2(r\sin\Theta\sin\psi) \cong \frac{r^2}{8}\sin^2\Theta\sin^2\psi \tag{120}$$

and

$$E_\theta(\theta,0) =$$

$$= \pi r\sin^2\Theta\int_{\psi_a}^{\pi}\sin^3\psi\cos\psi\, e^{jr\cos\Theta\cos\psi}\,d\psi + j\frac{\pi}{8}r^2\sin^2\Theta\cos\Theta\int_{\psi_a}^{\pi}\sin^4\psi\, e^{jr\cos\Theta\cos\psi}\,d$$

$$= \pi r\sin^2\Theta\Big\{J_0(r\cos\Theta)M_0^1 + 2\sum_1^\infty(-1)^n J_{2n}(r\cos\Theta)M_{2n}^1 + $$
$$+ j2\sum_0^\infty(-1)^n J_{2n+1}(r\cos\Theta)M_{2n+1}^1\Big\}$$

$$+ j\frac{\pi}{8}r^2\sin^2\Theta\cos\Theta\Big\{J_0(r\cos\Theta)M_0^2 + 2\sum_1^\infty(-1)^n J_{2n}(r\cos\Theta)M_{2n}^2 + $$
$$+ j2\sum_0^\infty(-1)^n J_{2n+1}(r\cos\Theta)M_{2n+}^2\Big\} \tag{121}$$

where

$$M_k^1 = \int_{\psi_a}^{\pi}\sin^3\psi\cos\psi\cos k\psi\,d\psi$$

$$M_k^2 = \int_{\psi_a}^{\pi}\sin^4\psi\cos k\psi\,d\psi \tag{122}$$

If not only $r\sin\Theta$ is small but Θ is also small, then, $r\cos\Theta \approx r$ and the expressions in the brackets of (121) become independent of Θ. Then,

$$E_\theta(\theta,0) = \pi r\sin^2\Theta\; K_1(r,\psi_a) + j\frac{\pi}{8}r^2\sin^2\Theta\cos\Theta\, K_2(r,\psi_a) \quad , \tag{123}$$

where the K_1 and K_2 are not functions of Θ and are the sums indicated in (121).

If $r\sin\Theta = u \gg 1$

$$\mathcal{J}_1(u\sin\psi) \cong -j\frac{1}{\sqrt{2\pi u}}\, e^{-j\frac{\pi}{4}}\, \frac{e^{ju\sin\psi} - j\, e^{-ju\sin\psi}}{\sin^{1/2}\psi}$$

$$\mathcal{J}_2(u\sin\psi) \cong -\frac{1}{\sqrt{2\pi u}}\, e^{-j\frac{\pi}{4}}\, \frac{e^{ju\sin\psi} + j\, e^{-ju\sin\psi}}{\sin^{1/2}\psi}$$

(124)

Introducing (124) into (119)

$$\sqrt{2\pi u}\; e^{j\frac{\pi}{4}}\, E_\Theta(\Theta,0) =$$

$$= 2\pi\sin\Theta \int_{\psi_a}^{\pi} \sin^{1/2}\psi\cos\psi\left[e^{jr\cos(\psi-\Theta)} - j\, e^{jr\cos(\psi+\Theta)}\right] d\psi$$

$$+ j\pi\cos\Theta \int_{\psi_a}^{\pi} \sin^{3/2}\psi\left[e^{jr\cos(\psi-\Theta)} + j\, e^{jr\cos(\psi+\Theta)}\right] d\psi$$

$$= \mathcal{J}_0(r)\sum_{i=1}^{4} N_0^i + 2\left(\sum_{i=1}^{4} N_{2n}^i\right)\left(\sum_{n=1}^{\infty}(-1)^n \mathcal{J}_{2n}(r)\right) + j2\left(\sum_{i=1}^{4} N_{2n+1}^i\right)\left(\sum_{n=0}^{\infty}(-1)^n \mathcal{J}_{2n+1}(r)\right)$$

(125)

where

$$N_k^1 = 2\pi\sin\Theta \int_{\psi_a-\Theta}^{\pi-\Theta} \sin^{1/2}(z+\Theta)\cos(z+\Theta)\cos kz\, dz \quad ,$$

$$N_k^2 = -j2\pi\sin\Theta \int_{\psi_a+\Theta}^{\pi+\Theta} \sin^{1/2}(z-\Theta)\cos(z+\Theta)\cos kz\, dz \quad ,$$

$$N_k^{\xi} = j\pi\cos\Theta \int_{\psi_a-\Theta}^{\pi-\Theta} \sin^{3/2}(z+\Theta)\cos kz\, dz \quad ,$$

$$N_k^{\eta} = -\pi\cos\Theta \int_{\psi_a+\Theta}^{\pi+\Theta} \sin^{3/2}(z+\Theta)\cos kz\, dz \quad .$$

(126)

The general formulas given by (125) and (126) are rather complicated to analyse the field as a function of Θ. Again, a somewhat simpler working expression can be found by selecting $\Theta = \frac{\pi}{2}$ and then varying the aperture angle in the neighbourhood of this value. The calculation can start directly from (119), which for $\Theta = \frac{\pi}{2}$

$$E_\Theta\left(\frac{\pi}{2},0\right) = 2\pi \int_{\psi_a}^{\pi} \sin\psi\cos\psi\, J_1(r\sin\psi)\, d\psi$$

$$= -\pi \int_{-\psi_a'}^{\pi/2} \sin 2\psi\, J_1(r\cos\psi)\, d\psi$$

$$= -\pi \int_0^{\pi/2} \frac{4}{\pi}\left[\frac{1}{2} - \frac{\cos 4\psi}{1.3} - \frac{\cos 8\psi}{3.5} - \frac{\cos 12\psi}{5.7} - \dots\right] J_1(r\cos\psi)\, d\psi$$

$$+ \pi \int_0^{\psi_a'} \sin 2\psi\, J_1(r\cos\psi)\, d\psi$$

$$= -\frac{\pi}{2} J_{\frac{1}{2}}\left(\frac{r}{2}\right) J_{-\frac{1}{2}}\left(\frac{r}{2}\right) + \pi \sum_{n=1}^{\infty} \frac{1}{(2n-1)(2n+1)} J_{\frac{4n+1}{2}}\left(\frac{r}{2}\right) J_{-\frac{4n+1}{2}}\left(\frac{r}{2}\right)$$

$$+ \pi \int_0^{\psi_a'} \sin 2\psi\, J_1(r\cos\psi)\, d\psi \quad , \qquad (127)$$

where the $\int_0^{\pi/2}$ integral was calculated from the formula given by Watson[24]. The remaining integral can be calculated

separately for $r\cos\psi_a' \ll 1$ and $r\cos\psi_a' \gg 1$. The most interesting practical case occurs if $\psi_a' \ll 1$. Then for arbitrary r

$$\int_0^{\psi_a'} \sin 2\psi \, J_1(r\cos\psi)\, d\psi \approx J_1(r)\, \frac{1-\cos 2\psi_a'}{2} \tag{128}$$

and the field

$$E_\Theta\left(\frac{\pi}{2},0\right) = -\frac{\pi}{2} J_{\frac{1}{2}}\left(\frac{r}{2}\right) J_{-\frac{1}{2}}\left(\frac{r}{2}\right) + \frac{\pi}{2} J_1(r)\left(1-\cos 2\psi_a'\right)$$
$$+ \pi \sum_1^\infty \frac{1}{(2n-1)(2n+1)} J_{\frac{4n+1}{2}}\left(\frac{r}{2}\right) J_{-\frac{4n+1}{2}}\left(\frac{r}{2}\right) \tag{129}$$

The series in (129) converges rapidly. Therefore, the expression is quite valuable for numerical calculations.

<u>Calculation of $E_\phi(\Theta, 0)$.</u>

From (116) and (110)

$$E_\phi(\Theta,0) = E_y = \iint \left[\bar{R}_0 \times (\bar{a} + \bar{b})\right]_y e^{jr\bar{R}_0\bar{\rho}_0}\, dA \,, \tag{130}$$

where

$$\left[\bar{R}_0 \times (\bar{a}+\bar{b})\right]_y \equiv \mathcal{E}_y =$$

$$= -R_x(a_z + b_z) + R_z(a_x + b_x) =$$

$$= -\sin\Theta\left[\sin\psi\cos\varphi\left(\sin^2\psi\sin^2\varphi - 1\right) + \sin^3\psi\sin^2\varphi\cos\varphi - \right.$$

$$\left. - \sin\Theta\left(\sin^2\psi\sin^2\varphi - 1\right)\right] + \cos\Theta\left[\sin^2\psi\cos\psi\sin^2\varphi - \right.$$

$$\left. - \cos\psi\left(\sin^2\psi\sin^2\varphi - 1\right) + \cos\Theta\sin\psi\cos\psi\sin\varphi\right] \tag{131}$$

For $\Theta = \frac{\pi}{2}$

$$\xi_y = -\cos^2\psi + \left(\sin\psi\cos^2\psi - \sin^3\psi\right)\cos\varphi - \sin^2\psi\cos^2\psi \tag{132}$$

$$E_\phi\left(\tfrac{\pi}{2}, 0\right) = -\int_{\psi_a}^{\pi}\cos^2\psi\, e^{jr\cos\Theta\cos\psi}\left\{\int_0^{2\pi} e^{jr\sin\Theta\sin\psi\cos\varphi}\, d\varphi\right\} d\psi +$$

$$+\frac{1}{2}\int_{\psi_a}^{\pi}\left(\sin\psi\cos^2\psi - \sin^3\psi\right) e^{jr\cos\Theta\cos\psi}\left\{\int_0^{2\pi}\left[e^{j(\varphi + r\sin\Theta\sin\psi\cos\varphi)} + e^{j(-\varphi + r\sin\Theta\sin\psi\cos\varphi)}\right] d\varphi\right\} d\psi -$$

$$-\frac{1}{2}\int_{\psi_a}^{\pi}\sin^2\psi\, e^{jr\cos\Theta\cos\psi}\left\{\int_0^{2\pi} e^{jr\sin\Theta\sin\psi\cos\varphi}\, d\varphi\right\} d\psi -$$

$$-\frac{1}{2}\int_{\psi_a}^{\pi}\sin^2\psi\, e^{jr\cos\Theta\cos\psi}\left\{\frac{1}{2}\int_0^{2\pi}\left[e^{j(2\varphi + r\sin\Theta\sin\psi\cos\varphi)} + e^{j(-2\varphi + r\sin\Theta\sin\psi\cos\varphi)}\right] d\varphi\right\} d\psi$$

$$= -2\pi\int_{\psi_a}^{\pi}\cos^2\psi\, e^{jr\cos\Theta\cos\psi}\, J_0(r\sin\Theta\sin\psi)\, d\psi +$$

$$+ j2\pi\int_{\psi_a}^{\pi}\left(\sin\psi\cos^2\psi - \sin^3\psi\right) e^{jr\cos\Theta\cos\psi}\, J_1(r\sin\Theta\sin\psi)\, d\psi -$$

$$-\pi\int_{\psi_a}^{\pi}\sin^2\psi\, e^{jr\cos\Theta\cos\psi}\, J_0(r\sin\Theta\sin\psi)\, d\psi +$$

$$+\pi\int_{\psi_a}^{\pi}\sin^2\psi\, e^{jr\cos\Theta\cos\psi}\, J_2(r\sin\Theta\sin\psi)\, d\psi \tag{133}$$

$$= -2\pi A_1 + j2\pi A_2 - \pi A_3 + \pi A_4 ,$$

where for $\Theta = \frac{\pi}{2}$

$$A_1 = \int_{\psi_a}^{\pi} \cos^2\psi \, J_0(r\sin\psi)\, d\psi = \int_{-\psi_a'}^{\pi/2} \sin^2\psi \, J_0(r\cos\psi)\, d\psi = \frac{1}{2}\int_{-\psi_a'}^{\pi/2} (1-\cos 2\psi) J_0(r\cos\psi)\, d\psi$$

$$A_2 = \int_{\psi_a}^{\pi} (\sin\psi\cos^2\psi - \sin^3\psi) J_1(r\sin\psi)\, d\psi = -\frac{1}{2}\int_{-\psi_a'}^{\pi/2} (\cos\psi + \cos 3\psi) J_1(r\cos\psi)\, d\psi$$

$$A_3 = \int_{\psi_a}^{\pi} \sin^2\psi \, J_0(r\sin\psi)\, d\psi = \frac{1}{2}\int_{-\psi_a'}^{\pi/2} (1+\cos 2\psi) J_0(r\cos\psi)\, d\psi$$

$$A_4 = \int_{\psi_a}^{\pi} \sin^2\psi \, J_2(r\sin\psi)\, d\psi = \frac{1}{2}\int_{-\psi_a'}^{\pi/2} (1+\cos 2\psi) J_2(r\cos\psi)\, d\psi \tag{134}$$

$$E_\phi\left(\frac{\pi}{2}, 0\right) =$$

$$= -\frac{\pi^2}{2} J_0\left(\frac{r}{2}\right) + \frac{\pi^2}{4} J_2\left(\frac{r}{2}\right) J_0\left(\frac{r}{2}\right) - j\frac{\pi^2}{2} J_0\left(\frac{r}{2}\right) J_1\left(\frac{r}{2}\right) -$$

$$- j\frac{\pi^2}{2} J_2\left(\frac{r}{2}\right) J_1\left(\frac{r}{2}\right) - \frac{\pi^2}{4} J_0^2\left(\frac{r}{2}\right) + \frac{\pi^2}{2} J_2\left(\frac{r}{2}\right) J_0\left(\frac{r}{2}\right) +$$

$$+\pi\Big\{ -\int_0^{\psi_a'} (1-\cos 2\psi) J_0(r\cos\psi)\, d\psi - j\int_0^{\psi_a'} (\cos\psi + \cos 3\psi) J_1(r\cos\psi)\, d\psi -$$

$$-\frac{1}{2}\int_0^{\psi_a'} (1+\cos 2\psi) J_0(r\cos\psi)\, d\psi + \frac{1}{2}\int_0^{\psi_a'} (1+\cos 2\psi) J_2(r\cos\psi)\, d\psi \Big\} \tag{135}$$

For $\psi_a' \ll 1$ and $r = \frac{\pi}{2}(2k+1) + \frac{\pi}{4}$, where k is a positive integer, the bracket in (135) becomes

$$\{\quad\} \cong -j\, 2 J_1(r)\, \psi_a'$$

and

$$E_\phi\left(\frac{\pi}{2},0\right) \cong \frac{3\pi^2}{4} J_2\left(\frac{r}{2}\right) J_0\left(\frac{r}{2}\right) - \frac{3\pi^2}{4} J_0^2\left(\frac{r}{2}\right)$$

$$-j\left[\frac{\pi^2}{2} J_0\left(\frac{r}{2}\right) J_1\left(\frac{r}{2}\right) + \frac{\pi^2}{4} J_2\left(\frac{r}{2}\right) J_1\left(\frac{r}{2}\right) + 2\pi J_1(r)\psi_a'\right] \tag{136}$$

For $r \gg 1$,

$$E_\phi\left(\frac{\pi}{2},0\right) \cong -\frac{3}{2}\pi^2 J_0^2\left(\frac{r}{2}\right) - j\left[\frac{\pi}{4} J_0\left(\frac{r}{2}\right) J_1\left(\frac{r}{2}\right) + 2\pi J_1(r)\psi_a'\right]$$

The total field along the x axis ($\phi = 0$, $\theta = \frac{\pi}{2}$)

$$|E|^2 = E_\theta\left(\frac{\pi}{2},0\right) E_\theta^*\left(\frac{\pi}{2},0\right) + E_\phi\left(\frac{\pi}{2},0\right) E_\phi^*\left(\frac{\pi}{2},0\right) , \tag{137}$$

where E_θ and E_ϕ are given by (127) and (135) for arbitrarily ψ_a and by (129) and (136) for $\psi_a' \ll 1$.

In the latter case

$$|E|^2 = \left[-\frac{\pi}{2} J_{\frac{1}{2}}\left(\frac{r}{2}\right) J_{-\frac{1}{2}}\left(\frac{r}{2}\right) + \right.$$

$$\left. + \pi \sum_1^\infty \frac{1}{(2n-1)(2n+1)} J_{\frac{4n+1}{2}}\left(\frac{r}{2}\right) J_{-\frac{4n+1}{2}}\left(\frac{r}{2}\right) + \frac{\pi}{2} J_1(r)(1-\cos 2\psi_a')\right]^2 +$$

$$+\left[\frac{3\pi^2}{4} J_0\left(\frac{r}{2}\right) J_2\left(\frac{r}{2}\right) - \frac{3\pi^2}{4} J_0^2\left(\frac{r}{2}\right)\right]^2 +$$

$$+\left[\frac{\pi^2}{2} J_0\left(\frac{r}{2}\right) J_1\left(\frac{r}{2}\right) + \frac{\pi^2}{4} J_1\left(\frac{r}{2}\right) J_2\left(\frac{r}{2}\right) + 2\pi J_1(r)\psi_a'\right]^2 \tag{138}$$

Given a fixed value to ψ_a', it is possible to determine from (138) an optimum r, which results in a minimum field along the x axis. Applying the Babinet principle, this method can be used to determine the optimum radii of a radiating spherical cup which extends over $0 \leq \psi \leq \psi_a$ and produces minimum field along the x axis.

4. <u>Thermal Radiation of Wire Gratings</u>

It was stated in the general discussion of the antenna noise (Section 2) that the thermal radiation of a wire-gratings reflector is approximately proportional to its projected area. For optical wavelengths, this fact is expressed by the familiar Lambert Law. However, this law is not valid if the surface dimensions of the radiator are small relative to the wavelength.

In this paragraph, the thermal radiation of wire gratings will be calculated for microwave frequencies.

Fig. 20 shows the assumed geometry. The z component of the electrical field at the point P of the 0th wire

$$E_{op} = K_1 \int_0^{2\pi} I_0 H_0^1(r_0)\, d\phi + \\ + K_1 \sum_{n=1}^{\infty} \int_{C_n} I_n H_0^1(r_n)\, d\phi + K_1 \sum_{n=1}^{\infty} \int_{C_{-n}} I_{-n} H_0^1(r_{-n})\, d\phi \,, \tag{139}$$

where

I_n = the z component of the instantaneous circumferential noise current on the surface of the nth cylinder. It will be assumed

that all the wires are at the same temperature, thus the time average of the root mean square currents are equal on all cylinders.

r_n = electrical distance between a typical point of the nth cylinder and the point P on the 0th cylinder , K_i $(i = 1, 2, \ldots)$ = factor of proportionality.

Only the first order interactions between the wires will be taken into account. Then,

$$r_0 = 2\rho \cos\frac{\phi}{2}$$

$$r_1 = \ell\left[4\left(\frac{\rho}{\ell}\right)^2 \sin^2\frac{\phi}{2} + 1 - 2\,\frac{\rho}{\ell}\sin\phi\right]^{\frac{1}{2}}$$

$$r_1 \cong \ell\left[1 - 2\frac{\rho}{\ell}\sin\phi\right]^{\frac{1}{2}} \cong \ell - \rho\sin\phi \qquad \text{if} \quad \frac{\rho}{\ell} \ll 1 \tag{140}$$

$$E_{op} = K_1\int_0^{2\pi} I_0 H_0^1(2\rho\cos\phi)\,d\phi + K_1\int_0^{2\pi}(I_1 + I_{-1})H_0^1(\ell - \rho\sin\phi)\,d\phi \tag{141}$$

The instantaneous current can be expressed as a Fourier series.

$$I_n = K_2\,\epsilon_n(t)\,e^{j\varphi_n(t)}\sum_0^\infty A_k\cos k\phi \tag{142}$$

where $\epsilon_n(t)\,e^{j\varphi_n(t)}$ is the complex instantaneous noise voltage along the surface of the nth wire. Inserting the first two members of the series from (142) into (141),

calculating the time average and taking into account that the total electrical field should disappear at the point P,

$$\int_0^{2\pi}(A_0 + A_1\cos\phi)\, H_0^1\left(2\rho\cos\frac{\phi}{2}\right) d\phi + \int_0^{2\pi}(A_0 + A_1\cos\phi) H_0^1(\ell - \rho\sin\phi)\, d\phi = 0 \tag{143}$$

From (143), the ratio of the Fourier coefficients

$$\frac{A_1}{A_0} = -\frac{\int_0^{2\pi}\left[H_0^1\left(2\rho\cos\frac{\phi}{2}\right)\right]d\phi + \int_0^{2\pi}\left[H_0^1(\ell-\rho\sin\phi)\right]d\phi}{\int_0^{2\pi}\cos\phi\left[H_0^1\left(2\rho\cos\frac{\phi}{2}\right) + H_0^1(\ell-\rho\sin\phi)\right]d\phi} \tag{144}$$

The instantaneous far field of the current on the 0th wire at a distance $R = L/\beta$

$$E_0 = K_3 \int_0^{2\pi} I_0 \frac{e^{-j\beta R}}{\sqrt{\beta R}} e^{j\rho\sin\phi}\, d\phi \approx$$

$$\approx K_4 \frac{e^{-jL}}{\sqrt{L}} \epsilon_0(t)\, e^{j\varphi_0(t)} \int_0^{2\pi}(A_0 + A_1\cos\phi)\, e^{j\rho\sin\phi}\, d\phi \approx$$

$$\approx K_5 A_0 \epsilon_0(t)\, e^{j\varphi_0(t)} \frac{e^{-jL}}{\sqrt{L}} \tag{145}$$

The total field of 2m + 1 wires in a distance L perpendicular to the plane of the wires

$$E = K_5 A_0 \sum_{n=-m}^{m} \frac{\epsilon_n(t)\, e^{-jL\left(1+n\frac{\ell}{L}\right)^{1/2}}\, e^{j\varphi_n(t)}}{\left[L\left(1+n\frac{d}{L}\right)^{1/2}\right]^{1/2}} \tag{146}$$

If $m\ell = w \ll L$

$$E = K_5 \frac{e^{-jL}}{\sqrt{L}} A_o \sum_{-m}^{m} \epsilon_n(t)\, e^{-j\varphi_n'(t)} \tag{147}$$

where

$$\varphi_n'(t) = n\frac{\ell}{2} - \varphi_n(t) \tag{148}$$

The total radiated power

$$P_{inst} = \frac{EE^*}{120\pi} =$$

$$= K_6 A_o A_o^* \left[2 \sum_{-}^{m} \sum_{k}^{m} \epsilon_k(t)\, \epsilon_i(t)\, e^{-j(\varphi_k' - \varphi_i')t} + \epsilon_o^2(t)\right] \tag{149}$$

The time average of a typical term in (149)

$$\overline{\epsilon_o^2(t)} = 4R_w kT\Delta f \quad \text{if } K = i$$

$$\overline{\epsilon_k(t)\, \epsilon_i(t)\, e^{-j(\varphi_k' - \varphi_i')t}} = 0 \quad \text{if } K \neq i \,. \tag{150}$$

where R_w is the skin resistance of the wire.

From (150), the time average of the noise power from the wire gratings

$$P_w = K_7 \frac{T\Delta f}{L} A_o A_o^* (2m+1) =$$

$$= K_7 \frac{T\Delta f}{L}\left(\frac{w}{\ell}+1\right)\left\{\int_0^{2\pi}\cos\phi\left[H_0^1\left(2\rho\cos\frac{\phi}{2}\right)+H_0^1(\ell-\rho\sin\phi)\right]d\phi\right\}\times$$

$$\times\left\{\int_0^{2\pi}\cos\phi\left[H_0^1\left(2\rho\cos\frac{\phi}{2}\right)+H_0^1(\ell-\rho\sin\phi)\right]d\phi\right\}^* \tag{151}$$

If $\ell = 2\rho$, the wire gratings becomes a solid reflector. In this case, the more accurate expression of r_1 should be used.

$$r_1 = 2\rho\left[\sin^2\frac{\phi}{2} + \quad - \sin\phi\right]^{1/2} \tag{152}$$

The radiated power of the corrugated solid reflector (See Fig. 21)

$$P_s = K_7 \frac{T\Delta f}{L}\left(\frac{w}{2\rho}+1\right)\left\{\int_0^{2\pi}\cos\phi\left[H_0^1\left(2\rho\cos\frac{\phi}{2}\right)+\right.\right.$$

$$\left.\left.+H_0^1\left(2\rho\left[\sin^2\frac{\phi}{2}+1-\sin\phi\right]^{1/2}\right)\right]d\phi\right\} \tag{153}$$

The screening factor κ for $\frac{w}{\ell} \ll 1$

$$\kappa = \frac{P_w}{P_s} =$$

$$= \frac{2\rho}{\ell}\,\frac{\left\{\int_0^{2\pi}\cos\phi\left[H_0^1\left(2\rho\cos\frac{\phi}{2}\right)+H_0^1(\ell-\rho\sin\phi)\right]d\phi\right\}_1\left\{\quad\right\}_1^*}{\left\{\int_0^{2\pi}\cos\phi\left[H_0^1\left(2\rho\cos\frac{\phi}{2}\right)+H_0^1\left(2\rho\left[\sin^2\frac{\phi}{2}+1-\sin\phi\right]^{\frac{1}{2}}\right)\right]d\phi\right\}_2\left\{\quad\right\}_2^*}$$

$$= \frac{2\rho}{\ell}\,Q(\ell,\rho) \tag{154}$$

The screening factor is proportional to the projected area and the correction factor Q. The upper limit of Q is unity by definition. The lower limit of Q ($\ell \gg \rho$) can be calculated from the asymptotic form of the Hankel functions, taking into account that $\rho \ll 1$.

From (154),

$$Q = \left(\frac{1}{1+q} \right) \left(\frac{1}{1+q} \right)^* = \frac{1}{(1+q)^2} \tag{155}$$

where

$$q = \frac{\int_0^{2\pi} \cos\phi \; H_0^1\left[2\rho \left(\sin^2\frac{\phi}{2} + 1 - \sin\phi\right)^{1/2}\right] d\phi}{\int_0^{2\pi} \cos\phi \; H_0^1\left[2\rho \cos\frac{\phi}{2}\right] d\phi} \tag{156}$$

For $\rho \ll 1$

$$H_0^1\left[2\rho\left(\sin^2\frac{\phi}{2} + 1 - \sin\right)^{1/2}\right] \cong -j\frac{2}{\pi} \ln \frac{1}{2\rho\left(\frac{3}{2} - \sin\phi - \frac{1}{2}\cos\phi\right)^{\frac{1}{2}}}$$

$$= -j\frac{2}{\pi}\left\{\ln\frac{1}{2\rho} + \frac{1}{2}\ln\frac{1}{\frac{3}{2} - \sin\phi - \frac{1}{2}\cos\phi}\right\}$$

$$H_0^1\left[2\rho\cos\frac{\phi}{2}\right] = -j\frac{2}{\pi}\ln\frac{1}{2\rho\cos\frac{\phi}{2}} =$$

$$= -j\frac{2}{\pi}\left\{\ln\frac{1}{2\rho} + \ln\frac{1}{\cos\frac{\phi}{2}}\right\}.$$

Thus

$$q = \frac{\frac{1}{2}\int_0^{2\pi}\cos\phi \ln\frac{1}{\frac{3}{2} - \sin\phi - \frac{1}{2}\cos\phi}\,d\phi}{\int_0^{2\pi}\cos\phi \ln\frac{1}{\cos\frac{\phi}{2}}\,d\phi} \cong 0.155$$

and $Q_{min} = 0.749$. Thus the limits for Q

$$0.749 \leq Q \leq 1 . \tag{157}$$

According to (157), the deviation from the Lambert Law is small. However, it should be noted that the circumferential current on the wire surface is calculated from the first order approximations, which apparently is a poor approach to use in determining the denominator of (154).

5. Some Applications of the Previous Results to the Optimum Ground Antenna Problem.

In the following, some practical antenna arrangements will be discussed, applying the results of the previous sections.

5.1 Feed System Problem.

Fig. 22 shows the cross-section of a cylindrical paraboloidal reflector with an aperture angle $\psi_{ap} < \frac{\pi}{2}$ and a focal point in F_p . This reflector is illuminated with a primary feed pattern $f_F(\psi)$ (For simplicity, a plane problem will be assumed in the following)

Suppose that this primary pattern is produced in the

following way. The beam of a directive source with a radiating center F_H is pointed towards F_P. However, before this radiation reaches the F_P region, a reflector, placed along the line C reflects the rays toward the paraboloid P. The geometry of the primary reflector can be determined so that the reflected primary wave will form a cylindrical waveform with a center at F_P. If the size of the primary reflector is large relative to the wavelength, then, the method of geometrical optics can be used to calculate the amplitude of the reflected wave, at least along a circular arc D close to the reflector. According to geometrical optics, the amplitude distribution varies slowly with the angle ψ, up to the angle ψ_{aF}. This angle is determined by the "last ray" which is reflected by the reflector (See Fig. 22). Thus, beyond the angle ψ_{aF}, the amplitude along the circular aperture can be considered zero. If the size of the primary reflector is large and $\psi_{aF} < \psi_{aP}$, then $f_F(\psi) \approx 0$ for $\psi > \psi_{aP}$ and the spillover radiation is eliminated independent of ψ_{aP}. Obviously, in practice, the size of the primary reflector cannot be very large and the precise pattern of the feed system should be determined from the formula valid for a finite size, circular, aperture. Although, there is a certain small distance between the reflector contour (which is a hyperbola) and the aperture circle, the phase

can still be assumed constant along the aperture line. On the other hand, the amplitude variation along the aperture line D is a function of the illuminating source pattern and the $\overline{F_H F_P}$ distance. The actual amplitude distribution can be expressed as a Fourier series containing only the even members, $A_k \cos k\psi$. In section 3.2.1, the pattern of these distributions was calculated for k = 0 and 1 and it is straightforward to generalize these results. However, for most practical purposes, the amplitude distribution can be approximated with a constant $\cos\psi$. If the polarization is parallel with the axis of the cylinder, then the feed pattern, for uniform distribution is given by (46) and for $\cos\psi$ distribution from (27), (41) and (42).

$$f_F(\Theta) = (-\Theta, ccc) + (\Theta, ccc) - j\left[(-\Theta, csc) + (\Theta, csc)\right],$$

$$(\Theta, ccc) = \int_{\Theta}^{\psi_{aF}+\Theta} \cos\psi \cos(r_F \cos\psi)\, d\psi,$$

$$(\Theta, csc) = \int_{\Theta}^{\psi_{aF}+\Theta} \cos\psi \sin(r_F \cos\psi)\, d\psi \tag{157}$$

where r_F and ψ_{aF} are defined on Fig. 12. Equations (46) and (157) give satisfactory design formulas for the cylindrical (plane) problem, however,

most practical antenna system employs axially symmetrical paraboloid reflectors. In these cases, the more complicated formulas of the spherical problem (See Section 3.2.2) should be used to calculate the feed pattern.

Fortunately in several practical cases, it is satisfactory to determine the η_o aperture efficiency and S suppression of the antenna system. Then, an approximate method can be used based on the assumption that one of the patterns expressed by (46) and plotted in Fig. (12) is the circularly symmetrical pattern of the feed system. This method can be justified by the error-eliminating effect of the integration necessary to calculate η_o and S.

Fig. 25 shows, in this somewhat hypothetical case, the variation of η_o and S with the ψ_{aF} aperture angle for $\varrho_\lambda = 1.52$ and 6.04 while $\psi_{aF} = 60°$.

As the figure indicates, for a given set of ϱ_λ and ψ_{aF} the aperture efficiency has a maximum. The existence of this maximum is determined by the aperture tapering and spillover radiation and is affected by the aperture blocking of the feed system. With increasing primary reflector size, the uniformity in the aperture distribution of the paraboloid increases in the outer range of the aperture, but decreases in the center because of the

aperture blocking. If the primary reflector size is very large, the effect of the aperture blocking predominates.

5.2 Radiation through a Wire Gratings Reflector.

It was mentioned in section 5.1 that a convenient feed pattern can be produced by a hyperbola cylinder reflector and the far field of this reflector can be calculated on the basis of a radiating circular aperture. A somewhat similar system exists in the case of a wire gratings reflector.

Suppose, that a feed illuminates a non-perfect reflector from the focal point, then this reflector will transmit a part of the incident wave, depending on the attenuation α of the wire gratings. If attenuation is independent of ψ, then the field along the rear side of the paraboloid will be proportional to the feed pattern. In the practical case, the size of the paraboloid is large relative to the wavelength. Then, the field, with the exception of the $\psi = \psi_{ap}$ range, can be calculated, using the method of geometrical optics, along a circle close to the rear surface of the paraboloid Neglecting the refraction through the wire gratings, the phase of this field will be constant along this aperture. According to (62), this aperture distribution produces a far field proportional with

$\alpha f_F(\theta)$ in the $0 \leq \theta \leq \psi_{aF}$ range.

The far field will be constant for $0 \leq \theta \leq \psi_{aF}$ and $\psi_{aP} \leq \theta \leq \frac{\pi}{2}$ if

$$f_F(\psi_{aF}) = \alpha f_F(0) = \sigma \ . \tag{158}$$

It will be less for $\psi_{aF} < \theta < \psi_{aP}$ assuming that the feed pattern agrees with Fig. 10. For instance, if the antenna system has a gain of 30 db and the feed system itself 10 db, then $\alpha = 50$ db is required to obtain $F_{avG} = -70$ db ($S = -40$ db). At the same time, a feed pattern with a very sharp and effective "cut-off" has to be employed.

Large α can be achieved by using -

a) a relatively dense wire gratings

b) double-wall wire gratings

c) solid reflector.

The aperture blocking of the primary reflector causes physical limitation in the case of low and medium gain antennas. The feed pattern with a sharp cutoff can not be realised for $\psi_a \leq \frac{\pi}{2}$. On the other hand, if the required gain is 50 db, the attenuation $\alpha = 30$ db already produces $F_{avG} = -70$ db.

$\alpha = 30$ db can be realised with a light wire gratings. The higher gain (larger aperture size)

permits the size of a larger primary reflector and the requirement of a sharp feed pattern cutoff is less severe. In this case, the aperture angle can be considerably smaller than $\frac{\pi}{2}$.

The lower value of α results in lower thermal radiation from the reflector. Thus, in the hypothetical case, when no spillover and edge current radiation contributes to the back radiation of the antenna, the noise temperature of the antenna as a function of the wire separation has a minimum.

Fig. 23 indicates the variation of $T_{AR} + T_{AG}$ with $\frac{l}{2d}$ for $G_F = 8$, $\psi_{aF} = 52°$, $\epsilon_R = 2\%$, $T_R = 300°K$.

5.3 Edge Currents

It was shown in the previous paragraph that the spillover radiation of the feed system and the transmission through the wire gratings decrease as the aperture size of the parabola increases. Thus, in high gain antenna systems, the rear side currents may become the major source of back radiation.

It is not the aim of the present study to discuss the relationship between the feed pattern, the geometry of the reflector and the complex amplitude of the rear current. However, it is physically obvious that the effect of the rear current can be decreased if the power associated with this current absorbed or radiated into the $\frac{\pi}{2} < \Theta \leq \pi$ hemisphere [25]. The

first solution is not recommended when low thermal noise has to be observed, because any resistive loss in the antenna increases the noise temperature of the system. A solution using the second method is indicated in Fig. 25. In this arrangement, the last section of the paraboloid is modified into a corrugated surface - wave transmission line. If the depth of the corrugations is $\lambda/4$, then this transmission line has a large surface impedance and no [26, 27] currents can be propagated in the direction of ξ. This system is narrow banded, but considerable bandwidth can be obtained at the expense of effectiveness, if the depth of the corrugations is varied. To limit the required length of the corrugated line, both sides of the paraboloid can be utilized. The radiation of the rear side can be directed into the forward hemisphere by means of a reflecting plate or parasitic radiator[26]. The radiation into the rear hemisphere can be calculated from the formulas given for the diffracted field of the I_z current element (see section 3.2.2).

The calculation assumes that no circumferential current flows on the reflector. However, this is the practical case, since the circumference of the reflector is large, and it is possible to build up a long, radially corrugated surface wave line at the edge of the reflector to eliminate the radial currents. On the other hand,

the length of the circumferential corrugated line, indicated on Fig. 24 should be restricted to a short length to avoid considerable increase in the reflector cost. The far field can be calculated from (77) and (78). If $\Delta < \frac{\lambda}{2}$, then the absolute value of the field is proportional to

$$|E_\theta| \cong \Big| \sin^2\psi_a \cos(\theta-\psi_a) J_0(r\sin\theta \sin\psi_a) + \sin^3\psi_a J_1(r\sin\theta\sin\psi_a)\Big| \Delta \tag{159}$$

If $\Delta > \frac{\lambda}{2}$ but $\Delta \ll r$

$$E_\theta = 2\pi \sin^2\psi_a \cos(\theta-\psi_a) \int_{\psi_1}^{\psi_2} J_0(r\sin\theta\sin\psi) e^{jr\cos\theta\cos\psi} d\psi + j2\pi \sin^3\psi_a \int_{\psi_1}^{\psi_2} J_1(r\sin\theta\sin\psi) e^{jr\cos\theta\cos\psi} d\psi . \tag{160}$$

If the currents are limited to a narrow strip with a width of Δ on the rear side of the paraboloid, the pattern shape is determined by r rather than Δ. Then it is worth while to place another ring source with a radius of r, but shifted along the axis of the paraboloid reflector, relative to the strip line. This second ring source can be a system of half-wave dipoles with parasitic excitement. By controlling the amplitude and phase of these dipoles, the radiation of the edge currents can be decreased in the

whole rear hemisphere.

5.4 Determination of the Optimum Antenna Parameters for a Given Aperture Size.

An antenna for a space communication system can be defined to be optimum if it results in the maximum possible range for a given cost. It is difficult to estimate the cost of the antenna mathematically, but it is obvious that the cost of the antenna system increases with ψ_{ap} while D_λ is fixed. An approximate analysis shows that the cost of a large paraboloid reflector varies as

$$c \cong \left(\frac{A_p}{A_o} \right)^2 , \tag{161}$$

where A_p is the surface of the paraboloid and A_o is the aperture area. The $c = c\ (\psi_{ap})$ function is indicated in Fig. 9.

The range of the communication system is proportional to

$$R \propto \left(\frac{\eta_o}{K + S} \right)^{\frac{1}{2}} \tag{162}$$

where K is a constant (See 26).

Combining (161) and (162), the range/unit cost

$$\frac{R}{c} \propto \left(\frac{A_o}{A_p} \right)^2 \left[\frac{\eta_o}{K + S} \right]^{\frac{1}{2}} \tag{163}$$

In the last equation, the first factor is only a function of ψ_{aP} while η_o and S are functions of ψ_{aP} and the characteristics of the feed system (ψ_{aF} , ρ_λ). The curves given in Fig. 12 cover a wide range of practical feed patterns. In each case, the aperture efficiency η_o and suppression S can be determined as a function of ψ_{aP} and then the $\frac{R}{c}$ function can be plotted. Fig. 25 shows the typical curves for $\psi_{aF} = 60^o$, while $\rho_\lambda = 1.52$ and 6.04. The digram indicates, that the optimum range/unit cost occurs at larger ψ_{aP} than the optimum of the aperture efficiency. Connecting the maxima of the R/c functions for various or for various ψ_{aF} , a curve can be obtained, which shows the optimum combinations of ψ_{aP}, ψ_{aF} and ρ_λ for the best R/c value. This graph is shown on Fig. 26, which can be called as the design diagram of the space antenna. Throughout this calculation, the following assumptions were made to calculate the value of K.

TABLE 2

D_λ	>	50	
f	=	1000 mc/s	
T_{Rec}	=	10.4 °K	(Maser)
T_{AL}	=	1.5 °K	($P_L/P_R = 0.5\%$)
T_{AR}	=	0.6 °K	($\kappa = 0.1$)
T_S	=	2.5 °K	(Fig. 3)

With these values K = 0.1

The $\varrho_\lambda \gg 1$ line in Fig. 26 indicates the maximum possible range/unit cost with the assumed feed system. This theoretical limiting case can be approached only if the size of the secondary reflector (D_λ) is very large. According to Fig. 5 in reference 19, the aperture efficiency (gain) increases until $d_\lambda < \frac{D_\lambda}{4}$. However, then the side lobe attenuation is less than 19 db, which cannot always be tolerated. If $d_\lambda \leq \frac{D_\lambda}{10}$, then the gain of the antenna is only 1 db less than the possible maximum and the side lobe attenuation is in the order of 26 db.

According to Fig. 26, the range/unit cost has its maximum between 66-80° if the size of the feed system is small. This is the case of the conventional (horn type) feed system. On the other hand, the aperture angle can be considerably decreased if ϱ_λ is large.

The use of the design diagram can be shown in an example.

Let us suppose that a paraboloid reflector is given with an aperture angle $\psi_{qp} = 60°$, and a diameter of $D = 85$ at $f = 1000$ mc/s. From the $D_\lambda \geq 10 d_\lambda$ requirement, $d_\lambda = 8.5$ can be selected. Then $\varrho_\lambda = 5.4$ and $\psi_{qF} = 52°$ determines the point P, along the $\psi_{qp} = 60°$ line which results in the maximum possible d_λ and the maximum possible $\frac{R}{c} = 1.84$. According to Fig. 26, this geometry results in $\eta_o = 84\%$, S = 7% and $T_{AG} = 10.5°K$. According to Table 2, the total noise temperature of the antenna $T_{AT} = T_A - T_{Rec} = 14.9°$ K.

On the other hand, the design diagram shows that about $T_{AG} = 1.6°K$ $(T_{AT} = 6°)$ can be obtained if ψ_{qp} is in the optimum range $(\psi_{qp} \approx 72°)$

6. CONCLUSIONS

An analysis of the ground antenna problems of space communications systems shows that the maximum range of a large antenna can be limited by the antenna noise rather than by the gain reducing character of the reflector in accuracy. The noise sources of a high gain paraboloid antenna can be divided into external (sky, ground) and internal (thermal radiation of the reflector, noise caused by the finite antenna loss resistance) components. The only way to decrease the celestial noise is to decrease the wavelength. The "ground noise" decreases with the emissivity of the ground surface and by the antenna suppression (radiation relative to the isotropic source) toward the ground. The reflector noise can be reduced by increasing the optical transparency of the reflector and the "resistive noise" can be decreased by eliminating the feeder line between the receiver and the feed point.

Among the various sources, back radiation results in the largest single noise component. This is caused by the spillover radiation of the feed, the currents on the rear surface of the paraboloid and the radiation through the reflector if it is a wire gratings. Mathematical calculations show that this radiation can be suppressed and a special feed pattern can be suggested to reduce the spillover radiation for aperture angles less than 90°. No experimental data is presented about the suggested feed system in this paper, but reference is given to

another work by the author, in which a large front to back ratio was obtained by the suggested feed system.

By utilizing the described methods, it would appear feasible to obtain antenna noise temperatures in the order of $10^{\circ}K$ or less.

LIST OF SYMBOLS

α = Attenuation.

α_1 = Angle between the normal of the radiating surface and the direction of the receiving antenna.

A_F = Geometrical aperture of the feed horn.

A_g = Projected geometrical area of the wire reflector

A_o = Aperture area.

A_p = Surface of the paraboloid.

A_s = Projected geometrical area of the solid reflector.

A_T = Effective antenna area of the space station.

β = $\frac{2\pi}{\lambda}$ = Propagation factor.

c = Velocity of the light.

C = $\frac{\pi}{4} P_T A_T$

δ = $\frac{\Delta\lambda}{\lambda} = \frac{\Delta f}{f}$ = Relative bandwidth of the receiver.

Δf = Receiver bandwidth

D_λ = $\frac{D}{\lambda}$ = Diameter of the ground antenna aperture expressed in wavelength.

dA = Elementary receiver antenna surface.

dA_1 = Elementary radiating surface.

ϵ = Emissivity of the gray body.

ϵ_G = Emissivity of the ground.

ϵ_R = Emissivity of the reflector.

η_F = Aperture efficiency of the feed horn.

η_o = Aperture efficiency of the perfect paraboloid.

$f_{H\pm}$ = Radiation pattern of the elementary Huygens source in the aperture at $\pm\psi$ angle.

$F(\psi,\varphi)$ = Power directional pattern of the receiver antenna.

F_{avG} = Average power radiation toward the ground.

$F_o(\psi, \varphi)$ = Power directional pattern of the elementary Huygens source.

$F_F(\psi, \varphi)$ = Power pattern of the feed system.

Γ_G = Reflection coefficient of the ground.

G_F = Gain of the feed system.

H_g = Geometrical factor of the wire gratings.

H^s = Geometrical factor of the solid reflector.

κ = Screening factor.

k = Boltzman constant = $1.38 \cdot 10^{-23}$ ws/°K

λ = Wavelength.

ℓ = Distance between two wires of the grating.

L = Perpendicular distance between a given point in the space and the plane of the wires.

μ = Permeability.

m = $\frac{t}{D}$

M = Specified signal to noise ratio.

P_{ext} = Noise power of a receiving system, introduced by external sources.

P_{inst} = Total instantaneous power radiated by the wire gratings.

P_L = Loss power of the antenna.

P_N = Total noise power in the receiving system.

P_{NL} = Noise power of the lossy antenna.

P_{No} = Noise power of the lossless antenna.

P_{Rec} = Specified receiver power for satisfactory communication.

P_S = Time average of the noise power radiated by a corrugated solid reflector.

P_T = Transmitter power.

P_W = Time average of the noise power from the wire gratings.

ρ = Radius of the wire.

ρ = Aperture radius.

r = Distance between the radiating surface and the receiving antenna.

R = Distance between the ground antenna and the space station.

R_L = Loss resistance of the antenna.

R_R = Radiation resistance of the antenna.

R_W = Skin resistance of the wire.

S = Radiation suppression of the antenna.

τ = Noise power ratio of the lossy to the lossless antenna.

t = Root mean square deviation of the reflector from the exact paraboloid.

T = Absolute temperature of the radiating surface.

T_A = Apparent temperature of the antenna.

T_{Aext} = External noise temperature of the antenna system.

T_{Aint} = Internal noise temperature of the antenna system.

T_{AL} = Apparent temperature of the lossy antenna.

T_{AG} = Apparent temperature of the ground.

T_{AR} = Apparent noise temperature of the reflector.

T_G = Thermodynamical temperature of the ground.

T_R = Absolute temperature of the reflector.

T_{Rec} = The receiver noise temperature.

T_S = Apparent sky temperature in the direction of the main beam.

T_T = Total apparent noise temperature of the receiving system.

ψ_a = Aperture angle.

ψ_{aF} = Aperture angle of the feed reflector.

ψ_{ap} = Aperture angle of the paraboloid.

Ω = Solid angle.

Ω_B = Equivalent beam cross-section of the antenna.

Ω_L = Solid angle of the lower hemisphere.

Ω_{UP} = Solid angle of the upper hemisphere.

REFERENCES

1) K. W. Finnes, W. D. Merrick, R. Stevens :
"GROUND ANTENNA FOR SPACE COMMUNICATION SYSTEMS"
(IRE.PGSET, March, 1960, p.p. 45-54).

2) J. P. Gordon, L. D. White :
"NOISE IN MASER AMPLIFIERS, THEORY AND EXPERIMENT"
(P. IRE. Vol. 46, p.p. 1588-1594, Sept., 1958).

3) F. A. Giordmaine, L. E. Alsop et al :
"A MASER AMPLIFIER FOR RADIO ASTRONOMY AT X BAND"
(P. IRE. Vol. 47, June 1959, p. 1063).

4) T. P. Merritt, F. F. Hall :
"BLACKBODY RADIATION"
(P. IRE. Vol. 47, Sept., 1959, p.p. 1435-1441).

5) R. H. Dicke :
"THE MEASUREMENT OF THERMAL RADIATION OF MICROWAVE FREQUENCIES"
(Rev. Sci. Instr., Vol. 17, p.p. 168-275, July 1946).

6) E. Levis, F. P. Casey and F. Vaccaro :
"POLARIZED RADIATION FROM CERTAIN THERMAL EMITTERS"
(Air Force, Cambridge Res. Center, Beford, Mass.
Technical Report 54-6, Feb. 1954)

7) G. E. Mueller :
"A PRAGMATIC APPROACH TO SPACE COMMUNICATION"
(P. IRE. Vol. 48, April, 1960, No. 4, p.p. 557-566)

8) J. D. Krauss :
"ANTENNAS"
(McGraw Hill Book Comp. Inc., 1950, p.23).

9) M. J. B. Scanlau :
"SOME MEASUREMENTS ON RADAR AERIALS USING STELLAR NOISE"
(Marc. Rev. XIII 1st Quarter 1960, p.p. 20-32).

10) H. Tunmer :
"ON A FEATURE OF GALACTIC RADIO EMISSION"
(Phil. Mag. Vol. 3, p.p. 370-376, April 1958).

11) A. G. Smith :
"EXTRATERRESTRIAL NOISE AS A FACTOR IN SPACE COMMUNICATIONS"
(P. IRE. Vol. 48, April 1960, No. 4, p.p. 593-599)

12) E. Weger :
"APPARENT THERMAL NOISE TEMPERATURES IN THE MICROWAVE REGION"
(IRE. Trans. on Ants. and Prop. V-AP-B No. 2,
March 1960, p.p. 213-217).

13) C. M. Rytov :
"THEORY OF ELECTRIC FLUCTUATIONS AND THERMAL RADIATION"
(Inst. Akad. Nauk SSSR, 1953).

14) M. L. Levin, C. M. Rytov :
"THERMAL RADIATION OF LINEAR ANTENNAS"
(Journal of Technical Physics, Vol. XXV, No. 2,
1955, p.p. 323-332).

15) D. G. Tucker :
"THE SIGNAL/NOISE PERFORMANCE OF SUPERDIRECTIVE ARRAYS"
(Acustica, Vol. 8, p.p. 53-62, 1958)

16) American Institute of Physics :
"TEMPERATURE, ITS MEASUREMENT AND CONTROL IN SCIENCE AND INDUSTRY"
(Reinhold Publishing Corporation, New York, p.p. 1164-1190).

17) Lionel S. Marks :
"MECHANICAL ENGINEERS HANDBOOK"
(McGraw Hill Book Company Inc., p. 382).

18) S. A. Schelkunoff :
"A MATHEMATICAL ANALYSIS OF LINEAR ARRAYS"
(BSTJ Vol. 22, 1943, Jan., p.p.80)

19) P. Foldes, S. Komlos :
"THEORETICAL AND EXPERIMENTAL STUDY OF WIDE BAND PARABOLOID
ANTENNA WITH CENTRAL REFLECTOR FEED"
(RCA Review, March, 1960, Vol. XXI, No. 1, p.p. 94-116).

20) E. B. Moullin :
"RADIO AERIALS"
(Oxford, Clarendon Press, 1949, p. 301).

21) J. K. Skwirkzynski, J. C. Thackray :
"TRANSMISSION OF ELECTROMAGNETIC WAVES THROUGH WIRE GRATINGS"
(Theoretical)
(Marconi Rev. Vol. XXII 1959 2nd Quarter, p.p. 78-90).

22) E. G. A. Goodall, J. A. C. Jackson :
"TRANSMISSION OF ELECTROMAGNETIC WAVES THROUGH WIRE GRATINGS"
(Experimental)
(Marconi Rev. Vol. XXII 1959 2nd Quarter, p.p. 91-98).

23) S. Silver :
"MICROWAVE ANTENNAS"
(New York, McGraw Publishing, Chapter 3).

24) G. N. Watson :
"THEORY OF BESSEL FUNCTIONS"
(Cambridge, University Press, 1944, Second Edition, p. 150)

25) R. C. Honey :
"ANTENNA DESIGN PARAMETERS"
(Standford, Contract D.A. 36-039 SC-73106).

26) M. J. Ehrlick :
"CORRUGATED SURFACE ANTENNAS"
(Conv. IRE 1953, p. 2)

27) E. M. T. Jones :
"AN ANNULAR CORRUGATED SURFACE ANTENNA"
(Proc. IRE. 1952 Jan.)

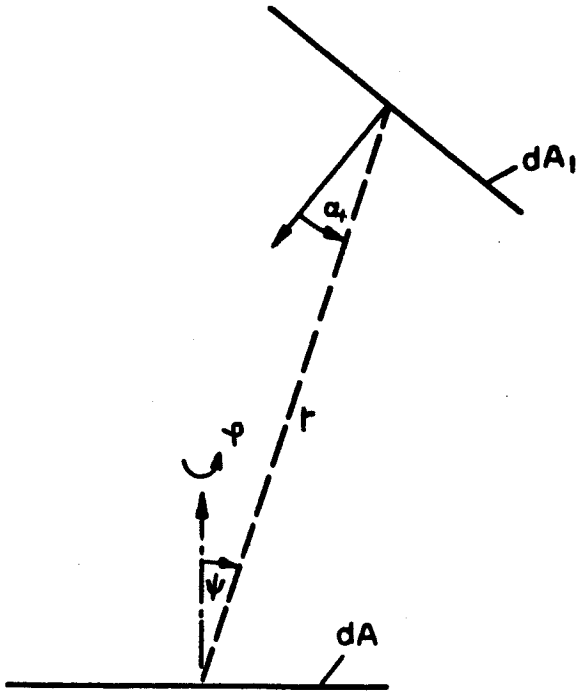

Fig. 1 - Thermal power exchange between two elementary surfaces.

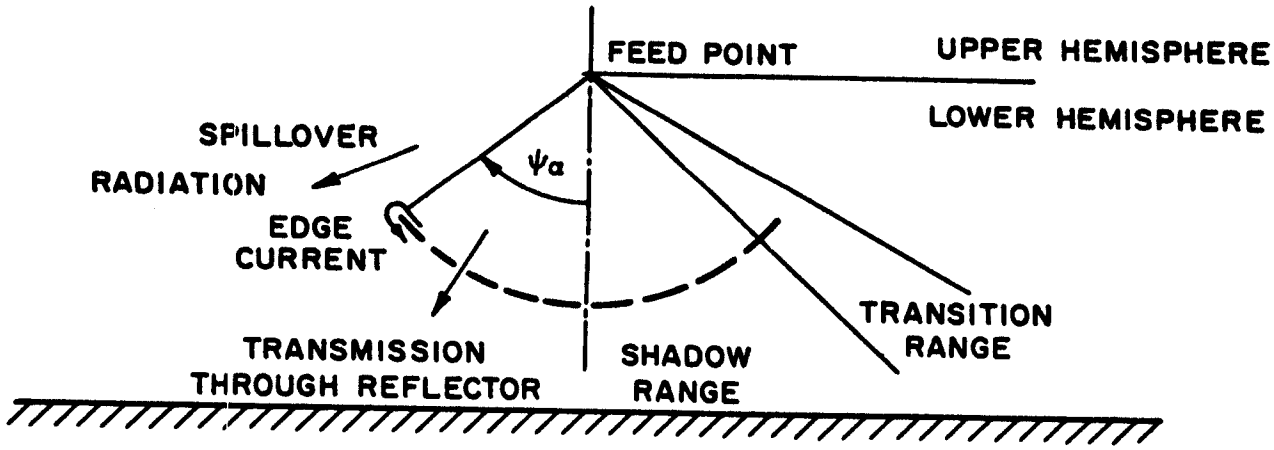

Fig. 2 - Antenna in the minimum thermal noise position and the possible sources of back radiation.

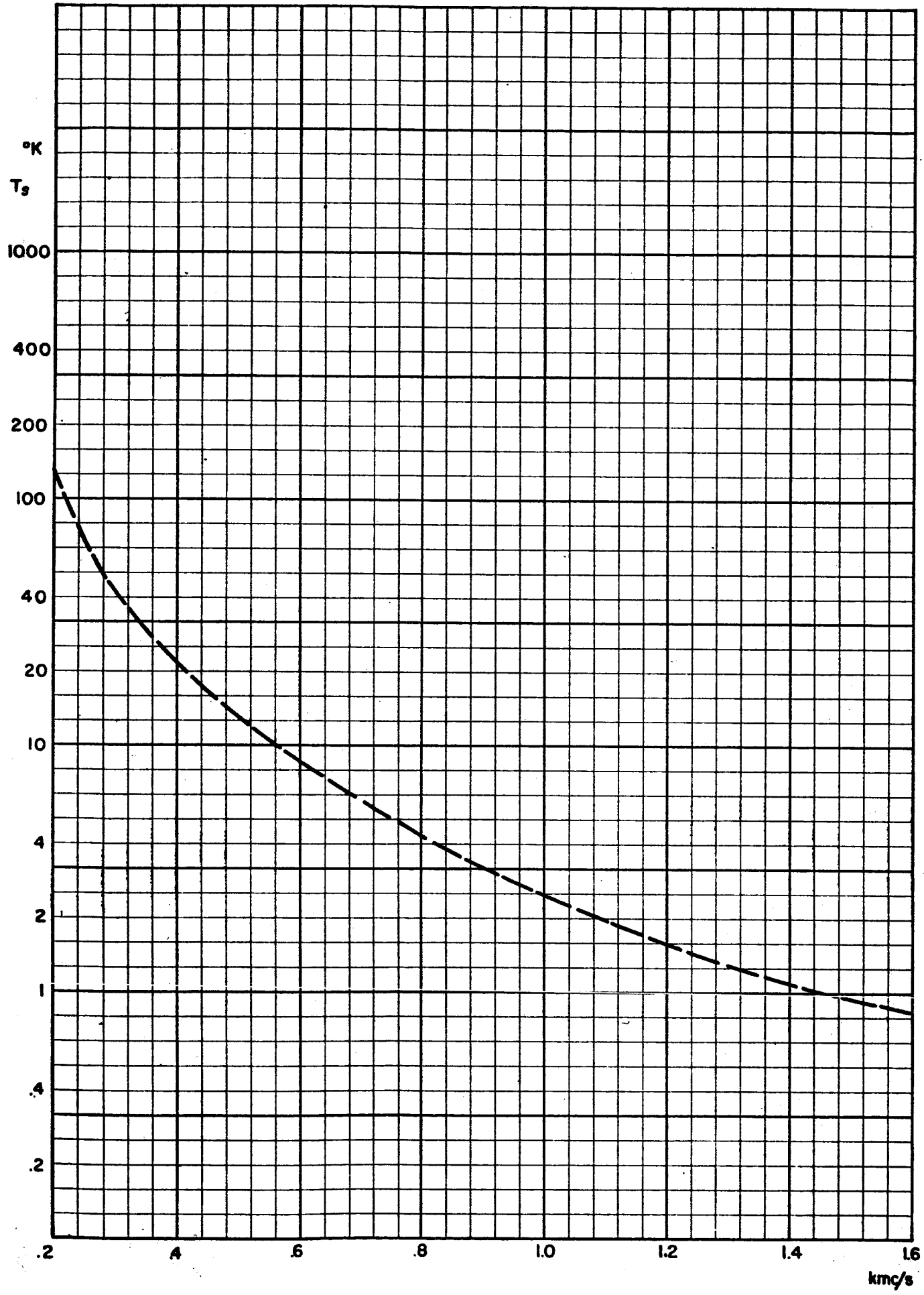

Fig. 3. - Noise temperature of the sky as a function of frequency.

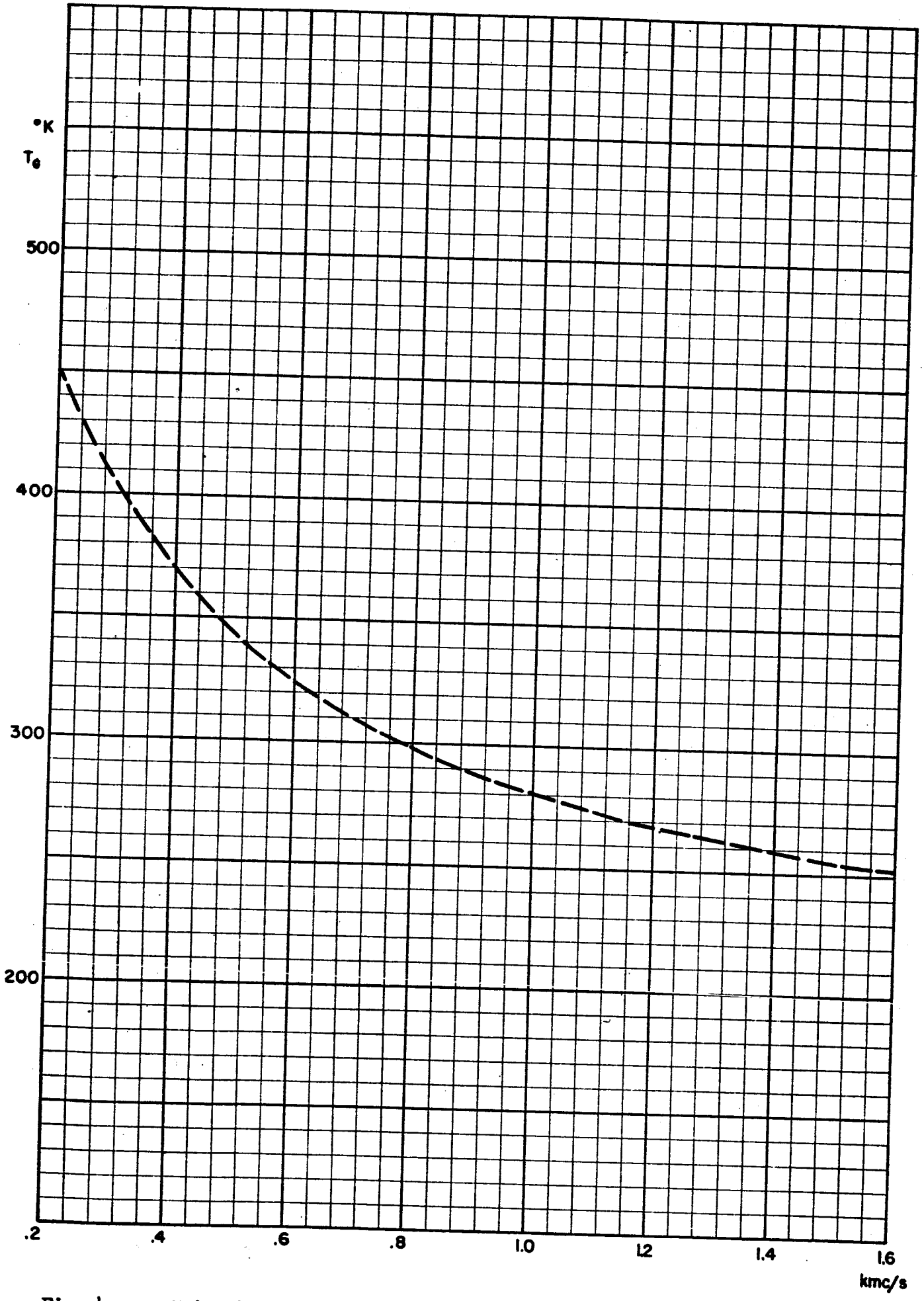

Fig. 4. - Noise temperature of concrete ground surface vs. frequency.

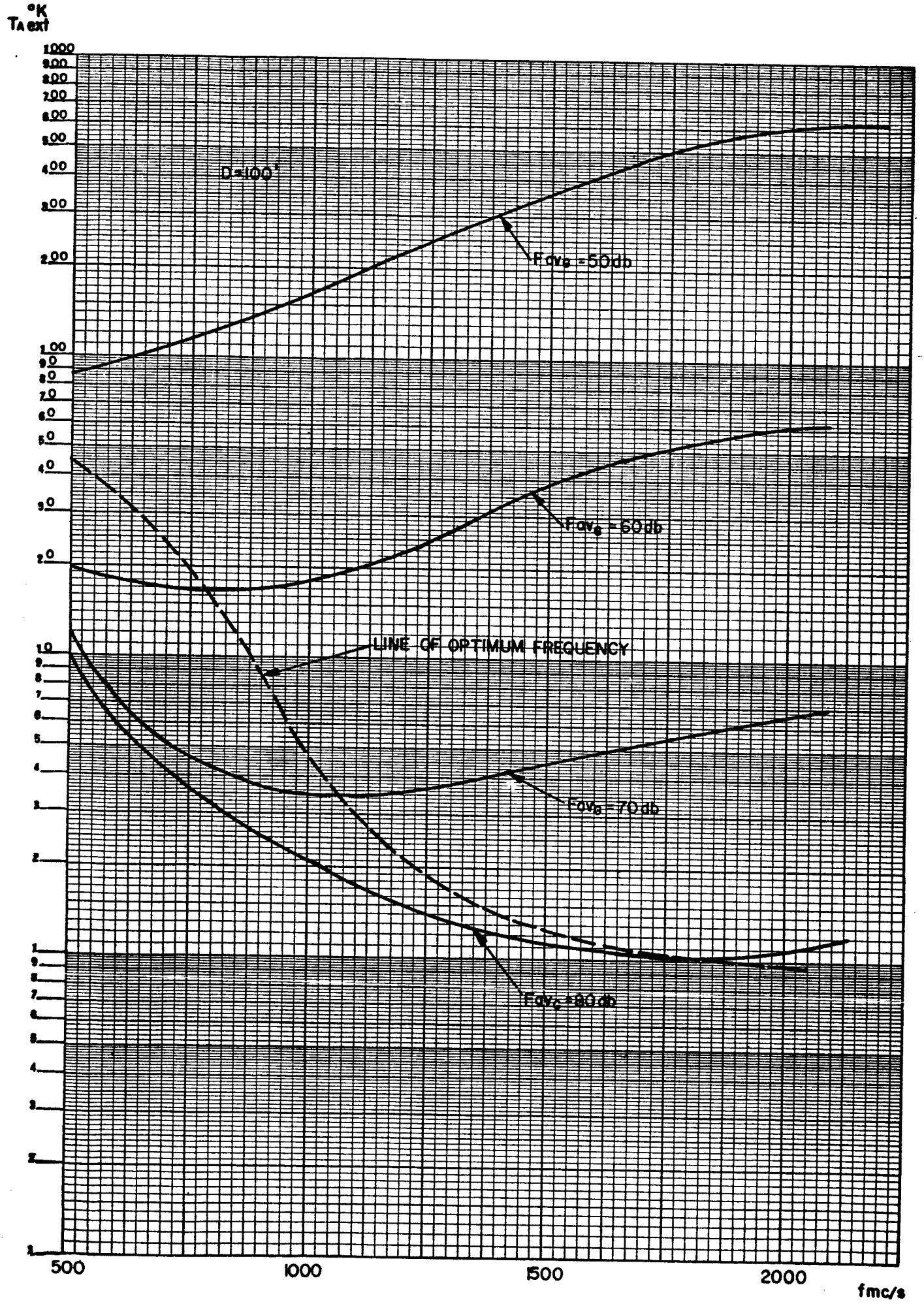

Fig. 5. - Apparent external noise temperature vs. frequency.

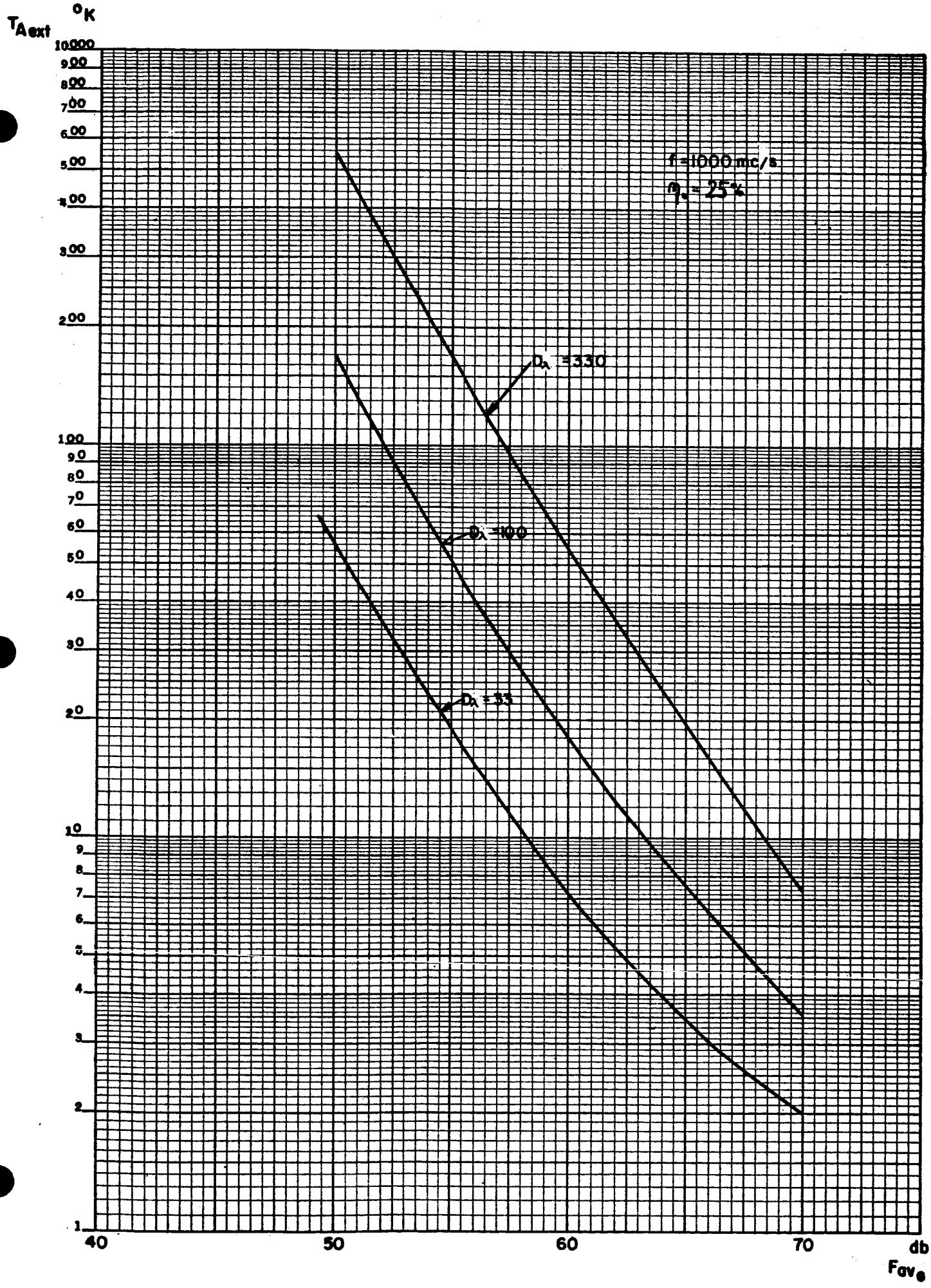

Fig. 6. - Apparent external noise temperature vs. level of back radiation.

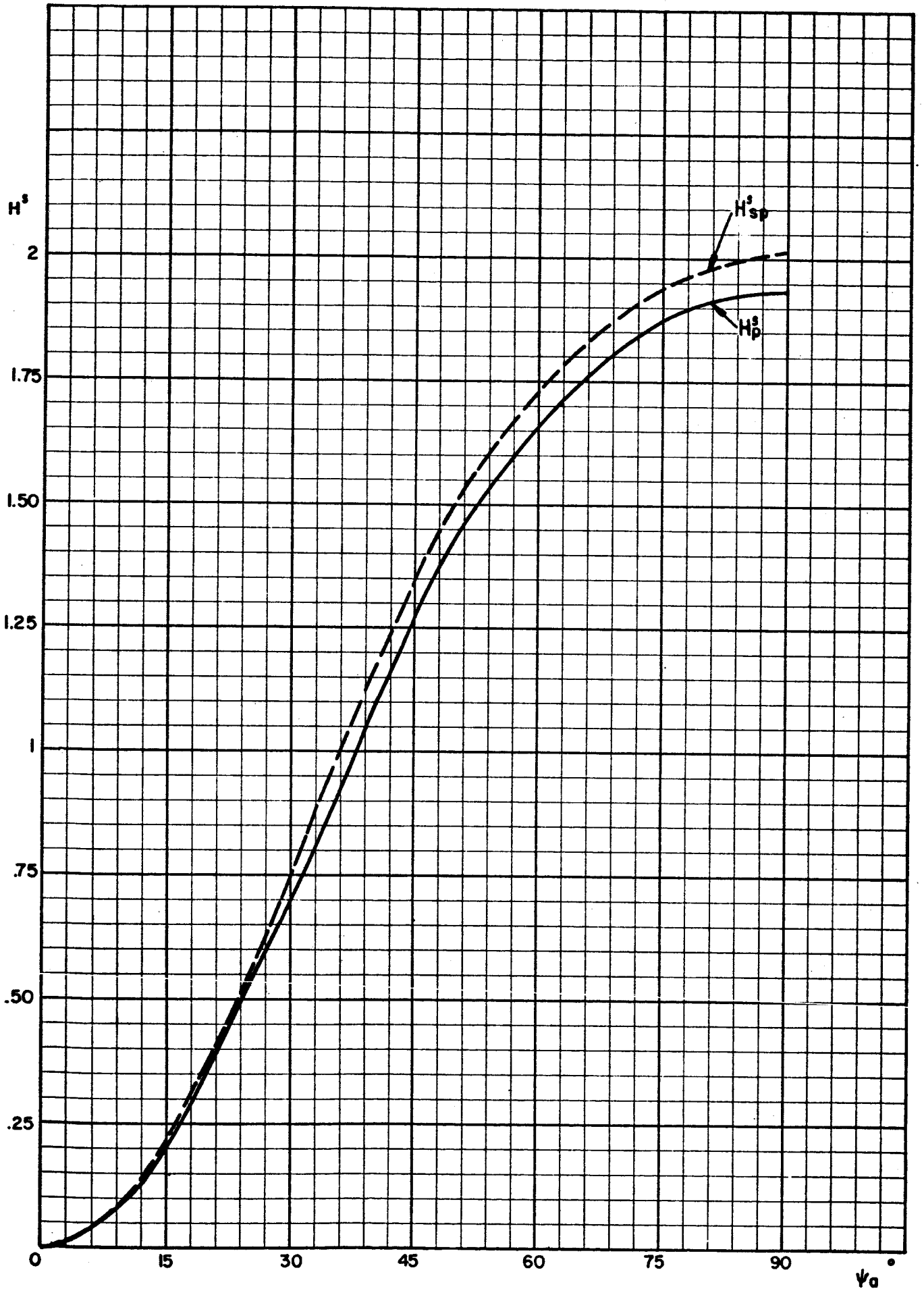

Fig. 7. - The geometrical factor of a solid spherical and paraboloidal reflector vs. ψ_a.

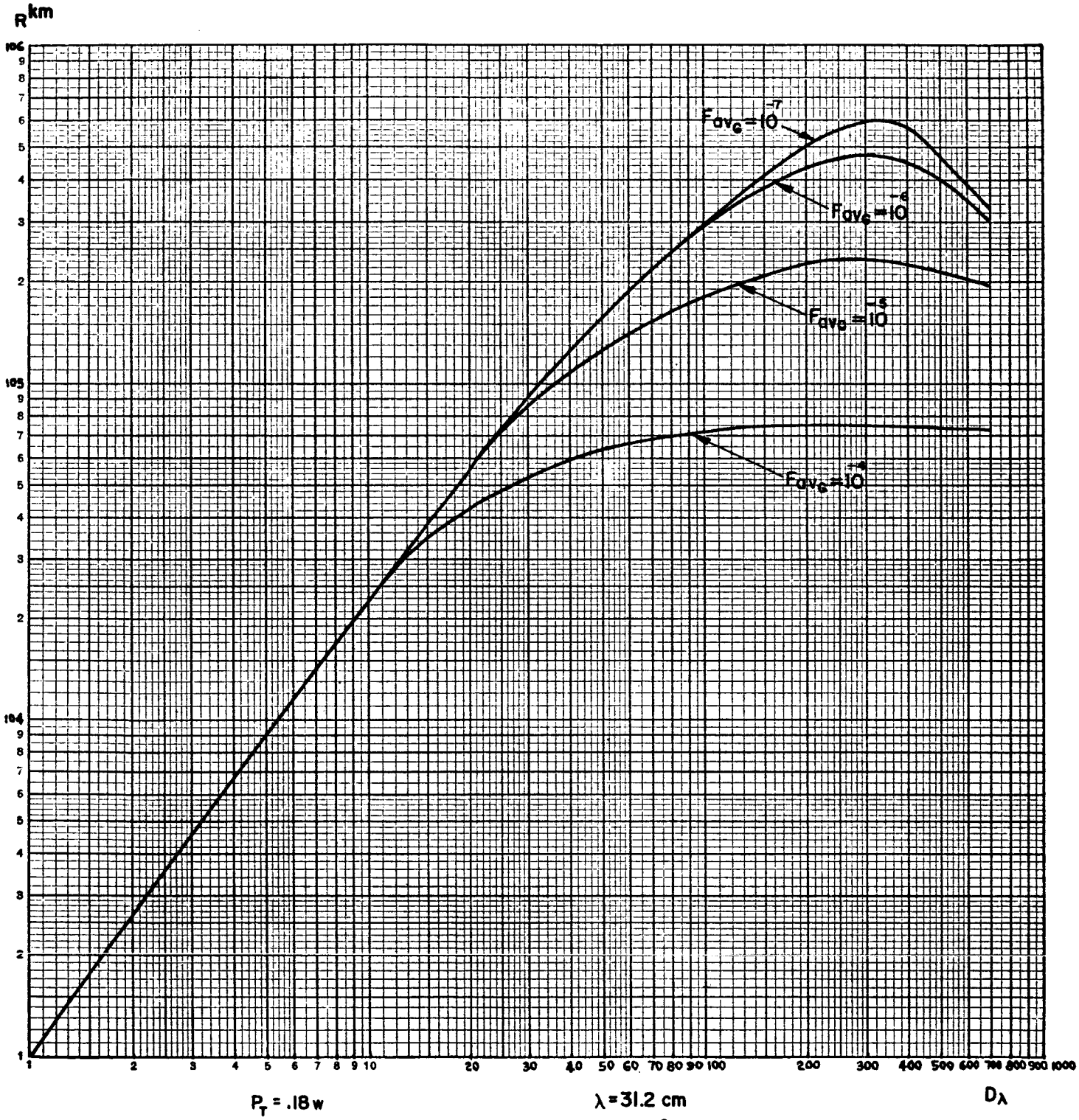

$P_T = .18$ w
Transmitter antenna = isotropic
$\eta_o = .5$
$m = 2.45 \; 10^{-4}$
$\Delta f = 20$ cps
$M = 10$ db

$\lambda = 31.2$ cm
$T_S = 2.7$ °K
$T_R = 20$ °K
$T_G = 290$ °K

Fig. 8. - Range variation of a space communication system with D_λ for various levels of back radiation.

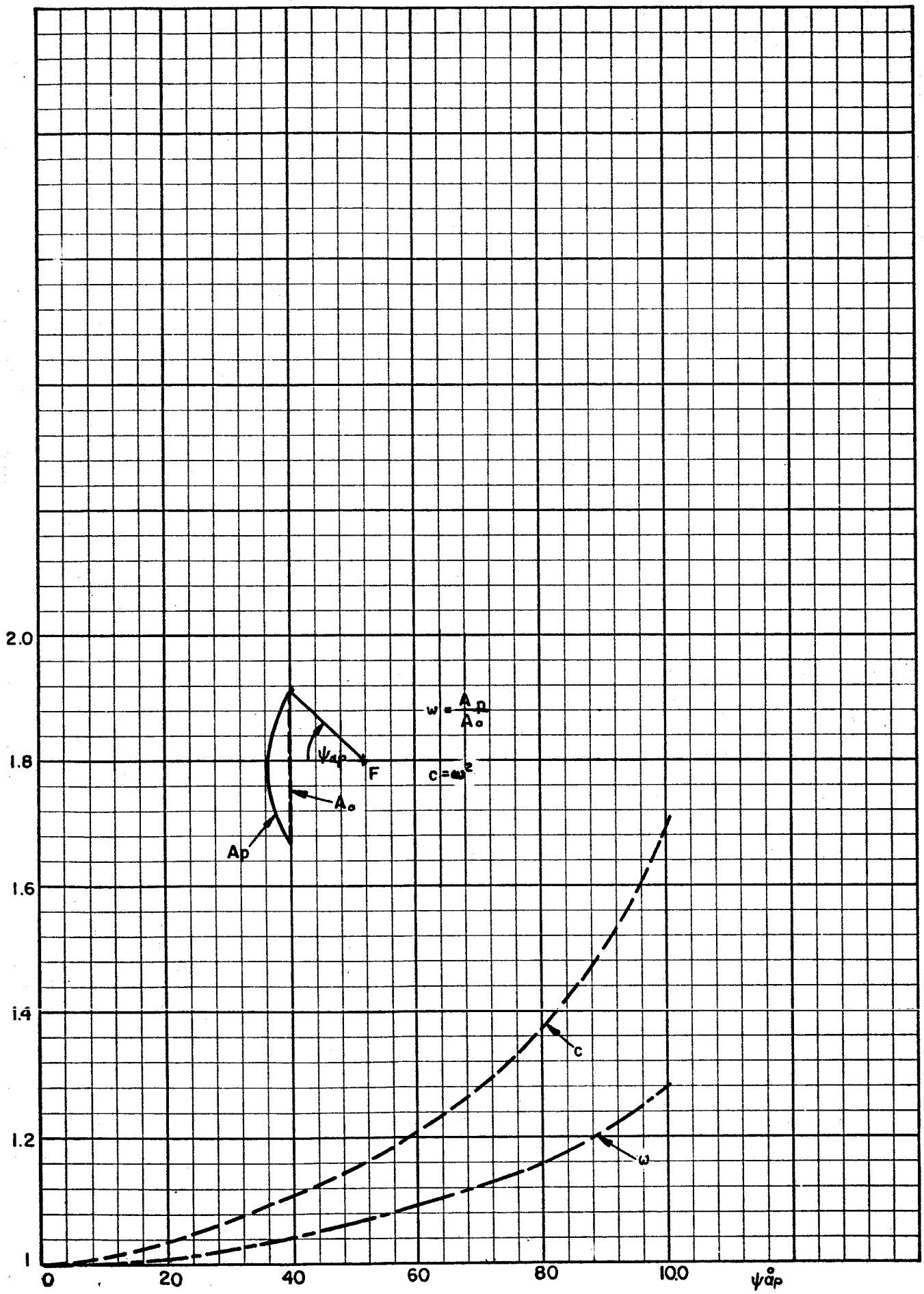

Fig. 9. - Paraboloid surface to aperture surface ratio vs. ψ_{ap}

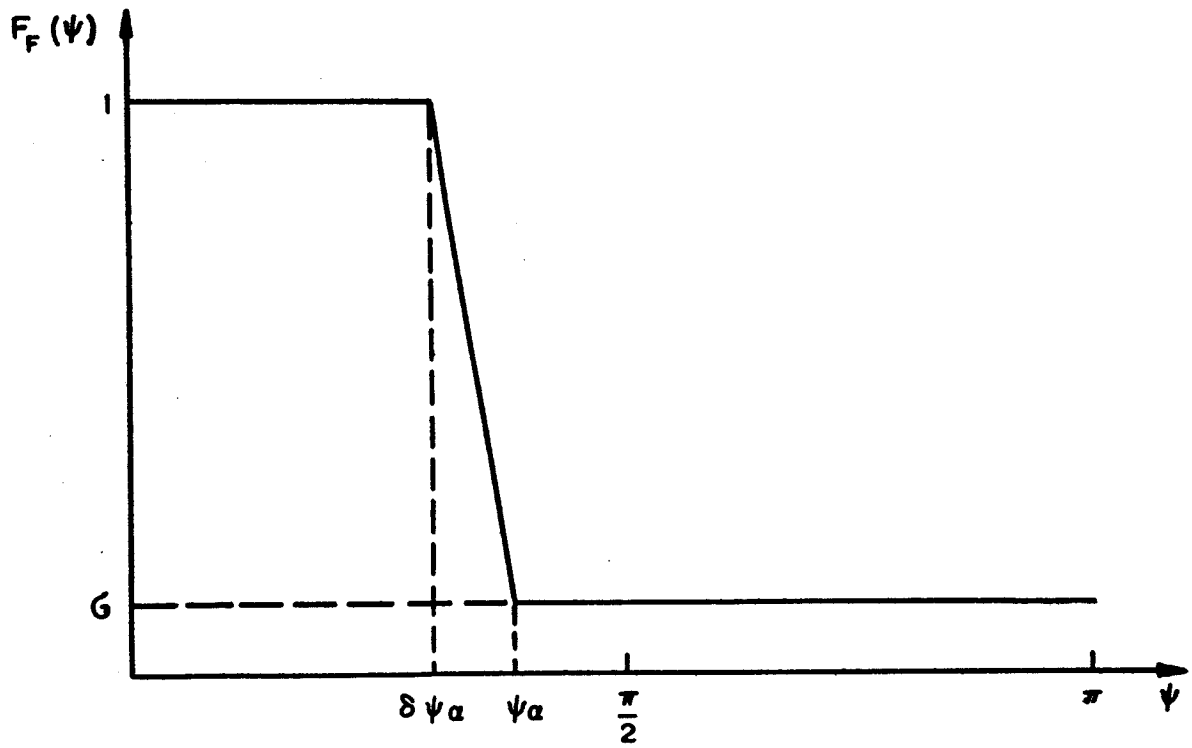

Fig. 10 - Ideal feed pattern for high aparture efficiency and low back radiation.

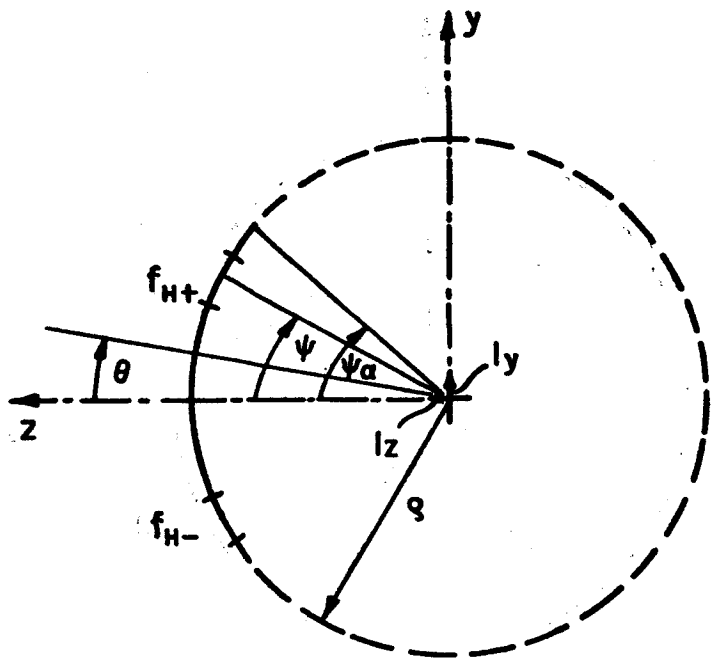

Fig. 11 - Geometry of a radiating circular cylinder.

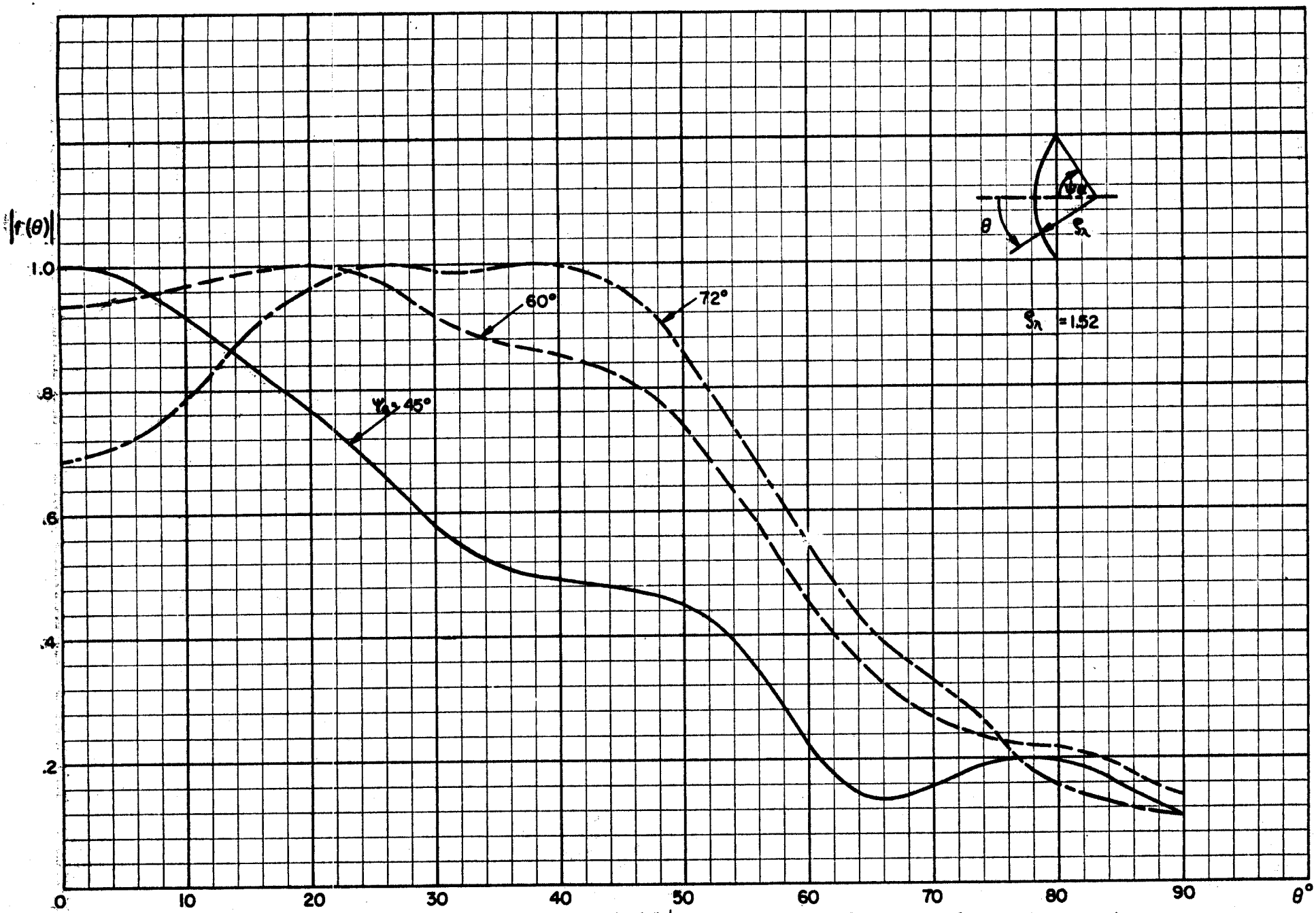

Fig. 12a. - Variation of $|f(\theta)|$ for ψ_a = 45°, 60°, 72° and ρ_λ = 1.52 .

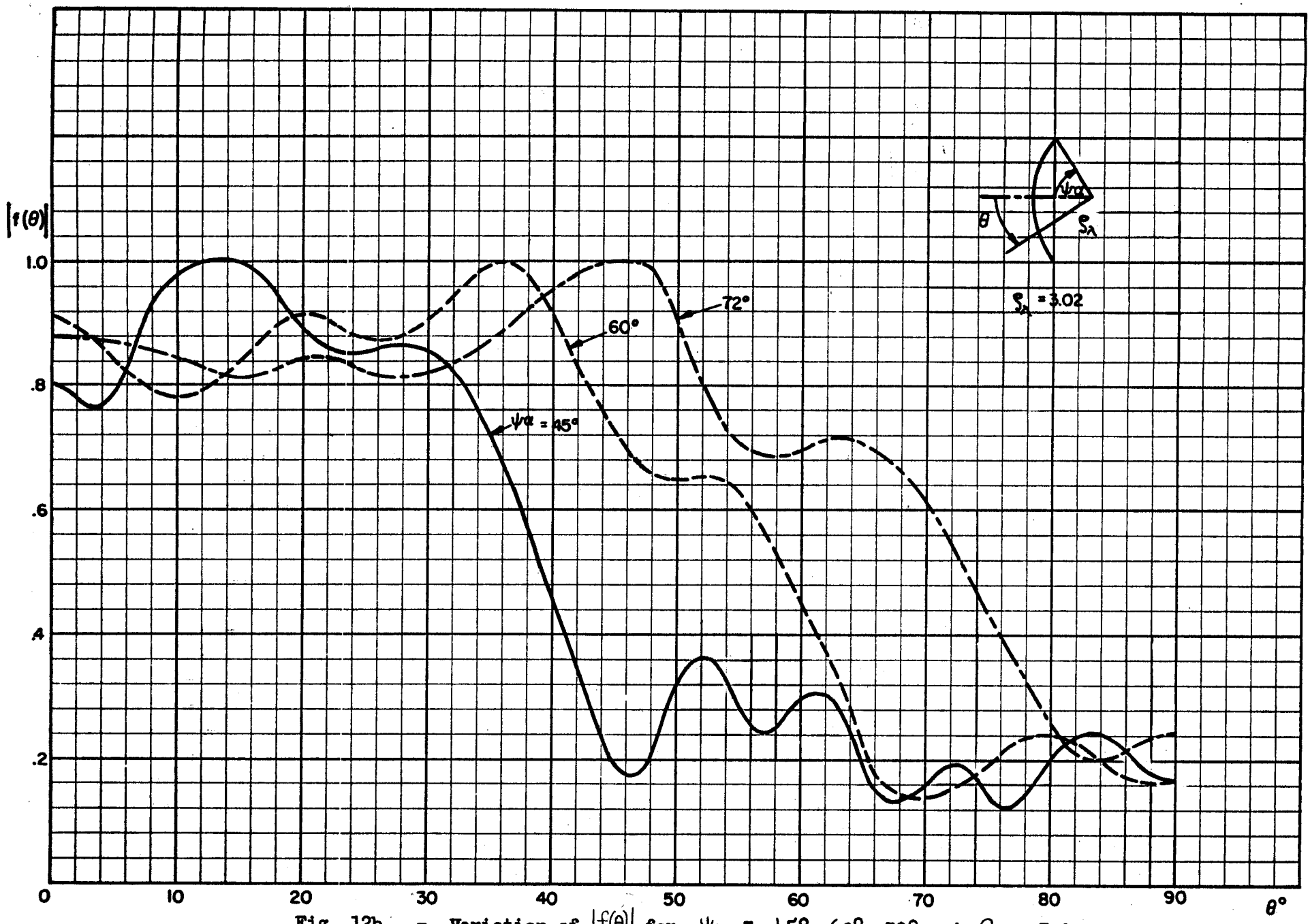

Fig. 12b. - Variation of $|f(\theta)|$ for ψ_a = 45°, 60°, 72° and ρ_λ = 3.02 .

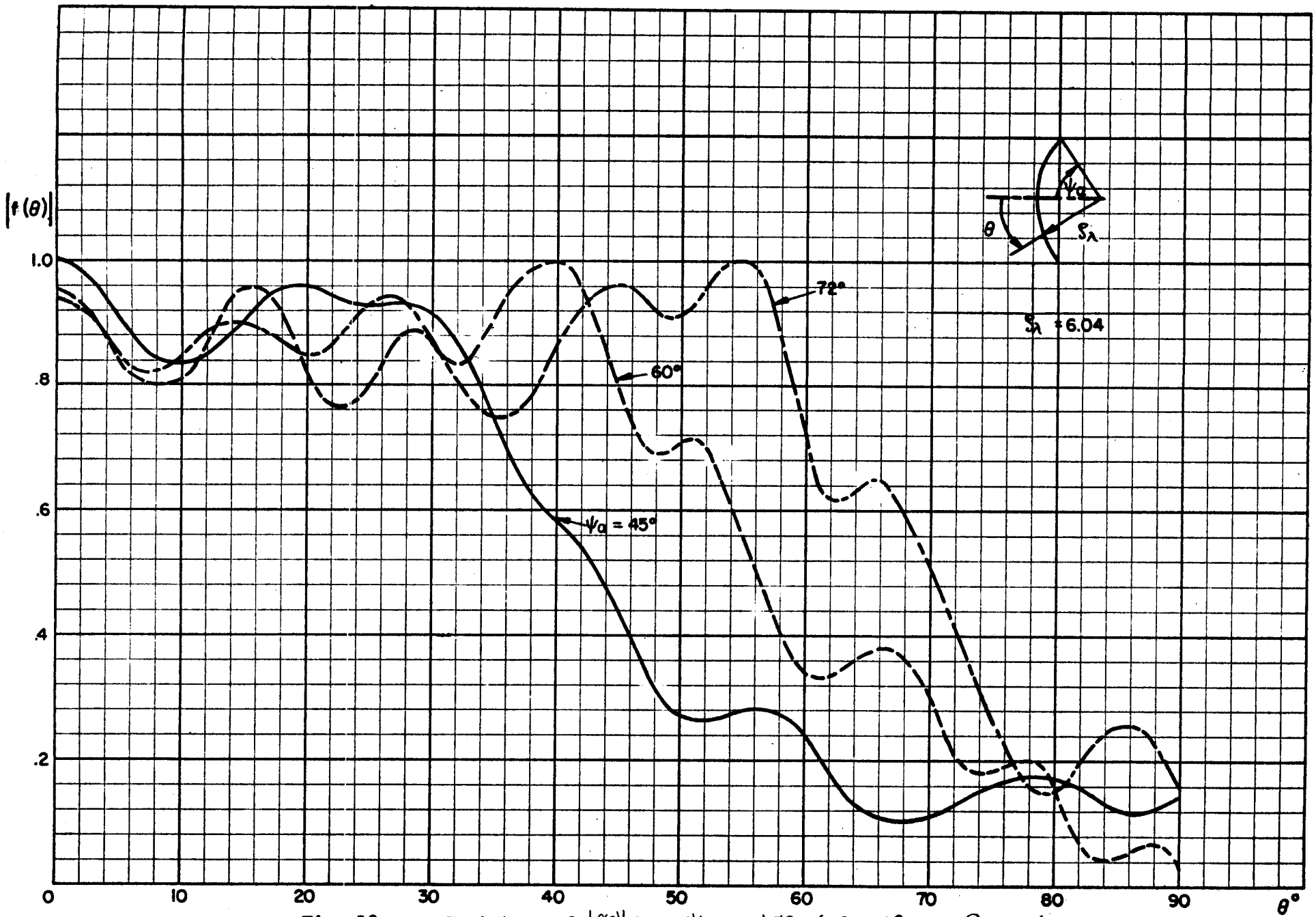

Fig. 12c. - Variation of $|f(\theta)|$ for ψ_a = 45°, 60°, 72° and ρ_λ = 6.09

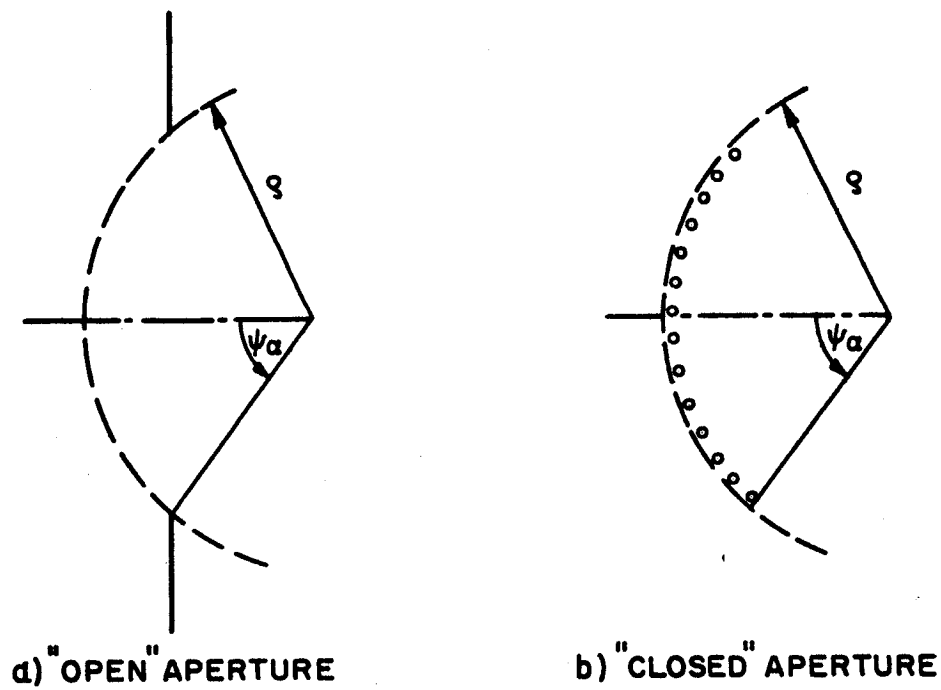

Fig. 13 - "Open" and "closed" apartures.

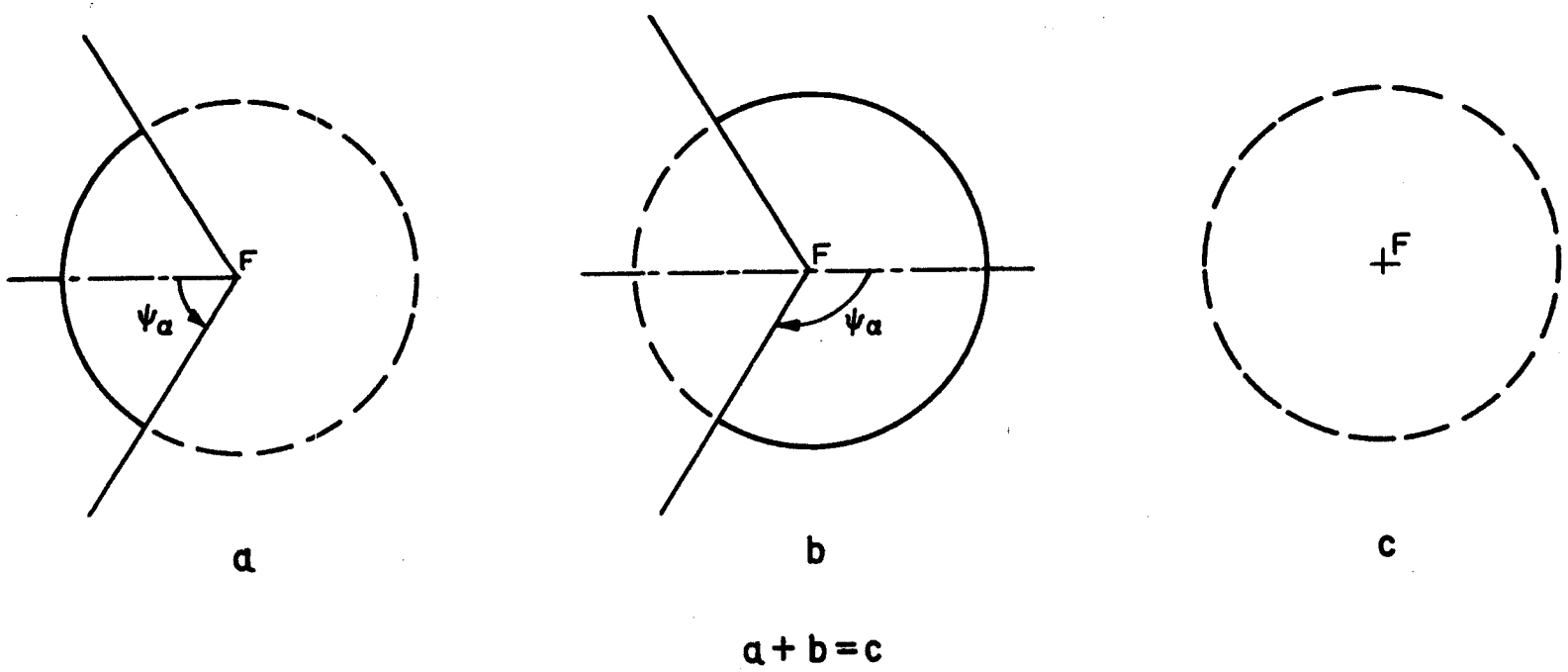

Fig. 14 - The Babinet principle.

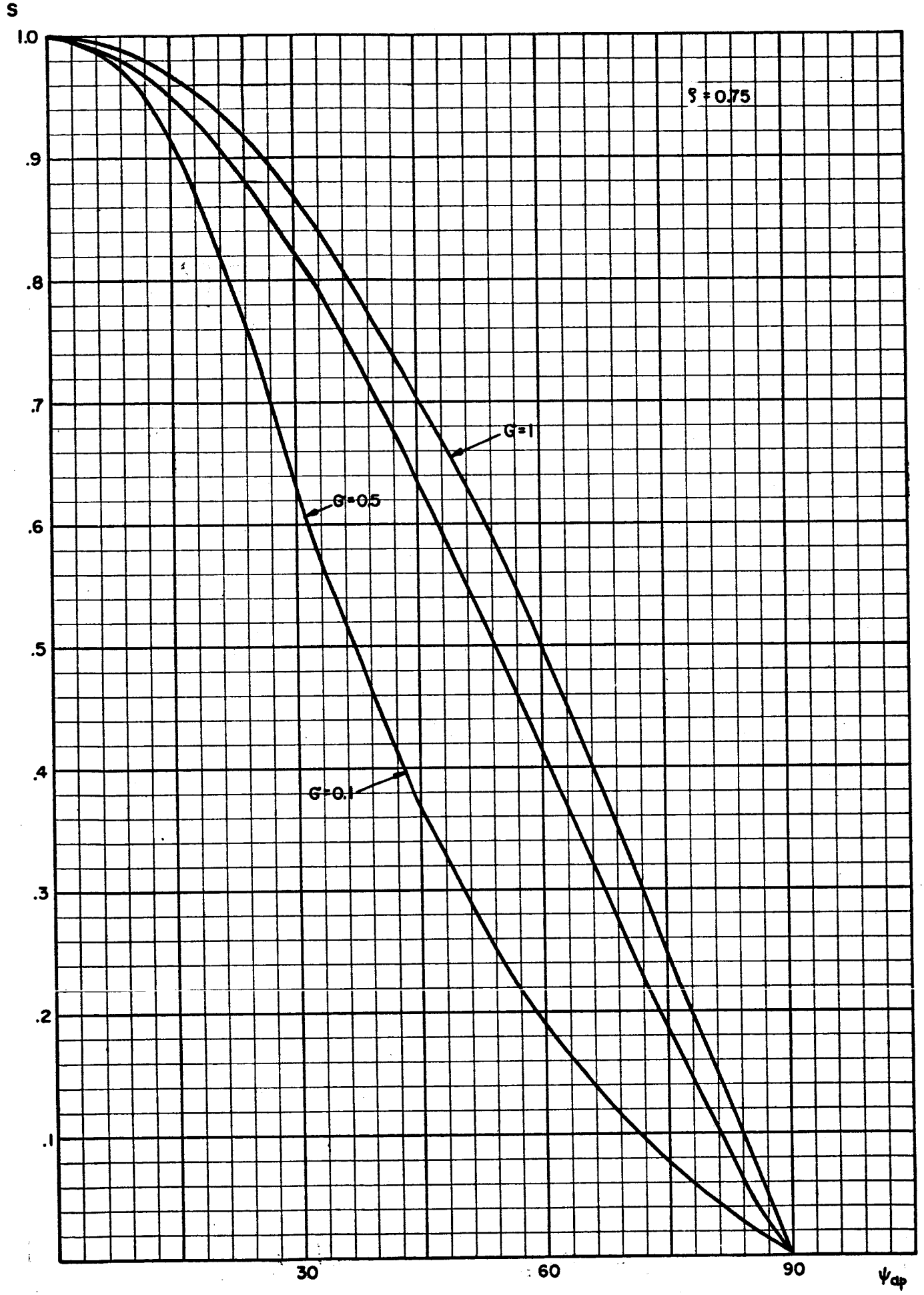

15. - Antenna suppression vs. ψ_{ap} for the feed pattern given on Fig. 10.

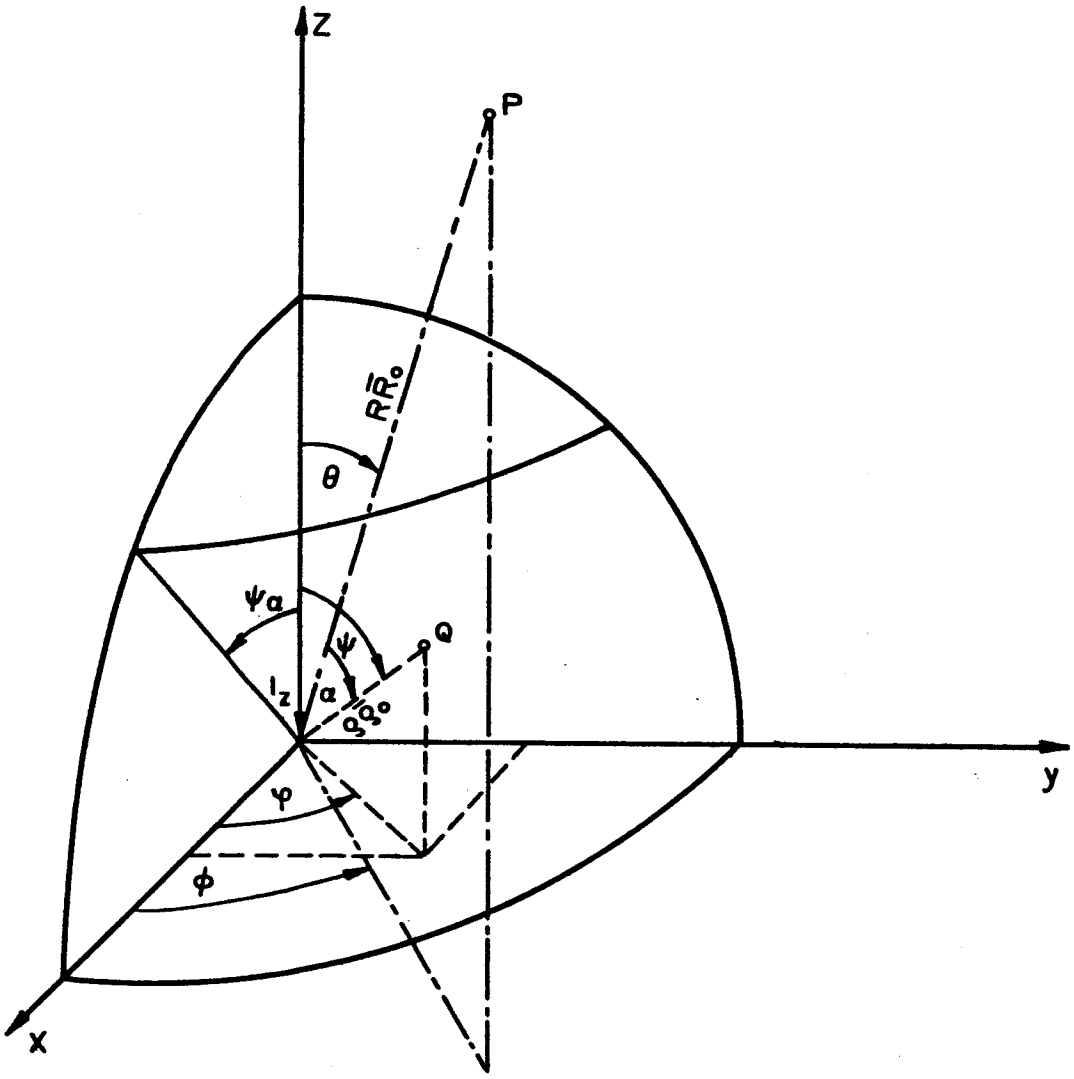

Fig. 16 - Geometry of a radiating spherical aparture for an I_z current element.

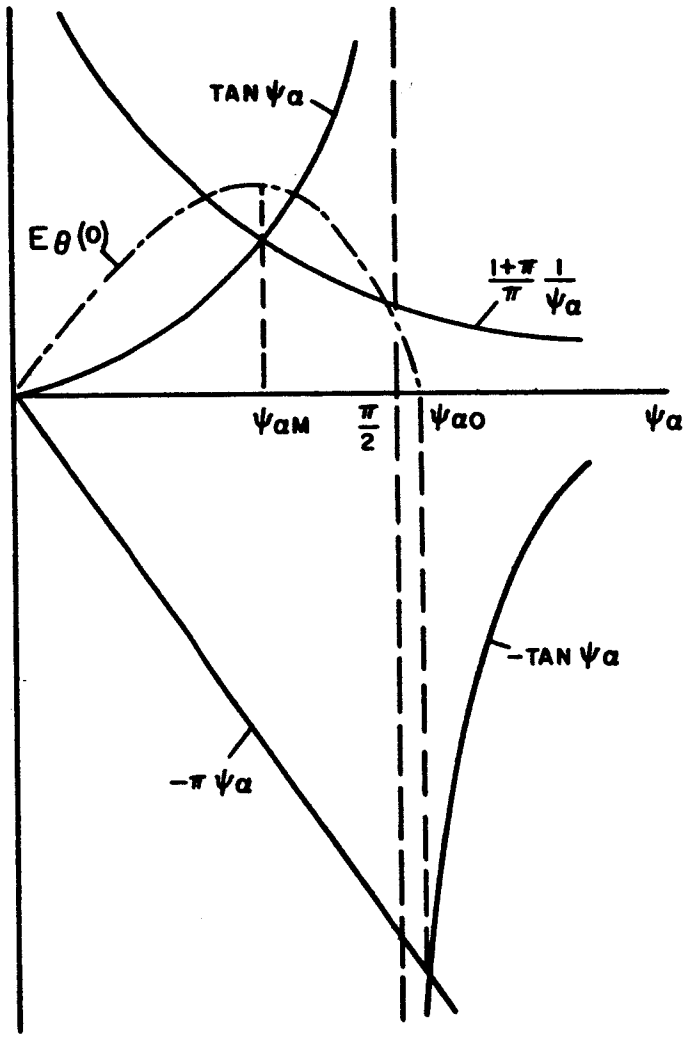

Fig. 17 - Variation of $E_\theta(0)$ vs. ψ_a for an I_z current element.

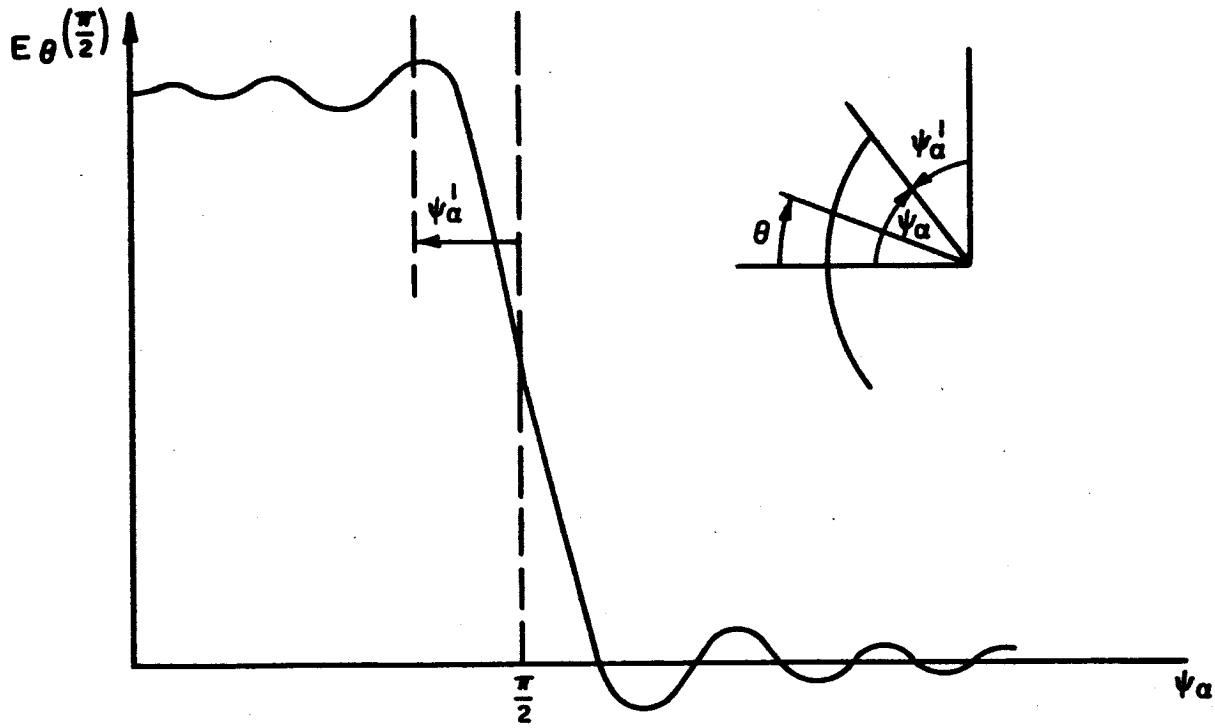

Fig. 18 - Variation of $E_\theta(\frac{\pi}{2})$ vs. ψ_a' for an I_z current element.

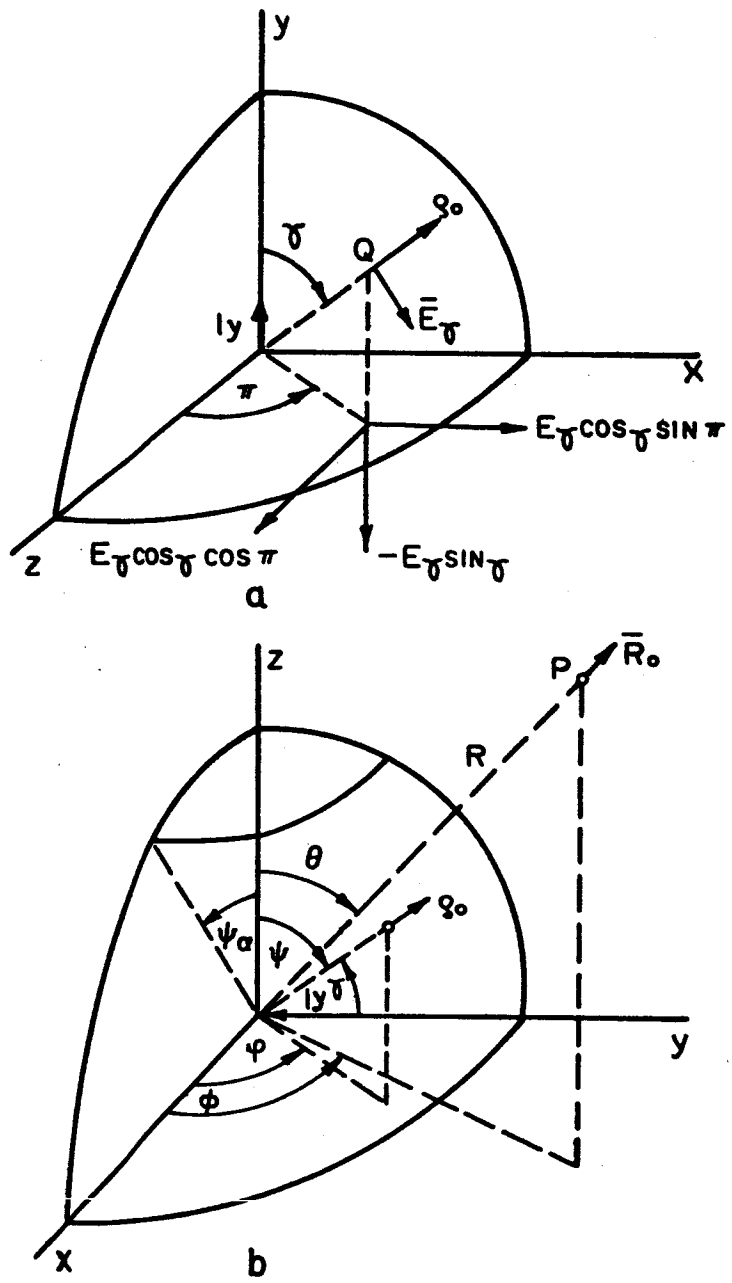

Fig. 19 - Geometry of a radiating spherical aparture for an I_y current element.

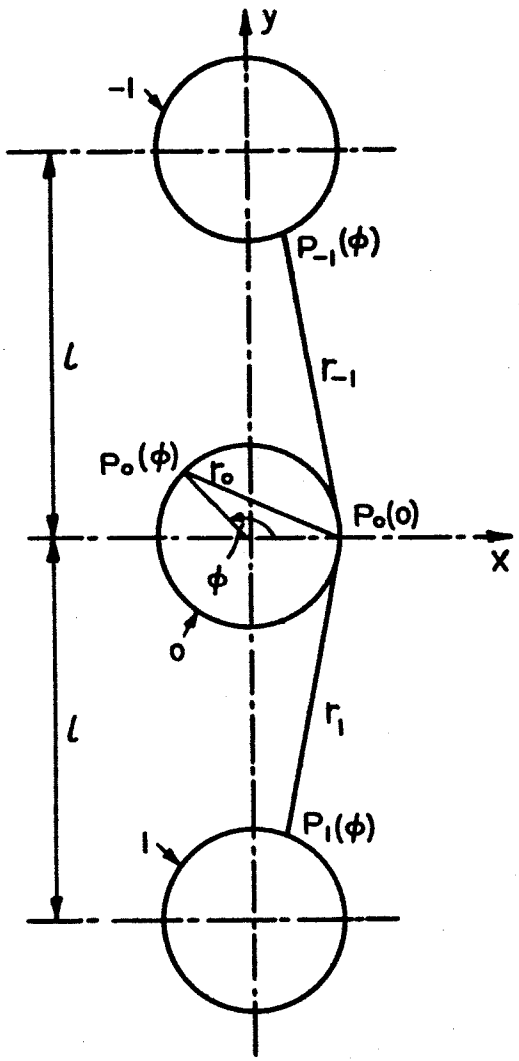

Fig. 20 - Geometry of a wire gratings.

Fig. 21 - Solid Thermal radiator with corrugations.

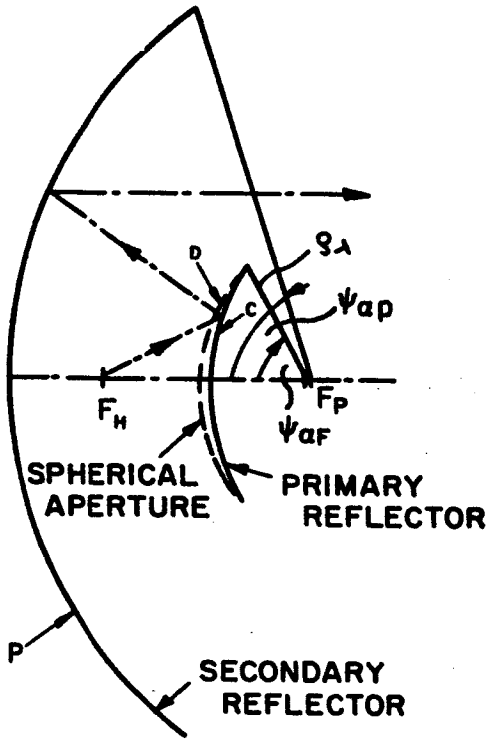

Fig. 22 - Geometry of a feed system with high antenna efficiency and small backradiation.

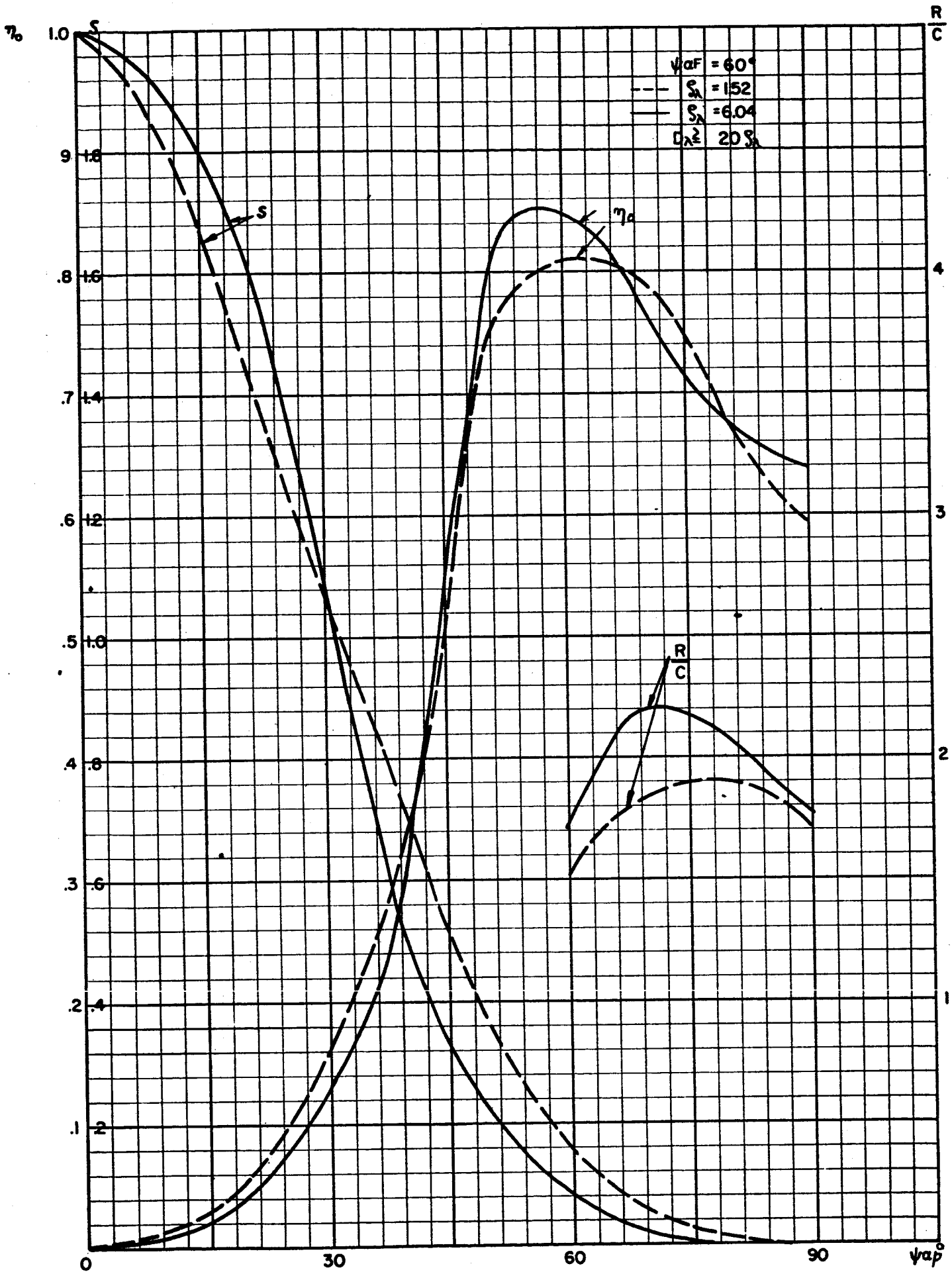

Fig. 23. - Variation of η_o, S and R/c vs. ψ_{ap}.

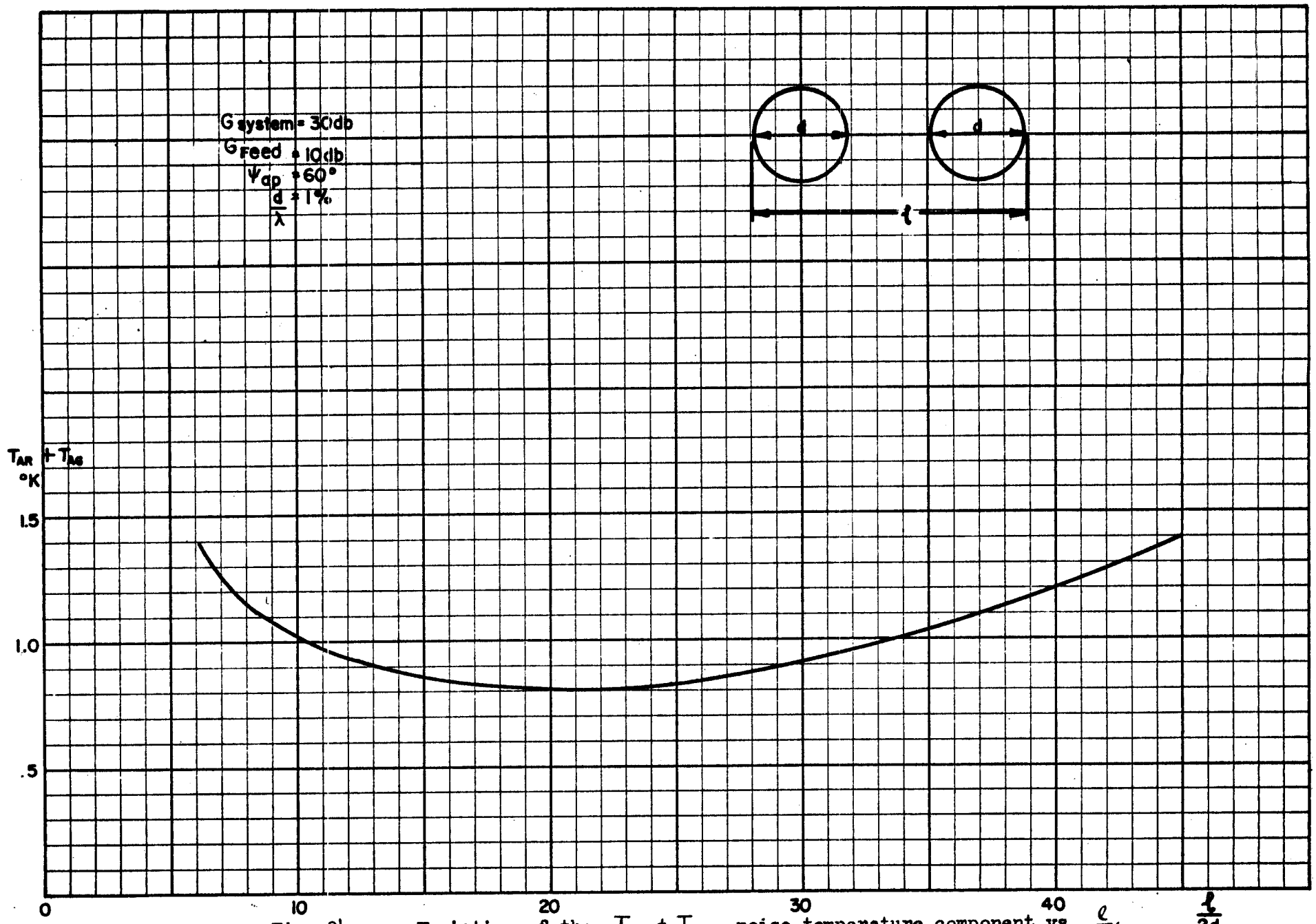

Fig. 24. - Variation of the $T_{AR} + T_{AG}$ noise temperature component vs. $\frac{\ell}{2d}$

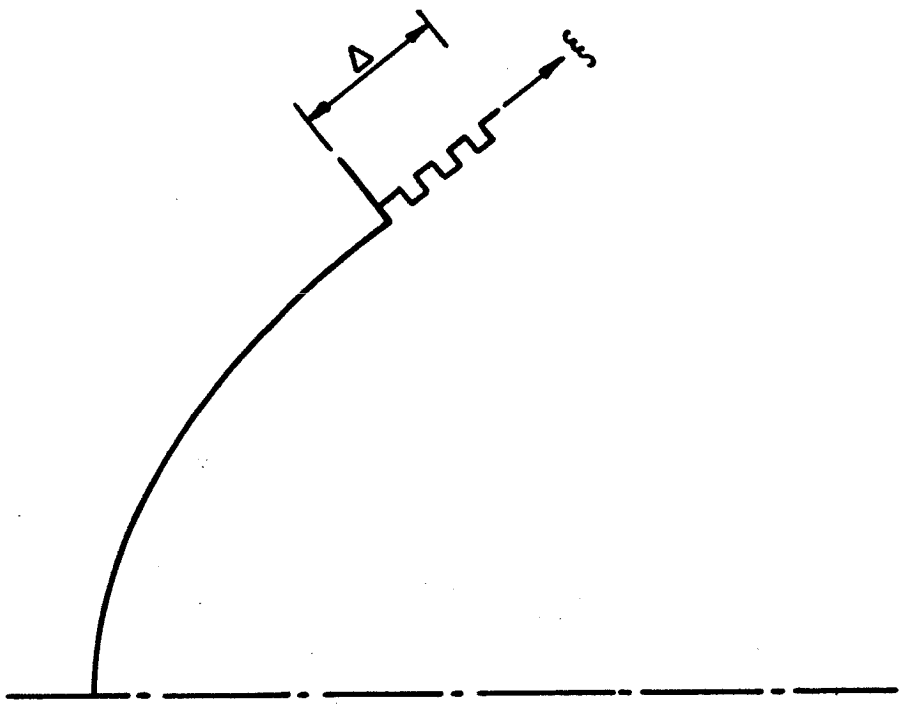

Fig. 25 - Reduction of the edge currents by the application of corrugations.

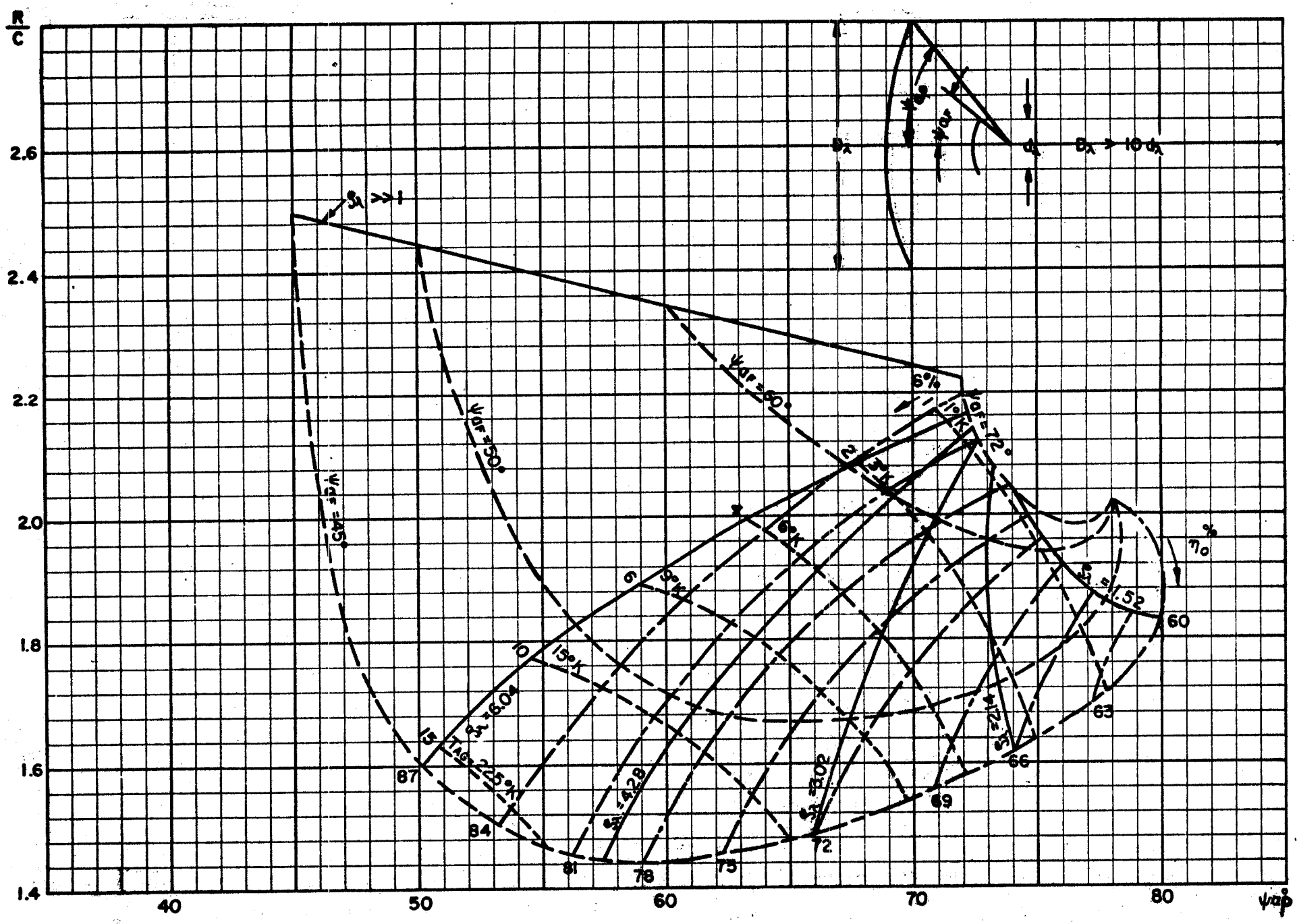

Fig. 26. - Design diagram of the optimum antenna.

JPL Contract No.: N-32195
RCA Victor Proj.: 3457-F
S.O.: 94260250

GROUND ANTENNA PARAMETERS

EFFECTING THE RANGE OF A

SPACE COMMUNICATION SYSTEM

PART II

(Application of some theoretical results for possible improvement of the existing 85 ft. diameter Goldstone paraboloid antenna.)

Submitted

to

JET PROPULSION LABORATORIES

Pasadena

by

Technical Products Division

RCA VICTOR COMPANY, LTD.

1001 Lenoir St.,

Montreal.

October 11, 1960.

Prepared by P. Foldes
Acting Supervisor

Approved by _____
Manager of the Ant. Group

Approved by _____
Manager, Engrg. Dept.

GROUND ANTENNA PARAMETERS

EFFECTING THE RANGE

OF A

SPACE COMMUNICATION SYSTEM

SUMMARY

A comparison between electrical and mechanical characteristics of different antenna systems shows that considerable improvement can be obtained by the application of a Cassegrain feed for the present $\psi_{ap} = 61^\circ$ aperture angle paraboloid. An increase in the aperture angle will result in futher improvement, but this increase is not economical under the present circumstances.

The detailed geometry of two antenna arrangements is calculated, one for 960 mc/s, one for 2400 mc/s, both using $\psi_{ap} = 61^\circ$. These arrangements using a so-called cross-horn type feed system which is theoretically satisfactory for both listening and tracking mode of operation.

Finally some recommendations are made for a short term experimental study and for a long term theoretical and experimental research.

TABLE OF CONTENTS

		Page
7.	GENERAL CONSIDERATIONS	2
8.	COMPARISON OF DIFFERENT ANTENNA ARRANGEMENTS USING THE SAME D = 85' DIAMETER PARABOLOID	2
9.	PRACTICAL REALIZATION OF THE FEED SYSTEM	14
	9.1 Realization of the horn assembly	14
	9.2 Realization of the primary reflector	20
	9.2.1. Determination of basic data	20
	9.2.2. The side lobe problem	28
10.	RECOMMENDED FURTHER WORK	37
	REFERENCES	39

7. GENERAL CONSIDERATIONS

The first part of this study indicated that, for a given paraboloid antenna, a Cassegrain type feed system yields a higher aperture efficiency, lower back radiation (noise temperature), and lower feeder loss than does an equivalent conventional horn feed system.

According to Fig. 26, the optimum aperture angle of the paraboloid, ψ_{aP} and the geometrical parameters of the hyperbolic reflector, (ψ_{aF} , d_λ) can be determined when a value for the aperture size, D_λ , is fixed. If both D_λ and ψ_{aP} are fixed the maximum possible range / unit cost figure, $\left[\frac{R}{C}\right]_{Max}$, for the antenna generally cannot be obtained. However, it is still possible to determine d_λ and ψ_{aF} in such a way that the figure of merit is the largest possible within the given circumstances. This range per unit cost value will be indicated as $\left[\frac{R}{C}\right]_o$. Obviously,

$$\left[\frac{R}{C}\right]_{Max} \geq \left[\frac{R}{C}\right]_o .$$

The following aspects of this problem will be discussed:

A) Comparison of different antenna arrangements, using 85 ft. diameter paraboloids.

B) Realization of the feed system required.

C) Recommendation for further work.

8. COMPARISON OF DIFFERENT ANTENNA ARRANGEMENTS USING THE SAME D = 85 FT DIAMETER PARABOLOID

In Table 3, the most important electrical and mechanical characteristics of six different antenna arrangements are compared. (See also Fig. 27) This table assumes a constant paraboloid diameter, with feed systems and operation wavelengths being varied.

The different systems to be considered may be grouped as follows :

A)	Present feed arrangement at Goldstone Station (four-turnstile feed),	$\psi_{ap} = 61^\circ$, f = 960 mc/s.
B)	Cassegrain feed,	$\psi_{ap} = 61^\circ$, f = 960 mc/s.
C)	Cassegrain feed, optimum ψ_{ap},	$\psi_{ap} = 69^\circ$, f = 960 mc/s.
D)	Cassegrain feed,	$\psi_{ap} = 61^\circ$, f = 2400 mc/s.
E)	Cassegrain feed, optimum ψ_{ap},	$\psi_{ap} = 69^\circ$, f = 2400 mc/s.
F)	Classical (horn) feed, optimum ψ_{ap},	$\psi_{ap} = 90^\circ$, f = 2400 mc/s.

The data for Table 3 was calculated from published characteristics of the Goldstone Station and from calculations based on the first part of this study. A Maser receiver with $T_{Rec} = 10.4^\circ K$ was assumed in each arrangement for the calculation of the R/C values.

A few comments might serve to clarify Table 3.

A) <u>Present antenna, f = 960 mc/s.</u>

By considering the theoretical pattern of the turnstile feed,* calculated values of $F_{G\,av} = 55.5$ db and S = 0.286 give an R/C of 0.94. These values indicate that relatively high power is radiated toward the ground; mainly as a result of the spillover radiation of the feed. The peak value of the power in the $\psi_{ap} \leq \psi \leq 90^\circ$ range can be estimated at 5.5 db. higher than $F_{G\,av}$. This is the result of an approximately 3.5 db. increase, caused by the difference between the peak and effective values of the field in the $\psi_{ap} \leq \psi \leq 90^\circ$ range

* Or the published noise temperature data.

and a 2 db difference, as the field in the $0 \leq \psi \leq \psi_{ap}$ range probably may be neglected. Thus the peak side lobe power in the spillover region can be estimated as about 50 db. below the main lobe level, which, according to our knowledge, is the approximate level of radiation in the spillover range.

This agreement is quite noticeable, since at present, this is the only available experimental data which verifies the theoretical considerations of Part I.

The relatively high spillover radiation most likely overrides all other types of radiation into the rear hemisphere. Thus, in this system, the contribution of rear (edge) currents can be neglected as far as noise temperature is concerned. Obviously, in systems where the spillover radiation is reduced, the effect of rear currents might be the limiting component in the total noise temperature.

Another noticeable characteristic of the present antenna is the relatively low aperture efficiency. According to the published data, this lower value is a result of the amplitude distribution in the aperture (caused by the special feed pattern), and not of the phase distribution in the aperture (caused by the inaccuracy of the reflector).

B) <u>Cassegrain Feed, $\psi_{ap} = 61^{\circ}$</u>

As the theoretical considerations have shown, improvement in the present antenna may be obtained by :

a) increasing the aperture efficiency,

b) decreasing the noise temperature.

The example in Section 5.4 indicated that values of $\eta_{\circ} = 84\%$, $T_{AT} = 14.9^{\circ}K$ and $R/C = 1.84$ can be achieved by employing a

spherical primary aperture with $\rho_\lambda = 5.4$, $\psi_{aF} = 52^\circ$ and $d_\lambda = 6.65$.
To further improve the aperture efficiency and decrease the noise temperature, ρ_λ may be increased. Unfortunately, this method inherently raises the side lobes which are close to the main beam.
As an example, what can be expected, Fig.28 indicates the variation of aperture efficiency, noise temperature, and level of first side lobes as a function of d_λ for $D_\lambda = 82.7$, $\psi_{aP} = 70^\circ$.
The spherical cup primary aperture can be realized by several means in practice. Probably the simplest form is a solid, Cassegrain type reflector, in which case the range / unit cost figure can be increased at the expense of the side lobe attenuation.
This method might prove tolerable in the appropriate application. However, it should be noted that the larger side lobe level near the main beam may increase the noise temperature if the orbit of the space object is in the neighborhood of the Sun, or other planets which are reflecting serious amounts of solar radiation.
In applications where high aperture efficiency and low noise temperature must be accompanied by low side lobe level, the screening effect of the primary reflector must be eliminated by some other means.[28, 29)]
It should be emphasized that the aperture efficiency and noise temperature data in table 3 were calculated from Fig. 26, which covers a somewhat ideal case.
In this the aperture distribution is assumed constant over the aperture sphere of the feed system. Actually, the aperture distribution decreases with ψ. This tapering is caused by the pattern shape of the illuminating feed horn and by space attenuation between the radiation centre of the horn, and different points of the hyperboloid

reflector surface. This tapering will have three major effects :

1. The aperture efficiency of the antenna system will be decreased.
2. The spillover radiation of the feed system, and hence the noise temperature, will be increased.
3. The side lobes close to the main beam will be decreased.

According to Fig. 26, the noise temperature component caused by the ground can be as low as $1^{o}K$. (This occurs for instance, when $\psi_{op} = 72^{o}$, $\rho_{\lambda} = 4.28$ and $\psi_{aF} = 70^{o}$). In that case, T_{AG} is negligible relative to the receiver noise temperature, or to the sum of the other noise components.*

D & E) <u>(Cassegrain Feeds, Freq. 2400 mc/s)</u>

These two arrangements are equivalent to the B and C arrangements, but are considered at 2400 mc/s. The gain is, of course, larger in this case. The most important special characteristic of the system is, however, that the screening effect of the primary reflector becomes smaller.

Assuming the presently available $\psi_{ap} = 61^{o}$, but increasing the frequency to f = 2400 mc/s, the radius of the spherical cup aperture will

* (Among these other components, the noise temperature corresponding to the edge currents was not analyzed in the study. No definite value for these effects is available at present, but these currents very likely cause more than $1^{o}K$ increase in noise temperature).

be $\rho_\lambda = 10.8$. This results in a $T_{AG} = 6^oK$ (compared to 10.4^oK at 1000 mc/s.). Accordingly, the total apparent antenna temperature will be decreased from 15° K to 10.6^oK. The $\frac{R}{C}$ figure increases to 2.08, while the aperture diameter increases to about $D_\lambda = 206$. This produces an approximately 7 db. increase in gain, assuming that a 0.25 rms. surface error along the paraboloid surface exists.[30]. The total increase in range relative to the present (Case A) conditions will be $2.25 \times \frac{2.08}{0.94} = 4.98$

F. Front Feed Paraboloid

Table 3 includes the most important data for a corresponding (classical) horn feed paraboloid.

The size of the feed horn was determined to give equal E and H plane beamwidths. The directivity of the horn and the aperture angle of the paraboloid were determined so as to optimize the R/C value of the system. The aperture efficiency and the ground component of noise temperature were calculated as well. From Table 3, it is evident that this system has many inferiorities in comparison to the Cassegrain system. (Low aperture efficiency, very large aperture angle). In this case, however, the screening effect is very small.

TABLE 3

(CHARACTERISTICS OF 6 DIFFERENT ANTENNA ARRANGEMENTS)

- (GEOMETRICAL) -

Item No.	Parameter	Freq. 960 mc/s.			Freq. 2400 mc/s.		
		A	B	C	D	E	F
1	Diameter, D ft.	85 ft.	85 ft.	85 ft.	85 ft.	85 ft.	85 ft.
2	Aperture Angle of Paraboloid, $\psi_{ap}°$	61°	61°	69°	61°	69°	90°
3	Aperture Size of Paraboloid in λ, D_λ	82.7	82.7	82.7	206	206	206
4	Aperture Size of first Reflector, d ft	-	6.82 ft.	7.20	6.34 ft.	8.22	-
5	" " " " " in wavelength d_λ	4	6.65	7.00	15.4	20	-
6	Focal length of Hyperboloid, A ft.	-	18.4 ft.		22 ft.		-
7	Eccentricity " " , B/A	-	0.82		0.858		-
8	Feed Angle of Horn, γ_H	-	12.5°		11°		-

TABLE 3

(CHARACTERISTICS OF 6 DIFFERENT ANTENNA ARRANGEMENTS)

- (GEOMETRICAL) -

Item No.	Parameter	Freq. 960 mc/s			Freq. 2400 mc/s.		
		A	B	C	D	E	F
9	Aperture of horn (non-tracking) or equivalent, a_λ	4	2.45		2.78		.64
10	Aperture angle of Primary Reflector, ψ_{aF}	-	52°	60°	55°	65°	
11	Radius of spherical cup Primary Aperture, ρ_λ	-	5.4	4.28	13.5	11.5	

TABLE 3

(CHARACTERISTICS OF 6 DIFFERENT ANTENNA ARRANGEMENTS)

- (ELECTRICAL) -

Item No.	Parameter	Freq. 960 mc/s.			Freq. 2400 mc/s.		
		A	B	C	D	E	F
1	Focal length of Paraboloid	36 ft.	36 ft.	30.9 ft.	36 ft.	30.91 ft	21.25 ft
2	Wavelength , λ	31.2 cm.	31.2 cm.	31.2 cm.	12.5 cm.	12.5 cm.	12.5 cm.
3	Gain of Horn , G_H		20 db.		21.2 db.		12.3 db
4	Tapering at the edge of the Hyperbola	-	4.4 db.	4.4 db	4.4 db.	4.4 db	-
5	Spillover loss	-	0.5 db.		0.5 db.		-
6	System beam with , α° 3 db.	1.1°	1°	0.97°	0.4°	0.38°	0.44°
7	Tracking Off-centering , β°	0.95°	0.17°		0.037°		.95°
8	$2\beta/\alpha$ 3 db.	1.72	0.34		0.19		1.72

TABLE 3

- (Continued)

(CHARACTERISTICS OF 6 DIFFERENT ANTENNA ARRANGEMENTS)

- (ELECTRICAL) -

Item No.	Parameter	Freq. 960 mc/s.			Freq. 2400 mc/s.		
		A	B	C	D	E	F
9	(a) Tracking Loss : because of Off-centering	-	0.4 db.	0.4 db.	0.2 db	0.2 db.	-
10	(b) Tracking Loss : because of Increased Spill-over radiation.	-	3.0 db.	3.0 db.	3.0 db	3.0 db.	-
11	(c) Total Tracking Loss	3 db.	3.4 db.	3.4 db.	3.2 db	3.2 db.	3 db.
12	Paraboloid aperture efficiency		76%	81%	78%	88%	57%
13	Overall aperture efficiency	44.6%	68%	72%	70%	78%	57%
14	System gain	44.8 db.	46.6 db.	46.8 db.	53.7 db	54.2 db.	52.8 db.
15	Spill-over (wide angle) side lobe level, K_s	-	31 db.	31 db.	36.5 db	36.5 db.	-
16	Screening (side lobe level) , K_{sc}	36 db.	30 db.	29.5 db.	32 db	31.5 db.	40 db.

- (Continued)

TABLE 3

(CHARACTERISTICS OF 6 DIFFERENT ANTENNA ARRANGEMENTS)

- (ELECTRICAL) -

tem No.	Parameter		Freq. 960 mc/s.			Freq. 2400 mc/s.		
			A	B	C	D	E	F
17	First (normal) side lobe	κ_o	22 db.	25-30 db.	25-30 db.	25-30 db.	25-30 db.	26 db
18	Noise temperature component, caused by ground radiation	T_{AG}	-	10.4° K	3° K	6° K	1.5° K	2° K
19	Total Antenna noise temperature	T_{TA}	42.3°K	15°K	7.4°K	10.6° K	6.9° K	7.4° K
20	Range per unit cost figure	$(\frac{R}{C})$	0.94	1.84	2.02	4.69	4.89	3.67

DEFINITION OF ANTENNA TYPES

Term		Feed	Dish	Freq.
A	Goldstone type antenna		61°	960 mc/s.
B	Same as "A", but with Cassegrain feed		61°	960 mc/s.
C	Same as "B", but ψ_{ap} (aperture angle) optimized		69°	960 mc/s.
D	Same as "B", except freq. at 2400 mc/s.		61°	2400 mc/s.
E	Same as "C", except at 2400 mc/s.		69°	2400 mc/s.
F	Horn feed, aperture angle optimized.		90°	2400 mc/s.

---

9. PRACTICAL REALIZATION OF THE FEED SYSTEM

The terminology to be used throughout the following discussion is given in Fig. 29. According to the drawing, the most primary part of the antenna is the horn assembly. The Cassegrain reflector, referred to as a "primary reflector" has a nominal hyperbolic shape unless otherwise specified. The horn assembly and primary reflector together constitute a "feed system", as it serves to feed the "secondary reflector" which is a paraboloid section unless otherwise specified. The combination of feed system and secondary reflector comprise the "antenna system". According to the three well-distinguishable parts of the system, individual reference will be made to the radiation pattern of the horn, feed system, and complete antenna system.

9.1 Realization of the Horn Assembly

Ideally, the horn (or horns) assembly must meet the following requirements :

1. Shall receive (or transmit) any polarizations from clockwise to counterclockwise circularly or elliptically polarized waves.
2. Shall provide listening or tracking (multilobe) mode of operation. Should it not be possible to provide a lossless electronic or mechanical switch, the horn assembly must be easily interchangeable to solve the above problems.
3. The horn assembly should provide uniform illumination along the hyperbolic reflector, which approximates the theoretically "ideal" amplitude distribution along the "spherical feed aperture".
4. The length of transmission line shall be a minimum to reduce feeder loss.
5. The input VSWR shall be small, but only in a narrow bandwidth.

In consideration for a transmitter antenna, a high VSWR may cause power loss and limitations in power handling capacity. For receiver antennas, the very low VSWR is advantageous as it may be possible to eliminate the lossy isolator at the Maser. Some of the ideal requirements are obviously contradictory to each other. The automatic change of polarization requires a switch, which introduces losses. This problem may be reduced in part, as the accessible location of the horn assembly would permit the use of a low-loss liquid nitrogen-cooled switching system. The simultaneous listening and tracking requirement necessitates a compromise in the gain, which is not always tolerable. Fortunately, the Cassegrain-type arrangement reduces the difference between listening and tracking modes. (See below). The short length of transmission line is a characteristic of the Cassegrain system, though there are deviations from the optimum, depending on the system layout. It is not mechanically convenient to place the receiver head deep within the reflector far from the vertex of the paraboloid. If the receiver is vertex-mounted, with the horn assembly mounted directly on the receiver, an excessively large horn is needed. This increase in horn size results in large horn gain with consequent high level of wide angle side lobes. If a length of transmission line is used between the receiver and horn, the loss is appreciably increased.

Based on the above consideration, a so-called "cross-horn" system can be used to meet the above requirements. Fig. 30 indicates the development of the individual horn and the four-horn assembly. One individual horn may support two independent orthogonal polariza-

tions. The generation of the horn shape may be followed in Fig. 30a and b.

Fig. 30a shows an ordinary rectangular horn for which the a and b dimensions are selected such that the 3 db. beamwidth in the E and H planes are the same. If a part of the top and bottom sections of this horn is replaced by short circuited waveguides which are in cutoff for the vertically polarized field, the original radiation pattern will be changed very little. Furthermore, the radiation pattern will be practically unchanged if horizontal fins are introduced into the horizontal section of the horn (Fig. 30b).

The resulting system is symmetrical in two planes, so a similar reasoning is valid for the horizontally polarized wave. By proper selection of the geometry of the fins, the E and H plane beamwidths may be made equal for both polarizations. If the vertical and horizontal polarizations are excited within the horns by two mutually perpendicular probes, and the relative phase between the probes is variable in the range $+90^{\circ}$ to -90°, the horn can radiate a right or left circularly polarized wave.

The front view of a 4-horn system is shown in Fig. 31. Fig. 31a indicates an arrangement in which the horns are set into the sides of each other, the cross shape being utilized to decrease the distance between the individual centers of radiation. The system shown in Fig. 31b is basically similar, but the outside of the horns has been slightly modified to further decrease the distance between the horns. Variations in fin size must be made to compensate for the change in the radiation patterns of individual horns.

The last step in the development of the horn system is to fix the

relative positions of the horn axes. If these axes are on a cylindrical surface, the maximum of the resultant pattern will be along the axis of the horn system. This produces extensive tapering in the field along the surface of the hyperboloid. The tapering can be reduced, and the spillover radiation maintained at the same level if the axes of the horns are on a conical surface and the aperture size of horns is increased at the same time. (Fig. 31c). The characteristics of the patterns for parallel and conically-mounted horns are indicated in Fig. 32.

In Fig. 32, the patterns are for in-phase feed horns. If the horns are out of phase, individual apertures may be considered separately, each horn producing a separate main beam in the secondary pattern. The position of the lobes in the multilobe pattern is basically determined by the aperture size of the horns and by the geometry of the hyperboloid reflector. (See later). At the same time, the side-lobe energy will be increased in multilobe operation, causing a decrease in the gain. The input terminals of the horns can be combined by a hybrid network as is described in Reference 1.

The aperture size of the individual horns is not critical with respect to overall aperture efficiency and noise temperature, and can be about 0.6 to 1.5λ. An increase in the aperture size of the horn makes it possible to increase the distance "A" between the center of the horn system F_H and the focal point of the paraboloid F_P . This shortens the transmission lines between the horn and feed point, assuming that the receiver head is at the vertex of the paraboloid. However, with larger

aperture sizes, the phase center of the individual horns moves further out from the axis of the paraboloid, thus increasing the tracking loss during multilobe operation. An even more serious limitation exists in the increased spillover radiation of the horns.

The size of one horn (a) and the focal length of the hyperboloid (A) can be determined from the more important limitations.

As will be shown later, one very important characteristic of the hyperboloid reflector is that it reduces the distance between the effective phase center of radiation from the system axis (Δ_R) in multilobe operation (See Fig. 33). This property of a hyperboloid makes possible the application of a relatively large Δ_H, hence also a large horn aperture.

Suppose that 3 db. reduction in gain can be tolerated during tracking. Then the beam will be off-centered by $\beta = \alpha/2$, where α is the 3 db. beamwidth of the main beam. But $\alpha = \frac{1}{\sqrt{\eta}\, D_\lambda}$ and $\beta = \frac{\Delta_R}{F}$

F represents the focal distance of the paraboloid.

Then

$$\frac{\Delta_R}{\lambda} = \frac{F}{2\sqrt{\eta}\, D}$$

Assuming $\eta = 70\%$, F = 36 feet and D = 85 feet, the calculated value of $\frac{\Delta_R}{\lambda} = 0.255$.

As Fig. 41 indicates for hyperboloids with eccentricity about 0.8, the $\frac{\Delta_H}{\Delta_R}$ ratio is in the order of 3. Thus, the center of radiation of one horn can be $\Delta_R = 0.75\lambda$.

The maximum size of one horn aperture therefore can be as large as about $2\Delta_H = 1.5\lambda$, which is satisfactory for most practical purposes.

During the listening mode of operation, the four circularly polarized horns radiate in phase and perform as one large aperture. On this aperture, the amplitude distribution approximates more closely, the constant amplitude distribution (highest possible aperture efficiency) than does a single horn of similar size. At the same time, the phase distribution is "pyramidal", and the centre of radiation is along the axis of the horn assembly behind the horn aperture. Fig. 34 compares the amplitude distribution of three horn arrangements :

a) One large horn

b) The 4-horn system with parallel axes.

c) 4-horn system with rotated horn axes.

The figure indicates that the rotation improves the overall symmetry as well.

The primary reflector is in the transition range between the Fresnel and Fraunhofer field. One characteristic of this "quasi" near field is that it is more uniform within a certain angular range and that it drops more rapidly outside this range than the Fraunhofer field. At the same time, the curvature of the radiated phase front is not circular in the range of the primary reflector and the radius of curvature of the phase front at any point along a propagating primary ray is larger than in the far field. This fact can be taken into account by correcting the shape of the primary reflector (see later), or, as a first approximation, by moving the horn system closer to the primary reflector, than was calculated from the Faunhofer theory.

The best approach is to design the primary reflector after the

exact amplitude and phase pattern of the horn assembly is known.

9.2 Realization of the Primary Reflector

9.2.1 Determination of Basic Data.

According to the previous discussions, a horn and a Cassegrain type (primary) reflector provides a simple approximation of the theoretically desired feed system. It was proven that very low noise temperature and high aperture efficiency can be obtained if the paraboloid reflector is illuminated by a spherical aperture in which the aperture distribution is constant.

Unfortunately, it is difficult to approach such a uniform amplitude distribution along a spherical aperture and any deviation from this distribution lowers the aperture efficiency and increases the noise temperature of the antenna.

In the following, the characteristics of the axially symmetrical hyperboloid reflector will be analyzed in some detail.

Fig. 35 shows a set of hyperbola contours, which are the axial intersections of such a set of hyperboloid reflectors.

A finite hyperbola section is determined by three parameters, namely the focal distance A, eccentricity $\frac{B}{A}$ and by the maximum diameter d, perpendicular to the main axis.

From the geometrical characteristics of the hyperbola, it follows that a point source radiation centered in one focal point (F_H) will be reflected as if it had been radiated from the other focal point (F_p). The notation refers to the fact that, in microwave antenna applications, the first focal point should coincide with the radiation center of the horn and the second

with the focal point of the paraboloid. This assumes that the hyperboloid reflector is the primary source of a paraboloid reflector.

Fig. 35 indicates the following basic characteristics :

1. The reflector is concave for $0 < \frac{B}{A} < \frac{1}{2}$ and convex for $\frac{1}{2} < \frac{B}{A} < 1$. From this, it follows that the angle between a ray and the axis of the reflector will be reduced by the reflector, when $\frac{B}{A} < \frac{1}{2}$ and magnified if $\frac{B}{A} > \frac{1}{2}$. The last ray, which hits the hyperboloidal reflector is particularly interesting. This ray encloses γ_H and $\pi - \psi_{oF}$ angles with the axis before and after reflection respectively. (See Fig. 36). This ratio is often termed the magnification of the hyperboloid reflector, although the ratio of the incoming and outgoing angles varies along the reflector.

2. The reflector has to intercept the largest possible amount of the horn radiation. From this point of view, the radiation towards and beyond γ_H should be negligible. (See Fig. 37). On the other hand, the extensive tapering along the reflector, which is increased by the geometrical characteristics of the hyperboloid reflector (See Fig. 38), decreases the aperture efficiency of the antenna system. The maximum overall gain occurs usually when the radiation

toward γ_H is about $-3 \sim -4$ db. relative to the maximum radiation. From this requirement, it follows that the directivity of the horn should be increased as $\frac{B}{A}$ increases, assuming constant reflector diameter.

3. From the fact that, by increasing $\frac{B}{A}$, the horn aperture increases also, it follows that the hyperboloid reflector is always in the near (or transitional) field of the horn. This increases the difficulty of the precise reflector design, but otherwise, has the electrical advantage that the field decreases more rapidly beyond the angle γ_H, than it does in the far field. (See Fig. 39).

4. Besides the tapering caused by the radiation pattern of the horn, the hyperboloid itself further modifies the pattern. The modification mainly consists of the aforementioned magnification, but the shape of the pattern itself changes slightly as well. Fig. 40 shows the pattern shape before and after reflection for various $\frac{B}{A}$, calculated on the basis of geometrical optics. $\frac{d}{A}$ = constant was assumed in this calculation and the aperture of the horn was varied to maintain -3 db. at the edge of the hyperboloid reflector.

5. If the radiation center of the horn does not coincide with the first focal point of the hyperbola, then the reflected wave is not exactly spherical. At an infinite distance from the hyperboloid reflector, obviously only the spherical wave component remains. The paraboloid, however, is in the near field.

   Generally, if a point source is at Δ_H distance from the

axis of the hyperbola, the reflected rays no longer have a single phase center and the "image" of the horn radiation will be blurred. (See Fig. 33). The defocussing(astigmatism) increases with Δ_H if $\frac{B}{A}$ is fixed or increases with $\frac{B}{A}$ if Δ_H is fixed.

However, for many practical purposes, the image can be approximated by a single point (F_p') which is the average radiation center of all the rays. The distance $\overline{F_pF_p'} = \Delta_R$ will determine the amount of linear phase error, which will be introduced into the aperture of the paraboloid and thus will determine the direction of the main beam. The $\delta = \overline{F'_{p-\Theta} \quad F'_{p+\Theta}}$ distance, on the other hand, characterizes the amount of astigmatism in the aperture distribution of the paraboloid. For an ideal system $\frac{\delta}{\Delta_R} \ll 1$, however $\frac{\delta}{\Delta_R}$ can be quite close to unity if $\frac{B}{A}$ or $\frac{d}{A}$ is large.

Another important characteristic of the hyperboloid reflector in tracking systems is that Δ_R can be either larger or smaller than Δ_H. In the more important practical case, $\frac{B}{A} > \frac{1}{2}$, when $\frac{\Delta_R}{\Delta_H}$ is smaller than unity. This very important fact makes possible the use of relatively large horn systems (4 horns for instance) for tracking purposes, without introducing a large Δ_R and thus too large beam off-centering.

Fig. 41 shows the relationship between $\frac{\Delta_H}{A}$ and the $r = \frac{\Delta_R}{\Delta_H}$ reducing factor for different $\frac{B}{A}$ values. The reduction factor expresses how many times larger off-centering can be employed at the horn aperture than if the horn system would be directly in the focal plane of the paraboloid.

6. Some rays reflected from the hyperboloidal mirror will re-enter into the horn and will cause a standing wave in the feed line. In narrow frequency bend systems, this fact is less interesting because the reflected wave can be compensated easily in the feed line. Nevertheless, this fact is also interesting from the radiation standpoint, because the center part of the hyperboloid reflector does not contribute to the radiation of the feed system and a minimum occurs in the pattern of the feed toward the paraboloid along its axis. This minimum increases the aperture efficiency of the system, but inherently increases the side lobe level also. The amount of reflected power into the horn increases as $\frac{B}{A}$ decreases.

On the basis of the above considerations, it is now possible to determine the three design parameters of the hyperbola, namely A, $\frac{B}{A}$ and $\frac{d}{A}$.

The selection of A is not critical. The usual practical value is $A = \frac{1}{2}F$ where F is the focal distance of the paraboloid. If A is larger than this value, then a large primary aperture is required. This increases the wide angle side-lobe level. If A is too small, then the transmission line losses are larger. With $A = \frac{1}{2}F$, the input of the horn can be close to the vertex of the paraboloid, which is the most convenient place for the receiver head.

In some systems, where particularly low first side lobes are required, A can be a parameter because its value expressed in λ has some effect on the aperture distribution in the paraboloid aperture. However, for the time being, this detail will not be discussed.

In the following $A = \frac{F}{2} = 18$ ft. will be assumed. Two particular cases will be investigated in all interesting practical detail.

a) An improvement of the present Goldstone Station at f = 960 mc/s. ($\psi_{aP} = 61^\circ$, $\psi_{aF} = 52^\circ$, $d_\lambda = 6.65$, Case B in Table 3).

b) The present Goldstone Station with a feed designed to f = 2400 mc/s. ($\psi_{aP} = 61^\circ$, $\psi_{aF} = 55^\circ$, $d_\lambda = 15.4$, Case D in Table 3).

The selection of the $\frac{B}{A}$ ratio involves some consideration. Strictly from the mechanical point of view, the smaller $\frac{B}{A}$ ratio is advantageous because it reduces the length of the reflector supporting rods. On the other hand, this is not the deciding factor, because the stability of the reflector position can be reduced as $\frac{B}{A}$ increases. This is caused by the fact that a decrease in the reduction factor r makes the reflector position less critical.

On the other hand, the intersection of the required aperture angle direction ψ_{aF} with the given d_λ lines (see Fig. 35) determines the endpoint of the reflector and of the required hyperpoloid ($\frac{B}{A}$).

Once A, $\frac{B}{A}$ and $\frac{d}{A}$ are determined, the γ_H "feed angle" is given. In the following examples, the feed horn apertures were determined from a requirement that the horn radiation is -4.4 db. toward the γ_H direction. This results in about 0.5 db spillover loss, approximately 30 db. spillover sidelobes and a tapering in the paraboloid aperture which is accompanied by about 70% overall aperture efficiency.

It is interesting to note that the control of the size of the horn aperture gives a possibility of varying the sidelobes and gain of the antenna system. When the antenna is pointed toward zenith, then relatively large first sidelobes can be tolerated and the maximum gain results in maximum overall signal to noise ratio. In this position, the horn aperture can be relatively small to provide a nearly constant illumination along the hyperboloid reflector.

When the antenna is directed horizontally, the nearby sidelobes cause a rapid increase in the antenna noise temperature. In this position, better signal/noise ratio can be obtained by reducing gain and lowering side lobe level. Both the spillover sidelobes and "normal" sidelobes are reduced if the feed produces more tapering along the hyperboloidal reflector. This can be obtained by using a larger horn aperture.

The horn aperture size can be easily controlled by varying the side walls. (See Fig. 42). Actually, the sidelobe attenuation can be made a function of the antenna position.

Once the system geometry is fixed, the field distribution in the paraboloid aperture can be calculated and from the aperture distribution, a more accurate pattern analysis can be made. Fig. 43 indicates the aperture distribution in three different antenna arrangements (constant illumination along the spherical cup aperture, parallel horn system with a hyperboloid reflector, rotated horn system with a hyperboloid reflector). In all cases, the aperture distribution was calculated from the

geometrical and from the wave optical approximations. All the analyzed arrangements approximate the case B in Table 3. In the case d, e and f on Fig. 43, the corresponding calculated aperture efficiencies are 84, 69.7 and 76% respectively. These figures are quite close to the measured aperture efficiency of a similar, Cassegrain antenna system (RCA, Type MM-600). This antenna has a measured aperture efficiency 60-80% in $\pm$ 15% relative frequency bandwidth. (See Fig. 45). Table 3 indicates that the sidelobes caused by the spillover radiation and screening may be in the order of 30 db. The question can be posed as to whether the first sidelobes of the undisturbed aperture distribution can be maintained at that low level with the accompanied high aperture efficiency. The answer is positive.

From the tables prepared by R. C. Hansen,[32] the Taylor distribution for $\kappa_o =$ 30 db. and n = 4, results $\beta\sigma = 1.2$, which is equivalent to $\eta_o = \frac{1}{(\beta\sigma)^2} = 69.4\%$. In Fig. 44, the Taylor distribution is compared with the aperture distribution of the parallel horn system. It is obvious that, from gain standpoint, the two distributions are close and the two calculated aperture efficiencies are practically identical. Considering the sidelobe attenuation, the two distributions are more different and the corresponding κ_o of the second case can be obtained only by numerical analysis.

It is interesting to note that the MM-600 antenna (where the sidelobes caused by the screening are the limiting factor) has,

at f = 2350 mc/s, κ_o = 24 db. with approximately η = 80% aperture efficiency.

9.2.2 The Sidelobe Problem

Fig. 46 indicates the usual sidelobe distribution of a double-reflector type antenna with the corresponding terminology. From the operational standpoint, an ideal antenna has to have the largest possible gain for a given, constantly low level of sidelobes. It has to be emphasized that this requirement is not equivalent to the more common requirement where the possible narrowest main beam is specified together with a given, constantly low level of sidelobes.

The uniform sidelobe level can not be realized in practice and usually a different average sidelobe level is specified for the forward and for the rear hemisphere.

It is worthwhile to include here a short summary about the relationship between gain and sidelobe level.

It can be easily seen that the low sidelobe level is important not only from the point of view of low noise temperature, but also because it provides a serious limitation for the gain in the event of a very high gain being required. If the main beam is very narrow and the sidelobe attenuation is only moderate, then the power content of the sidelobes cannot be neglected relative to the main lobe power. When the sidelobe level is fixed, the total radiated power remains practically constant as the main beamwidth is decreased. Thus, the gain

being the ratio of main lobe power density relative to the total power density, remains constant also.[31] From this, it follows that the gain cannot exceed the reciprocal value of the average sidelobe level.

As an example, take case D in Table 3. This antenna arrangement has 53.7 db. gain. In the front hemisphere, the "normal" sidelobes and the sidelobes resultant from the screening effect of hyperboloid reflector, taper off rapidly and their contributions to the average side lobe level are not serious. However, the spillover radiation of the feedhorn is substantial over a wide angular range. As Table 3 indicates, the maximum of this spillover radiation occurs at the border line of the geometrical shadow zone determined by the horn position and the hyperboloid. This shadow zone ends at $\gamma_H = 11^\circ$ from the axis of the main beam and sidelobe level caused by the spillover radiation is $K_s = 36.5$ db. This side lobe is caused by the outer part of the main lobe of the horn radiation and the next lobe is approximately 9 db lower. From thence, the spillover sidelobes follow the $\frac{\sin u}{u}$ pattern ($u = \pi a_\lambda \sin \Theta$).

In the above case, 4 sidelobes occur between $11^\circ < \Theta < 119^\circ$ in the analysed main plane. The corresponding levels of these side lobes are 36.5, 45.5, 49.7, 52.9 db. Taking into account that the above values are peak levels, the average power level in the $11^\circ < \Theta < 119^\circ$ range is approximately 50 db. This radiation occupies 75% of the total sphere ($\psi_{ap} = 61^\circ$) thus behind the paraboloid, the average power level should be $F_{avG} = 58$ db

from the gain balance standpoint alone.

For this antenna arrangement $T_{AG} = 6\ ^{o}K$ was calculated as the ultimate possibility for the noise temperature component caused by the ground. From $T_{AG} = 6^{o}K$ and $D_{\lambda} = 206$, Fig. 6 indicates that $F_{avG} = 69$ db. is required. This is 11 db. higher than the value determined by the gain limitations. On the other hand, Fig. 6 shows, that the same antenna will become gain limited if $T_{AG} > 50^{o}K$ is only required.

Table 4 numerizes the different type of sidelobe components, their range of occurrence and the methods of decreasing their level.

It is quite difficult to analyze most the sidelobe sources and the corresponding sidelobes, but their importance amply justifies the necessity of an extensive general study.

No. 4 and No. 8 in Table 4 were analyzed in some detail in several hypothetical cases where the calculations were relatively simple. (See Part I)

Some measured data is available to determine # 3 and some limits were given in Table 3. The effect of inaccuracy (# 6) is discussed in the literature [30], although not for the aperture distribution used in Cassegrain type systems. The same is applicable to # 1.

Here only, the most important type of sidelobe will be discussed, namely, that which is caused by the screening effect of the center reflector.

TABLE 4

CHARACTERISTICS OF SIDELOBE COMPONENTS

	Type or reason	Range of occurrence	Methods of decreasing
1.	Normal interference.	Near to main lobe	More tapering in paraboloid aperture.
2.	Screening of hyperboloid reflector	$0 \leq \theta \leq \pi - \psi_{ap}$	Decreasing size of hyperboloid; semi-transparent primary reflector.
3.	Spillover radiation of horn	$\gamma_H \leq \theta \leq \pi - \psi_{ap}$	Decreasing A.
4.	Direct radiation of hyperboloid reflector	$0 \leq \theta \leq \pi - \psi_{ap}$	More tapering along hyperboloid reflector.
5.	Finite size of horn (astigmatism)	"	Decreasing horn size.
6.	Inaccuracy of reflectors	"	Increasing accuracy.
7.	Rear current on secondary reflector	$\pi - \psi_{ap} \leq \theta \leq \pi$	More tapering in paraboloid aperture; corrugations at edge of reflector.
8.	Transmission through secondary reflector	"	Increase density of gratings.

A technique can be employed in which the center reflector is built up from a honeycomb type lens with a reflection coefficient in the order of 90%. The geometry of this lens can be selected so that the field transmitted through the lens will be a continuation of the unobstructed aperture field distribution. This field should be inphase with the wave reflected from the paraboloid and because of the continuance in the amplitude distribution, the usual screening effect of the solid hyperboloid reflector will be eliminated. Such a system will obviously have a narrow bandwidth, but would be satisfactory for space communication antennas.

The geometry of the lens can be calculated as follows :

$$\beta\left[R + (\varrho - \ell) + \varrho\cos\psi + \varrho_M\cos\psi'_{ap}\right] + \phi + 2\pi k = \beta\left[R + (B - R\cos\alpha_1) + \varrho_M\cos\psi'_{ap} - z\right] + z\beta_g \quad , \tag{164}$$

$$\frac{f(\alpha_1)}{R(\alpha_1)}\left[1 - \Gamma(\alpha_1)\right] = \frac{f(\alpha_2)}{\varrho(\psi_2)} \quad . \tag{165}$$

Equations (164) and (165) respectively, may be called the phase and amplitude equations of the reflecting lens. The first equation shows that, in the aperture plane P, the phase is constant. The second expression indicates that the amplitude distribution in this plane is identical with the illumination resulting from a feed radiating toward the paraboloid from the point F_p. The two equations describe a system in which the aperture distribution in

plane A varies continuously between $0 \leq r \leq 1$ with no screening effect.

The quantities in the equations are defined in Fig. 47. $\Gamma \angle \phi$ is the reflection coefficient of the lens at the input surface (s), and $\beta_g(r)$ is the propagation constant with the lens along the z axis. It is assumed that the reflection coefficient of the lens at the output surface (y) can be eliminated by a quarter wave matching section.

On the basis of Fig. 47, the following equations can be written

$$R(\alpha_1)\sin\alpha_1 = \rho(\psi_2)\sin\psi_2 = \rho(\psi_2)\frac{R(\alpha_2)}{\ell(\psi_2)} , \tag{166}$$

$$\Gamma = \frac{\lambda - \lambda_g}{\lambda + \lambda_g} = \frac{\beta_g - \beta}{\beta_g + \beta} , \tag{167}$$

$$r = \ell \sin\psi . \tag{168}$$

If the contour 's' is fixed as a hyperbola, then the relationship between α_2 and ψ_2 is given by : $\psi_2 = g(\alpha_2)$ (169)

Similarly, from equations (166) and (169), α_2 can be expressed as a function of α_1,

$$\alpha_2 = h(\alpha_1) . \tag{170}$$

The index of refraction n_1 at the angle α_1

$$n_1 = \frac{\lambda}{\lambda_{g1}} . \tag{171}$$

Simplifying (164) and using (171)

$$\rho_1(1 + \cos\psi_1) - \ell_1 + \left(\frac{\phi_1}{2\pi} + k\right)\lambda - B + R_1\cos\alpha_1 = z(n_1 - 1) . \tag{172}$$

ϕ_1 is the phase of the reflection coefficient at α_1, R_1, z_1 and n_1 are the special values of these quantities at α_1. n_1 can be expressed from the phase equation

$$n_1 = \frac{2 - \frac{f_2 R_1}{f_1 \rho_2}}{\frac{f_2 R_1}{f_1 \rho_2}}$$

$$= \frac{2 - \frac{f[h(\alpha_1)]\, R(\alpha_1)}{f(\alpha_1)\, \rho\{g[h(\alpha_1)]\}}}{\frac{f[h(\alpha_1)]\, R(\alpha_1)}{f(\alpha_1)\, \rho\{g[h(\alpha_1)]\}}} \equiv n_1(\alpha_1) \tag{173}$$

According to (173), it is possible to express explicitly the index of refraction as a function of the polar angle (α_1) of the horn pattern.

From (172) and (173), the thickness of the lens

$$\frac{z_1}{\lambda} = \frac{\rho_\lambda[g(\alpha_1)]\left(1 + \cos[g(\alpha_1)]\right) - \ell_\lambda[g(\alpha_1)] - B_\lambda + R_\lambda(\alpha_1)\cos\alpha_1 + \left(\frac{\phi(\alpha_1)}{2\pi} + k\right)}{n_1(\alpha_1) - 1} \tag{174}$$

(174) does not describe the effect of the matching section on the output (y) surface. The calculation for this more general case is more complicated and is not included here.

It is interesting to note however, that in a practical case, when $\frac{f_2}{f_1} = \frac{1}{2}$ and $\frac{R_1}{\rho_2} = \frac{1}{3}$, the value of Γ is $\frac{5}{6}$.

One possible way of building a lens with a variable index of refraction is by making use of a metallic lens. In this case, the index of refraction is determined by the separation of the metal plates, perpendicular to the polarization. Then

$$n = \frac{\lambda}{\lambda_g} = \left[1 - \left(\frac{\lambda}{2a}\right)^2\right]^{\frac{1}{2}} .$$

For $\Gamma = \frac{5}{6}$, the value of refraction coefficient is (11)$^{-1}$. In this case, the separation between the plates is very close to $\lambda/2$ and the lens is quite frequency-sensitive. In the case of a circularly polarized incoming wave, the lens should have a honeycomb structure.

A well-known property of the metallic lens is that, in certain circumstances, spurious reflected lobes can occur from the input surface.[33, 34]

According to Fig. 48, such spurious reflections appear in the directions where the edges of the plates are radiating inphase. There

$$x = y \pm k\lambda \quad , \qquad k = 0, \pm 1, \pm 2 \ldots . \tag{175}$$

But

$$x = b\cos\left(\frac{\pi}{2} - i\right) = b \sin i \quad , \tag{176}$$

$$y = b\cos\left(\frac{\pi}{2} - \theta\right) = b \sin\theta \quad , \tag{177}$$

$$b \sin i = b \sin\theta + k\lambda \quad , \qquad a = b \sin\alpha \quad , \tag{178}$$

$$\sin i = \sin\theta + k\frac{\lambda}{a}\sin\alpha = \sin\theta + k\frac{\sin\alpha}{a_\lambda} \quad . \tag{179}$$

Special cases

1) $k = o$

$\sin i = \sin \theta$ $\qquad i = \theta$

This is the normal case. The angle of the reflected wave is equal to the angle of the incoming wave.

2) $|k| > o.$ $\qquad a_\lambda > \frac{1}{2}$

From equation (179), it can be seen that no spurious reflected waves can occur until $|\alpha| < 45^\circ$ which is well within the practical cases. Thus, only the regular reflection can occur while $|\alpha| < 45^\circ$ and a metallic lens can be used for the purpose of pattern synthesis.

It is interesting to compare some antenna arrangements from the standpoint of aperture distribution synthesis.

1) Feed horn, paraboloid. This system has one (limited) degree of freedom; the pattern shape of the horn.

2) Feed horn, hyperboloid and paraboloid reflector combination. Additional (limited) degree of freedom as a result of the hyperboloid reflector.

3) Feed horn, hyperboloidal reflecting lens, paraboloid reflector. Additional (limited) degree of freedom, used for eliminating the screening.

4) Feed horn, general reflecting lens, general secondary reflector This system has a complete degree of freedom in relation to the conventional paraboloid antenna. It can realize any amplitude

distribution, with constant phase, in the aperture of the secondary reflector. (Within the geometrical optical approximation).

The fourth case will not be discussed here. However, it should be noted that this arrangement may provide an approach for an optimum gain, low sidelobe level antenna system.

10. Recommended Further Work

The present study has attempted to summarize some of the most important problems of high gain, low noise temperature antennas, particularly those which employ two reflecting surfaces. However, available time has not permitted any further investigation of some other interesting details. Furthermore, within the limits of the present study, it was not possible to make any experiments and thus prove the more vital part of the theory or obtain data where the mathematical analysis is not practical.

Obviously, further work would be required to add more theoretical and experimental detail to the present study. This work can logically be divided into two parts. One, to cover the short term requirements for the improvement program of the present Goldstone antenna, the second to carry on theoretical and experimental work in the search for more effective and economical low noise antenna systems.

1) <u>Short Term Program (Experimental)</u>

1.1 Development of the cross-horn system. Near and far field pattern testing of such systems.

1.2 Determination of the optimum feed system for the $\psi_{ap} = 61^{\circ}$ aperture angle paraboloid. Investigation of the effect of aperture angle on η and T_{AG} at least within the $61^{\circ} \leq \psi_{ap} \leq 90^{\circ}$ aperture angle range, particularly in the neighbourhood of Cases B, C, D and E in Table 3.

1.3 Investigation of the effect of edge currents.

2) <u>Long Term Program</u> (Theoretical and Experimental)

Investigation of the -

2.1 <u>Sidelobe problem in the front hemisphere</u>

2.1.1 Effect of screening. (Reflecting lens)

2.1.2 Wide angle radiation of horn. (Further means of horn pattern shaping)

2.1.3 Normal sidelobe distribution. (Application of nonparabolic reflector).

2.1.4 Effect of reflector accuracy.

2.2 <u>Sidelobe problem in the rear hemisphere.</u>

2.2.1 Physical nature of rear current generation and its control.

2.2.2 Possibility of directing rear current radiation into the front hemisphere.

2.3 <u>Possibility of position controlled sidelobe attenuation.</u>

REFERENCES

28. C. A. COCHRANE, "High Frequency Radio Aerials"
U.S. Patent No. 2,736,895; Feb. 28, 1956.

29. P. FOLDES, "Semitransparent Reflector For Cassegrain Antenna"
RCA Patent Disclosure; Oct. 11, 1960.

30. J. RUZE, "The Effect Of Aperture Distribution Errors On the Radiation Pattern".
NRL Rept. 4019 (ASTIA-AT1-202826); April 28, 1952.

31. R. C. HANSEN, "Gain Limitations Of Large Antennas"
IRE Trans. on Ant. and Prop. Vol. AP-8, No. 5, Sept., 1960, pp. 490-495.

32. R. C. HANSEN, "Tables Of Taylor Distributions For Circular Aperture Antennas"
Microwave Lab., Hughes Aircraft Co., Culver City, Calif. Rept. No. TM 507; Feb., 1959.

33. J. F. CARLSON, A. E. HEINS, "The Reflection Of An Electro-Magnetic Plane Wave By An Infinite Set Of Plates"
Quarterly, Applied Math. 1947, No. 4, p. 313.

34. C. A. COCHRANE, "An Experimental Verification Of The Theory Of Parallel Plate Media"
Prac. IEE. Vol. 97, Pt. III, 1950, p. 72.

----oOOOo----

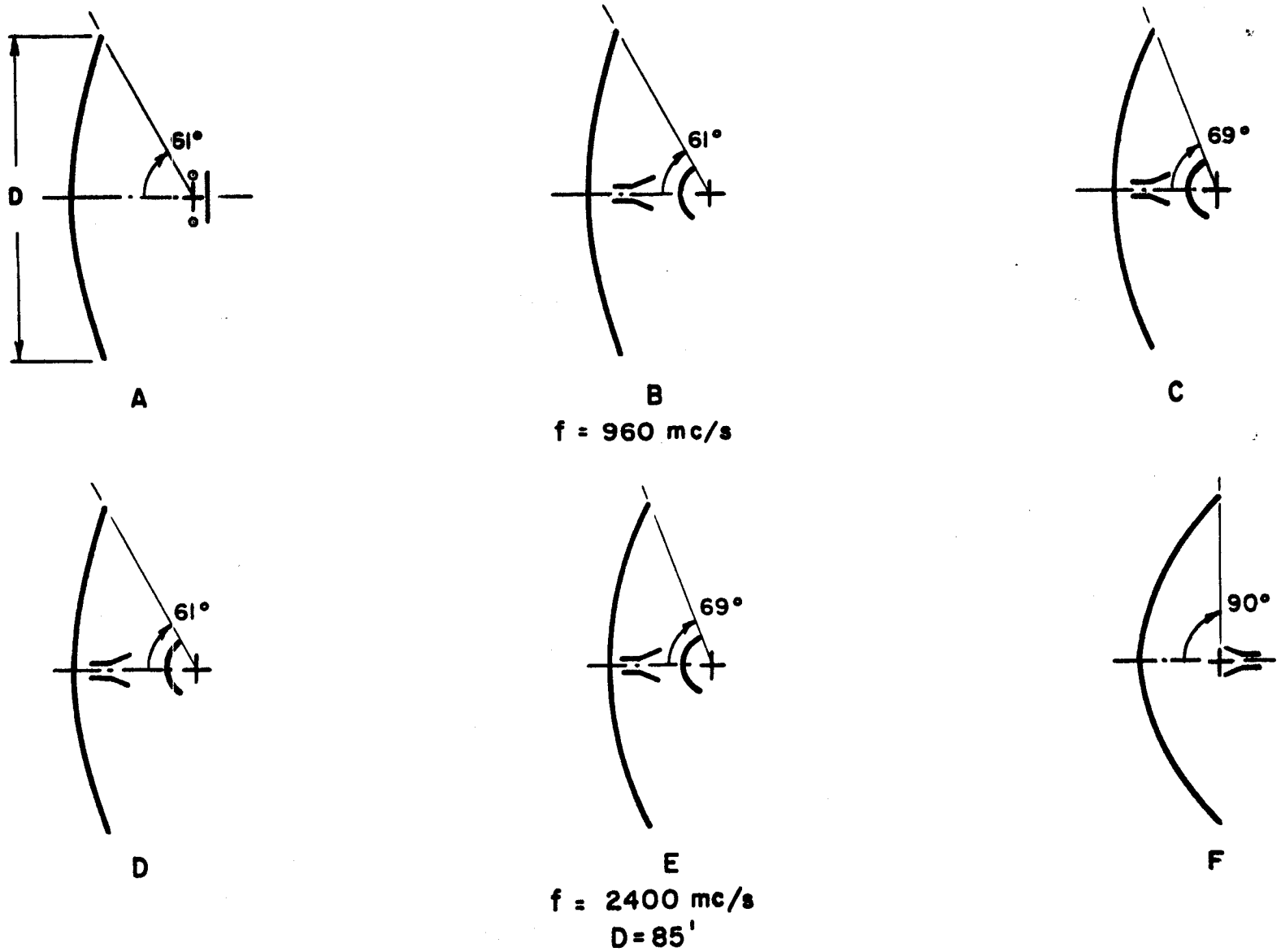

Fig. 27. Comparison between six different antenna arrangements.

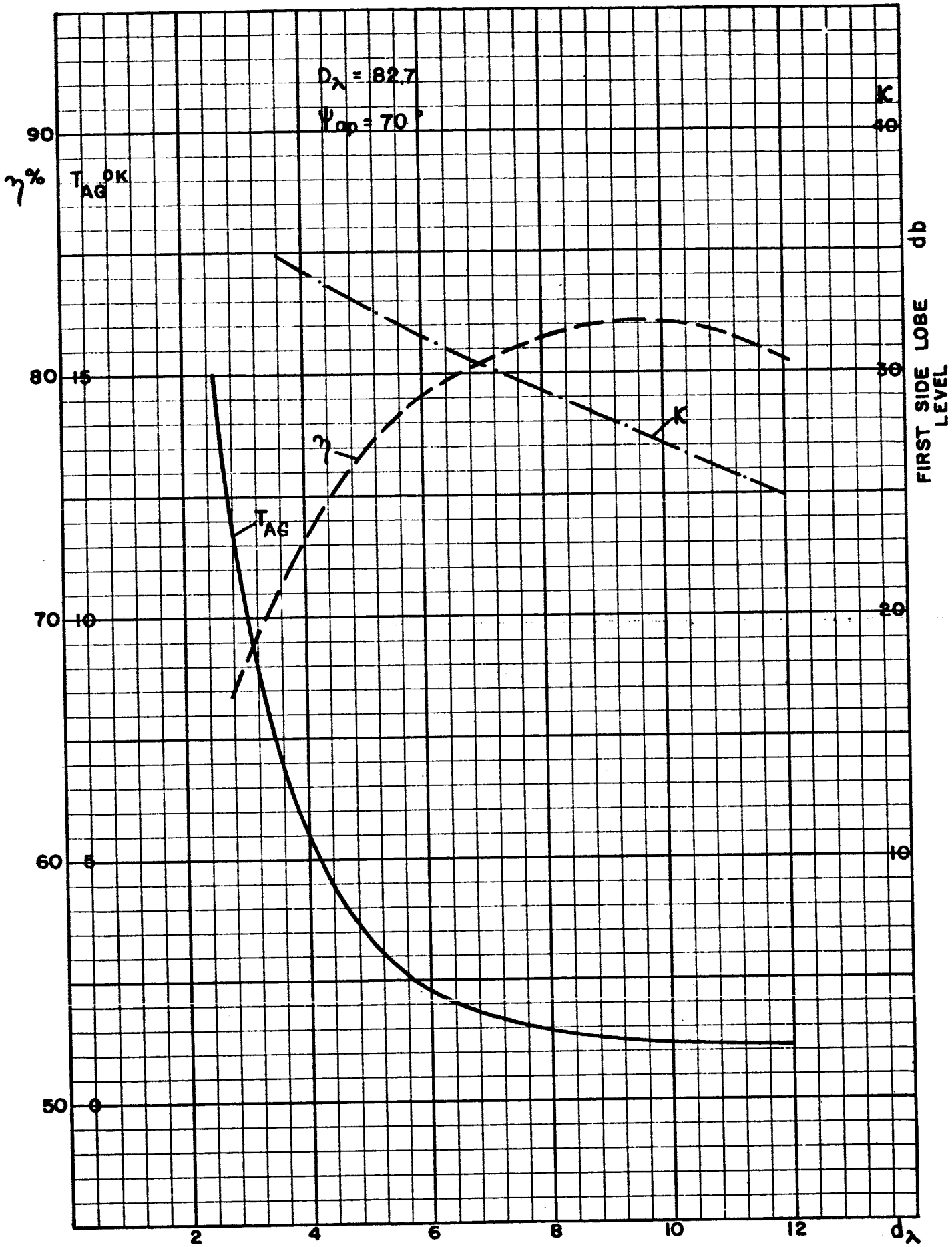

Fig. 28. Variation of aperture efficiency, noise temperature and first side lobe level as a function of the size of primary reflector.

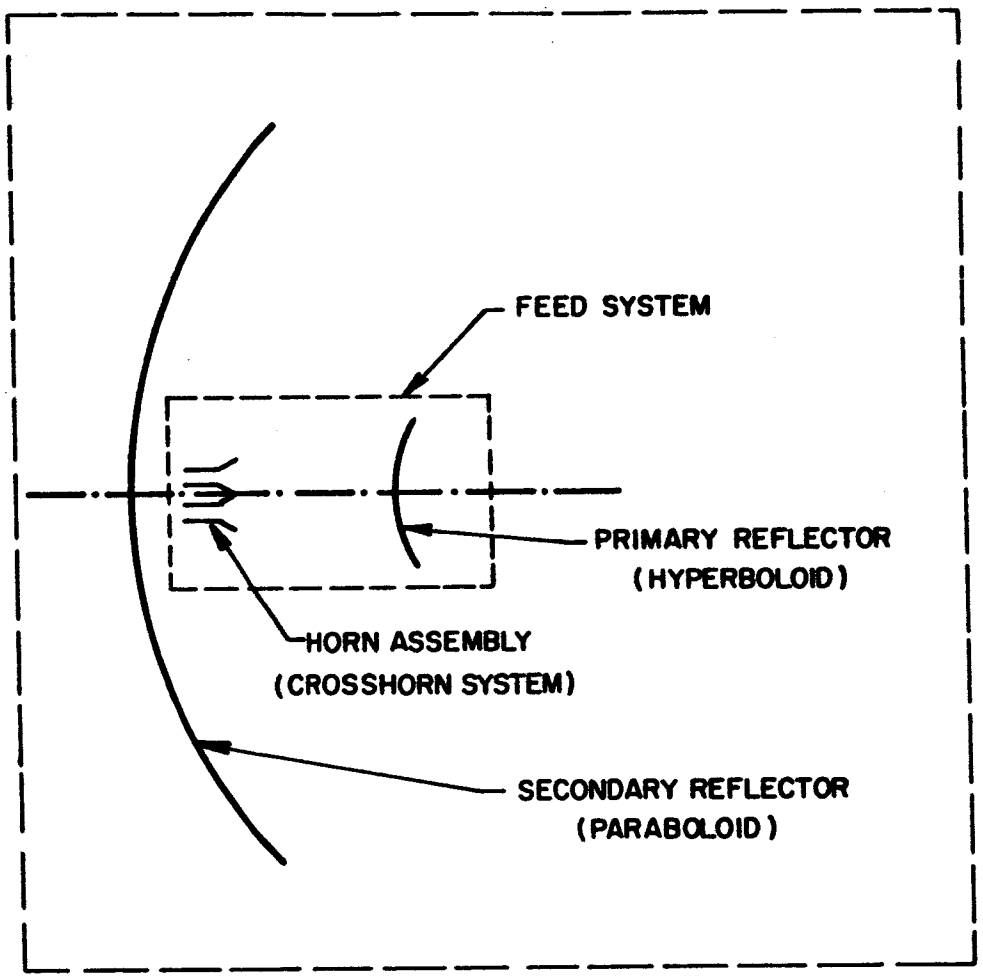

ANTENNA SYSTEM

Fig. 29 Terminology for the antenna arrangement.

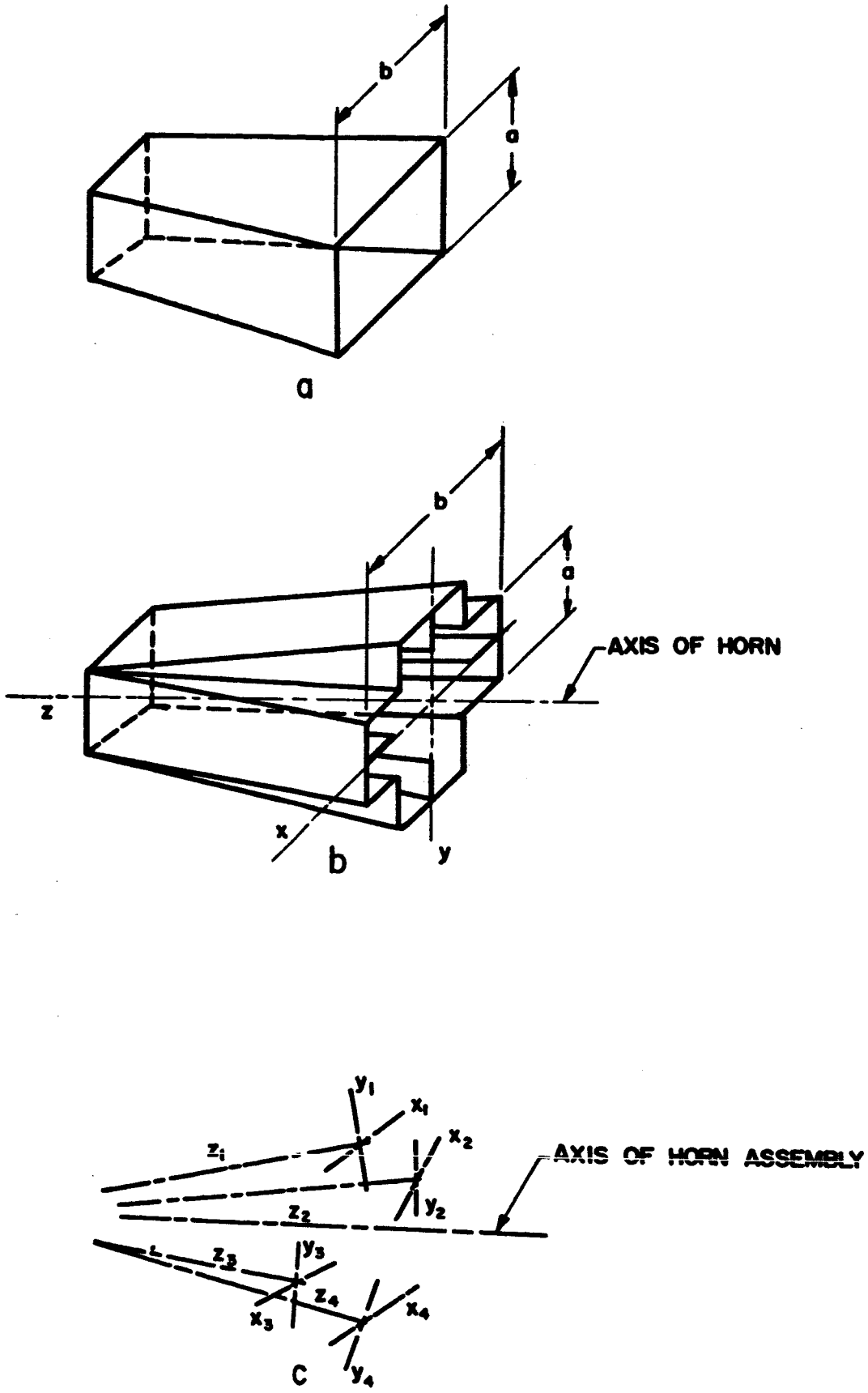

Fig. 30. Development of the feed system.

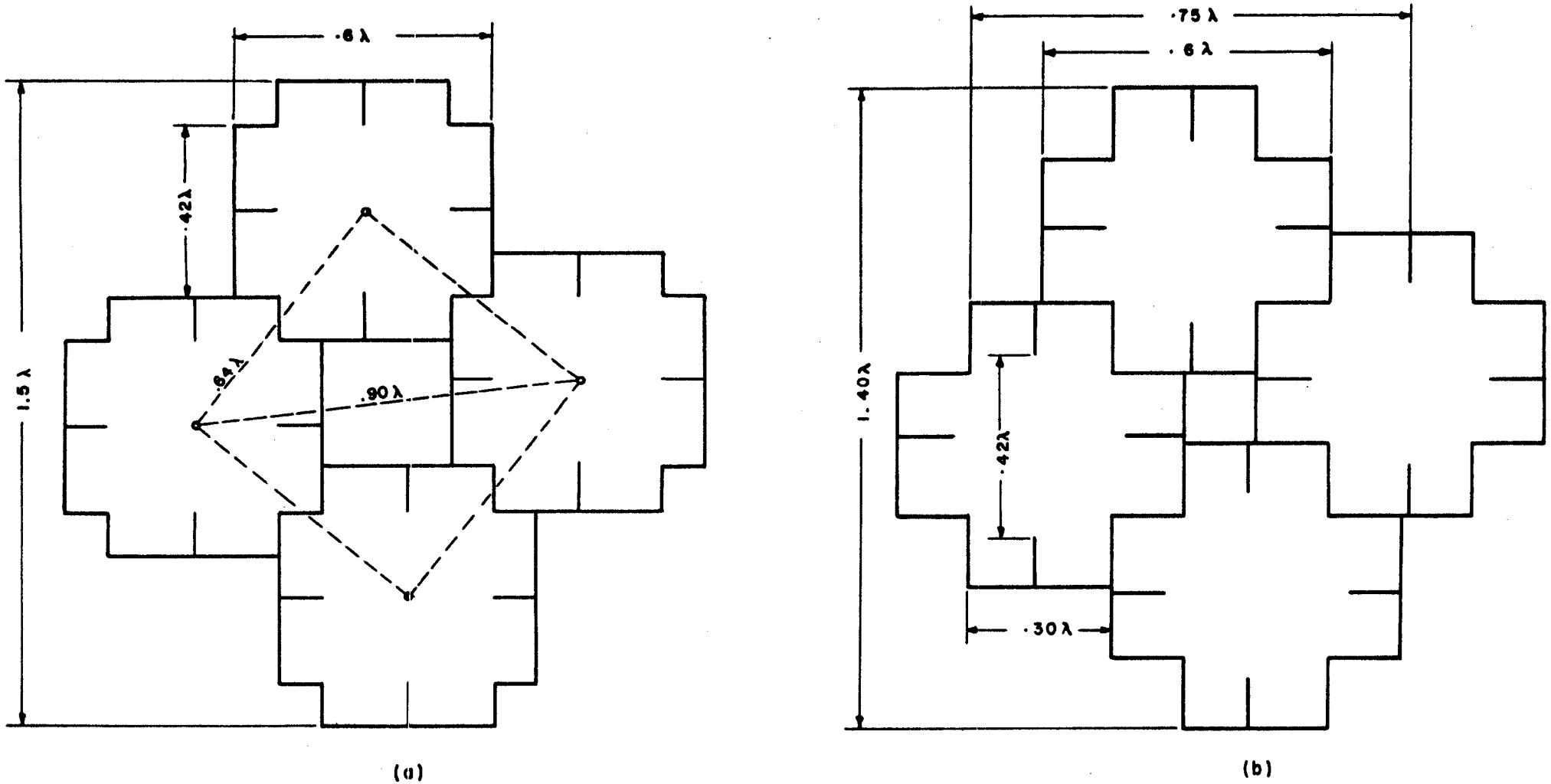

Fig. 31. Front view of the four crosshorn feed.

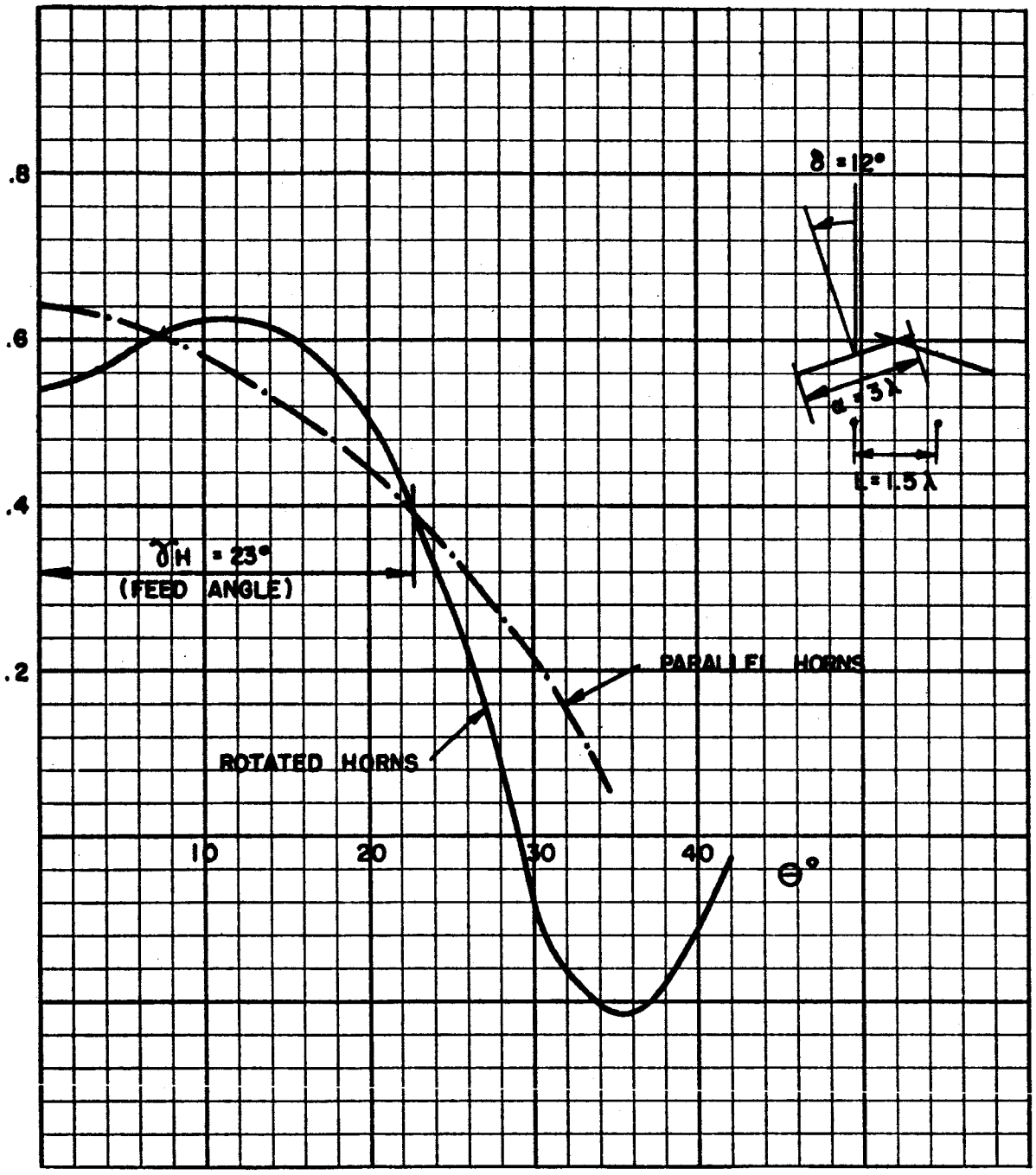

Fig. 32. Pattern of the horn assembly in the case of parallel and conically aligned horns.

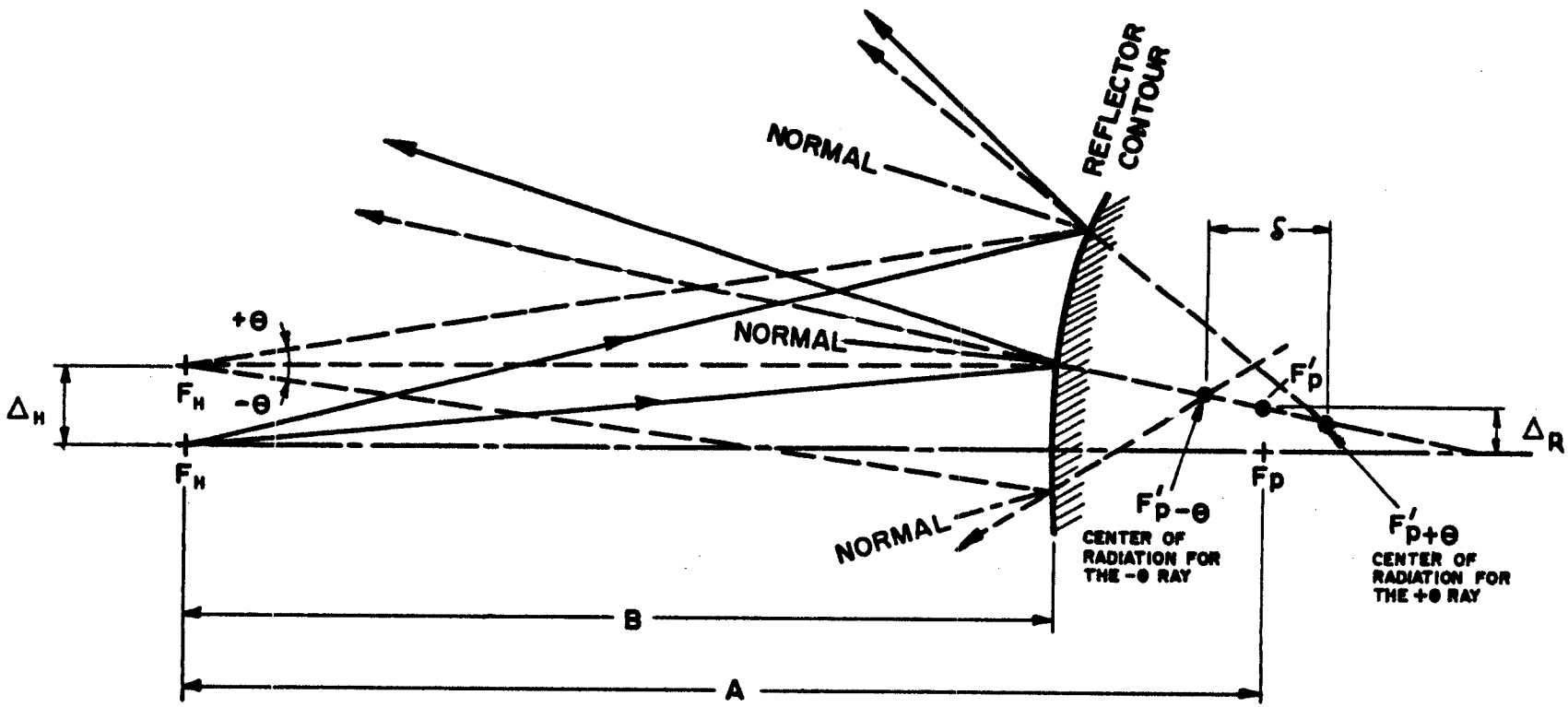

Fig. 33. Dependency of the image phase center from the horn position.

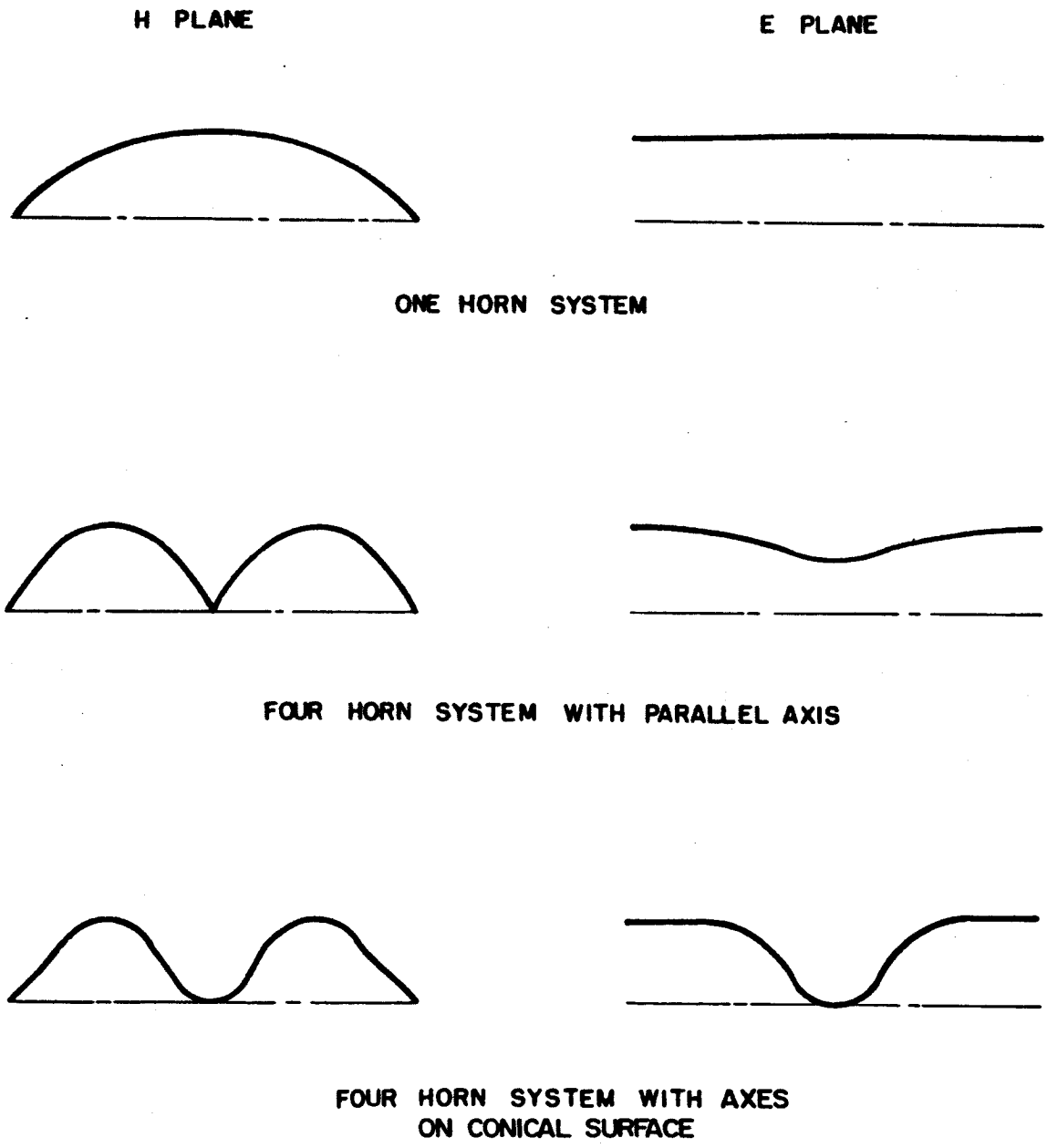

FIG. 34. Amplitude distribution in the aperture of different horn assemblies.

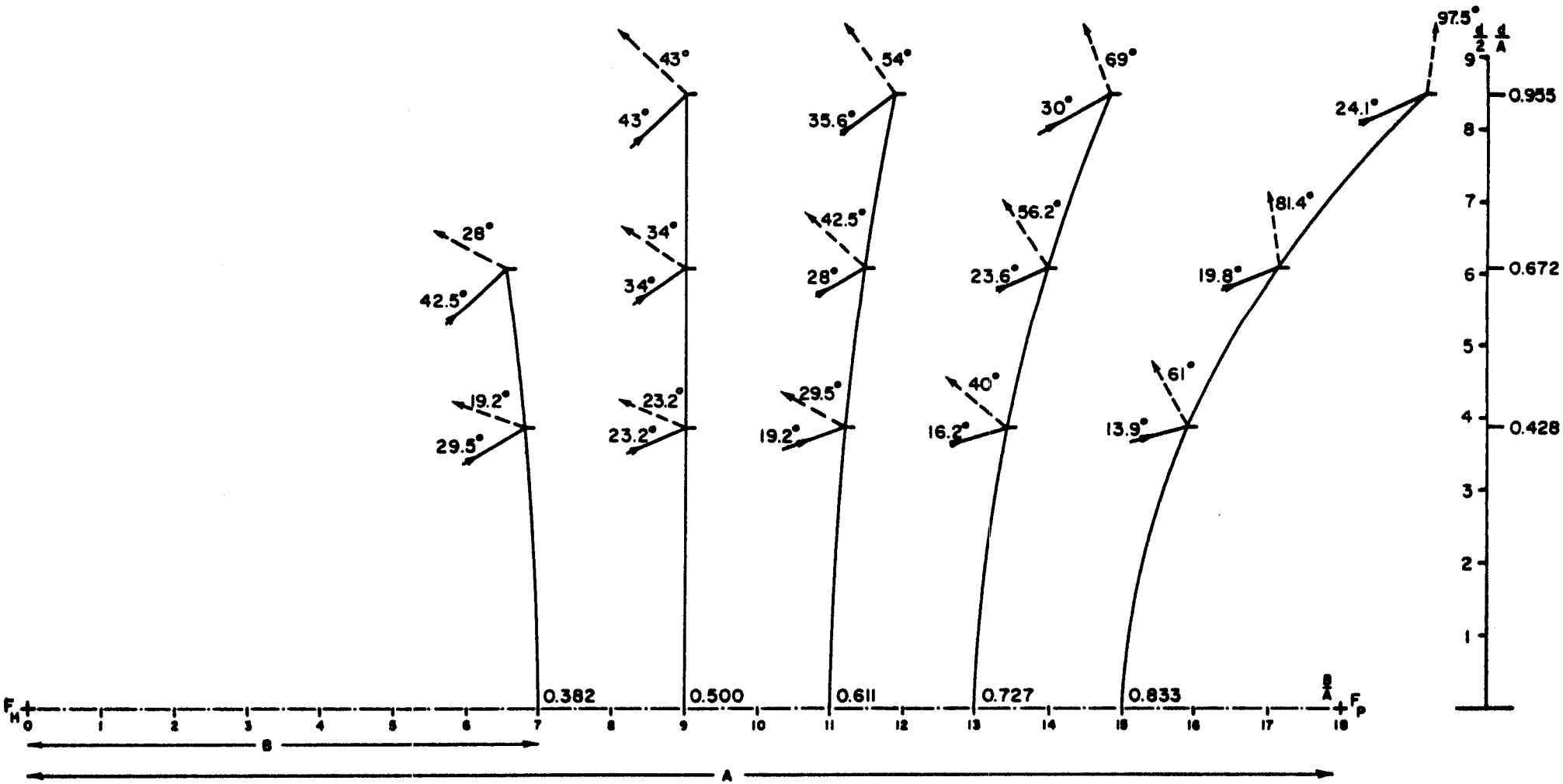

Fig. 35 GEOMETRICAL CHARACTERISTICS OF HYPERBOLA REFLECTOR

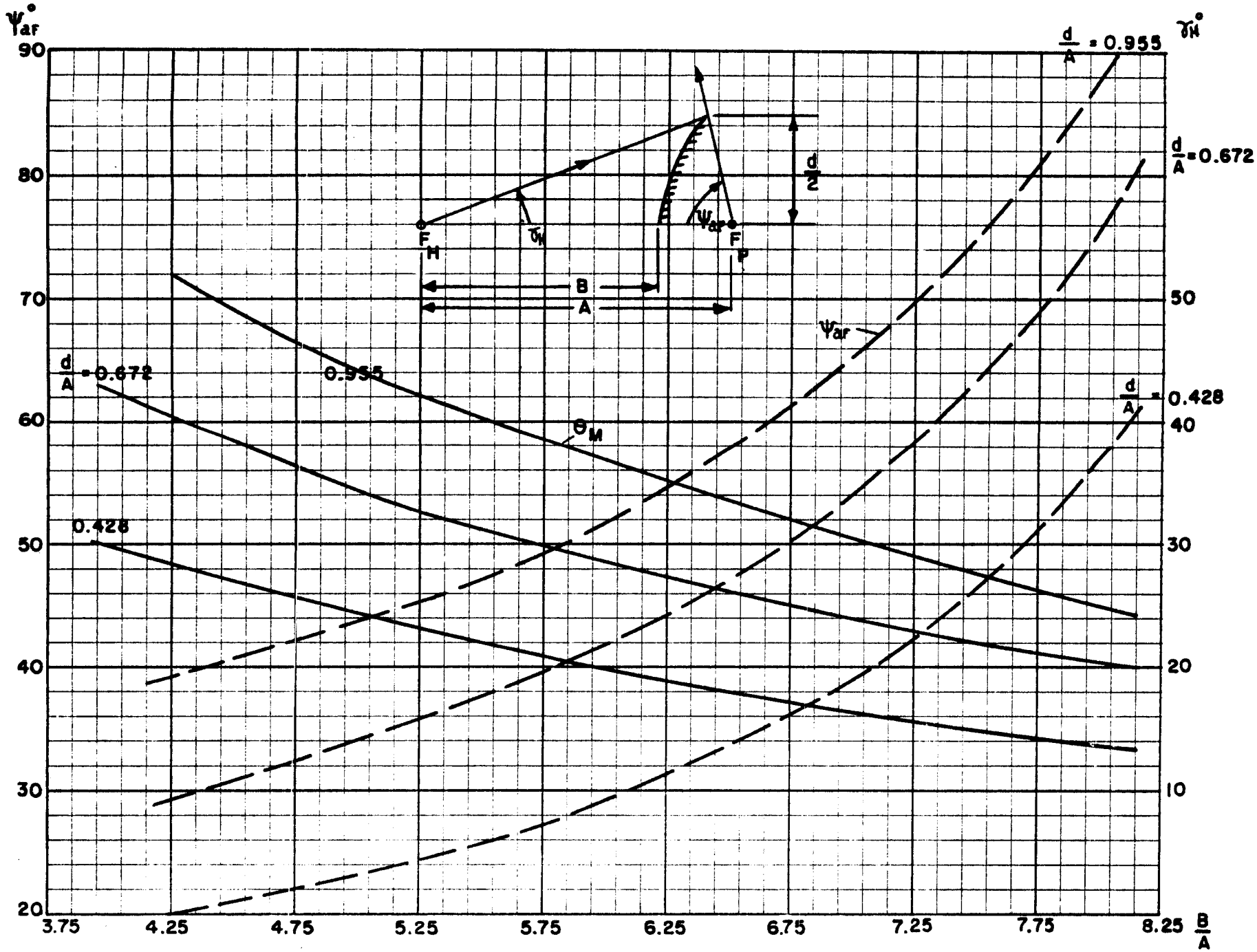

Fig. 36. Reduction and magnification characteristics of the hyperboloid reflector.

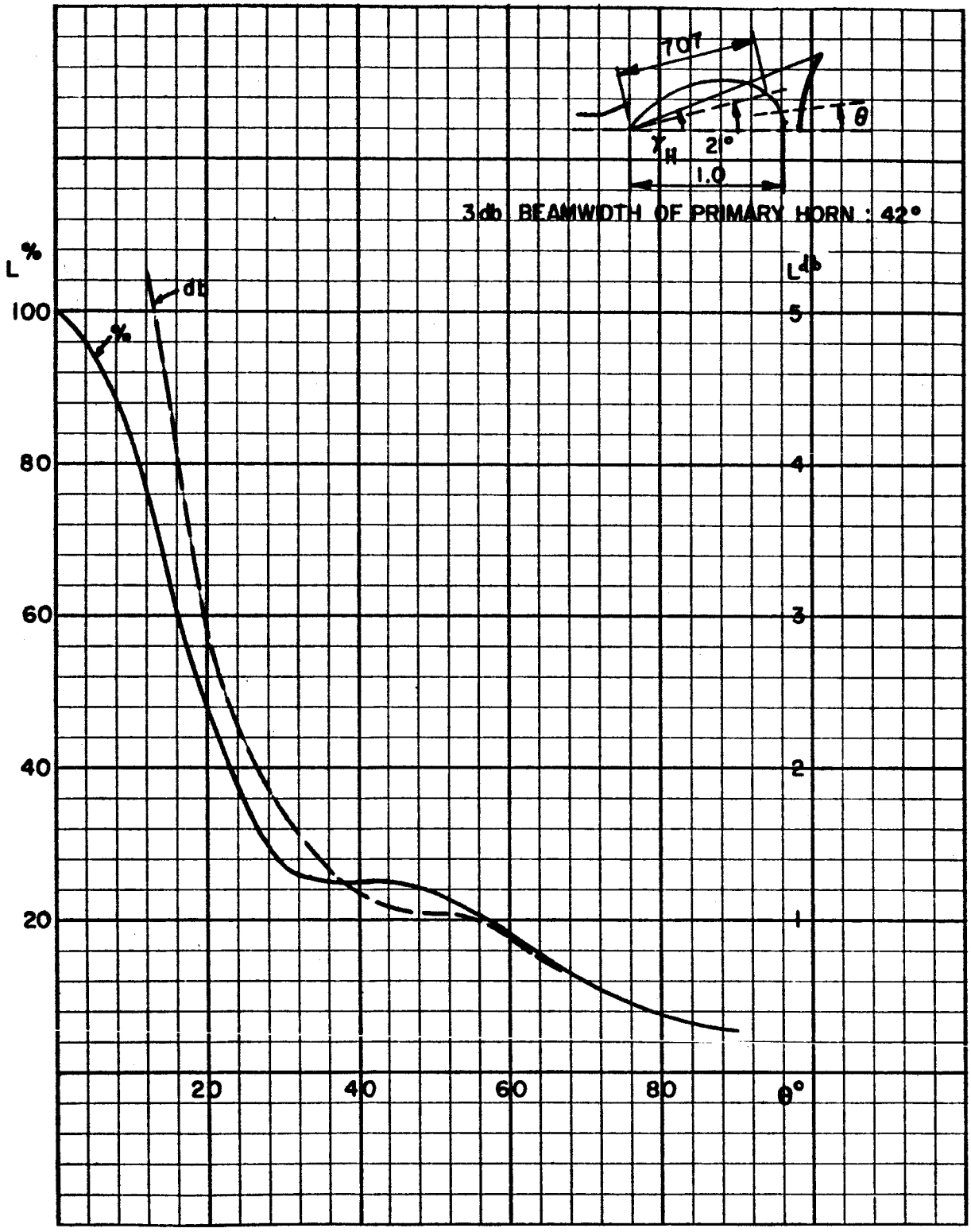

Fig. 37. Spillover loss caused by the unintercepted horn radiation.

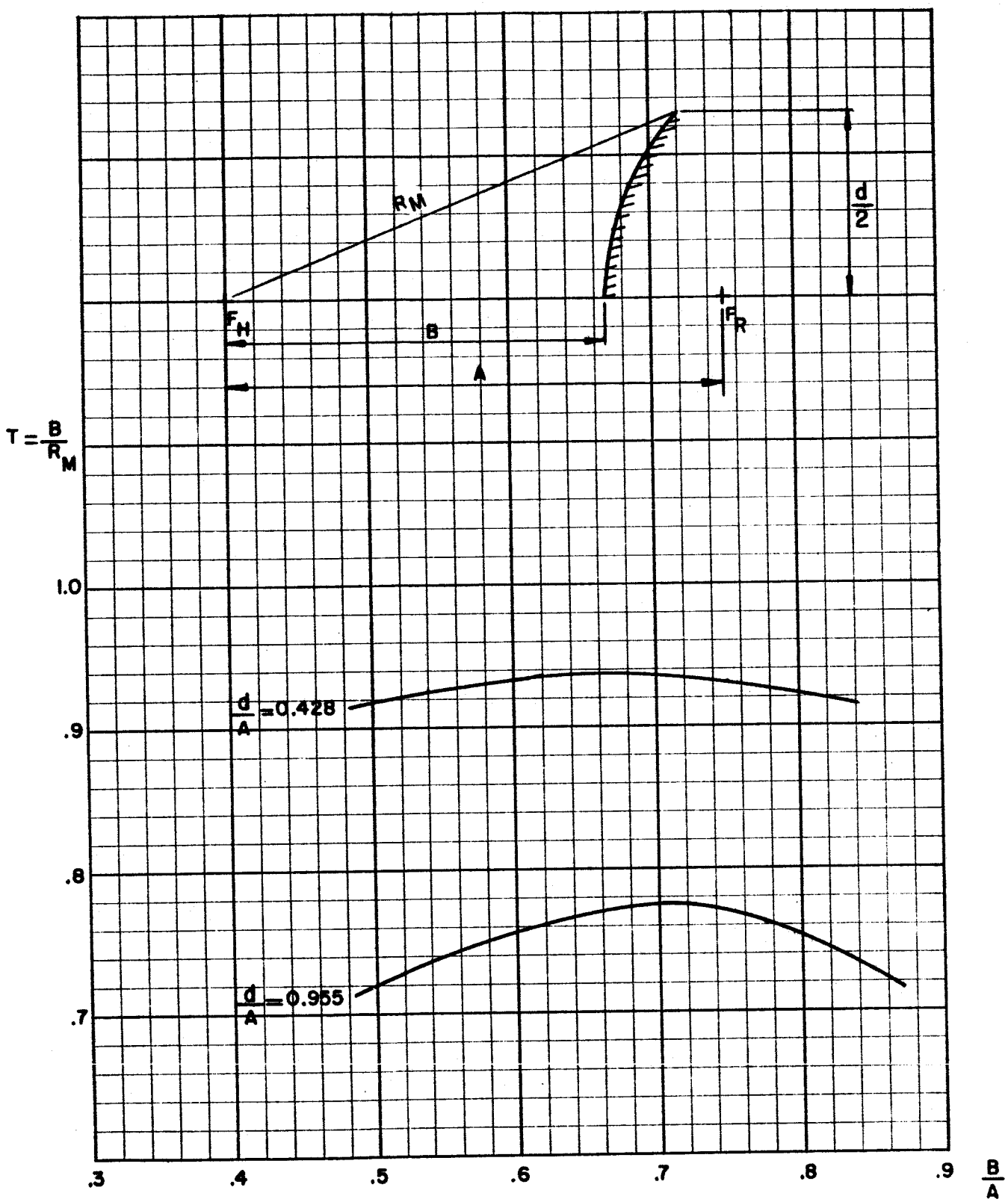

Fig. 38. Geometrical tapering characteristics of the hyperboloid reflector.

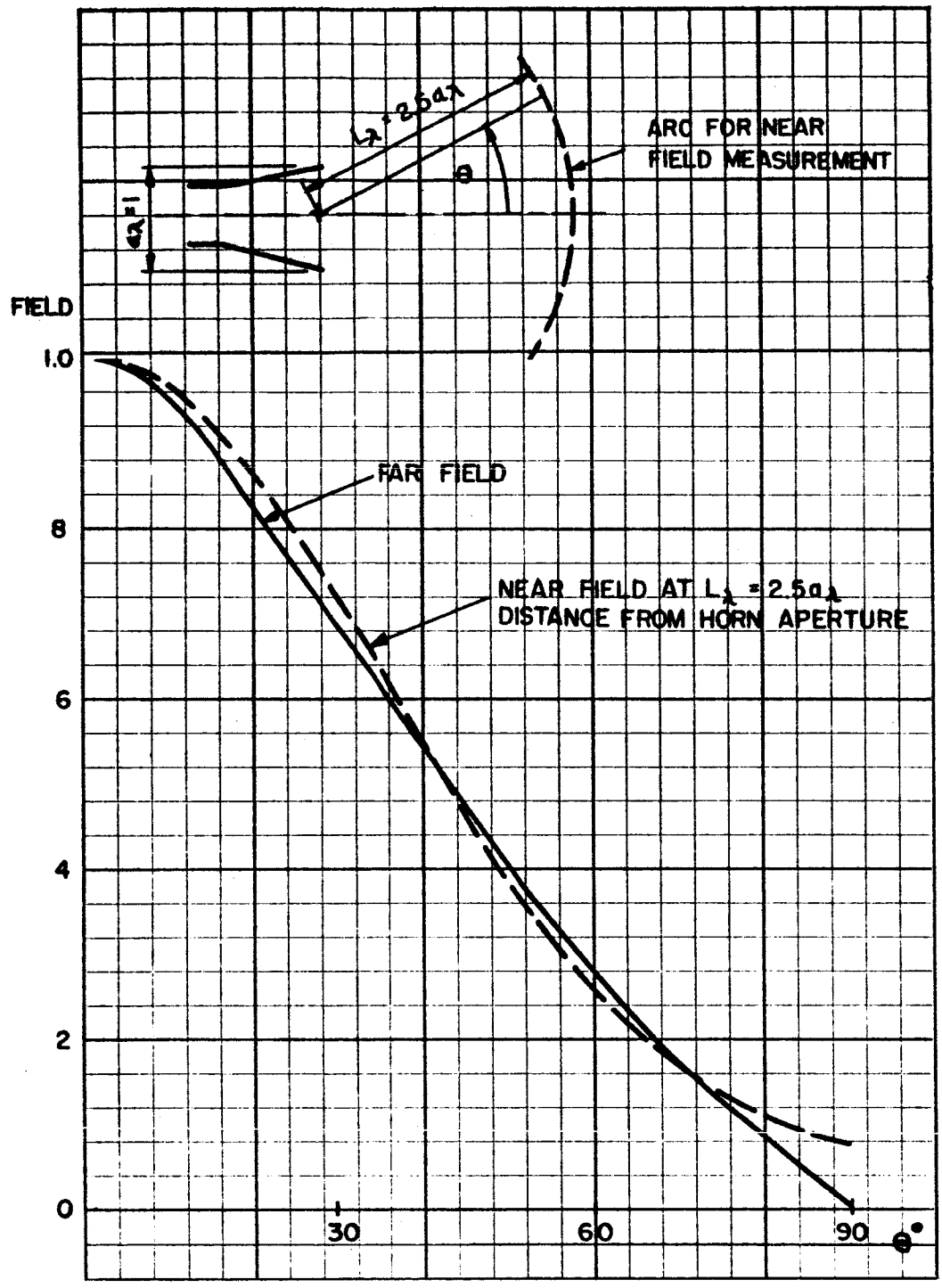

Fig. 39. Difference between the far field and near field pattern of the horn (measurement).
Near field is measured on the range of primary reflector

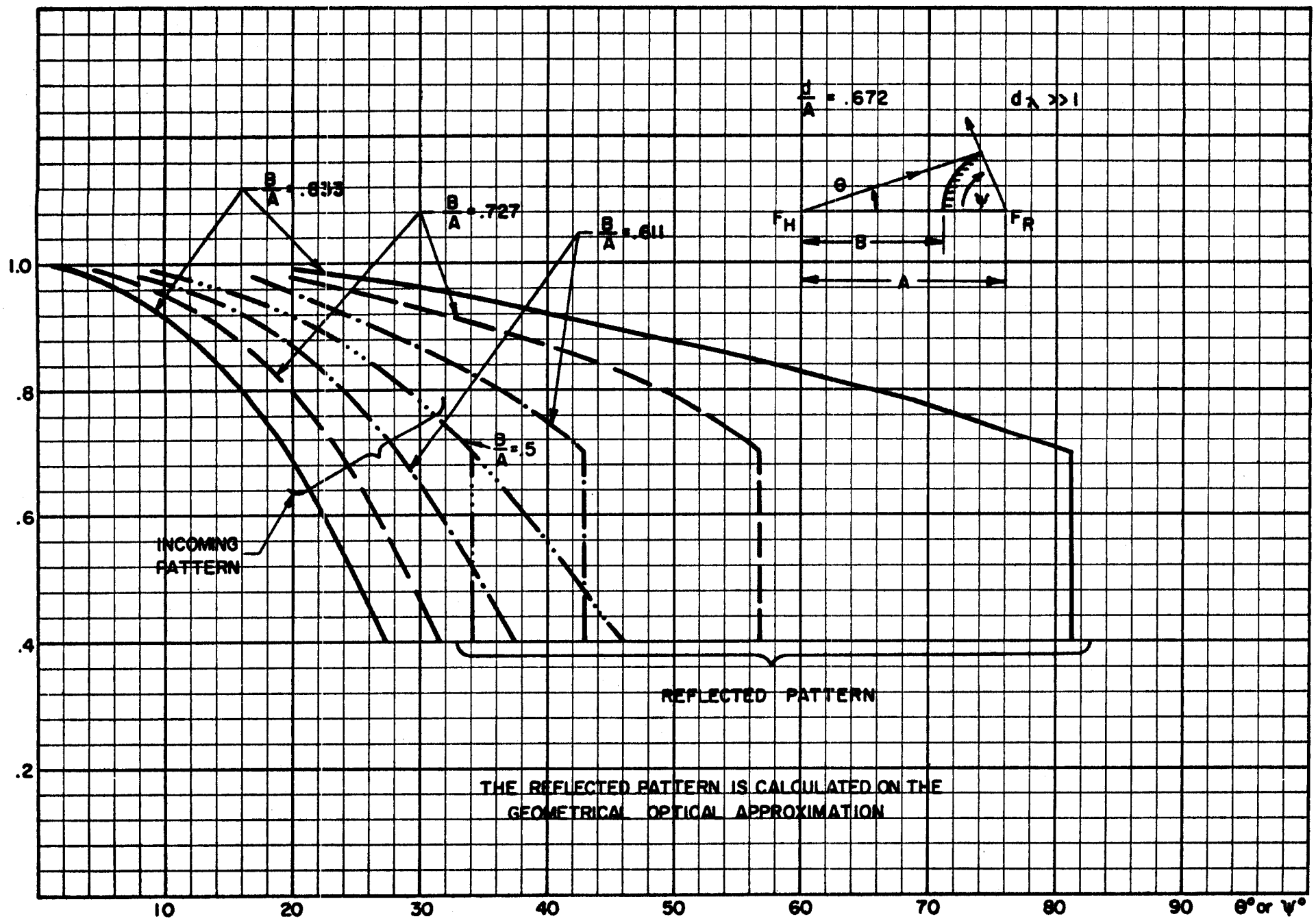

Fig. 40. Pattern shaping effect of the hyperboloid reflector.

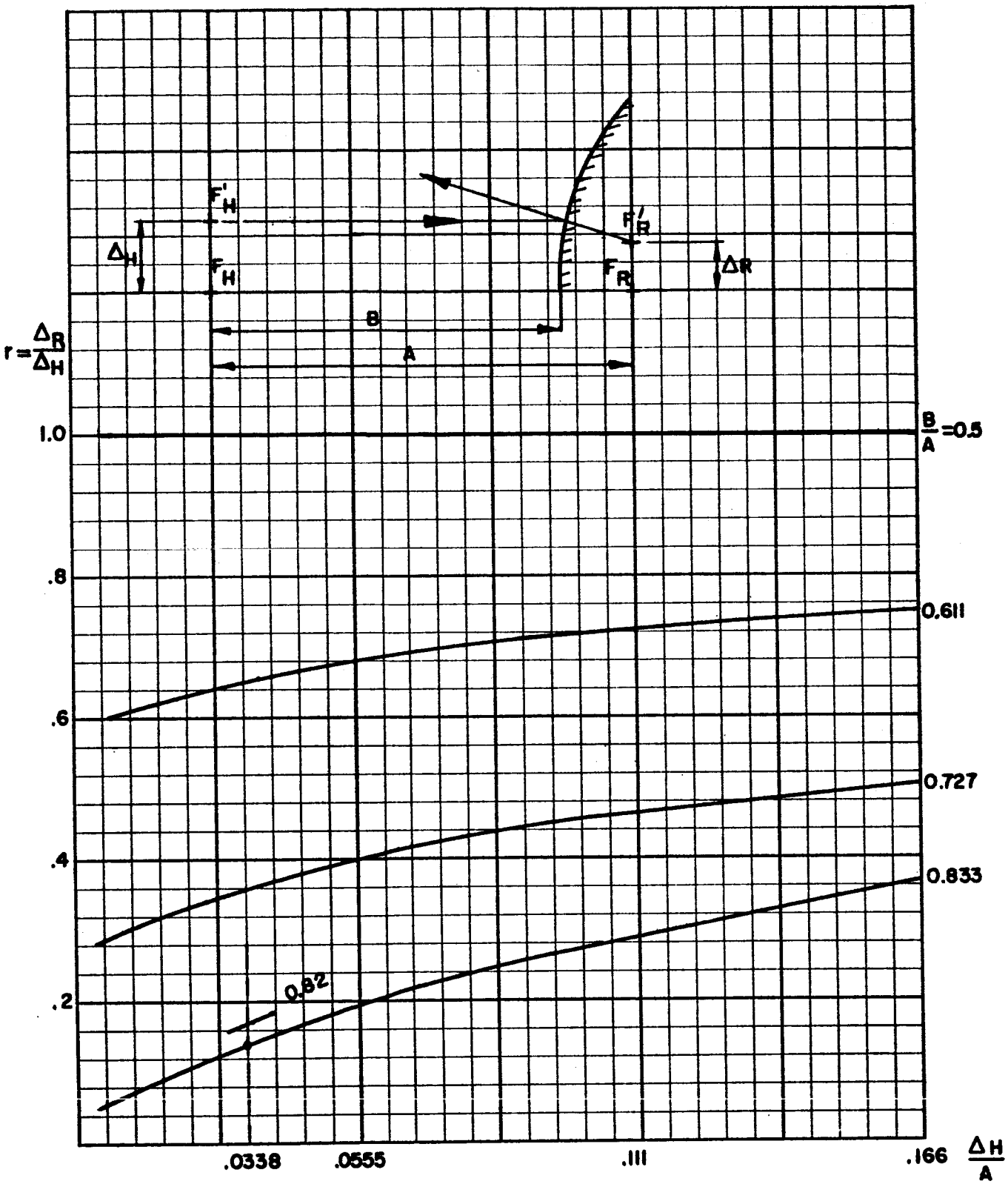

Fig. 41. Position of the image phase center.

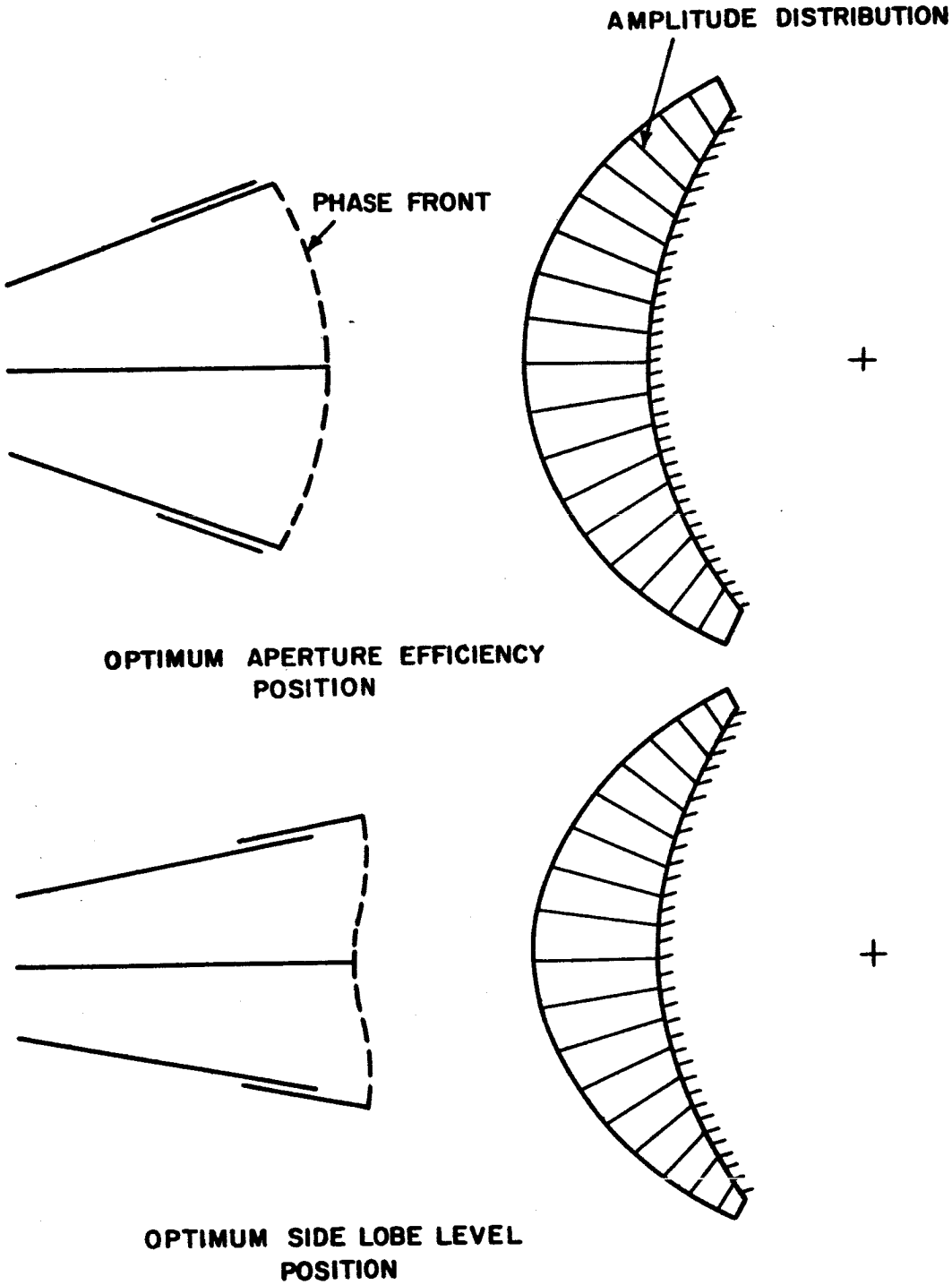

Fig. 42. Control of aperture efficiency and side lobe level by variable size horn.

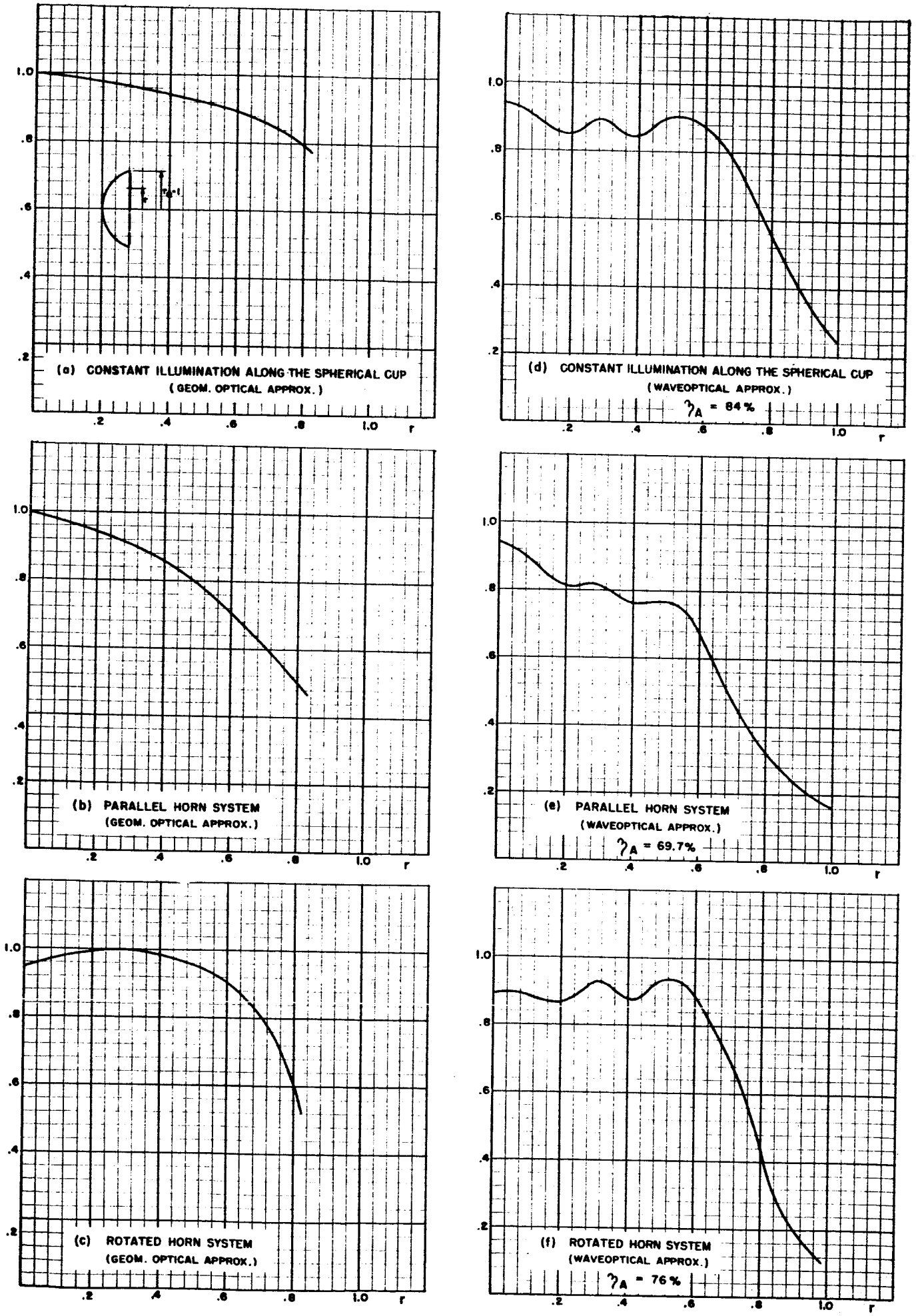

Fig. 43 FIELD DISTRIBUTION IN THE PARABOLOID APERTURE FOR VARIOUS ARRANGEMENTS.

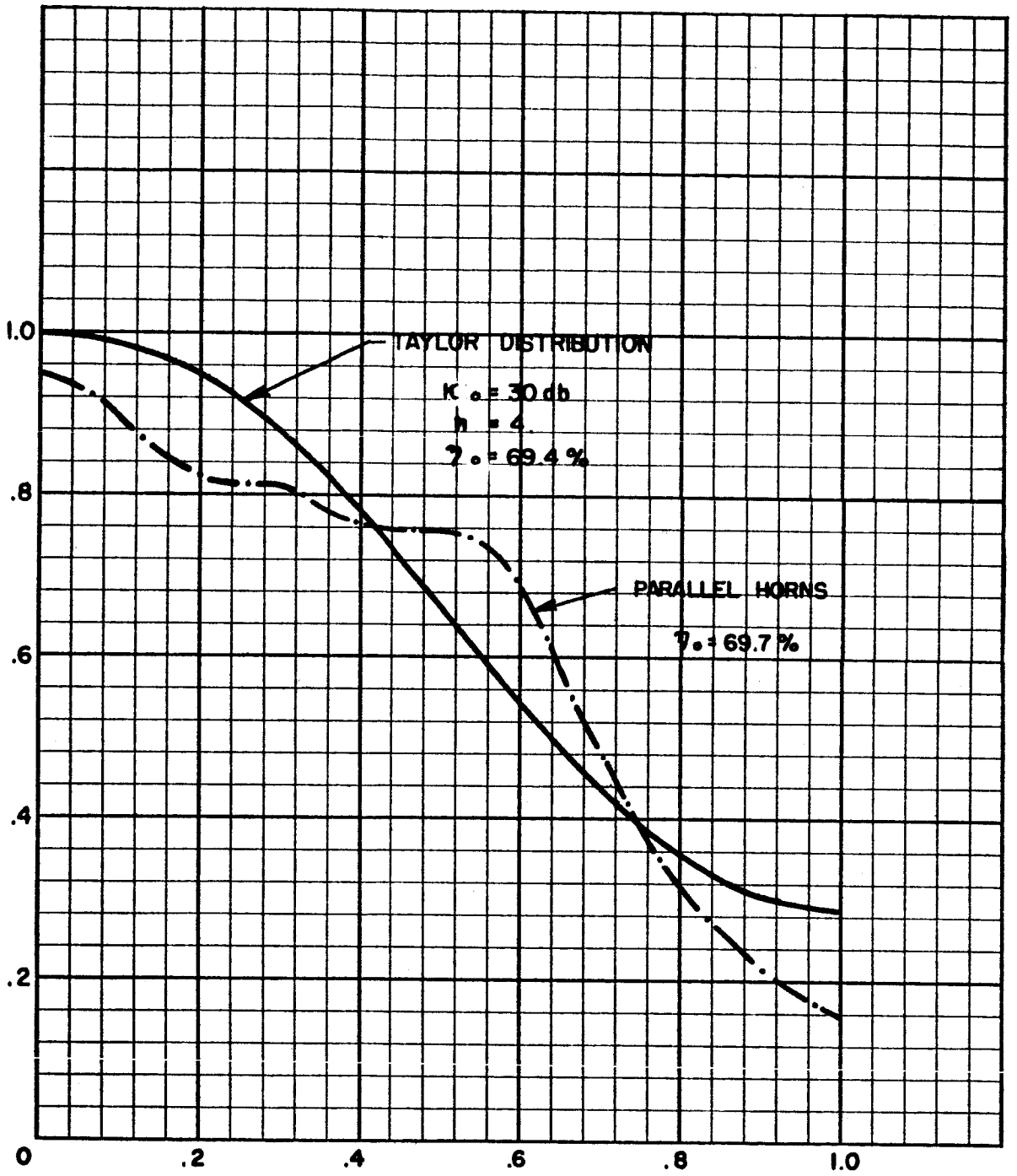

Fig. 44. Comparison between the aperture distribution of the parallel horns system and a Taylor distribution which has approximately identical aperture efficiency.

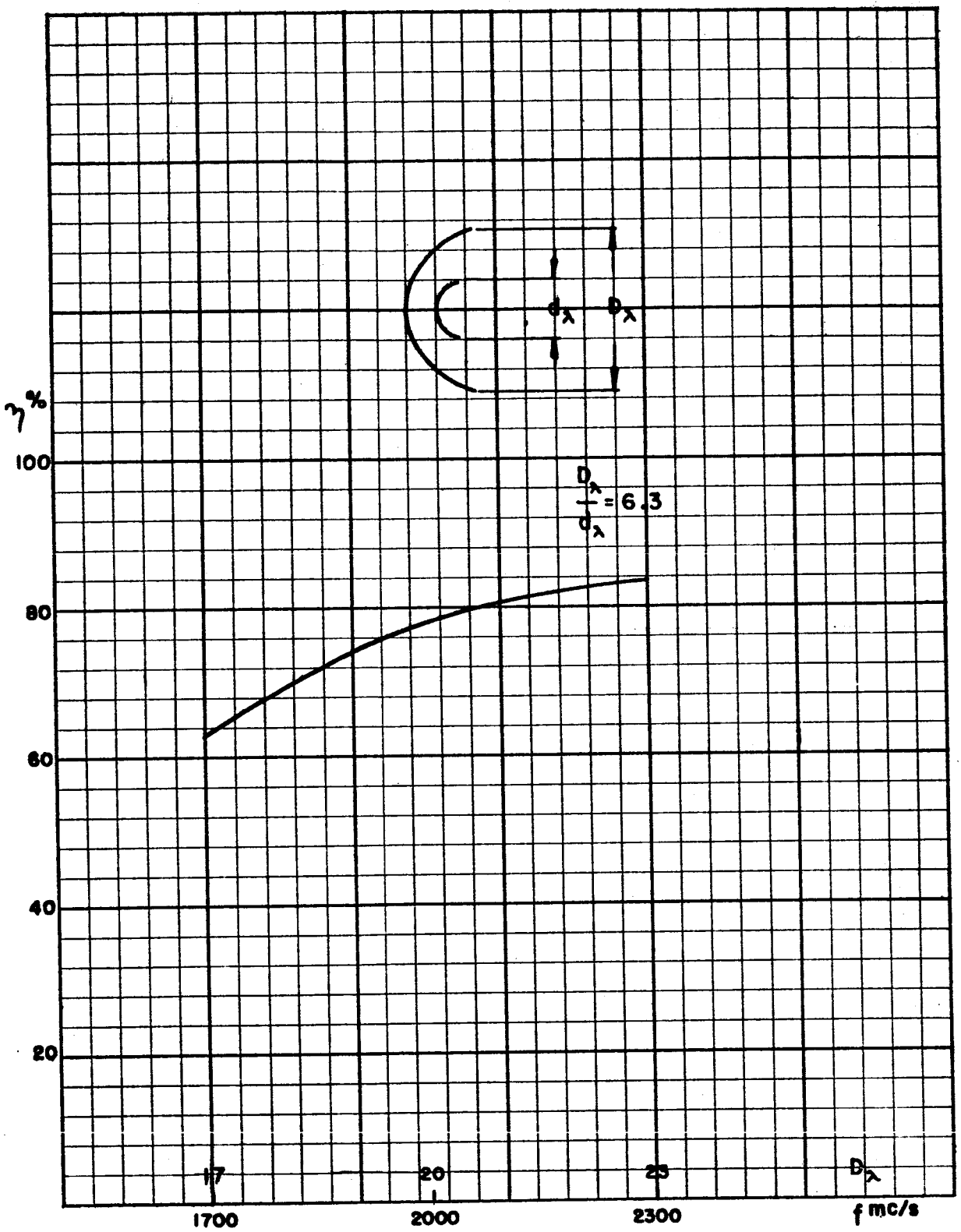

Fig. 45. Aperture efficiency of a typical (MM-600 type) Cassegrain antenna.

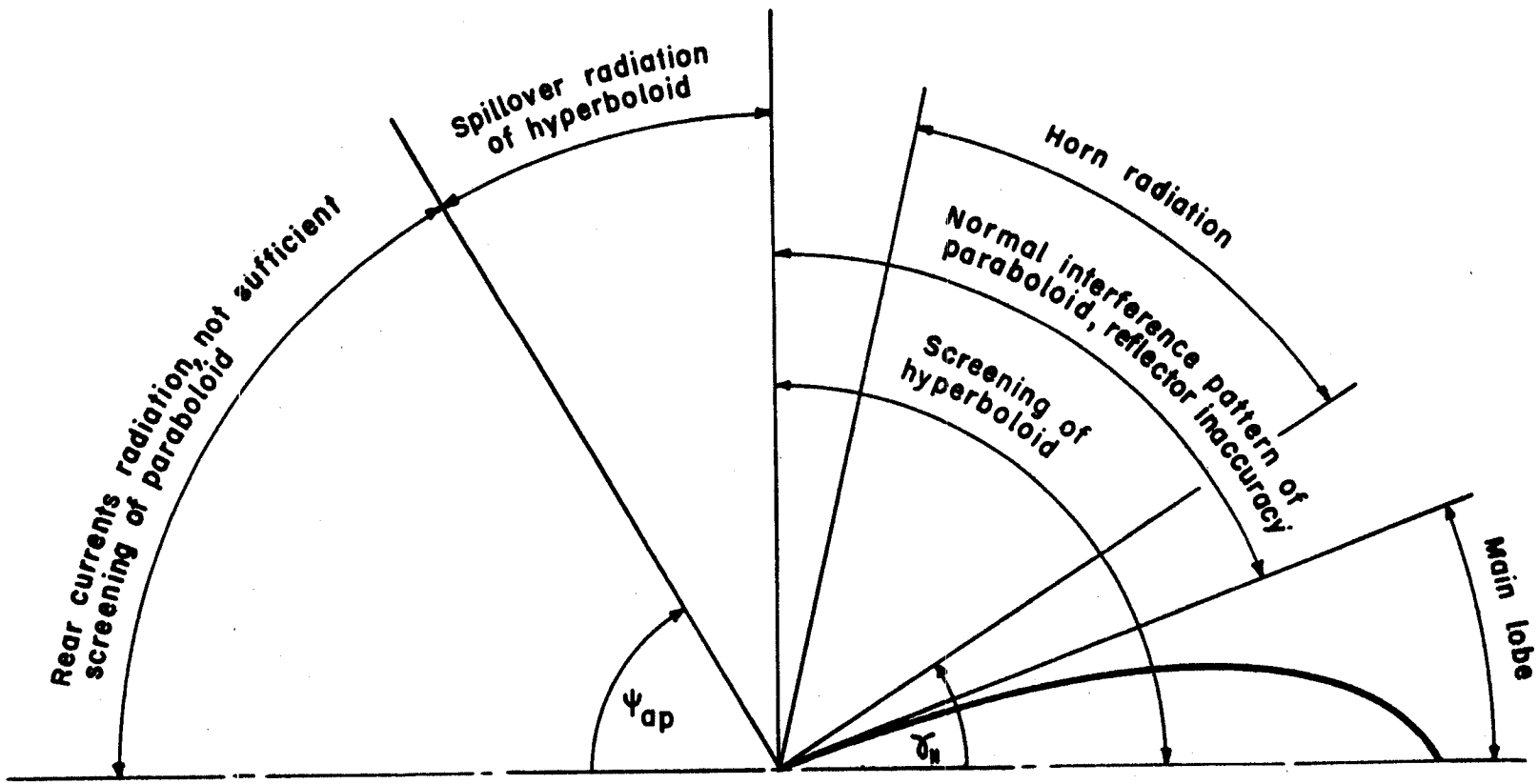

Fig. 46. Occurrence of different side lobe components.

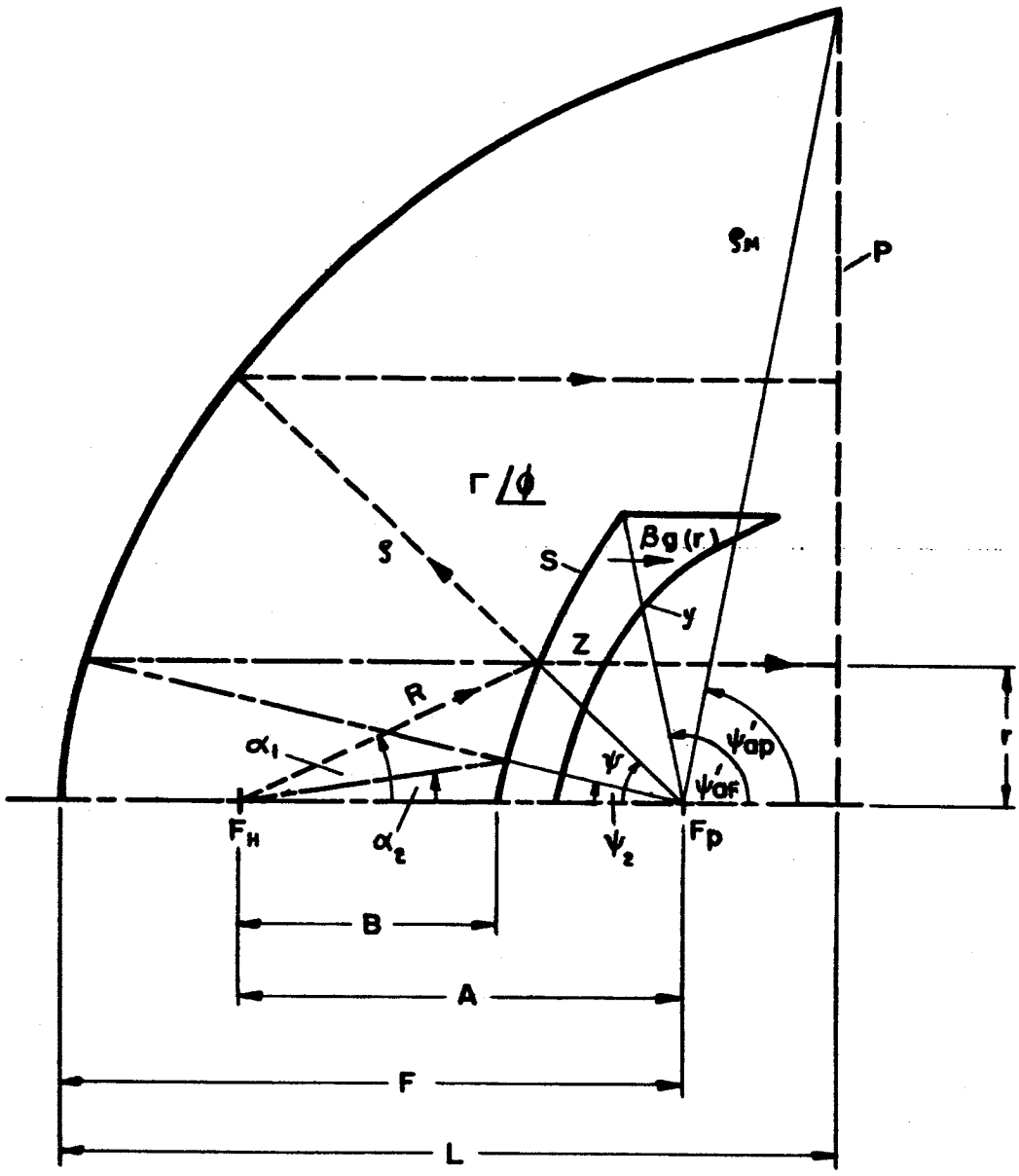

Fig. 47. Geometry of the semireflecting lens and paraboloid arrangement.

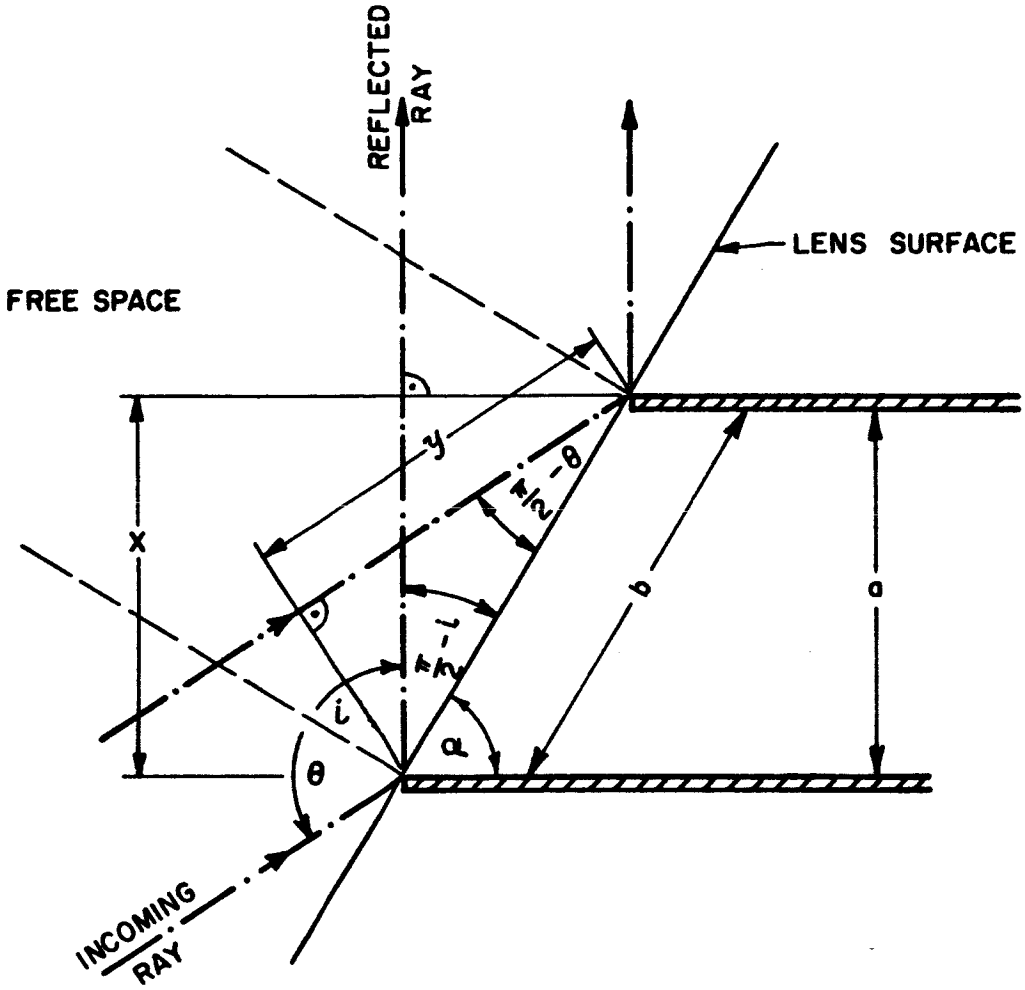

METALLIC LENS

Fig. 48. Geometry of the metallic lens. (honeycomb structure)

JPL Order No.: N1-109280

N1-109281

RCA Victor

Proj.: 3457 - F

S.O. : 94260250

GROUND ANTENNA PARAMETERS

AFFECTING THE RANGE OF A

SPACE COMMUNICATION SYSTEM

PART III

EXPERIMENTAL EVALUATION OF CASSEGRANIAN ANTENNA SYSTEMS

Submitted

to

JET PROPULSION LABORATORIES

Pasadena, California.

by

Technical Products Division

RCA VICTOR COMPANY, LTD.

1001 Lenoir St.,

Montreal.

April 10, 1961

Prepared by P. Foldes

K.M. Jasinski.

S.G. Lumb

Approved by

(Supervisor of Ant. Group)

TABLE OF CONTENTS

PART III

11. INTRODUCTION

12. THE SOURCE SYSTEM

- 12.1 Design Requirements.
- 12.2 Basic Elements of the Source System.
- 12.3 Measuring Set-up.
- 12.4 Experimental Results.

13. THE PRIMARY REFLECTOR

- 13.1 Equations of the Surface.
- 13.2 List of Tested Hyperboloids.
- 13.3 Modifications of the Hyperboloid Surface.

14. THE FEED SYSTEM

- 14.1 General Characteristics of the Feed Pattern.
- 14.2 Method of data Processing.
- 14.3 K-Band Horn with Various Hyperboloids.
- 14.4 V-Band Horn with Various Hyperboloids.
- 14.5 K-Band 4 horn Cluster with Hyperboloids.
- 14.6 V-Band 4 horn Cluster with Hyperboloids.
- 14.7 Design Procedure of a Cassegranian Type feed System Based on the Experimental Data.

15. THE SECONDARY REFLECTOR

- 15.1 Selection of Aperture Angles.
- 15.2 Selection of Reflectors.

16. PATTERN MEASUREMENTS ON THE ANTENNA SYSTEM

- 16.1 Selection of system Parameters for far field Measurements.
- 16.2 Description of test set-up.
- 16.3 Results of Measurements.

17. CONCLUSIONS

18. ACKNOWLEDGEMENTS

11. INTRODUCTION

In the theoretical part of this study the range per unit cost figure of large, space communication antennas was investigated on the basis of a simplified model. The essence of this model was, that the primary reflector can be represented as a spherical aperture with a simplified field distribution. On the basis of this simple model the most important electrical characteristics, like aperture efficiency and noise temperature were calculated.

Although the theory of spherical aperture can be generalized into arbitrary aperture distributions, the calculations become rapidly very tedious as the complexity of the distribution function increases. Consequently an experimental study is well justified. It can be expected that an experimental study not only confirms the theoretical considerations in the analized simple cases, but adds considerable new light to the theoretical knowledge and initiate further analitical investigations.

The experimental study was centered around three major areas. These areas were: the source system, the feed system and the antenna system. The source system is defined as the transition medium between the guided and freely propagated waves. In the analized models the source system consisted of a special horn or system of horns. The feed system is defined as the combination of the source system with a primary reflector. In the analized models the primary reflectors were solid-surface hyperboloids. The antenna system is defined as the combination of the feed system with a secondary reflector. In the analized models the secondary reflectors were paraboloids with solid surface.

11. (Cont'd)

The experiments were aimed to collect as many useful data as possible and provide fairly complete design aids for this type of (Cassegranian) antenna system.

In the source system the aperture size, number of horns and orientation angle of the individual horns were varied. In the feed system hyperboloids with different diameter, focal length and aperture angles were combined with various source systems. In the antenna system paraboloids with two different aperture angles were combined with various feed systems. Finaly most of the measurements were performed at two frequencies (24000 and 34000 mc/s). Some of the measured data will be published in a separate report.

Due to the relatively large volume of experimental material, the data will be presented with minimum required explanation and the emphasis will be on graphical representations.

12. THE SOURCE SYSTEM

12.1 Design Requirements

According to the definition of the source system given in the Introduction, the "classical" paraboloid antenna consists of a source system and a secondary reflector. In such a system only the source characteristics controll the aperture distribution, once the aperture angle of the paraboloid is fixed.

12. 12.1 (Cont'd)

Although, in a double reflector system, the three parameters of the primary reflector (diameter, d_h; focal length, A; and aperture angle ψ_{ah}) increases the number of free parameters, the importance of source control is not diminishing.

If the secondary reflector is fixed as a paraboloid, then the feed system should radiate a spherical wave. The first question to be answered is: what should be the phase front of the illuminating wave at the primary reflector?

Fig. 49 shows various ways to obtain spherical wave front from the primary reflector. (It will be assumed in the following, that the analized radiator is a transmitting antenna.) In Fig. 49a the incoming wave is a diverging spherical wave with a center at F_1, the reflected wave is an other spherical wave with a center at F_2.

The reflector is a hyperboloid. In Fig. 49b the incoming wave is a plane wave, the reflecting surface is a paraboloid, while in Fig. 49c, the incoming wave is a converging spherical wave and the reflector is an elipsoid. If the separation R between the source of the incoming wave and the reflector is finite, then in case a the size of the source should be small compared to $\sqrt{R\lambda}$ while in cases b and c the source size should be large measured in $\sqrt{R\lambda}$.

12. 12.1 (Cont'd)

In other words, the hyperboloid reflector is a typical "far field" control device, while the paraboloid and elipsoid primary reflectors are more suitable for near field transformations.

The mathematical simplicity of the far field structures made case (a) more attractive to the antenna designers then the two other arrangements. The present study will be concentrated also in that direction. However, it should be stated, that in practical systems the $R \gg \frac{a^2}{\lambda}$ (a = aperture size of source) requirement can not be fulfilled and the hyperboloid cannot be illuminated by a true spherical wave.

Using the following definitions,

near field: $0 \leq r < 1$ $\quad r = \frac{R}{R_o}$, $R_o = \frac{a^2}{\lambda}$ (1)

transition field: $1 \leq r \leq 2$ (2)

far field: $2 \leq r \leq \infty$ (3)

The hyperboloid will be in the transition field. The theoretical aberration of the wave from the true spherical wave front in the transition field range is indicated by Fig. 50 for a typical case.

As mentioned, the main emphasis during this experimental study was on the hyperboloid reflector, which has to be illuminated by a diverging spherical wave. However, in multihorn, manopulse systems, higher degree of power concentration along the hyperboloid can be obtained utilizing a plane wave or a converging spherical wave. Therefore some investigation was carried out into this direction.

12. 12.1 (Cont'd)

The second problem in the source design is the selection of the amplitude distribution along the primary reflector surface. Ideally this amplitude distribution should be constant within the aperture angle of source (Ψ_H) (see Fig. 49a) and should be zero for larger angles. With finite size source this requirement obviously cannot be fulfilled. Amplitude tapering along the reflector and spill over radiation beyond the reflector occures, which reduces the overall aperture efficiency. Deviation from the axial symmetry in the source pattern has a similar effect.

Based on the above considerations, the source pattern can be characterized by the following parameters:

1) Distance factor: r .
2) Average tapering of the field at the edge of hyperboloid: $T = \frac{E_E(\Psi_H) + E_H(\Psi_H)}{2}$, where E_E and E_H is the radiation pattern of the source in the E and H plane respectively.
3) Assymetry of edge tapering: $A_e = \frac{E_E(\Psi_H)}{E_H(\Psi_H)}$
4) Average of the first sidelobe level: κ_1

The following design aims can be set for these parameters:

$$r > 1 \quad , \quad -5\ db > T > -9\ db \quad , \quad A_e < 1\ db \quad , \quad \kappa_1 > 18\ db.$$

According to the calculations T has to be in the given range to obtain maximum aperture efficiency. At the same time the condition for the side lobe level assures that the wide angle backlobes of the feed system are on or somewhat below the isotropic level. For instance if G_{HORN} = 23 db, κ_1 = 18 db, then the wide angle side lobe level in the pattern of the complete antenna 23 - 18 = +5 db above the level of the isotropic source.

12. 12.1 (Cont'd)

All design requirements have to be maintained for two ortogonally (or circularly) polarized waves.

12.2 Basic Element of the Source System

The fin loaded pyramidal horn was selected as the basic element of the source system. Such a horn is described in Sec. 9 of Pt. II. That type of horn has several advantages relative to the simple pyramidal horn, such as:

1) The E plane pattern can be widened and the H plane pattern narrowed by increasing the height of the fins. By proper selection of fin height the two pattern - widths can be made equal at any arbitrary power level of the main lobe.

2) Increasing the number of fins, the side lobe level $\mathcal{K}_1$ in the E plane decreases, while in the H plane slightly increases. By proper selection of the number of fins the first side lobes can be made equal in both planes.

3) The square shaped horn retains its two symmetry plane, therefore, behaves identically for two perpendicular polarizations.

4) The corners of the horn can be removed (See Fig. 30b) and thus the distance between horn centers in monopulse horn clusters can be reduced.

The typical dimensions of the fin loaded horns are indicated on Fig. 51. Altogether 5 different horn geometries were realized. Table 1 summarizes their geometries and frequency bands.

Table 1

Geometrical data of the developed fin loaded horns

Notation	L	a_o	a_1	a_2	a_3	S	W	N	Kmc/s. fo	cm λ_o	$\frac{a_1}{\lambda_o}$	Phase error in aperture at
S-10	7.50"	3.20"	4.619"	3.470"	3.470"			3	2.388	12.553	.924	
S-14	7.50"	3.20"	6.231"	4.681"	4.681"			3	2.388	12.553	1.246	
X	20.313"	1.28"	7.062"	5.313"	3.625"	.491"	.031"	6	7.6	3.944	4.548	·129λ
K	7.382"	.420"	2.212"	1.720"	1.720"	.220"	.030"	6	24.0	1.25	4.50	·137λ
V	5.079"	.280	1.522"	.834"	.834	.146	.026	4	34.0	.882	4.38	·134λ

The two S-band horns were designed to result in 10 and 14 db tapering at $\psi_{ap} = 61^o$. The X, K and V band horns were designed to provide a nominaly 4.5λ large aperture size. In the X band horn the fins were placed along the direction of propagation, i.e. the distance between the fins varied along the axis of the horn. The phase error of this horn in the aperture was kept small.

In the V-band horn the phase error was somewhat larger, but the fins were placed parallel with each other. Finally in the K band horn the phase error in the aperture is even larger. The X-band horn resulted in almost completely symmetrical main beam, with K_1 = 22 db, while the V-band horn had only K_1 = 15.5 db and the K-band horn K_1 = 15 db.

The S-10, S-14 and X horns were tested only as individual radiators. The K and V horns were combined also into 4 horn systems, with various angles between horns. In the later systems horn-type power dividers and particularly bent waveguide sections were used to feed the horns. (See Fig. 52).

12. 12.2 (Cont'd)

The radiation patterns of all horns were tested in the transition and far field. The input VSWR was measured only on type S-10 and S-14 and the effect of matching screws to the pattern was investigated.

12.3 Measuring Set-up

All source system and feed system measurements were performed indoors, in a reasonable reflectionless chamber. The typical test arrangement is shown on Fig. 53. The antenna under test was used as a receiver and was mounted on the turntable by dielectric supporting elements appr. 5' above the ground. The received signal was fed into a crystal detector and amplified by a calibrated selective voltmeter (HP-615B). The calibration of the selective voltmeter was compared with the attenuator of the HP-616B and HP- 618B signal generators in the S and X band respectively and by a precision r-f attenuator (PRD-192F1) in the V-band.

The source system and feed system pattern generally is interesting only in less than 30 db dynamic range. It was found that within this limit the calibrated selective amplifier provides less than 1 db error, therefore this calibration was accepted for time saving.

The output of the selective amplifier was fed into a Sanborn recorder. Level calibration on the recorder paper was applied by the means of the attenuator of signal generator or calibrated amplifier. The angular calibration was obtained by time marker signals. The estimated error in the level measurement is 1.5 db and in the angle measurement is $\pm 1^{\circ}$.

12. 12.3 (Cont'd)

The transmitter unit was a standard signal generator or a waveguide mounted klystron. The transmitter horn was supported by a rail mounted pole to ease the distance adjustment between transmitter and receiver antenna. The receiver antenna was surrounded by a triangular shaped absorbing wall, built from the absorber, made by Goodrich Co. Ltd. The reflection coefficient of this absorber is less than 30 db in the frequency band above 20 Kmc/s.

12.4 Experimental results

Fig. 54 shows the various characteristics of the S-10 horn. Fig. 54 a is the far field pattern in the E & H plane with N = 2. As N=3 results in better symmetry, the 3 fin loading was accepted for the final designs. Fig. 54 b shows the pattern when 4 matching screws were placed, one into the middle of each wall close to the troat of the horn. The VSWR of this arrangement is better then 1.035 in $\pm$ 2% frequency band.

Fig. 55 indicates the far field pattern of the S-14 horn. Having narrower beam then the S-10 horn (T (61°) = -14 db) the pattern of this radiator is more sensitive to any impedance compensating element then the smaller horn. First four irises close to the aperture plane were tried for matching purpose, however this resulted in A_e = 6 db assymetry at $\psi = 61^{o}$. Later a symmetrical 4 screw tuning was accepted for impedance compensating purpose.

Fig. 56 presents the photograph of the S-14 horn.

12. 12.4 (Cont'd)

Fig. 57 indicates some data of the X horn. In sequence this horn was built first and the important dimensions of the large gain horn ($a = 4.5\lambda$) were determined on this unit.

In Fig. 57a the theoretical E and H plane 3 db beamwidth of a square horn vs. frequency is plotted without and with fin loading respectively. The fin loaded case was calculated on the basis, that no E field exists between the fins parallel with the fin surface.

Fig. 57b indicates the measured 3 db beamwidths for the fin loaded case. The height of the fins corresponds to Fig. 57a. It can be seen that the beamwidth in the E plane is wider and in the H plane narrower then is predicted in Fig. 57a. This shows, the otherwise expected fact, that the parallel component of E field between fins is not zero, furthermore, that the perpendicular component does not follow anymore the "sin x" distribution but it is modified into a more uniform distribution.

Fig. 57c indicates field distributions in the horn aperture for the simple, pyramidal horn, for the fin loaded aperture, one assuming the simplified theory and the other experimental results.

Fig. 57d shows the 3 db beamwidth for somewhat reduced fin height, finaly Fig. 57 e indicates the pattern at f = 7680 mc/s for the same geometry. It should be noted, that the very high degree of symetry indicates the validity of the field distribution in Fig. 57 c.

12. 12.4 (Cont'd)

Fig. 58 is the photograph of the X horn.

Fig. 59 and 60 represents the pattern of the K and V horn respectively. It should be noted the relatively poor E plane side lobe level. The aperture dimensions of these horn were identical with the X-horn. (measured in wavelenths) However, these horns were shorter to save space and the fins were soldered into parallel grooves to save manufacturing time. In horns with low E plane side lobe level these simplifications are not permitted.

Further attempts were made to shape the source pattern by combining four fin loaded horns. A mechanism was built (see Fig. 61) which controlled the position of the 4 K-horns continuously. In this arrangement a horn type power divider distributes the input wave toward four flexible w.g. sections. The flexible w.g.-s are connected with the horns. In this set up the angle between the horn and cluster axis can be varied from 4 to 11° while the positions of the center of horn apertures remains constant.

At the input of each horn, matching screws were placed to compensate the variations in the flexible w.g. during horn positioning. Unfortunately the quality of power division was still not satisfactory and the flexible waveguides introduced untolerable instability at 24 Kmc/s. Therefore only a few measurements were taken with this set-up. Fig. 62 indicates two typical patterns and the corresponding power level of individual horns.

12. 12.4 (Cont'd)

The high side lobe level can be interpreted as the consequence of unequal power division and phasing; furthermore, of the large, non-illuminated center hole in the middle of the overall aperture. A comparison between Fig. 62 and Fig. 59 shows the very important fact that the pattern of the 4 horn system is smoother around the maximum, then the pattern of the single horn system. The flatness of the top of main beam can be characterized by the ratio of the beamwidth between first minimums to the 3 db beamwidth. This ratio is 2.43 for the single horn and is improved to 1.91 in the 4 horn cluster.

On the basis of the experienced mechanical instability a somewhat less ambitious power divider was built for the V horns. In this a constructed rigid waveguide power divider was used, with position angles $\vartheta = 5^{\circ}$, 0° and -3° (see Fig. 63). The not illuminated center area was decreased by larger corner cutouts in the horns. This system was measured at 24 and 34 Kmc/s. At the lower frequency the effect of center hole is even smaller, because the smaller electrical distance between horns reduces the space variation of the array factor.

The quality of power division was checked by placing attenuators into all horns but one and recording the patterns. As Fig. 64 indicates (for $\vartheta = 0^{\circ}$, f = 24 Kmc/s) the radiated powers of the horns were within .5 db equal. The patterns were measured in the horizontal (H) plane. The relative level difference between the pattern of horn 1 and 4 indicates that the axis of cluster had some vertical tilt during this test.

12. 12.4 (Cont'd)

Fig. 65 represents the near field and far field pattern of the $\gamma = 0^{o}$ cluster at f = 24 and 34 Kmc/s. It can be seen that by increasing frequency the sidelobe level deteriorates. This is partly caused by the increasing electrical distance between horns and even more so by the increasing error in the relative amplitude and phase of individual horns.

Fig. 66 and 67 shows the similar data of the -3° cluster. The $\gamma = -3^{o}$ cluster is the only analyzed source system which produces converging spherical wave. The theoretical focal point is approximately 20" from the horn apertures. Beyond this point the wave is diverging again. The special feature of this near field can be characterized by the 6 db width of a plane aperture perpendicular to the axis of the cluster vs distance from the cluster.

Fig. 68 shows, that this width is minimum about 17", close to the theoretical focal point. At this distance is the transition between the converging and diverging spherical wave, and here an approximate plane wave front exist. It is interesting to note that at this distance the size of the equivalent 6 db aperture is about 3", approximately identical with the aperture width of the cluster.

13. THE PRIMARY REFLECTOR

13.1 Equations of the Surface

During the present experimental program the $1 < r < 2$ distance range was investigated. Here the primary source of radiation can be assumed as a

13. 13.1 (Cont'd)

point source. This assumption (which is only approximate) determines a hyperboloid surface for the primary reflector. A finite hyperboloid is characterized by three parameters. These parameters for the present practical purpose can be selected as A, the focal distance of hyperboloid, d_h, the diameter of hyperboloid and ψ_{ah}, the aperture angle of hyperboloid.

The calculation of the reflector surface is straightforward. The equations of hyperboloid for reference purpose will be included here.

In the coordinate system given on Fig. 69, z_λ, r_λ are surface coordinates in wavelength.

$$z_\lambda = \frac{A_\lambda^2 - k_\lambda^2}{2(A_\lambda + k_\lambda \sec\psi)}, \quad r_\lambda = z_\lambda \tan\psi = \frac{A_\lambda^2 - k_\lambda^2}{2(A_\lambda + k_\lambda \sec\psi)} \tan\psi \qquad (4)$$

where the k_λ constant is determined by the three hyperboloid parameter $(A_\lambda, d_{h\lambda}, \psi_{ah})$

$$k_\lambda = 2B - A = \frac{d_{h\lambda}}{2\tan\psi_{ah}} \left\{ \left[\tan^2\psi_{ah} + \left(\frac{2A_\lambda}{d_{h\lambda}} \tan\psi_{ah} - 1 \right)^2 \right]^{1/2} - \frac{1}{\cos\psi_{ah}} \right\} \qquad (5)$$

The thickness of the reflector

$$t_\lambda = \frac{1}{2}\left(A_\lambda - k_\lambda - d_{h\lambda} \cot\psi_{ah}\right) \qquad (6)$$

Finally the excentricity

$$e = \frac{B}{A} = \frac{1}{2} + \frac{k_\lambda}{2A_\lambda} \qquad (7)$$

13.2 <u>List of Tested Hyperboloids</u>

To be able to obtain a fairly complete investigation of the effect of hyperboloid parameters 12 different reflectors were constructed. These reflectors, with the addition of the 1:1.5 frequency band covered the following parameter ranges.

$$8 \le d_{h\lambda} \le 23, \qquad 26.6 \le A_\lambda \le 70$$

$$55^\circ \le \psi_{ah} \le 100^\circ$$

Table 2 summarizes the main geometrical parameters and surface coordinates of the reflectors.

TABLE 2

LIST OF GEOMETRICAL DATE OF HYPERBOLOIDS

HYPERBOLOID NO:	1		2		3		4		5		6	
ψ_{ah}	55°		55°		55°		55°		55°		55°	
d_h	3.917"		5.026"		5.875"		3.917"		5.026"		5.875"	
A	17.526"		17.526"		17.526"		13.055"		13.055"		13.055"	
t	.450"		.555"		.626"		.428"		.516"		.572"	
B+t	16.155"		15.766"		15.469"		11.684"		11.295"		10.998"	
	r"	z"	r"	z"	r"	z"	r"	z"	r"	z"	r"	z"
	0	1.822	0	2.314	0	2.683	0	1.800	0	2.276	0	2.629
	.159	1.819	.202	2.311	.235	2.678	.157	1.797	.199	2.272	.230	2.625
	.319	1.809	.405	2.299	.470	2.667	.315	1.788	.399	2.262	.461	2.614
	.481	1.794	.611	2.280	.709	2.645	.475	1.773	.601	2.244	.695	2.594
	.645	1.772	.820	2.253	.952	2.615	.638	1.752	.808	2.220	.934	2.567
	.812	1.742	1.034	2.217	1.200	2.574	.804	1.725	1.020	2.187	1.180	2.531
	.985	1.705	1.254	2.172	1.457	2.523	.976	1.690	1.238	2.145	1.435	2.485
	1.162	1.660	1.482	2.116	1.723	2.461	1.153	1.647	1.466	2.093	1.700	2.428
	1.347	1.605	1.719	2.049	2.001	2.385	1.338	1.595	1.704	2.031	1.980	2.359
	1.540	1.540	1.969	1.969	2.294	2.294	1.533	1.533	1.956	1.956	2.276	2.276
	1.743	1.463	2.232	1.873	2.605	2.186	1.739	1.459	2.225	1.867	2.594	2.176
	1.958	1.371	2.513	1.760	2.9376	2.057	1.958	1.371	2.513	1.760	2.937	2.057

TABLE 2 (Continued)

HYPERBOLOID NO.	7		8		9		10		11		12	
ψ_{ah}	99°		55°		58°		100°		58°		75°	
d_h	2.037"		7.615"		9.819"		5.906"		5.906"		5.906"	
A	7.087"		19.780"		41.197"		27.067"		27.067"		27.067"	
t	.561"		.782"		1.203"		1.681"		.732"		1.050"	
Bit	7.248"		17.114"		38.129"		27.588		25.222"		26.276"	
	r"	z"	r"	z"	r"	z"	r"	z"	r"	z"	r"	z"
	.000	.399	.000	3.448	.000	4.271	.000	1.160	.000	2.577	.000	1.841
	.070	.396	.301	3.443	.373	4.264	.203	1.152	.225	2.573	.322	1.828
	.141	.388	.604	3.427	.748	4.242	.410	1.126	.451	2.560	.651	1.788
	.215	.372	.911	3.401	1.127	4.205	.624	1.080	.680	2.537	.992	1.718
	.293	.349	1.224	3.363	1.512	4.153	.850	1.012	.912	2.505	1.354	1.613
	.377	.317	1.545	3.313	1.905	4.084	1.093	.917	1.149	2.463	1.745	1.464
	.470	.272	1.876	3.250	2.308	3.998	1.360	.785	1.392	2.411	2.179	1.258
	.576	.210	2.221	3.172	2.725	3.891	1.661	.605	1.643	2.346	2.674	.973
	.700	.123	2.582	3.077	3.157	3.763	2.010	.354	1.903	2.268	2.953	.791
	.850	.000	2.964	2.964	3.610	3.610	2.429	.000	2.174	2.174		
	1.019	-.161	3.370	2.828	4.086	3.429	2.953	-.521	2.460	2.064		
			3.808	2.666	4.591	3.214			2.762	1.934		
					4.909	3.068			2.953	1.845		

13. 13.2 (Cont'd)

Fig. 70 is the photograph of the reflectors. The reflectors were manufactured with approximately $\pm 2\tau$ surface accuracy.

During the measurements nominally two frequencies were used: f_1 = 23.88 Kmc/s and f_2 = 34.40 Kmc/s. If no other note is given, then f_1 and f_2 refers to these two frequencies. The two frequencies give a scale factor of 10 and 14.4 respectively for the full size Goldstone antenna at f_o = 2388 mc/s.

13.3 Modifications of the Hyperboloid Surface.

It was mentioned previously that the simple hyperboloid surface gives only first order approximation of the required primary reflector. The reflector surface can be modified to:

1) compensate the phase error caused by the finite size of source (see Fig. 50),
2) decrease the effect of edge currents,
3) transmit a part of illuminating field and thus decrease screening effect.

The first attempt did not reach the experimental stage until this report was concluded. Two methods were tried out to decrease the effect of edge currents.

Fig. 71 indicates a stepping at the rear of the reflectors. The top and bottom parts of these steps are $\lambda/4$ apart in the direction of the main beam,

13. 13.3 (Cont'd)

therefore, the radiation from the corresponding sections can partly compensate each other. Unfortunately no such a reduction was observed. On one of the reflectors in Fig. 70 grooves can be seen, close to its edge. The groove depth is equal to $\lambda/4$ to provide high surface impedance and a barrier against the propagating radial reflector currents. Four grooves were cut into this reflector. The grooves were filled by wires, and during the experiment the wires were gradually removed. Two effects were observed:

1) The backradiation of the reflector was gradually reduced as the number of grooves was increased (a total reduction appr. 2 db was measured).
2) The shape of the main beam was slightly affected (accidentally improved) in the angular range which corresponded to the grooves on the reflector. The later fact indicates a possibility of beam shaping by controlling the surface impedance of the reflector.

Some preparatory work was conducted during the present experimental study to provide data for the design of semi-transparent reflectors. This work included the measurement of transmission coefficients through perforated metallic sheets with various hole diameters and angles of incidence. The attenuation of transmitted field is shown in Fig. 72.* The angular dependency shows approximately the cos. law. In the case of a semi-transparent reflector the transmitted field has to be transformed into a plane wave by some kind of lens. It has to be noted that the data plotted in Fig. 72 can be used to calculate the transmitted field through the primary reflector and thus determine the noise temperature component corresponding to this

*) No. 1: d_H = 5/16", 60% transparency

No. 2: d_n = 1/2" , 60% transparency

13. 13.3 (Cont'd)

transmitted field. For the 85' Goldstone station $d_H \cong 0.4''$, transparency 60% which gives $\alpha \cong 20$ db and $T_{AG_{eff}} = 3.75\ ^\circ K$

14. THE FEED SYSTEM

14.1 General Characteristics of the Feed Pattern

Each feed system was formed from a horn or horns directed toward the hyperboloid along or close to the axis of hyperboloid. The distance between horn and hyperboloid was set originally into the nominal position, corresponding to the geometrical optics. Then this distance was varied about the nominal value, to determine the "best focal distance". The definition of the "best focal distance" is obviously arbitrary. Increasing the horn-primary reflector distance the illumination on the reflector tends to be more uniform, which produces more uniformity in the aperture distribution of paraboloid. Unfortunately the spillover radiation increases at the same time. The closer separation has the opposite effects. The finiteness of source size causes mainly a quadratic phase error, which can be compensated by closer separation.

In most cases smoother main lobe was obtained by such a displacement, particularly, when the dia. of hyperboloid was relatively small ($<15\lambda$). The most logical basis of the best focal distance selection is the one which results in highest aperture efficiency and lowest noise temperature. This definition was used in the data procession of the experimental results. It has to be noted that by increasing the diameter of the hyperboloid, while maintaining the size of horn, the "best focal distance" approaches more and more the optical focal distance.

14. 14.1 (Cont'd)

During the pattern test of feed system the first focal point of hyperboloid was placed into the pivot point of turntable. Doing so it is possible to analyse the field of hyperboloid more or less separately from the horn radiation in the range of the main lobe. ("Main lobe" refers here to the hyperboloid pattern). The test horn was therefore placed in the far field of the hyperboloid pattern, but not into the far field of the feed system. The size of the feed system was in some cases quite large ($A_\lambda = 75$) which would result in a several hundred feet distance. On the other hand the far field of hyperboloid can be found in the range of 10 - 20 feet from the analized reflectors.

In some cases the near field of the reflector radiation was also recorded, which gives an even clearer picture about the reflected field. As a matter of fact the paraboloid reflector is in the near field of the hyperboloid in the antenna system.

Fig. 73 shows a typical half pattern of a feed system. At $\psi \cong 0$ the field is small, because of the screaning caused by the horn. The angular region of the shadow becomes smaller for a given horn as A increases. It has to be noted however, that d_h has to be increased simoultaneously to maintain the pattern of hyperboloid, therefore the screaning caused by the hyperboloid increases also. Around the angle $\psi_s = \frac{a}{2A}$ (a = the aperture size of horn) the reflected field of hyperboloid is scattered from the edge of horn. The ripples in this range may be as large as ± 2 db, however, they are restricted to a very small angular range of ψ , and therefore to a small

14. 14.1 (Cont'd)

part of the paraboloid aperture, close to the center. The amplitude of these ripples can be reduced somewhat by increasing the radius of curvature at the edge of horn. The range $\psi_s < \psi < \psi_{10}$ can be defined as the main lobe of the hyperboloid pattern. Here ψ_{10} is the angle, where the field drops to -10 db relative to the maximum. Within the range of the main lobe the beam shape can be further characterized by the ripple amplitude. These ripples are caused by the finite size of the hyperboloid, phase error introduced by the finite source system and interference between the horn and hyperboloid radiation. These ripples introduce also sidelobes into the secondary pattern and reduce the gain. One of the most important characteristics of the Cassegranian type feed is the rapid change in the feed pattern around ψ_{10}. The existance of the high derivative of the field at ψ_{10} makes possible the simoultaneous realization of high aperture efficiency and low spillover radiation toward the rear hemisphere of paraboloid reflector. The magnitude of this derivative increases approximately linearly with the diameter of hyperboloid. The slope in well adjusted systems is practically free from superimposed ripples. In fact one of the simplest way to check the proper hyperboloid horn separation is to examine the ripples in the hyperboloid pattern at ψ_{10}.

It was found that in systems, where the horn spillover and hyperboloid tapering is properly compromized for optimum gain $\psi_{10} \approx \psi_{ah}$. In the angular range $\psi_{10} < \psi < \pi - \psi_H$ usually very small field exists. This field is determined by the wide angle sidelobe level of the source. However,

14. 14.1 (Cont'd)

around $\pi - \psi_H$ (ψ_H = aperture angle of horn) again a larger field can be found, mainly determined by the first and second side lobes of the source pattern and the edge tapering of the hyperboloid. The source usually has about 20 db gain, while the feed system developed for the 85' Goldstone antenna has about 10 db gain. If 10 db edge taper is applied on the hyperboloid, (i.e. the -10 db part of the source main lobe is directed toward the edge of hyperboloid) than the spillover lobe at $\pi - \psi_H$ is approximately equal with the level of the main lobe in the hyperboloid pattern. This indicates that the maximum of wide angle side lobe level in the secondary pattern is the difference between the antenna gain and feed system gain. Fortunately this peak radiation exists only around $\pi - \psi_H$ and contains only 10 - 15% of the total power, because it is limited into narrow angular range and its effect to the antenna system gain can be tolerated.

Finally the last characteristic region of the hyperboloid pattern is at $\psi = \pi$, where an approximately $\left(d_{h\lambda}\right)^{-1}$ radian wide, relatively high gain backlobe can be found. The power content of this lobe is always negligible, however it may contribute to the nearby sidelobe level of the secondary pattern.

All the measured patterns show the mentioned characteristics and besides of these a considerable percentage indicates assymetry. The assymetries can be attributed to the following reasons:

14. 14.1 (Cont'd)

1) The axis of horn does not coincide with the axis of hyperboloid.
2) The effective radiation center of the feed does not coincide with the pivot point of the turntable.
3) The test horn is not directed toward the center of radiation.
4) In four horn system source, the power division and phase equality between horns are imperfect.
5) Non perfectness of the absorbing wall.

The patterns can be made symmetrical within the resolution of recorder however, it is not always practical to spend the required time to obtain perfect symmetry. Instead of this the left and right side part of the pattern can be averaged when some asymmetry exists.

14.2 Method of Data Processing.

Some of the interesting data (variation of ψ_s, ψ_{10}, $\left.\frac{d f(\psi)}{d\psi}\right|_{\psi=\psi_{10}}$, level of wide angle side lobes) can be easily obtained as a function of horn - hyp. distance, ψ_{ah}, a, frequency, etc. However the most important data; the expected aperture efficiency (η_o) and noise temperature caused by ground radiation (T_{AG}) are the results of relatively lenthy integration. Therefore, these later data were determined only in the more interesting cases by numerical integration.

If the feed pattern is an axially symmetrical real function $f(\psi)$ and illuminates from the focal point a perfect paraboloid with an aperture angle ψ_{ap}, then the aperture efficiency can be expressed as:

14. 14.2 (Cont'd)

$$\eta_o = \eta_s \eta_A \tag{8}$$

where

$$\eta_s = \frac{P_P}{P_T} \tag{9}$$

is the power split coefficient. Here P_P is the power directed toward the paraboloid and P_T the total power radiated by the feed system.

$$P_T = 2\pi \int_0^{\pi} f^2 \sin\psi \, d\psi \quad , \quad P_P = 2\pi \int_0^{\psi_{ap}} f^2 \sin\psi \, d\psi \tag{10}$$

η_A is the aperture distribution coefficient

$$\eta_A = 2 \frac{\left[\int_0^1 f(r)\, r\, dr \right]^2}{\int_0^1 f^2(r)\, r\, dr} \tag{11}$$

where the relationship between r and

$$r = \frac{\sin\psi}{\cos^2\frac{\psi}{2}} \quad \frac{\cos^2\frac{\psi_{ap}}{2}}{\sin\psi_{ap}} \equiv g(\psi) \tag{12}$$

Table 3 gives the $r = g(\psi)$ function for $\psi_{ap} = 61°$ and $90°$

TABLE 3

NORMALIZED APERTURE COORDINATE OF THE PARABOLOID

	$\psi_{ap} = 61°$	$\psi_{ap} = 90°$
ψ	r	r
0	.00000	.00000
5	.07412	.04366
10	.14853	.08749
15	.22350	.13165
20	.29935	.17633
25	.37635	.22169
30	.45488	.26795
35	.53527	.31530
40	.61789	.36397
45	.70318	.41421
50	.79163	.46631
55	.88375	.52057
60	.98014	.57735
61	1.00000	
65		.63707
70		.70021
75		.76733
80		.83910
85		.91633
90		1.00000

14. 14.2 (Cont'd)

By the use of this table the $f[g(\psi)]$ function can be found and the numerical integrations can be carried out. The explicit formula of the aperture efficiency

$$\eta_0 = 2 \frac{\int_0^{\psi_{ap}} f^2 \sin\psi \, d\psi}{\int_0^{\pi} f^2 \sin\psi \, d\psi} \frac{\left\{ \int_0^1 f[g(\psi)] r \, dr \right\}^2}{\int_0^1 f^2[g(\psi)] r \, dr} \tag{13}$$

The supression S can be also determined from the measured $f(\psi)$ pattern. Using the definition in eq. (11) Part I.

$$S = \frac{\int_{\psi_{ap}}^{\pi/2} f^2 \sin\psi \, d\psi}{\int_0^{\pi} f^2 \sin\psi \, d\psi} \tag{14}$$

The value of the noise temperature component which corresponds to this radiation (See eq. (26) and (9) in Part I)

$$T_{G_{eff}} = \frac{1}{2} S T_{AG} = \frac{S}{2} \left[\epsilon_G T_G + \Gamma_G T_s \right] \tag{15}$$

At f_0 = 2388 mc/s, $\epsilon_G \cong 0.88$, $\Gamma_G \cong 0.80$ and $T_s = 2.5\,^\circ K$.

Furthermore T_G = 330° K thermodynamical temperature can be assumed for the dry sand around the Goldstone station. Then

$$T_{G_{eff}} = 147\, S \quad {}^\circ K \cong 1.5\, S^{\%} \quad {}^\circ K \tag{16}$$

From eq. (16) can be seen that $S \approx 4\%$ can be tolerated for a low noise feed system.

To calculate the wide angle side lobe level of the antenna system the gain of the feed system gain is also required. This is

$$G_F = \frac{2}{\int_0^{\pi} f^2 \sin\psi \, d\psi} \tag{17}$$

14. 14.2 (Cont'd)

The antenna system gain, if $G_0 = \pi^2 D_\lambda^2$ is the maximum, non super-directive gain,

$$G_S = \eta G_0 = \eta_A \eta_S \eta_T G_0 = \pi^2 \eta_A \eta_S \eta_T D_\lambda^2 \tag{18}$$

where

$$\eta_T = e^{-16\pi^2 m^2 D_\lambda^2} \tag{19}$$

is the tolerance factor introduced by inacuracies of the paraboloid reflector. (Ruze formula) The wide angle side lobe level in the antenna system pattern caused by the direct feed system radiation

$$K_{(\pi-\psi_H)} = K_W = G_S^{db} - G_F^{db} - f(\pi-\psi_H)^{db} \qquad db \tag{20}$$

14.3 <u>K-band Horn with Various Hyperboloids</u>

Fig. 74 shows a typical pattern measured with the K horn and the H_3 hyperboloid. Similar patterns were taken with other hyperboloids and from these patterns some basic data calculated. These data are shown in Fig. 75-79.

Fig. 75 indicates the aperture efficiency η_0 and supression S vs horn-hyperboloid separation R. Each curve shows an optimum distance, Ropt.

Fig. 76 is the plot of the maximum aperture efficiencies vs. d. It can be seen that for a given horn an optimum d_h exists, but this optimum is very wide. There is only little dependency on the optical focal distance. The maximum aperture efficiency is determined only by the edge tapering. This should be kept almost the same for any optimum combination. See also Fig. 77 which indicates the η_0 versus edge tapering (T). . It can be seen that $7.5 < T < 10$ db results in $65\% < \eta < 71\%$, while the diameter of hyperboloid varies within relatively wide limits.

14. 14.3 (Cont'd)

Another characteristic of the system is shown on Fig. 78 which indicates the slope of the feed system pattern at γ_{10} vs d. The increase in the slope is approximately linear with d. Fig. 79 exhibits the average variation of the main lobe level in the angular range $\gamma_5 < \gamma < \gamma_{10}$ vs. R. The variation (ripples) show a minimum around Ropt. Fig. 80 is the photograph of a typical K-band feed system.

14.4 V-band Horn with Various Hyperboloids

Fig. 81-85 show similar results for the V-band horn as Fig. 75-79 have shown for the K-band system. In this system the horn geometry is somewhat different then in the K-band horn (see Sec. 12.3 and 12.4). Also a little larger variety of hyperboloids is available.

Fig. 86 and 87 indicates the optimum pattern, which was measured with the H_8 hyperboloid.

The distance of test horn was D = 11 feet.

The above geometrical data can be compared with the optimum arrangement obtained from the far field measurement of the antenna system. (Fig. 119b) The close agreement between the endresults of the two independent approaches is more than noticable.

14.5 K-band 4 Horn Cluster

Only a few pattern were taken on this system, because of lack of required mechanical stability in the flexible waveguide circuit.

14. 14.5 (Cont'd)

Fig. 88 shows a highly unsatisfactory pattern of this system (H_2 hyperboloid, R = 194, $\gamma_H = 6^o$). The assymetries and large ripples in the main lobe indicate large errors in the power division and phase between the horns.

14.6 <u>V-band 4 Horn Cluster at f_1 21.6 Kmc/s and f_2 = 34 Kmc/s.</u>

In this cluster system the amplitude and phase of the individual horns can be controlled independently by variable attenuators and phase shifters. During the available time only the $\gamma = -3^o$ cluster was tested in details.

This system provides a slightly converging wave for the hyperboloids. The "focal point" of this 4 horn system is appr. 20" from the aperture of horns along the axis of the feed system. Such a system assures approximately equal tapering from the individual horns at the edge of hyperboloid, if the hyperboloid is approximately 20" from the cluster.

Fig. 89 indicates the aperture efficiency and S of such systems vs. R.

Fig. 91 shows the aperture efficiency vs. aperture angle of hyperboloid.

Fig. 92 is the $\eta_{o\,max}$ curve vs. d_h, and Fig. 93 is the T vs. $\eta_{o\,max}$ plot Particularly interesting is the $\left.\frac{d\,f(\tau)}{d\tau}\right/_{\tau=\tau_{10}}$ and v vs. R. curve for the H_{10} hyperboloid (Fig. 94, 95).

The slope is very large and the main lobe shows very small ripples. This indicates that the converging type near field phase front can be advantageously

14. 14.6 (Cont'd)

combined by a wide angle hyperboloid to provide almost phase error free feed system pattern and a relatively high aperture efficiency. Note, that in the optimum case the aperture efficiency is only about 0.5 db smaller then in the optimum, horn system.

Fig. 96 shows the pattern of a typical feed system combination. Fig. 97 and 98 show patterns aperture efficiency and supression of hyperboloids with $\gamma_{ah} = 90^{\circ}$ and 58° respectively at f = 34.4 Kmc/s.

The patterns of 4 horn cluster indicate that it is possible to obtain for the sum pattern of a four horn system approximately the same aperture efficiency as for the best single horn system. The importance of this fact is obvious; it makes potentially possible to use the same feed system for listening and monopulse operations while sacrifizing only a very small amount of system gain.

14.7 <u>Design Procedure of a Cassegranian Type Feed System Using the Experimental Data.</u>

The measured and processed data of the previous sections makes possible to prepare a design flow diagram for a low noise, Cassegranian type antenna, which contains only one feedback route. (See Fig. 99)

It can be assumed that the input parameters are:

$T_{AGeff.}$ = noise temperature component corresponding to ground radiation;

G = required gain of the antenna system;

14. 14.7 (Cont'd)

γ_{ap} = aperture angle of paraboloid;

η_T = tolerance factor of paraboloid surface;

K_W = wide angle side lobe level in the antenna system pattern, caused by source system spillover radiations and screening of hyperboloid.

The input parameters on Fig. 99 are in circles. The endresults (the geometry of the two reflectors) are in double lined rectangulars. Unfortunately it is not possible to obtain the endresults directly from the input parameters because of the feedback route between η and D. However η can be determined approximately if an assumption is made for η_o

From the results given in the previous sections a diagram can be constructed for the relationship between a, A and d. (See Fig. 100) Selecting any three corresponding values on the basis of this diagram η_o will be approximately maximum. The maximum value of η_o will be in most cases $0.65 < \eta_o < .80$, therefore the $\eta_o = 0.72$ average value can be selected as a first approximation in the design flow of Fig. 99. After the more precise value of a, A and d is known the second approximation of η_o can be found and the calculation repeated if necessary.

The determination of γ_{ah} requires some consideration. If $\gamma_{ap} \geq 90°$ than the spillover radiation of feed system practically does not exist for $\gamma < 90°$ and γ_{ah} can be selected strictly for optimizing η_o . For $\gamma_{ap} < 90°$ a diagram can be prepared which shows the relationship between $S, d_k; \gamma_{ap}$ and γ_{ah} (see Fig. 101).

14. 14.7 (Cont'd)

In many cases of large antenna design the construction and testing of a small scale model already provides considerable difficulties. On the other hand the experimental work on the small scale feed system is relatively simple. Therefore it is very important to know, to what extent is it possible to extrapolate the antenna system characteristics from the measured pattern of feed system.

The preparation of the previous charts for η_0, S, K_W served partly for this purpose. As an addition in Fig. 103 a full antenna system pattern (envelope of sidelobes) is prepared from a typical measured feed pattern. Fig. 102 indicates the measured feed system pattern which was used for this calculation. (Fig. 102a is the average of measured feed system pattern, 102b is the ripple component on the main lobe of feed pattern. The far field pattern can be compared and further discussed by the corresponding pattern measured on the antenna system (Fig. 119a).

Once the pattern of the antenna system is known the noise temperature can be calculated not only for vertical antenna position, but as a function of the elevation angle. Fig. 104 gives an example for this calculation. Although this calculation is in principle very simple and involves only the integration of the antenna system pattern, numerically the computation is quite tedious. It involves basically the volume determination of an assymetrical space pattern. The calculation includes also the effect of atmospheric attenuation.

15. THE SECONDARY REFLECTOR

15.1 Selection of Aperture Angle.

The geometries of secondary reflectors were determined on the following basis:

1) One secondary reflector should be the small scale model of the 85' Goldstone antenna with an aperture angle $\gamma_{ap} = 61°$
2) To cover wide range of aperture angles a second reflector should be selected close to $\gamma_{ap} = 90°$
3) The aperture diameter measured in wavelength should be maintained approximately constant while γ_{ap} is varied.
4) The surface tolerances of these dishes should correspond to the existing Goldstone antenna.

Some relatively accurate paraboloid reflectors were available as a current mass produced item within the RCA plant at Montreal. This dish has a focal distance F_p = 23.63" and an aperture angle γ_{ap}= 104°. Utilizing this available spinning the geometry of the two paraboloids were selected as Table 4 indicates.

TABLE 4

Dish No.	F_p''	D_p''	$\gamma_{ap}°$	f kmc/s	D_λ	t''_{req}
1	23.63	56.0	61	34	164	0.017
2	23.63	120	104	24	240	0.025

To make possible the use of the same spinning (F_p = const and $D_\lambda \approx$ const) two frequencies were used. The required value of the rms surface deviation t_{req} was obtained on the assumption, that t = 0.250" for the 85'

15. 15.1 (Cont'd)

Goldstone paraboloid. The effect of these tolerances on η_T can be obtained from Fig. 105.

15.2 Selection of Reflectors

The main problem associated with the secondary reflectors is the proper value of the rms surface tolerance, t. A parabolic template with $\pm 2\tau$ tolerance was constructed and a dish supporting turntable was built. (See Fig. 106 and 107) 12 dishes from the production line were mounted on this turntable and the gap between the template and surface of dish was measured with gap-gauge. 8 points were checked along the parabolic arc and the dishes were set into 6 angular positions. Consequently a total of 48 surface points were measured on each dish and the circumferential, meridian and total rms deviation $\sigma_c, \sigma_m, \sigma_t$ were calculated separately. Two of the best dishes were selected and then, by small deformations of the surface the surface accuracy was improved. After the surface accuracy reached the required quality the backframes were attached, using pads between reflector and frame, to avoid any further deformation.

Table 5 shows the surface deviations of the accepted #1 Dish, after the correction of surface was finished.

TABLE 5

Absolute value of deviations of #1 dish from paraboloid template.

(In thousands of inches)

	0°	60°	120°	180°	240°	300°
5"	1.8	3.2	10.8	5.2	1.8	6.2
10"	2.7	20.3	2.3	9.7	2.7	7.7
15"	3.3	8.7	6.7	3.3	5.3	3.3
20"	5.0	10.0	5.0	15.0	25.0	10.0
26"	0.7	8.3	25.7	13.7	23.3	8.3
28"	2.7	3.7	21.3	27.3	23.7	18.7

RMS deviation along the parabolic are: $\sigma_R = 7.91\ \tau$

RMS deviation along the r = const lines: $\sigma_c = 12.27\ \tau$

Total RMS deviation: $\sigma_T = 14.60\ \tau = 0.0146"$

The value of σ_T deteriorated to only $\sigma_T' = 16.8\ \tau$ after the backframe and supporting structure for the hyperboloid was assembled.

Fig. 108 shows the No. 1 dish ($\gamma_{ap} = 61^\circ$) with one of the feed systems. The support of the feed was constructed such a way that both the hyperboloid and horn can be easily adjusted in positions within wide limits. The horn can be rotated along its axis. The local oscillator is mounted directly on the output of the horn and is protected by a housing.

16. PATTERN MEASUREMENTS ON THE ANTENNA SYSTEM

16.1 Selection of System Parameters for far Field Measurements.

When the antenna gain and front to back ratio are simoultaneously large the farfield pattern measurement should cover a very wide power range, The space attenuation, α_S, between transmitter and receiver antenna further increases the required total dynamic range, therefore

$$\alpha_T = \alpha_S \alpha_A \tag{21}$$

α_A is given, however, α_S can be minimized. The power ratio of the received to transmitted signal

$$\alpha_S = \frac{P_R}{P_T} = \frac{G_T A_R}{4\pi R^2} \tag{22}$$

where

$$G_T = \eta_{Tr} \pi^2 \frac{D_T^2}{\lambda^2} \tag{23}$$

$$A_R = \eta \frac{\pi}{4} D_P^2 \tag{24}$$

$$R = 2 \frac{D_T^2 + D_R^2}{\lambda} \tag{25}$$

η_{Tr} = aperture efficiency of transmitter antenna,

η = aperture efficiency of receiver (measured) antenna,

D_T = diameter of transmitter antenna,

D_P = diameter of receiver antenna,

R = distance between the two antenna.

Inserting (23) (24) and (25) into (22)

$$\alpha_S = \frac{\pi}{64} \eta_{Tr} \eta \frac{D_P^2 D_T^2}{(D_T^2 + D_P^2)^2} \tag{26}$$

α_S is minimum, if $D_P = D_T = D$

$$\alpha_{Sm} = \frac{\pi^2}{256} \eta_{Tr} \eta \tag{27}$$

16. 16.1 (Cont'd)

Assuming the usual aperture efficiencies $\eta_{Tr}\eta = \cdot 26$, $\alpha_{sm} = 10^{-2} = -20db$. In the V-band the Raytheom klystron delivers $P_T = 10^{-2} W$ and the noise level of a superheterodyne receiver with 3 mc/s bandwidth is about $P_R = 10^{-11} W$ which results in $\alpha_T = 10^{-9} = 90db$ dynamical range. The above system therefore provides an $\alpha_A = 70db$ pattern measuring range. It has to be noted that provided $D_P = D_T = D$ the given range of α_A is independent of the gain of the measured antenna assuming that the required distance

$$R = 4D_\lambda^2 \lambda \qquad (28)$$

is assured.

For the V band model $D_\lambda = 163$, $\lambda = 0.872 . 10^{-2} m$ $R_V = \cdot 57 miles.$

The actual distance was about this value, R_V = 0.39 mile. The existing path lenght error is very small in this arrangement. This error reduces the measured gain by $\Delta G_V \approx 2\% \approx \cdot 1db$ This error is small, however, it can be taken into account in the gain measurement.

For the K-band model at f = 22 kmc/s, D_λ = 224, λ = 1.36 10^{-2} m R_K = 1.57 mile, the path length error $\Delta_K = 0.234\lambda_K$, ΔG_K = 18.1% ($\approx$ -0.73 db)

16.2 <u>Description of Test Set-up.</u>

The far field pattern measurements were performed at the antenna test site of RCA Victor Company (St. Matthieu, Quebec).

The block diagram of the measuring equipment is indicated on Fig. 109. The transmitter and receiver antenna were mounted at 26 and 17 feet above the ground level at a distance of 2060 feet. The height difference

16. 16.2 (Cont'd)

approximately compensated the slight slope of the ground surface. Photographs 110 and 111 show the test towers with the antennas.

At the transmitter site a klystron served as the transmitting oscillator. Once this antenna was aligned and the klystron adjusted no servicing was required here with the occasional change of antenna polarization. The transmitter was unattended.

At the receiver site the level of incoming signal was monitored by a horn, which has 30 db gain at f = 34.4 kmc/s. This horn was used at the same time for relative gain measurements.

Two types of receiver systems were used. For analysing the main beam region and adjusting the antenna a crystal receiver was used. This receiver results in quite satisfactory stability and about 50 db signal to noise ratio when the antenna is directed toward the transmitting antenna and the modulating frequency of transmitter antenna is accurately tuned to the selective voltmeter receiver.

During a period of 8 hours 3 db loss in sensitivity was experienced caused by the drift of audio frequency. An additional ±1.5 db variation was observed when the wind reached 30 miles/hours velocity. The later variations may decrease the useful measuring range, however no measuring error occurs if the signal of the reference horn is recorded by another channel of the Sanborn recorder.

16. 16.2 (Cont'd)

For wide angle radiation measurements a superheterodyne receiver system was used which increased the sensitivity to about 66 db. In fact using the integration properties of the recorder when measurements are several times repeated, the useful range can be extended by another 10 db in both cases.

The turntable is adjustable to 0.95 rpm or 0.105 rpm. The latter speed is more satisfactorily taylored to the time constant of the recorder.

As was mentioned previously two test paraboloids were built with known surface accuracies. In this report only the data measured on the #1 dish will be included.

The single horn and 4 horn V band cluster was used as a source system. Various hyperboloids were tested as primary reflectors with different size aparture angle and focal distance.

The axial off axis and angular position of the horn was adjustable in this set-up. At the same time the axial and angular position of the primary reflector was variable too. The change of polarization was accomplished by the rotation of the horn.

The available frequency(34.4kmc/s) resulted in $D_p = 163\lambda$ for the paraboloid aparture diameter. This gives $G_o = 3.49 \cdot 10^5$ (55.3 db) gain for perfect paraboloid and $G_o \eta_T = 3{,}49 \cdot 10^5 \times 0.677 = 2{,}00 \cdot 10^5$ (53.6 db) gain for the actual paraboloid. (The η =-1.7 db tolerance factor is a

16. 16.2 (Cont'd)

result of the 17 rms surface tolerance of the paraboloid. Since the Goldstone antenna supposed to be operated with $D_p = 206$ aparture size, approximately 1.8 db has to be added to the measured gain figures to obtain the actual data of the full size antenna at 2388 mc/s.

The gain data were determined by two independant methods:

a) Using the 30 db gain reference horn.

b) Integrating the pattern, taking into account the part which is between the -50 db points. (Approximately the part of pattern which is above the level of isotropic radiator.)

The calculated gain values are corrected by the 0.1 db gain loss, caused by the path length error between transmitter and receiver antennas.

16.3 Results of measurements.

The maximum gain was obtained by the H8 hyperboloid (see Fig. 112).

Using the pattern integration methods the gain of this arrangement is G = 52.19 db (53.99 db in the case of Goldstone dish). The gain comparison methods resulted in 52.10 db value on the measured model. (53.90 db in the case of Goldstone dish.) The overall measuring accuracy is estimated better than ± 0.3 db. The 53.95 ± 0.30 db averaged gain with a single horn system for the Goldstone dish seems to be a good value. However, it should be noted that the available V-band horn has relatively high side lobes which can be eliminated in the full size model by using the same horn design as the X-horn. (Radial fins instead of the parallel fins.)

16. 16.3 (Cont'd)

It is expected that the use of this horn will further improve the gain. This improvement may be 0.2 db. It is interesting to compare the 53.95 db gain figure with the corresponding theoretical value. (See Table 3 in Part II, page 11) In this 53.7 db gain is predicted under item 4, column D. Taking into account the approximate nature of these calculations and the inaccuracies of the pattern measurements the agreement is surprisingly good.

In the following a series of far field data of the antenna system is presented. This series is far from being complete, but indicates the basic effects of the geometrical parameters of the antenna system.

Fig. 112 shows the H plane and E plane pattern of the optimum antenna arrangement. It can be seen that the pattern shows a great degree of axial symmetry close to the main beam, however the wide angle sidelobes are occupying a wider angular range in the E plane then in the H plane as a result of not completely satisfactory sidelobes of the horn in this plane.

Fig. 113 shows in detail the main beam region of a typical antenna system. For approximate gain calculation purpose it is practical to introduce two concepts: P_{10} = the equivalent beamwidth of a pattern, which is trunketed at the total cone angle 1° (within this equivalent angular region the same amount of power is radiated as within a cone with 1° beamwidth).

16. 16.3 (Cont'd)

P_{1^o} = the percentage of power which is radiated between the cone with 1° total angle and the cone which is determined by the 50 db points of the pattern.

Using these two figures the gain of the antenna

$$G = 4\pi \left(\frac{57.3}{\beta_{1^\circ}}\right)^2 \cdot \frac{1}{P_{>1^\circ}}$$

Fig. 114 indicates the pattern envelope of a system which is operated by the H8 hyperboloid. The region of screening sidelobes and spillover sidelobes are quite distinctly noticeable.

Fig. 115 shows a typical example for the variation of the beam shape with the distance between horn and hyperboloid. The shape of the main beam is affected by two factors; the amplitude distribution along the hyperboloid and the phase error in the reflected waves of the hyperboloid. The diagram shows a definite optimum. This optimum distance is somewhat smaller than the distance calculated from the geometrical optics. On the other hand the geometrical focal points of the paraboloids and hyperboloids are very close for optium gain operation.

Fig. 116 indicates a very interesting and usefull characteristic of a practical double reflector system.

Fig. 116a shows a single paraboloid which is illuminated by a point source, located in its focal point. Such a system can not be realized exactly.

Fig. 116b represents a practical system in which the paraboloid is illuminated by a finite sized source (horn). In this case the horn has to

16. 16.3 (Cont'd)

be shifted toward the paraboloid to compensate its finite size and a phase front can be obtained which coincides with the linear phase front only at points 1 and 2.

Fig. 116c indicates a paraboloid-hyperboloid system in which the hyperboloid is shifted toward paraboloid and the horn toward the hyperboloid to obtain higher order phase compensation. The phase front coincides with the linear phase front at points 1, 2, 3 and 4.

Experimental data shows that the gain maximum occurs in such arrangement assuming that the tapering at the edge of hyperboloid is properly selected.

Fig. 117 represents the variation of the pattern envelope with the size of hyperboloid, maintaining the distance between the two elements constant. It can be seen that the spillover sidelobes are increasing rapidly if the size of hyperboloid is beyond a certain value.

Fig. 118 indicates that an optium hyperboloid size exists for any given horn. In this figure the aperture efficiency is plotted for three hyperboloid sizes. The value of M and K was determined in each case to obtain maximum gain. The maximum aperture efficiency is 72% with M = 15.10".

When a larger M is desirable without increasing the size of the hyperboloid and horn, M can be increased with some loss of the aperture efficiency. However in this case not only the aperture efficiency decreases, but simultaneously the spillover radiation increases (see Fig. 119).

16. 16.3 (Cont'd)

Figures 120, 121, 122 and 123 give some information about the positioning tolerances required in a Cassegranian feed system.

Fig. 120a shows the effect of axial misalignement of the hyperboloid. A 0.6λ axial misalignment increases the 3 db width of the main lobe from 0.44° to 0.54°.

Fig. 120b indicates the loss of received signal as function of axial misalignement.

Fig. 121 indicates that the axial misalignment of horn is less critical. 3λ axial misalignment causes only 0.2 db reduction in the gain.

Fig. 122 shows the variation of received signal with the off axis position of the horn. This figure contains data about the monopulse or scanning properties of the feed.

Fig. 123 represents the variation of received signal with the angular position of hyperboloid. This figure may serve for the proper design of a quadrupol structure, when the required angular stability of the main beam is specified.

Fig. 124 indicates the envelope of side lobe level for different quadrupole structures. The "quadrupoles" were made from perforated metal sheets, with 0.25" lobe diameter and 40% transparency.

16. 16.3 (Cont'd)

The noise temperature component caused by ground radiation of the optium arrangement can be calculated from Fig. 81. According to this figure the average power level relative to isotropic radiator toward ground is -11 db and S = 4.1%. The noise temperature component $T_{Geff} = 6.15\,°K$. This quite closely agrees with the theoretical value (6°K) and with the value calculated from feed system measurements (5.1°K).

CONCLUSIONS

A number of general and particular conclusions can be made from the experimental measurements. These can be summarized as follows:

1. The gain: screening and wide angle side lobe characteristics of large Cassegranian systems can be very accurately calculated from the geometrical optics.

2. The noise temperatures of such an antenna can be determined from wave optical calculations, from integration of measured feed system pattern or from integration of measured antenna system pattern. The three values agree very closely. The predicted data can be compared by direct radiometer measurements, however, such measurement have not been done on Cassegranian systems.

3. Pattern of antenna system can be determined very closely from the measured data of feed system. This may be very useful in a very large antenna system, where even the construction and testing of a small scale antenna is difficult.

4. A paraboloid with $D_p \cong 206\lambda$ dia. and a hyperboloid with $d_h \cong 20\lambda$ dia can be combined into a Cassegranian system with 54 db overall gain, $T = 10.6^{\circ}$ K.

CONCLUSIONS (Cont'd)

antenna noise temperature, including all feeder loss. This data refers to the existing Goldstone antenna with Cassegranian feed.

5. From Fig. 112 it is possible to extrapolate some of the basic data of the 240' paraboloid. Here the size of paraboloid diameter is approximately 3 times larger. This gives 9 db additional gain (63 db). If the size of hyperboloid and distance between horn and primary reflector is doubled ($A_\lambda \cong 120$, $d_{h\lambda} \cong 40$) without changing the size of horn, then spillover radiation relative to the isotropic source is unchanged (this level will be about -50 db relative to main lobe) while the -50 db point of the "screening" sidelobes will occur at 1/3 of the angle where the -41 db point occures in Fig. 112. This gives for the -50 db point approximately 3° measured from main maximum.

ACKNOWLEDGEMENTS

The authors wish to express their deep appretiation to the Jet Propulsion Laboratories. There, the interest of Dr. E. Rechtin, R. Stevens, P. Potter, W. Merrick and others initiated, and continuous support made possible the completion of this study under various contracts. The participants of this investigations also would like to thank the management of RCA Victor Company, Ltd. for the help they received, and particularly to G.B. MacKimmie and J. Collins who tried to maintain the preferance of this job in a period when the Company had already some other urgent commitments. Also acknoledgement should be paid to H. Hings for useful suggestions regarding the manuscript of this report and N. Tenne-Sens and T. Szirtes who contributed to the mechanical design and check-up of various antenna models.

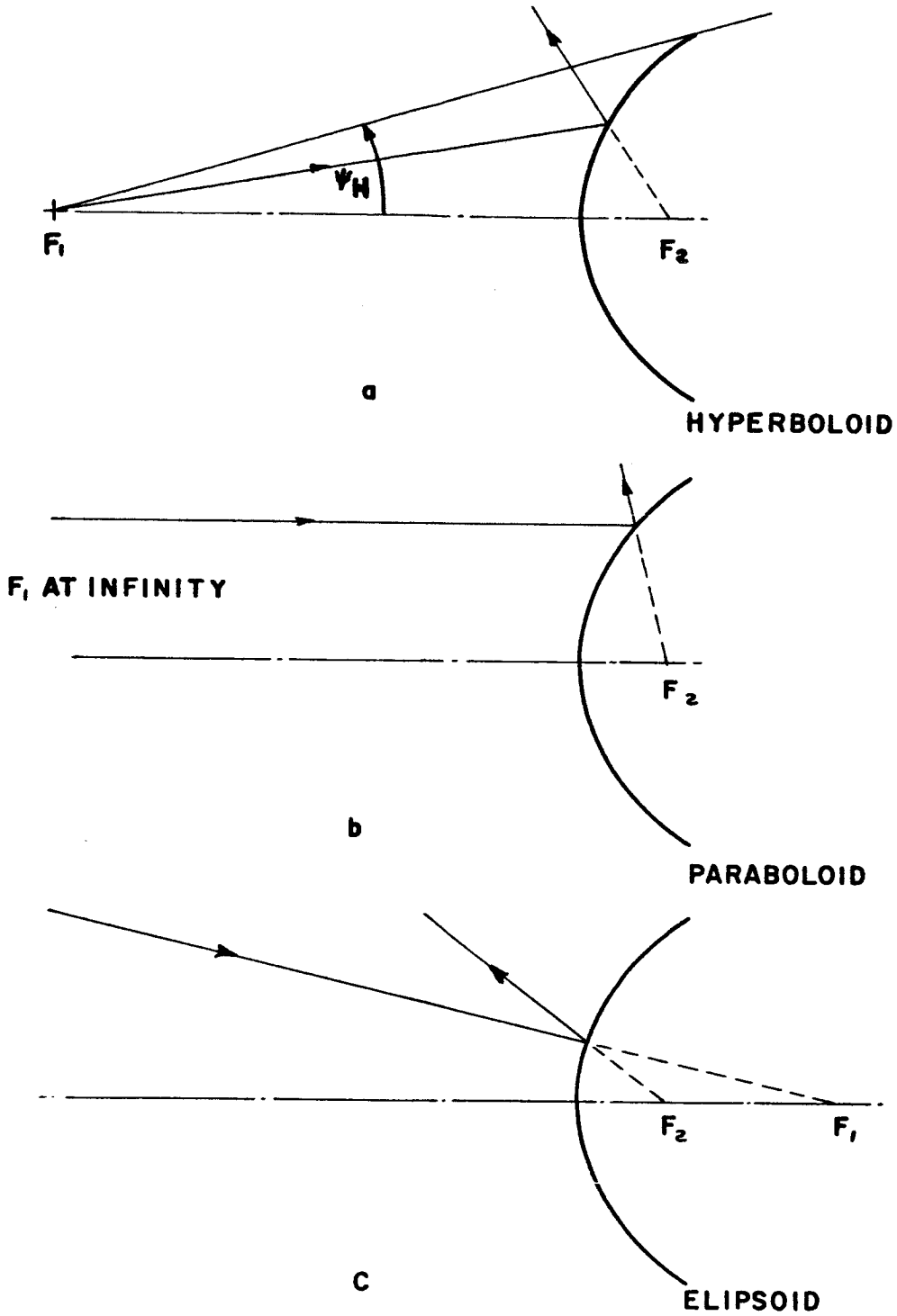

FIG. 49

SOME POSSIBLE SHAPES OF PRIMARY REFLECTORS

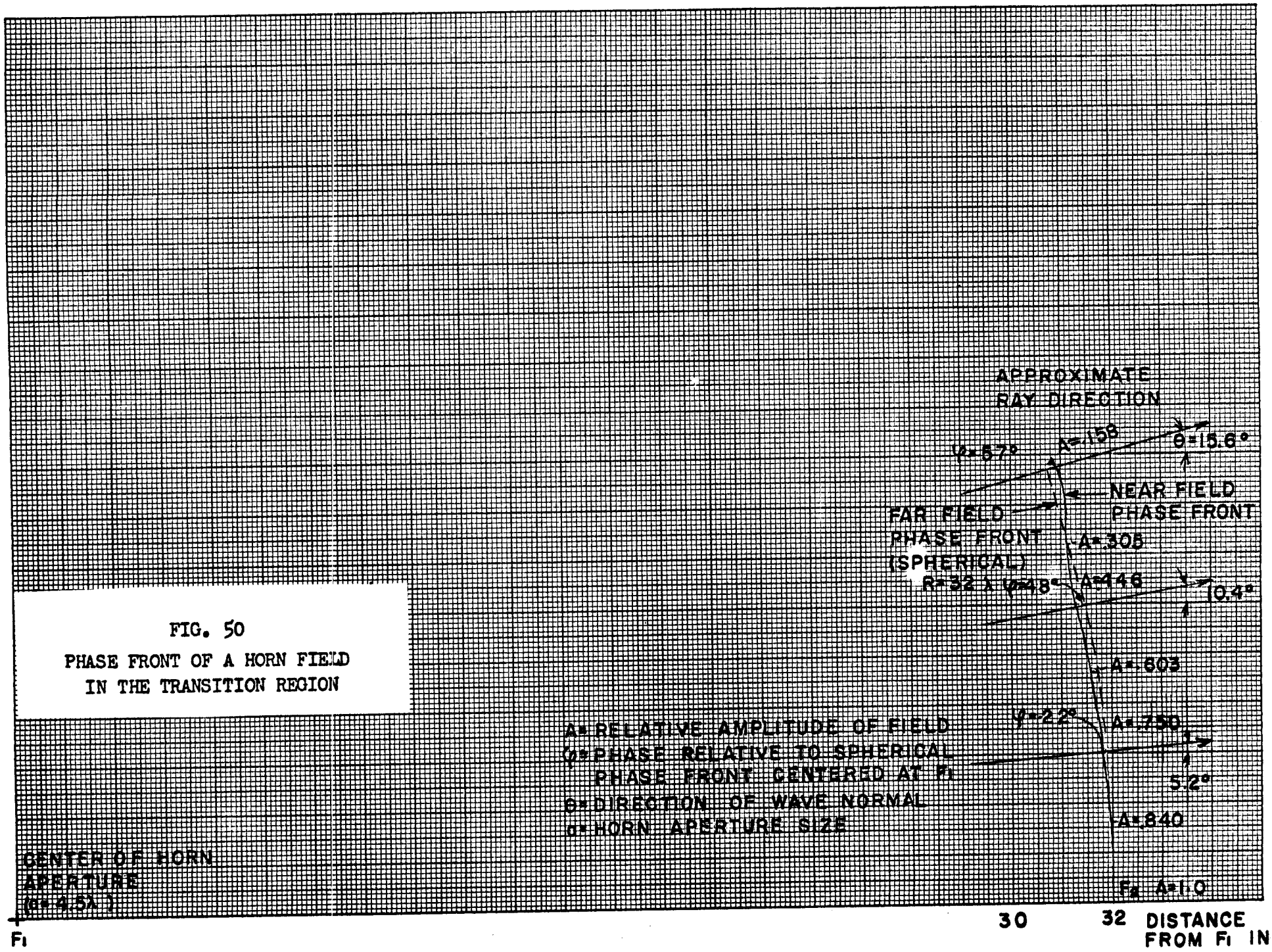

FIG. 50

PHASE FRONT OF A HORN FIELD
IN THE TRANSITION REGION

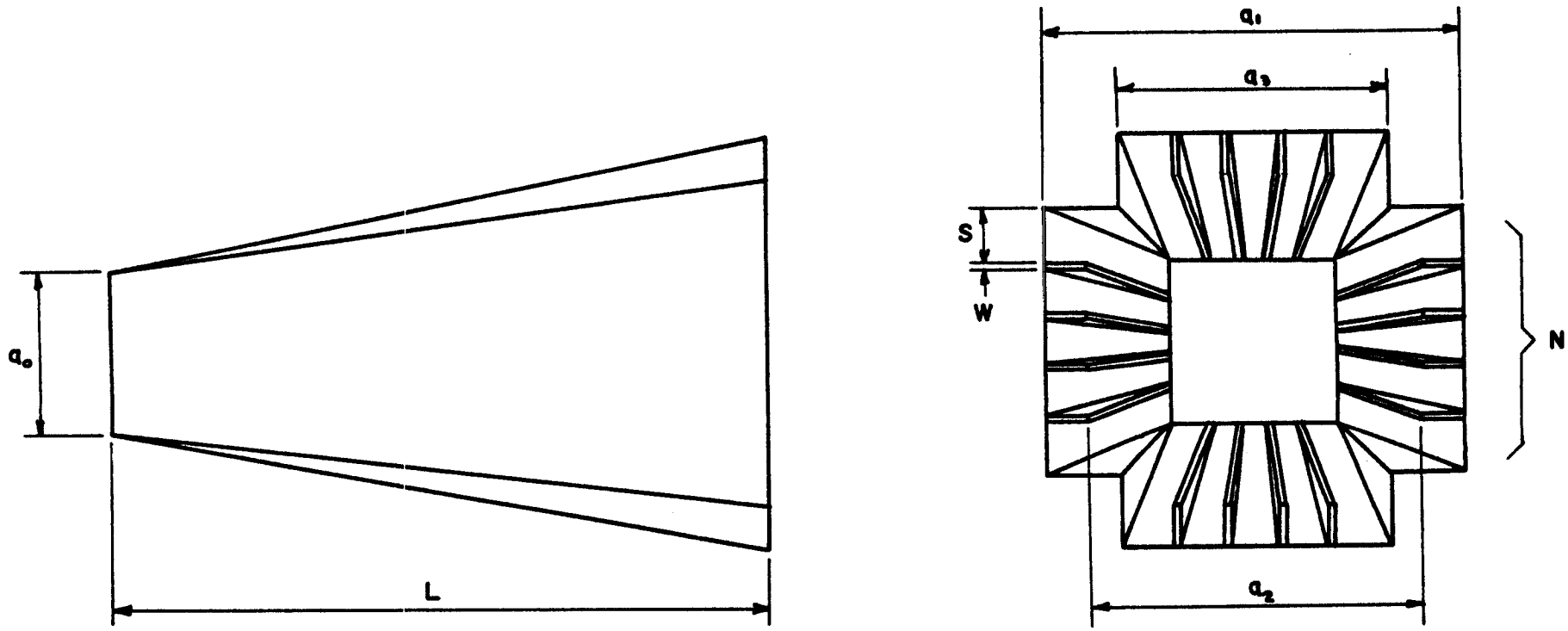

FIG. 51

TYPICAL DIMENSIONS OF THE FIN LOADED HORN

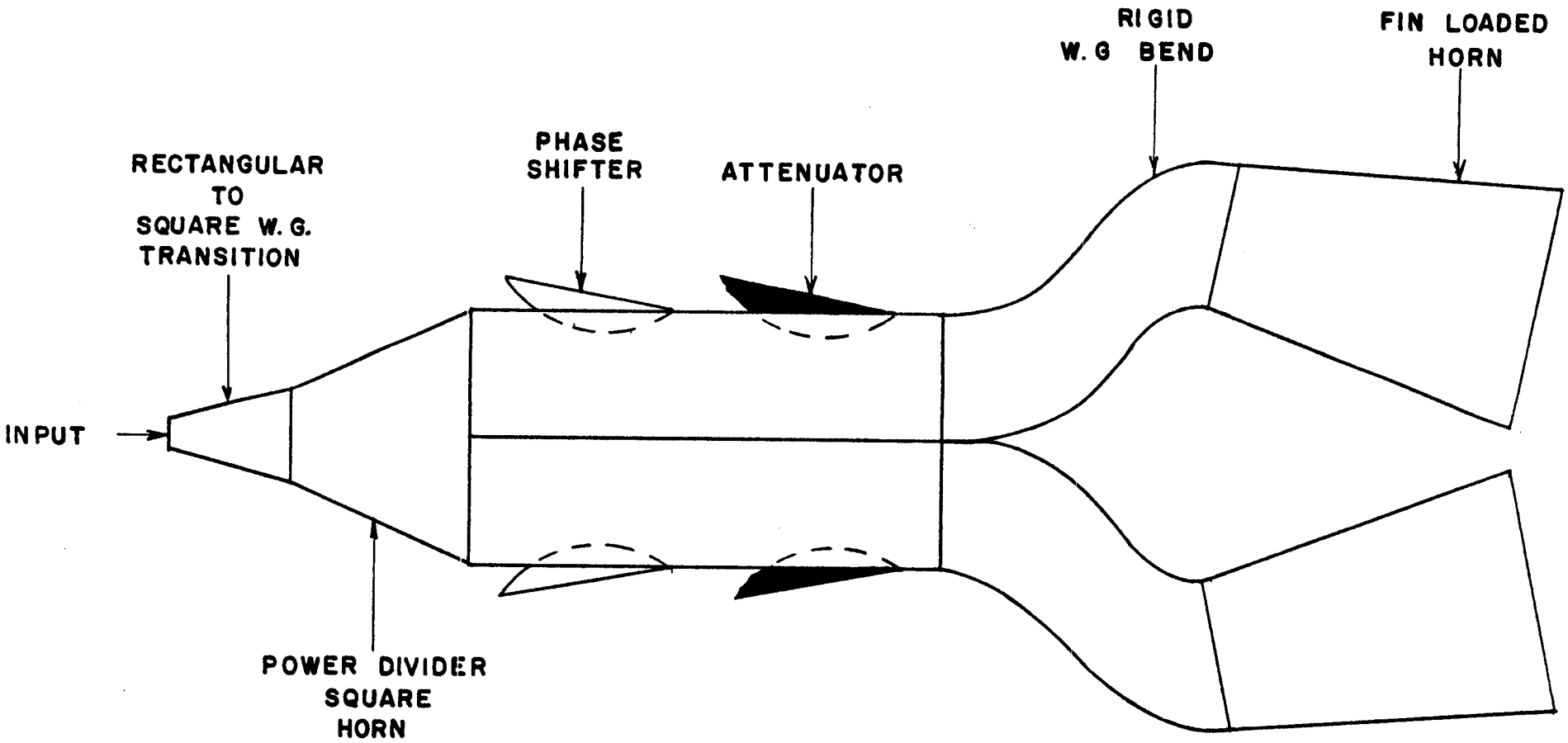

FIG. 52

WAVEGUIDE POWER DIVIDER
FOR THE FOUR HORN CLUSTER

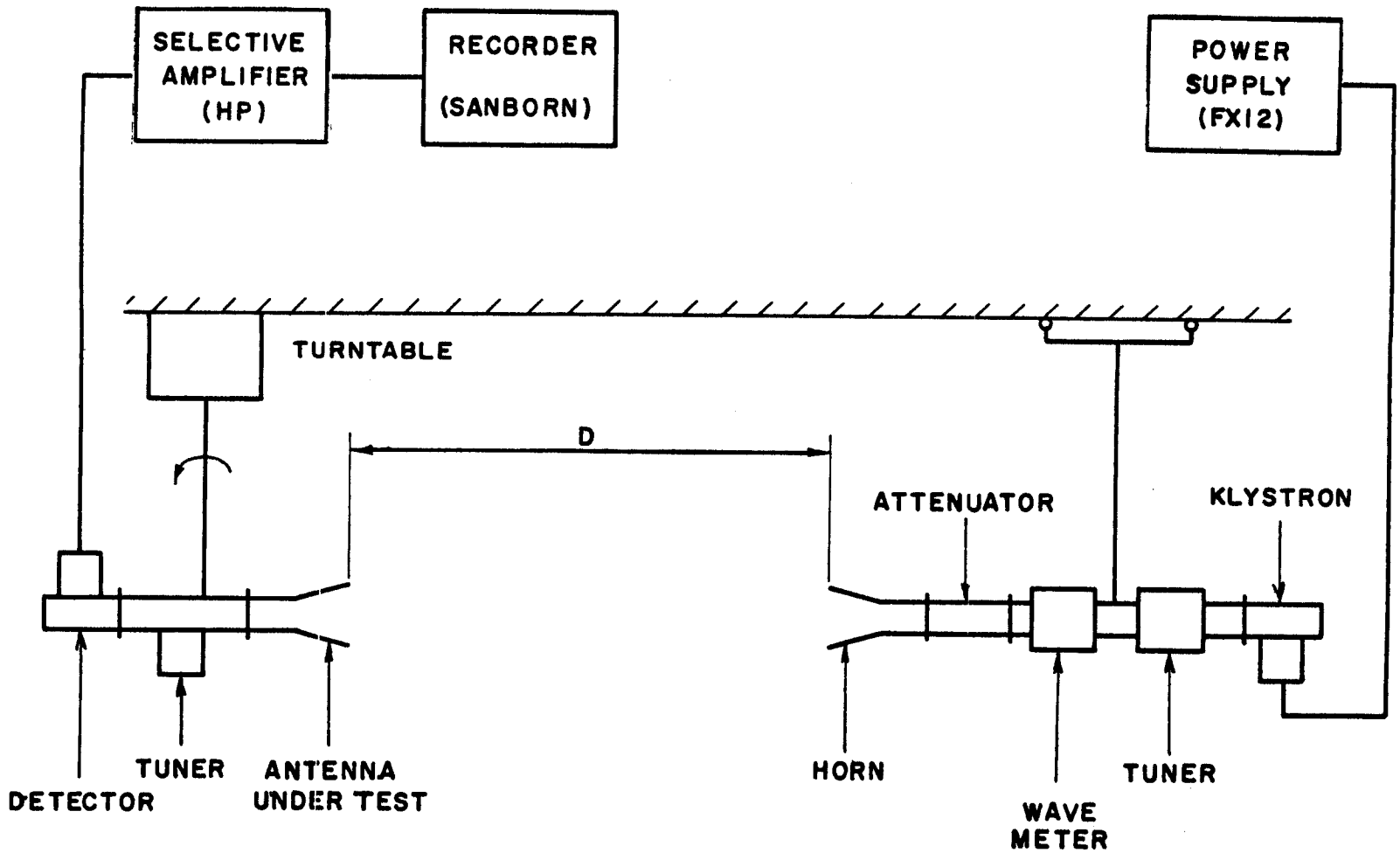

FIG. 53

TEST ARRANGEMENTS
FOR THE SOURCE SYSTEM MEASUREMENTS

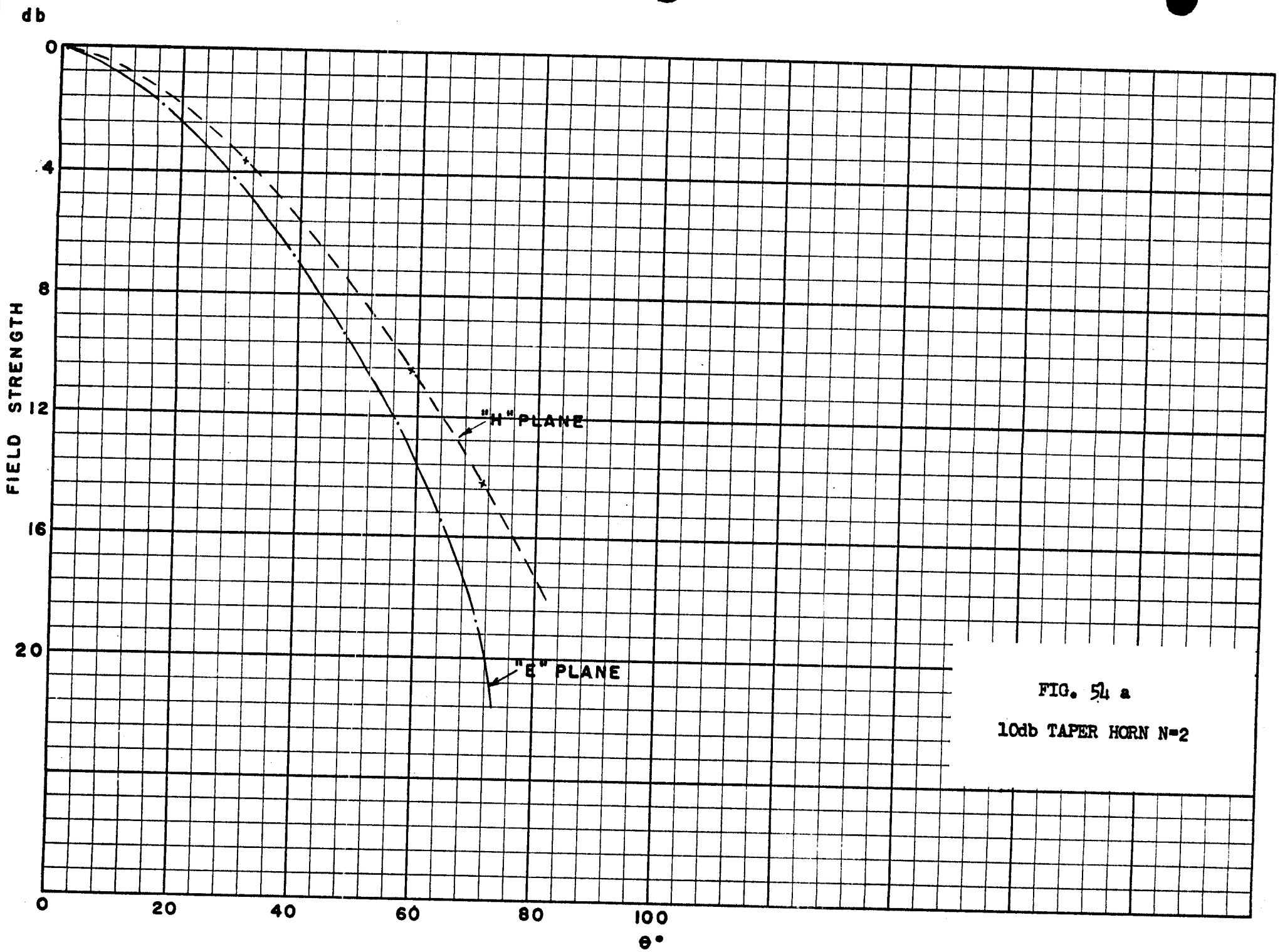

FIG. 54 a

10db TAPER HORN N=2

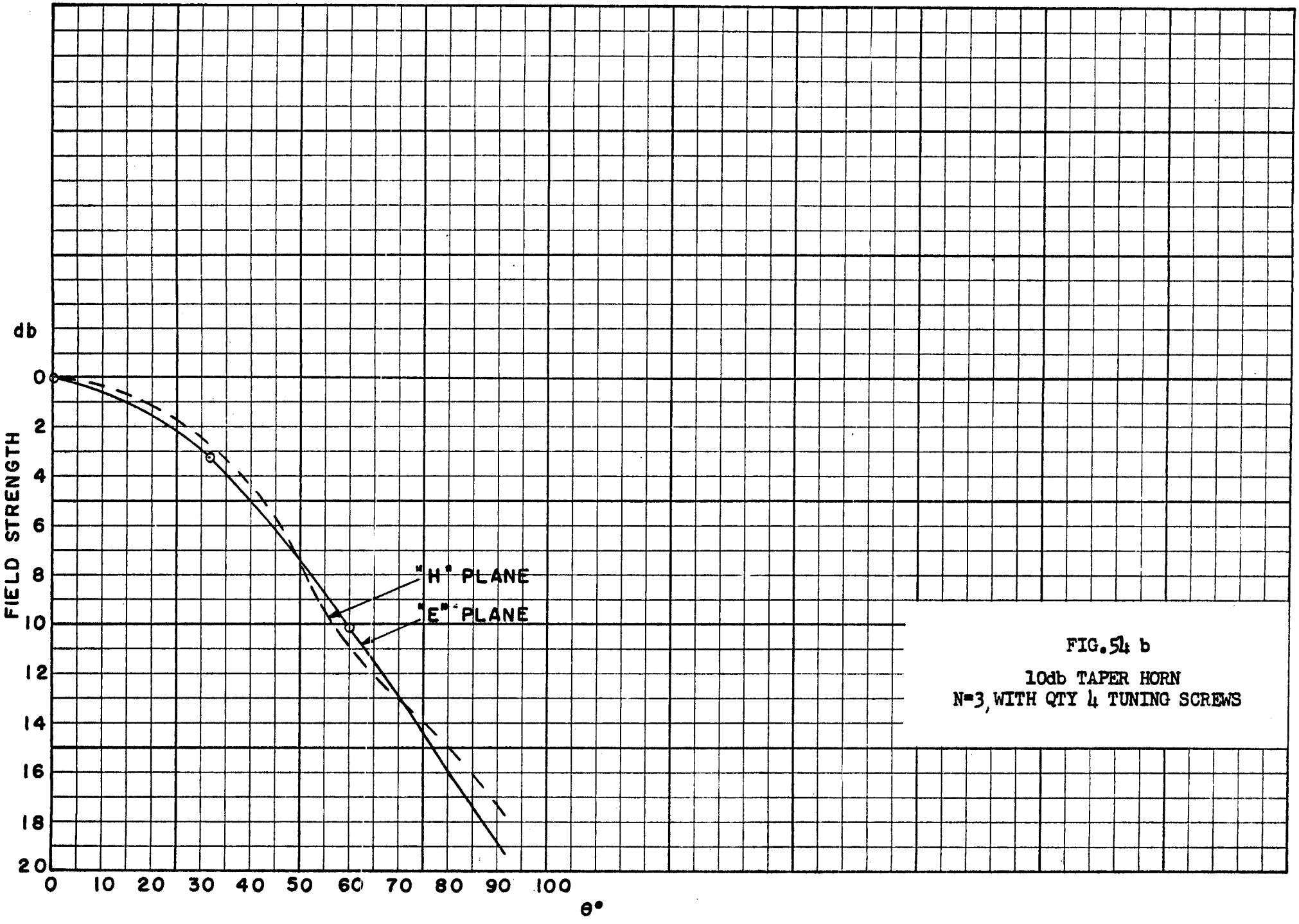

FIG. 54 b

10db TAPER HORN
N=3, WITH QTY 4 TUNING SCREWS

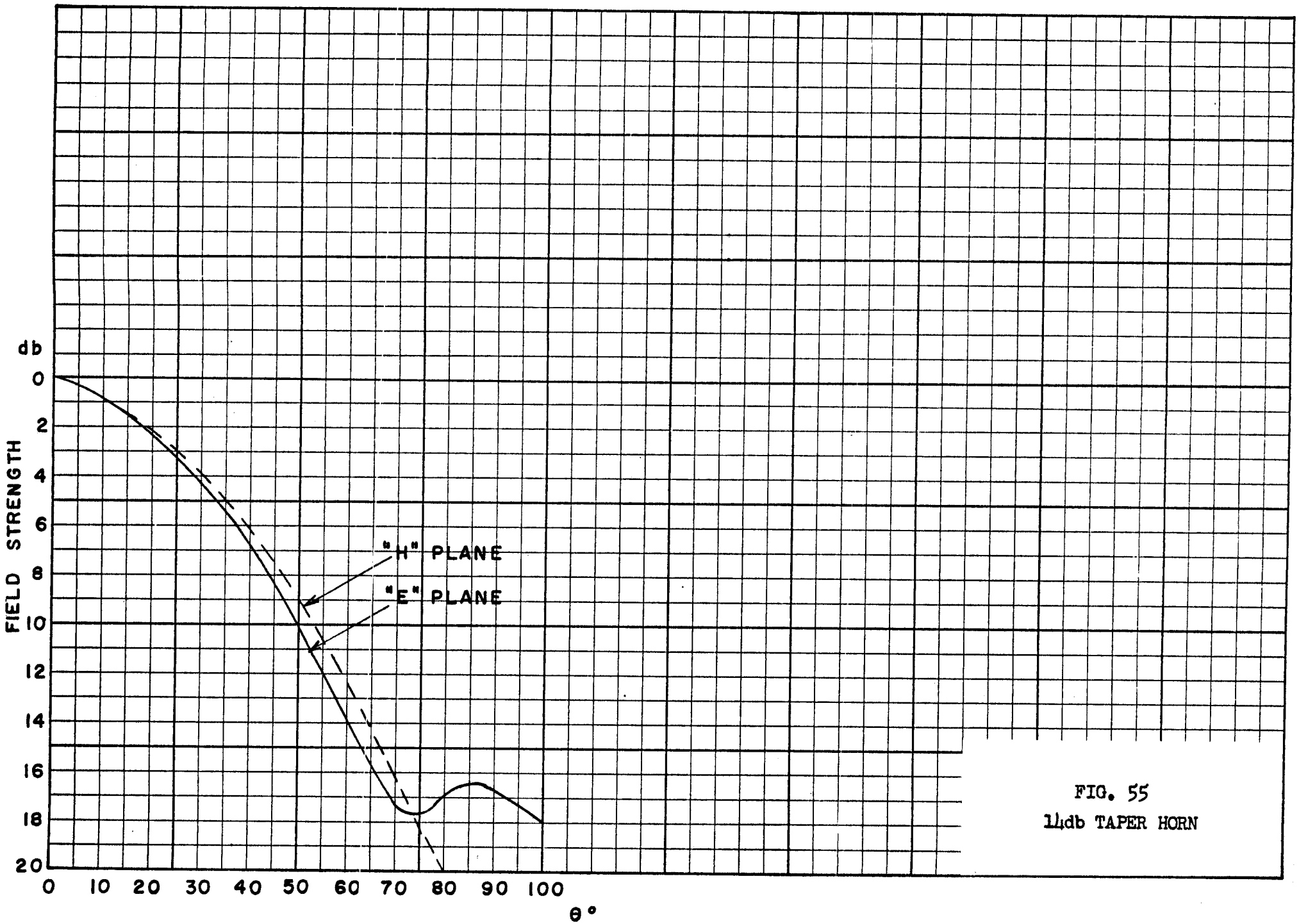

FIG. 55
14db TAPER HORN

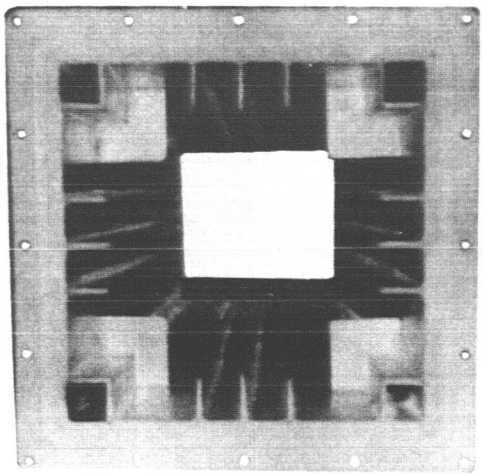

FIGURE 56. THE 14 DB HORN

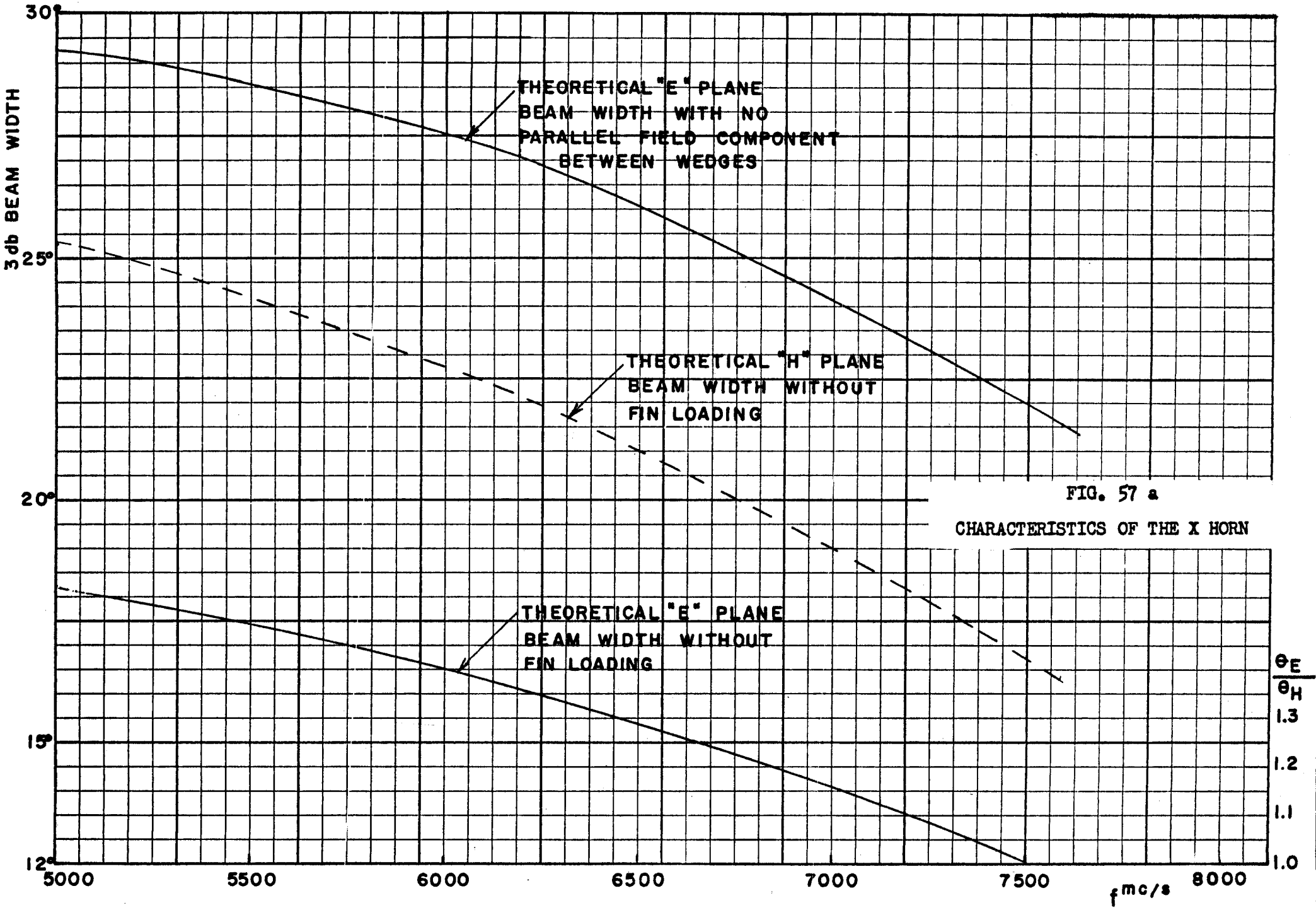

FIG. 57 a

CHARACTERISTICS OF THE X HORN

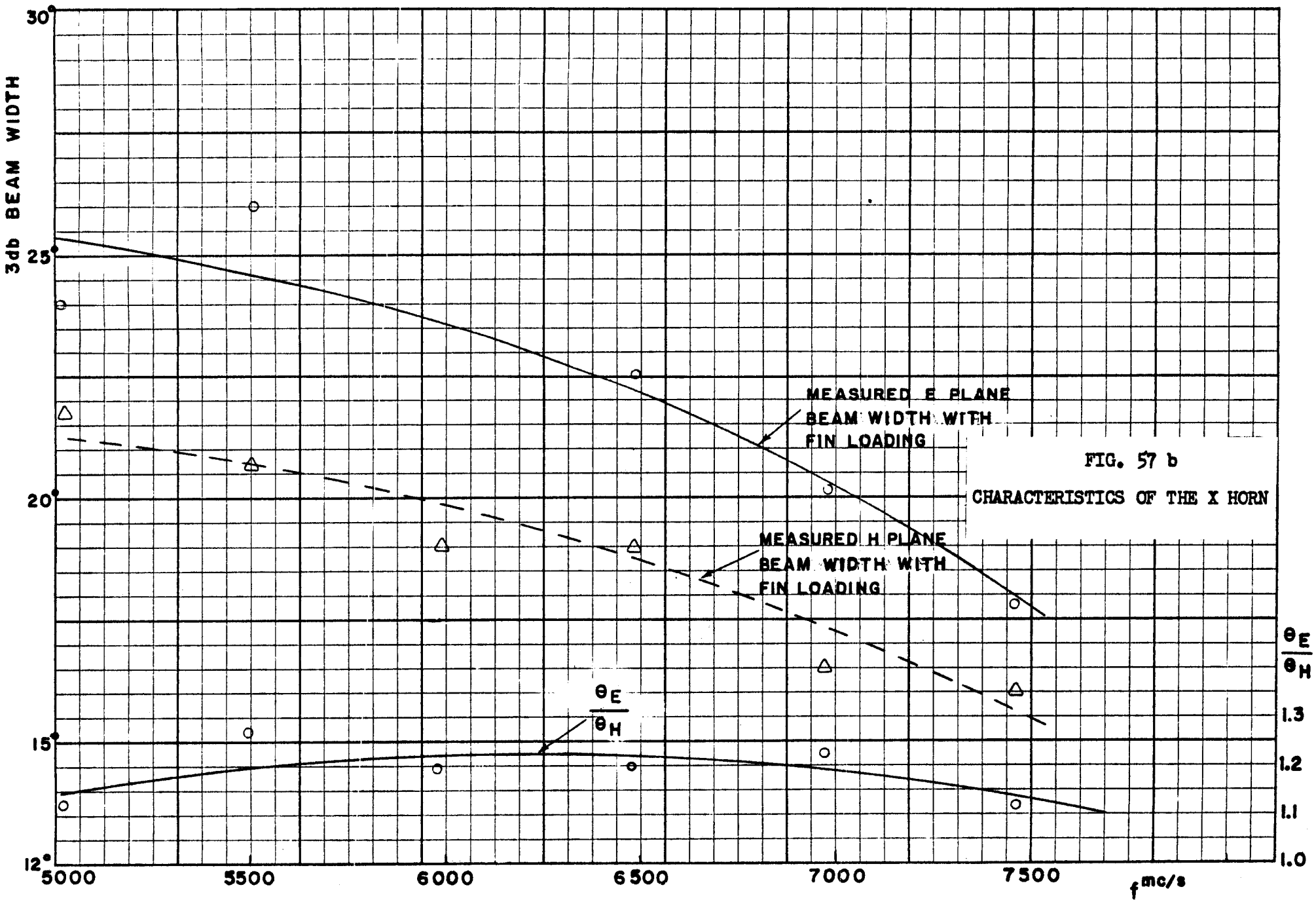

FIG. 57 b

CHARACTERISTICS OF THE X HORN

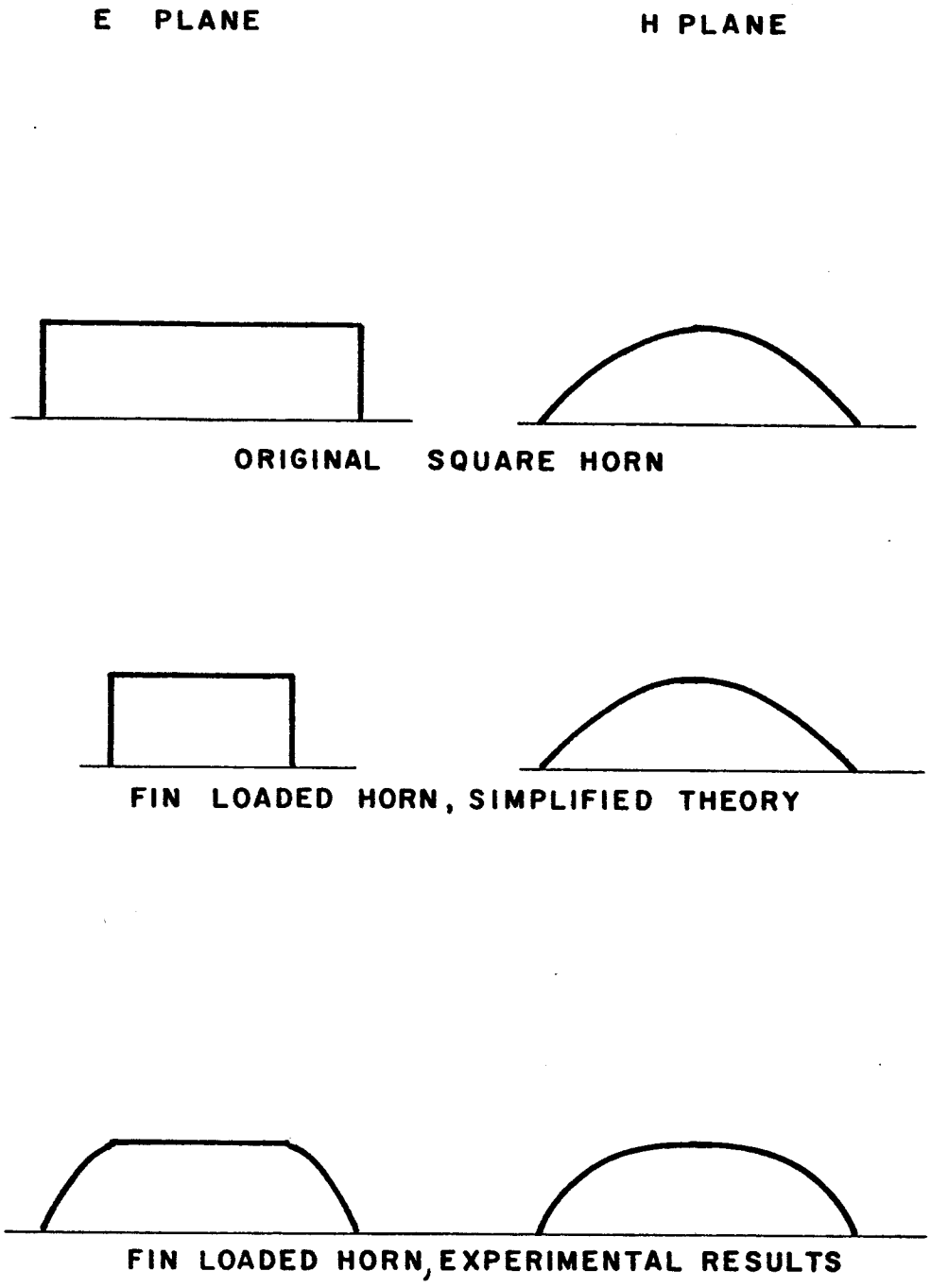

FIG. 57 c

CHARACTERISTICS OF THE X HORN

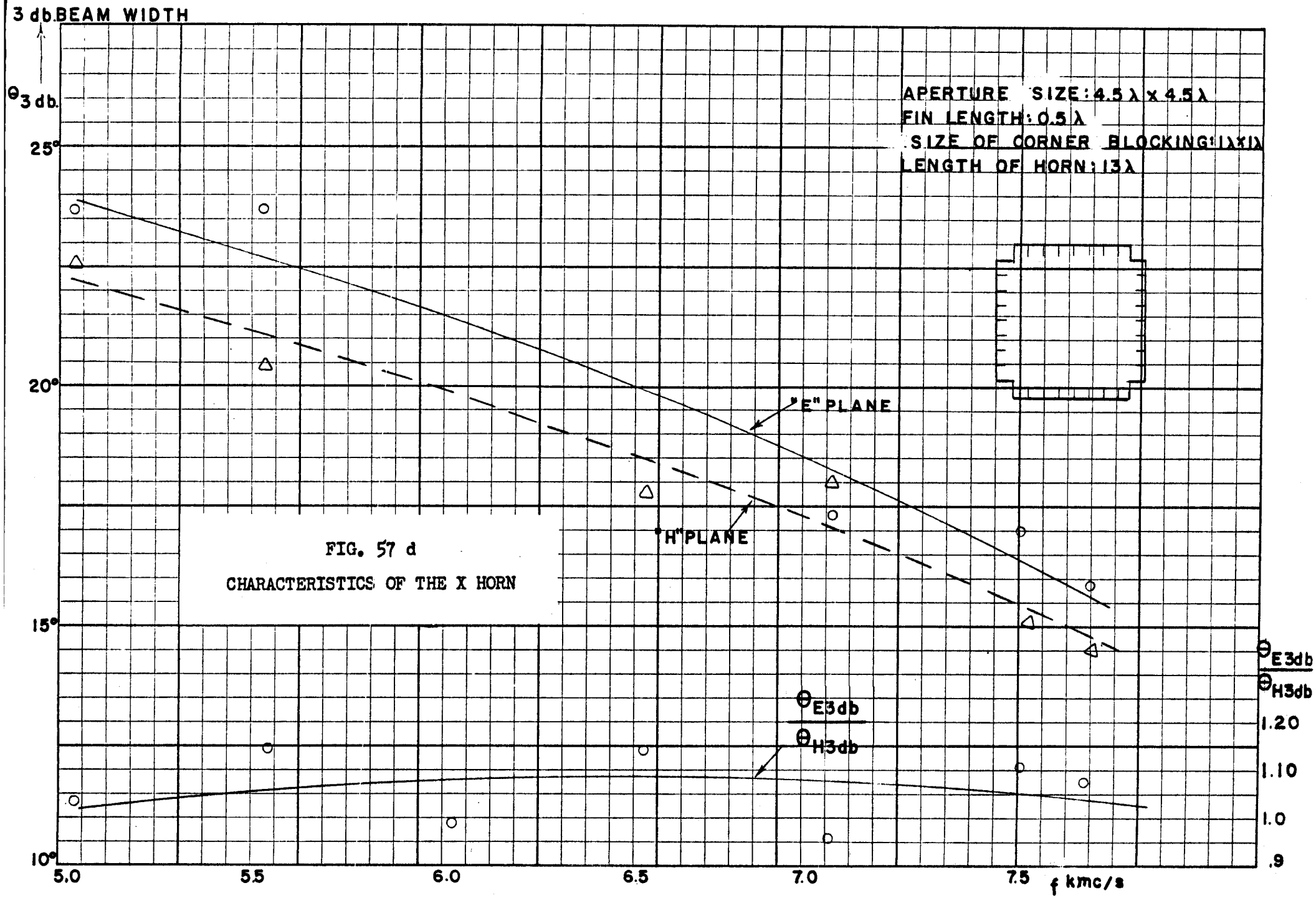

FIG. 57 d

CHARACTERISTICS OF THE X HORN

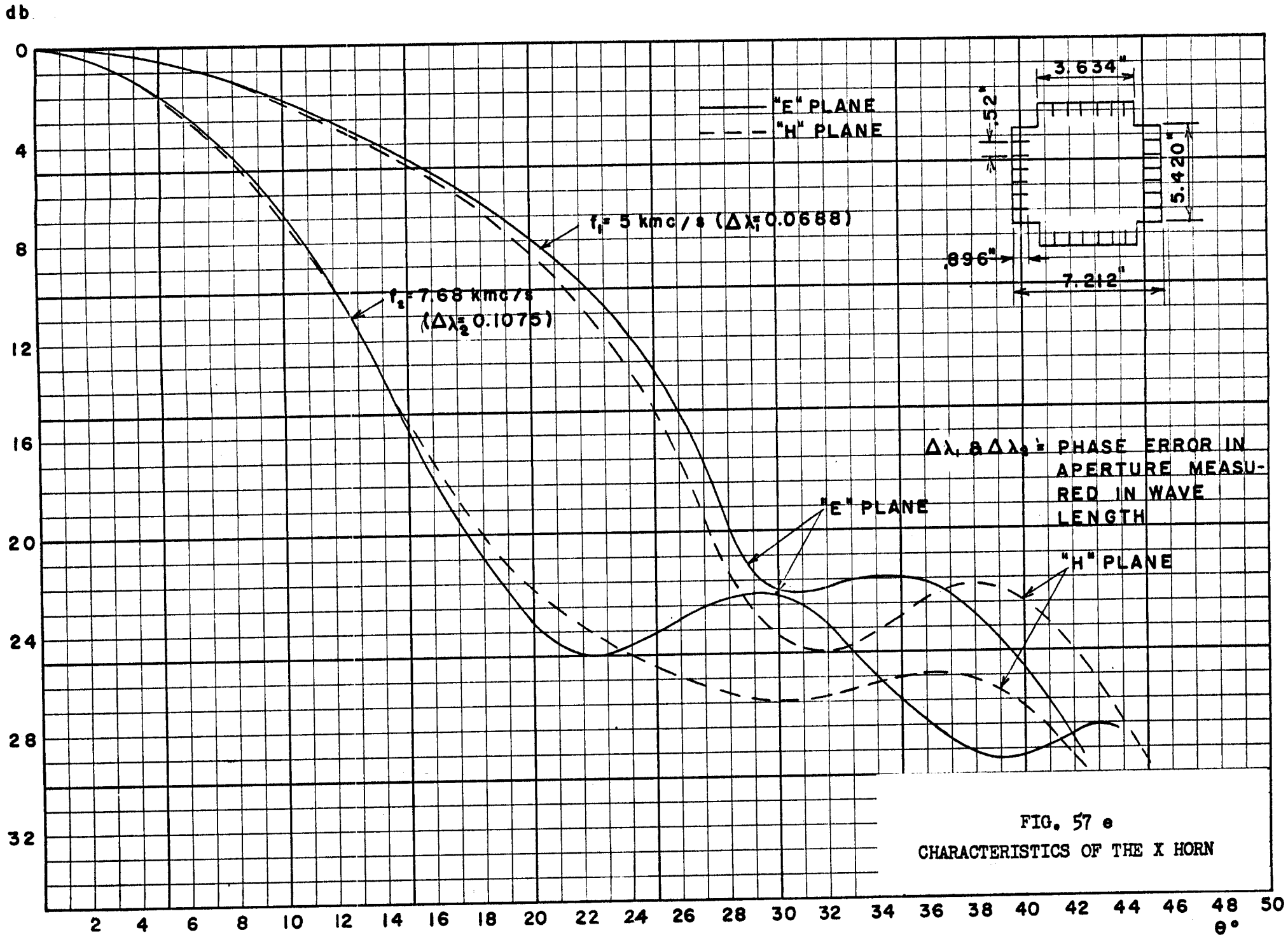

FIG. 57 e
CHARACTERISTICS OF THE X HORN

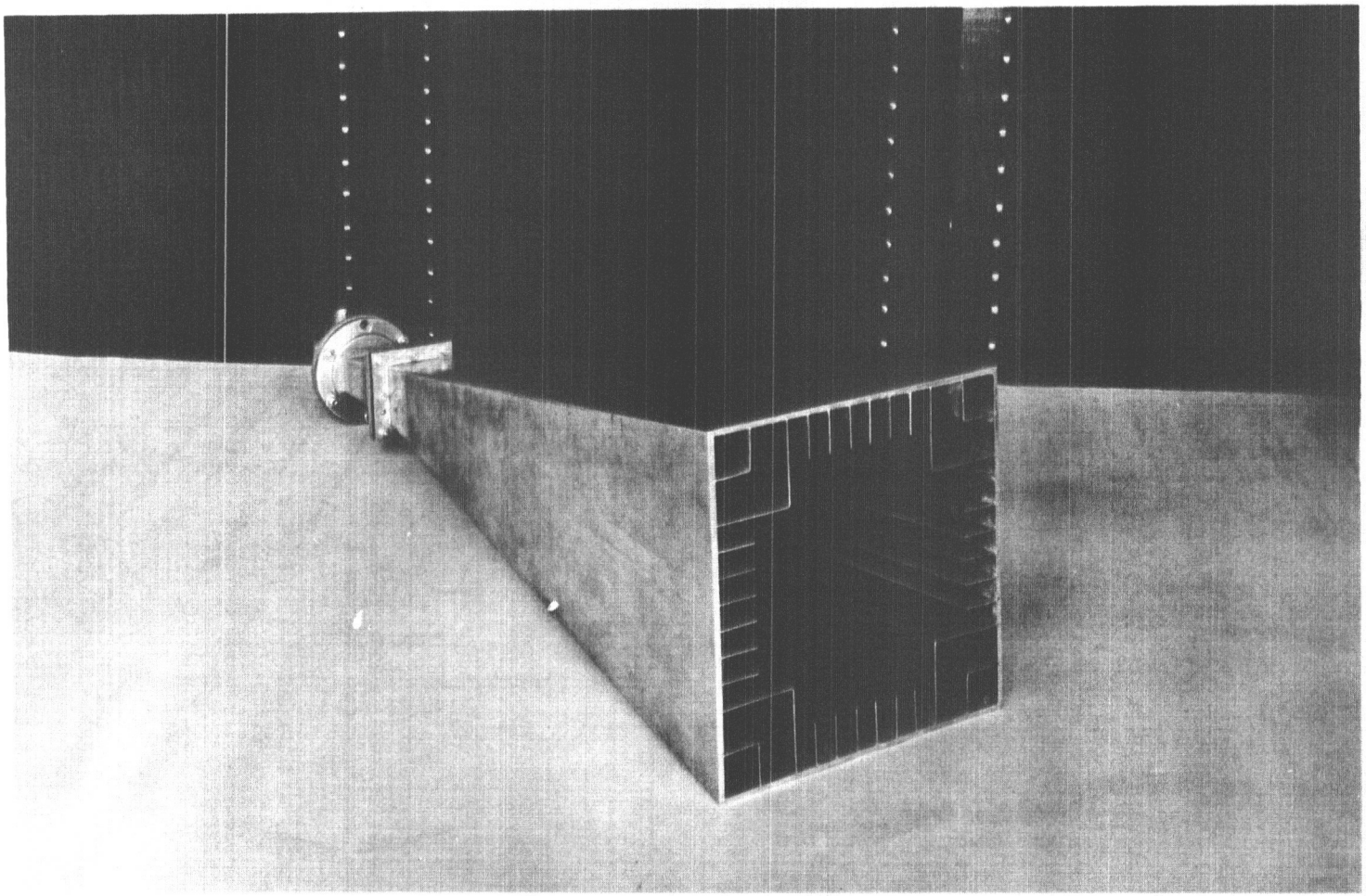

FIG. 58
PHOTOGRAPH OF THE X HORN

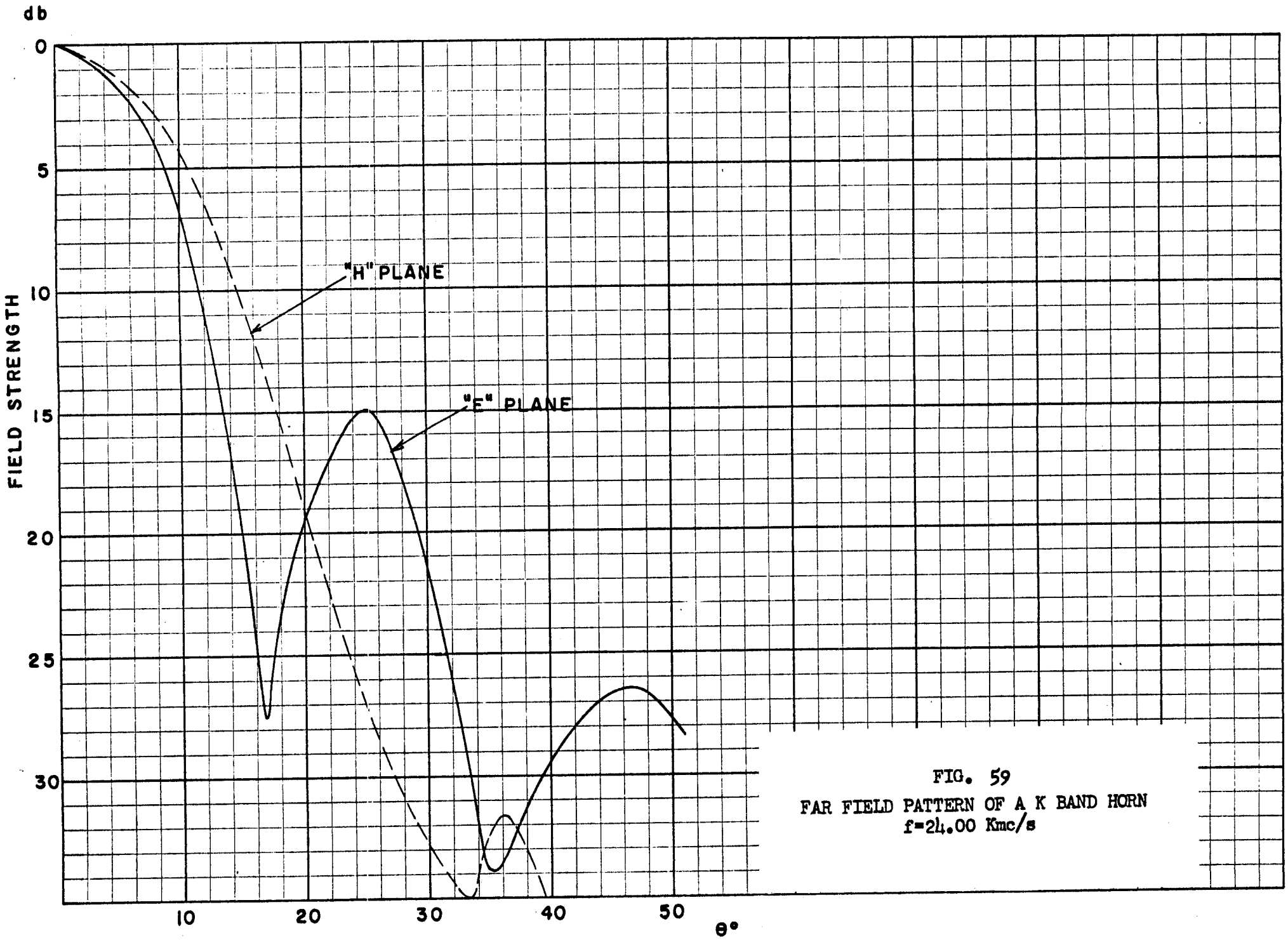

FIG. 59
FAR FIELD PATTERN OF A K BAND HORN
f=24.00 Kmc/s

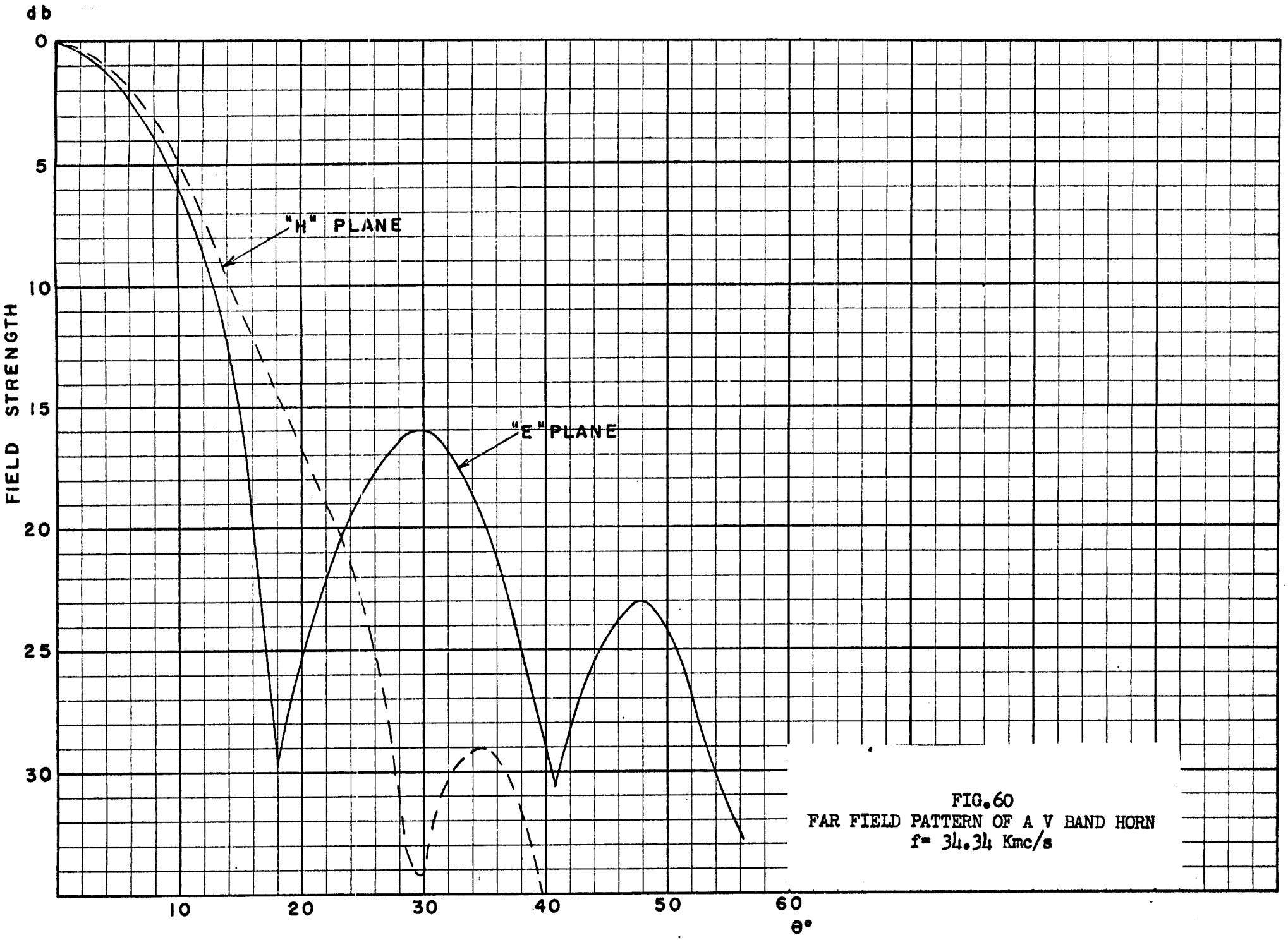

FIG. 60
FAR FIELD PATTERN OF A V BAND HORN
f= 34.34 Kmc/s

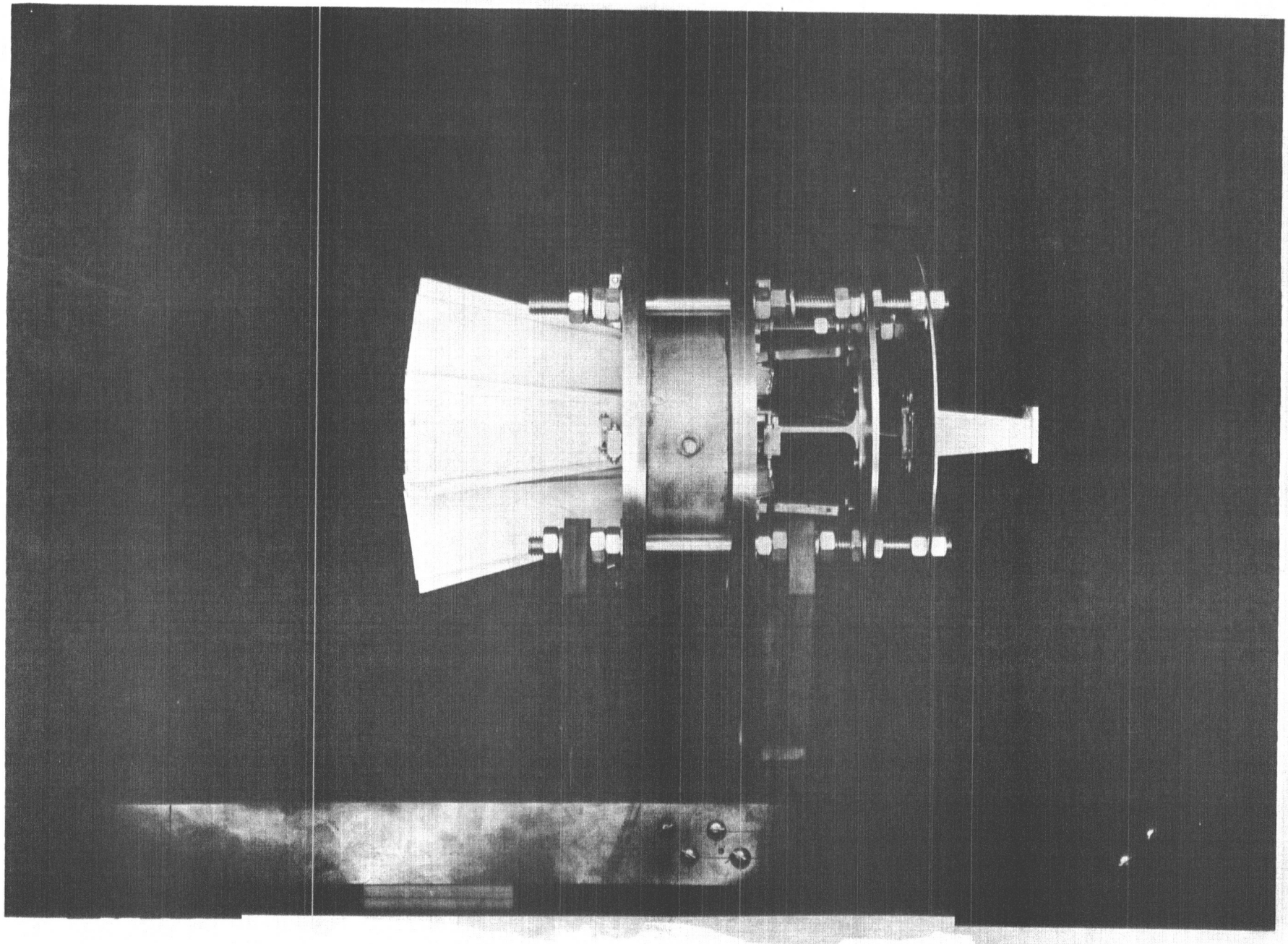

FIG. 61 a
PHOTOGRAPH OF THE ADJUSTABLE K CLUSTER

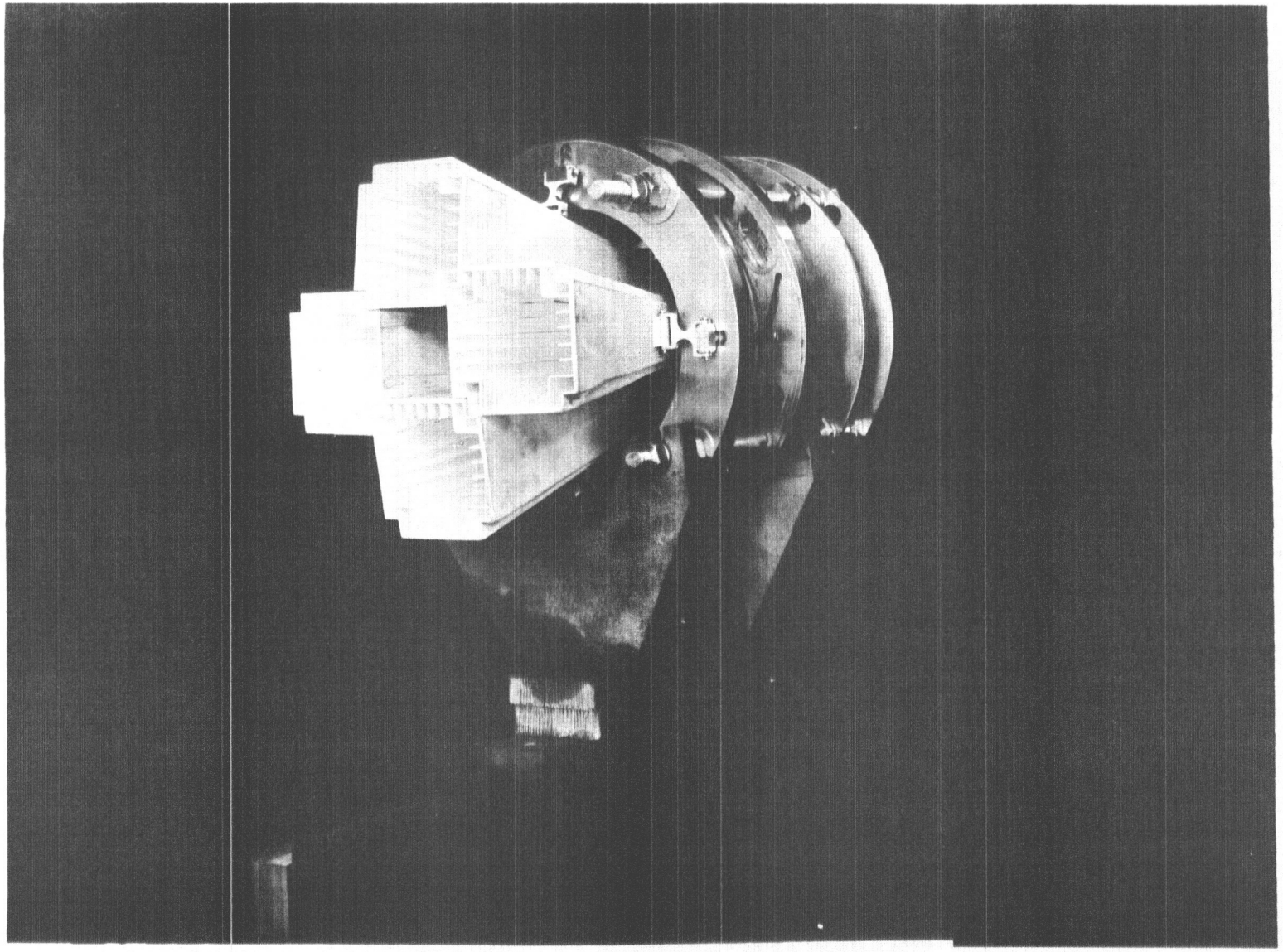

FIG. 61 b
PHOTOGRAPH OF THE ADJUSTABLE K CLUSTER

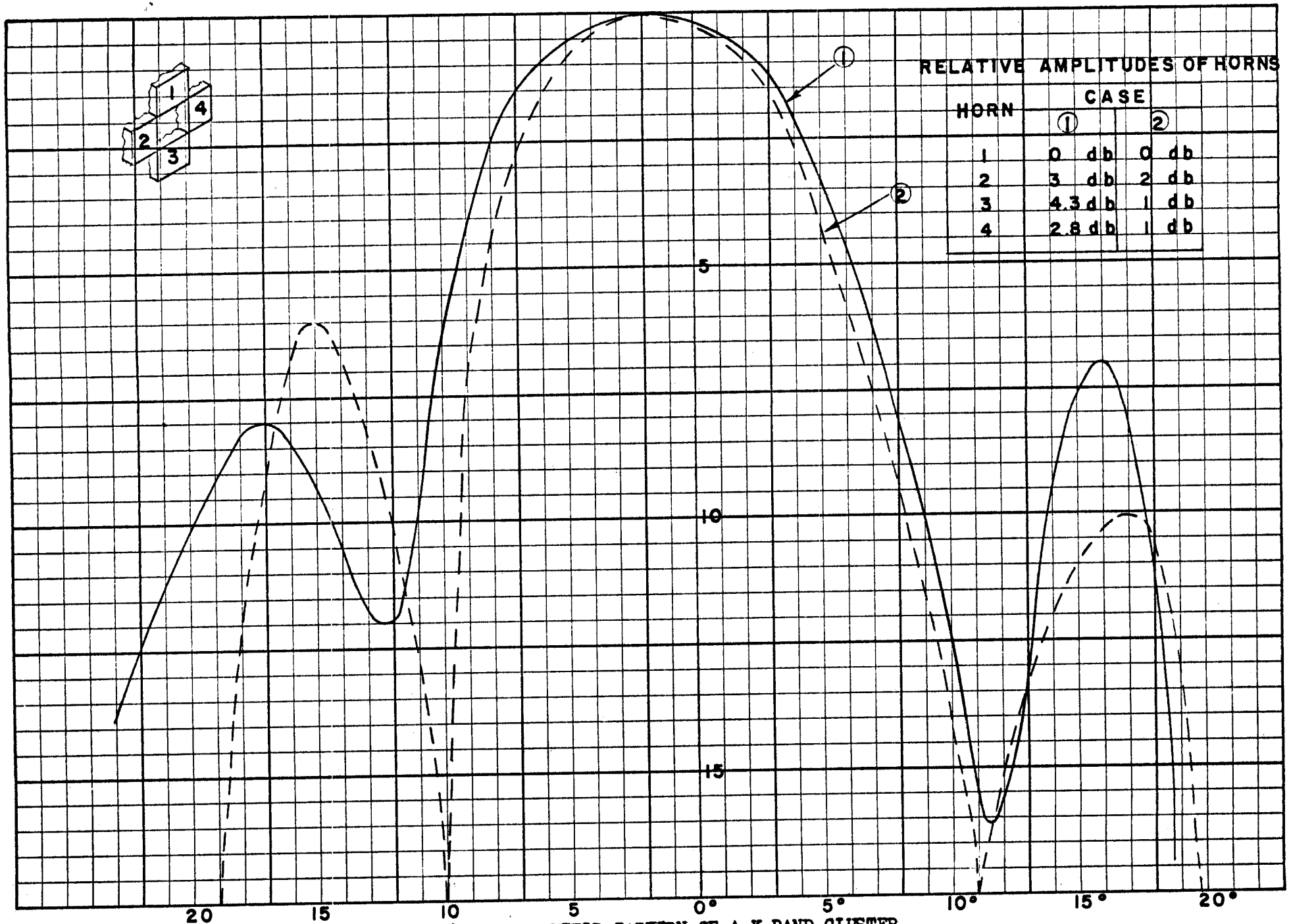

RELATIVE AMPLITUDES OF HORNS

HORN	CASE ①	CASE ②
1	0 db	0 db
2	3 db	2 db
3	4.3 db	1 db
4	2.8 db	1 db

FIG. 62 FAR FIELD PATTERN OF A K BAND CLUSTER

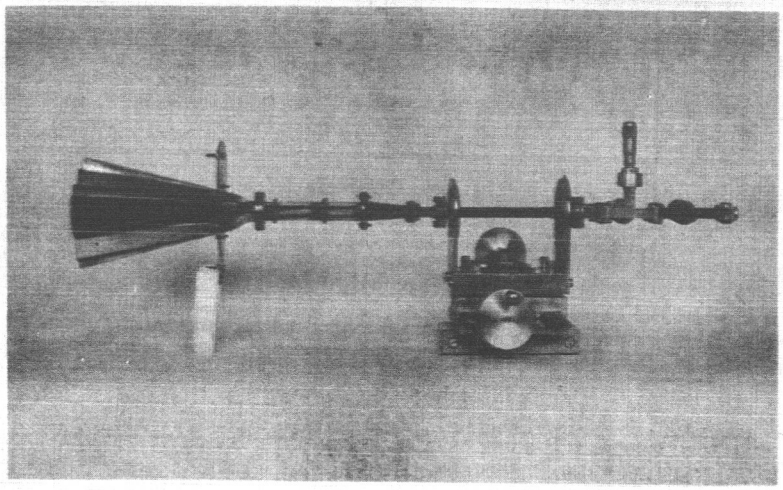

a) $\gamma = +5^{\circ}$

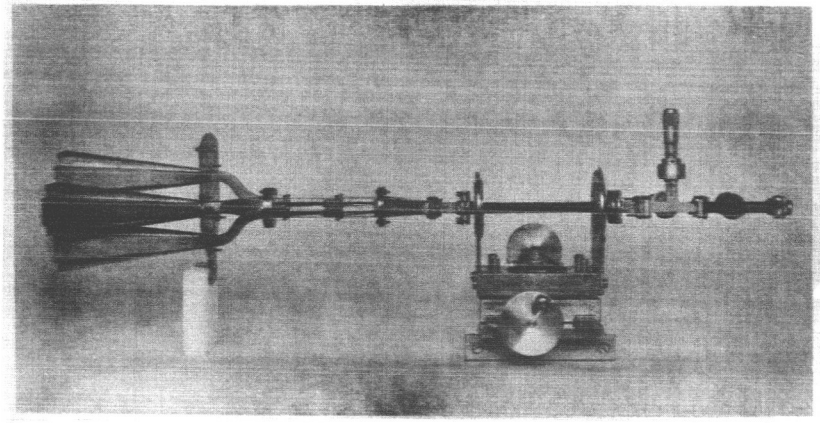

b) $\gamma = 0^{\circ}$

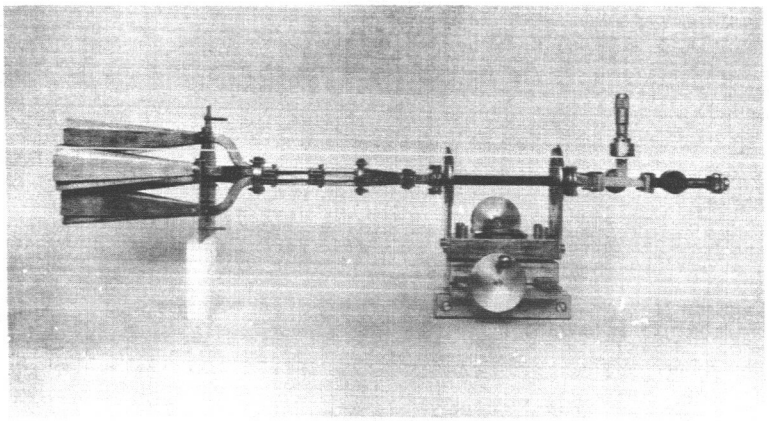

c) $\gamma = -3^{\circ}$

FIG. 63 PHOTOGRAPH OF THE V CLUSTER.

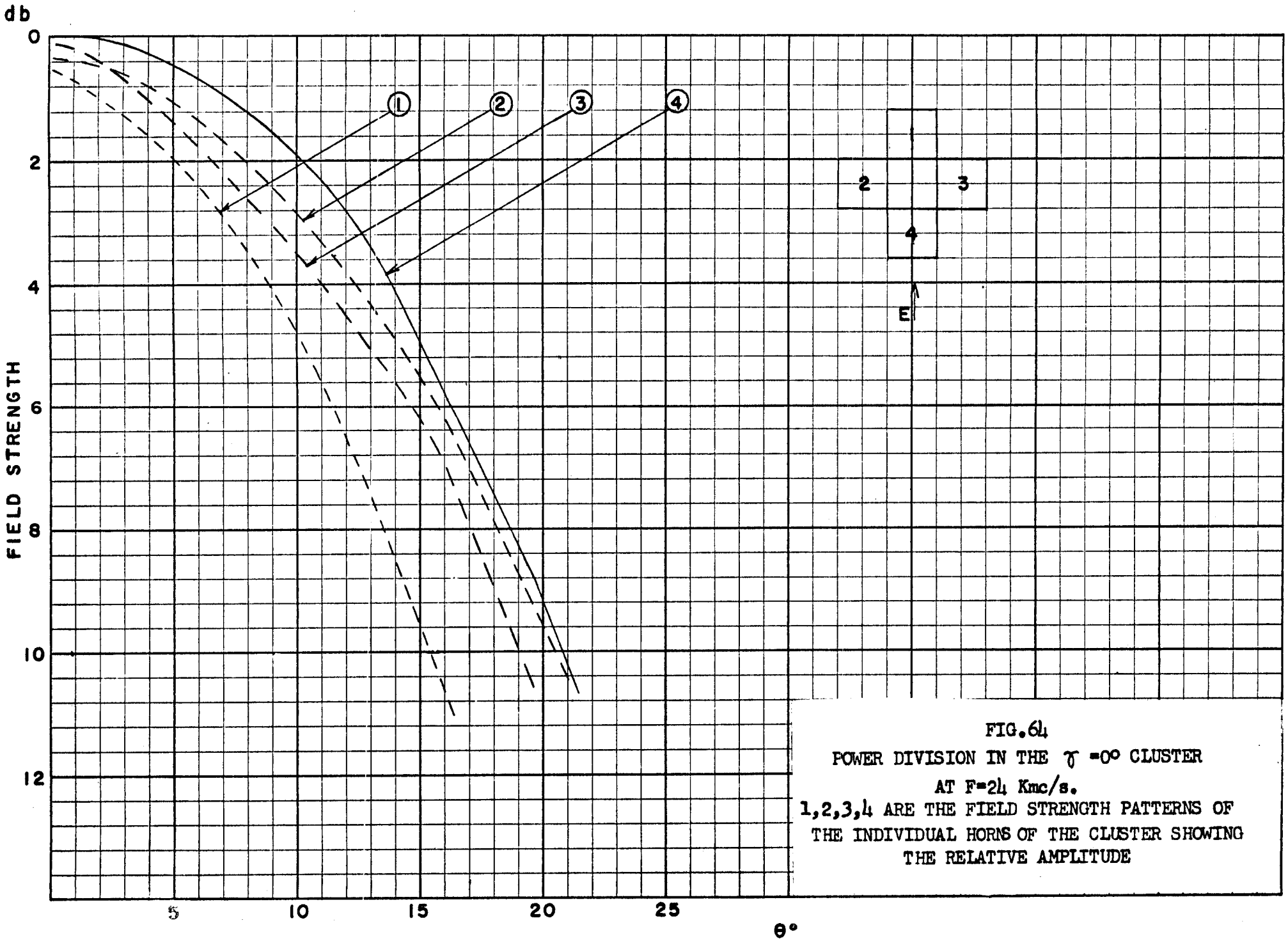

FIG. 64
POWER DIVISION IN THE $\gamma = 0°$ CLUSTER
AT F=24 Kmc/s.
1,2,3,4 ARE THE FIELD STRENGTH PATTERNS OF THE INDIVIDUAL HORNS OF THE CLUSTER SHOWING THE RELATIVE AMPLITUDE

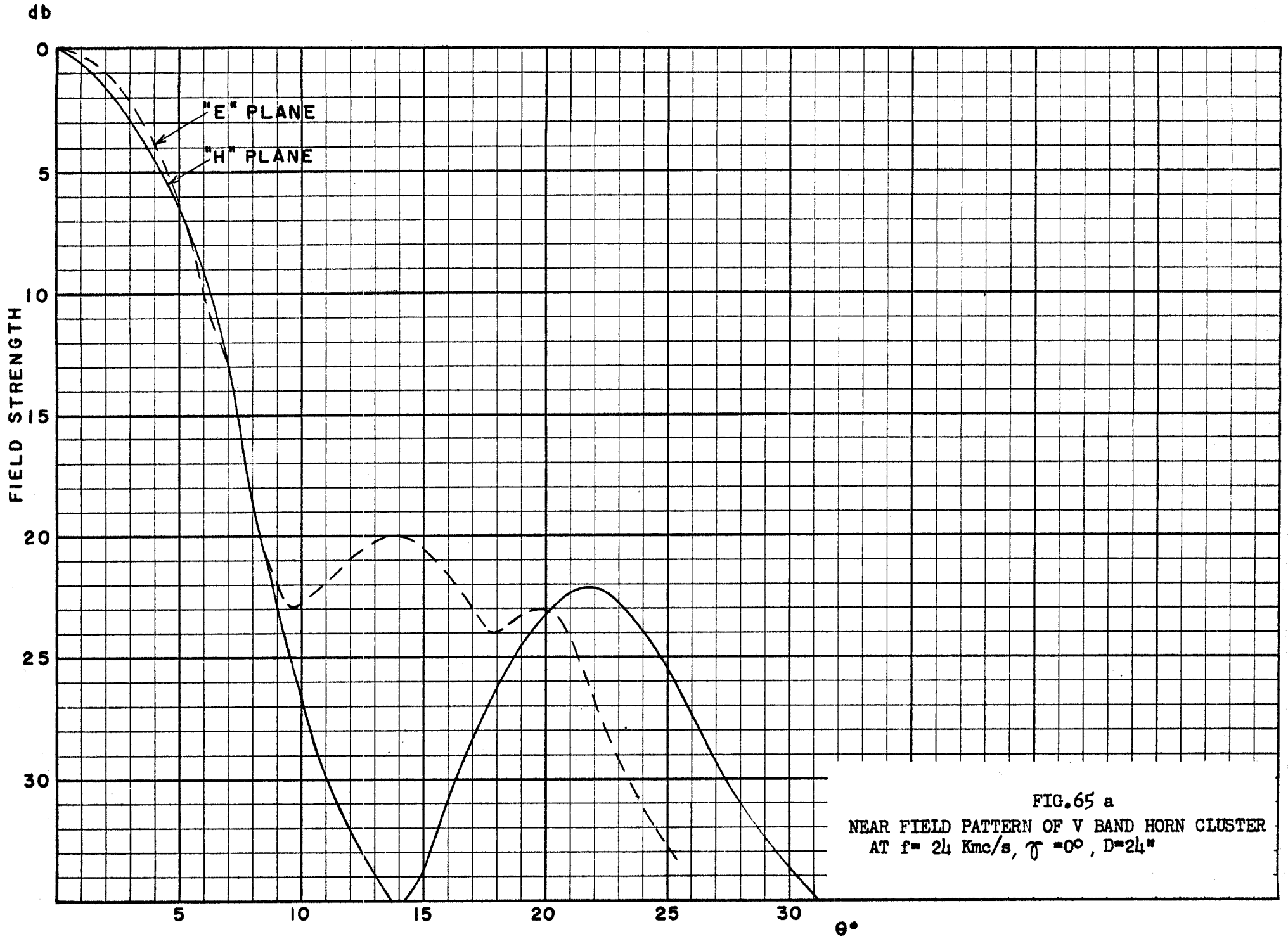

FIG. 65 a
NEAR FIELD PATTERN OF V BAND HORN CLUSTER
AT f= 24 Kmc/s, τ =0°, D=24"

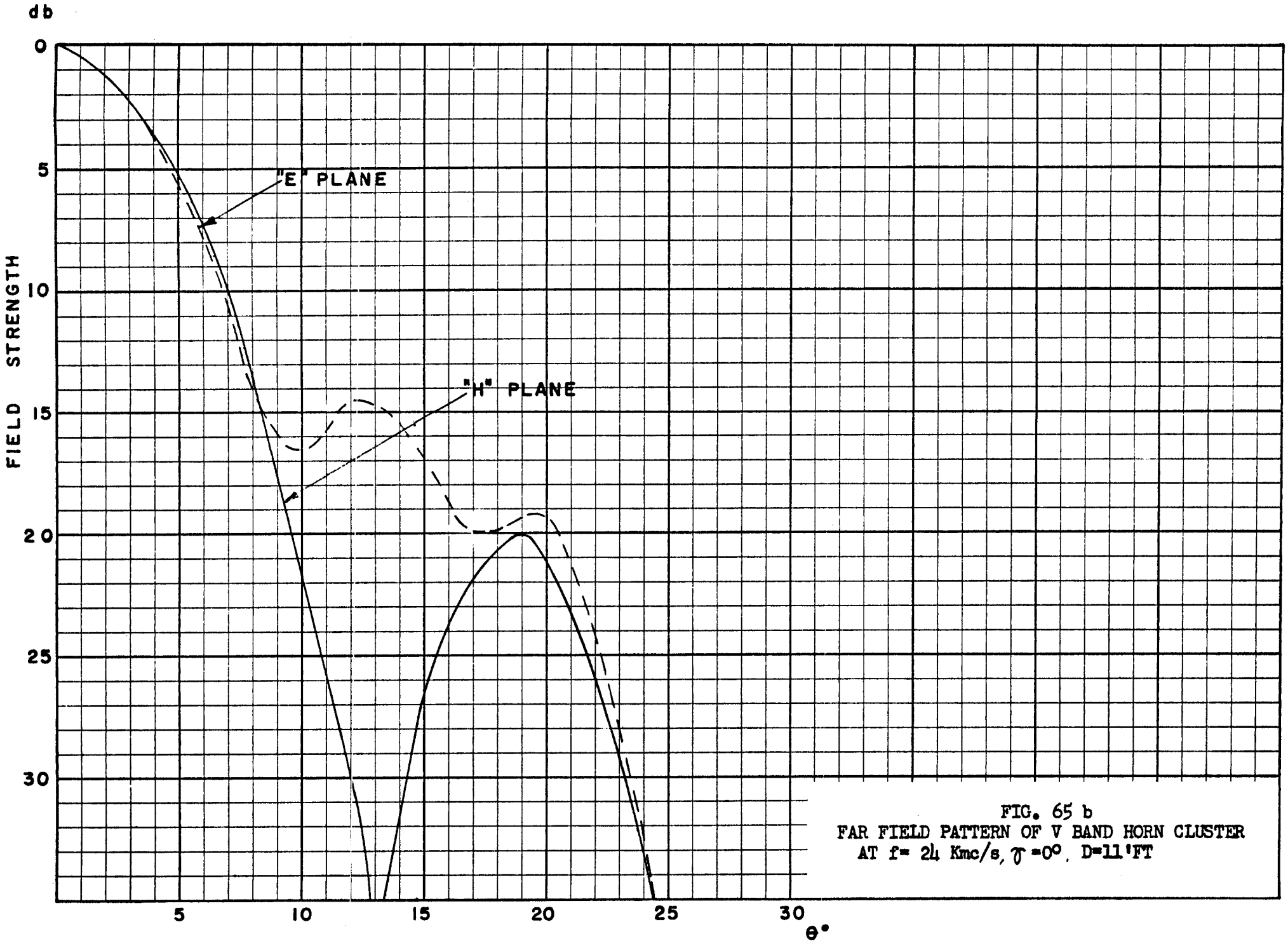

FIG. 65 b
FAR FIELD PATTERN OF V BAND HORN CLUSTER
AT f= 24 Kmc/s, γ =0°, D=11'FT

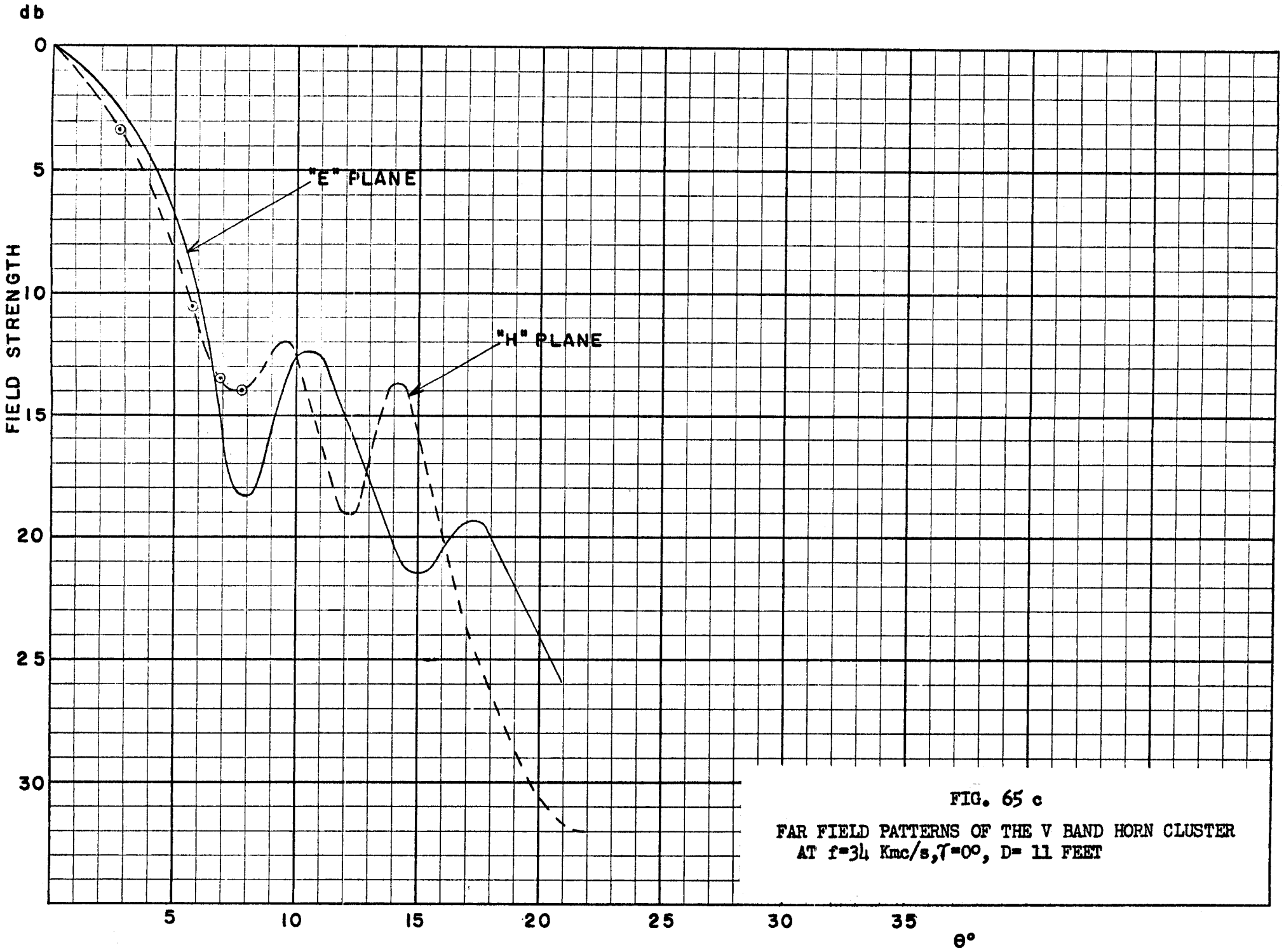

FIG. 65 c

FAR FIELD PATTERNS OF THE V BAND HORN CLUSTER
AT f=34 Kmc/s, τ=0°, D= 11 FEET

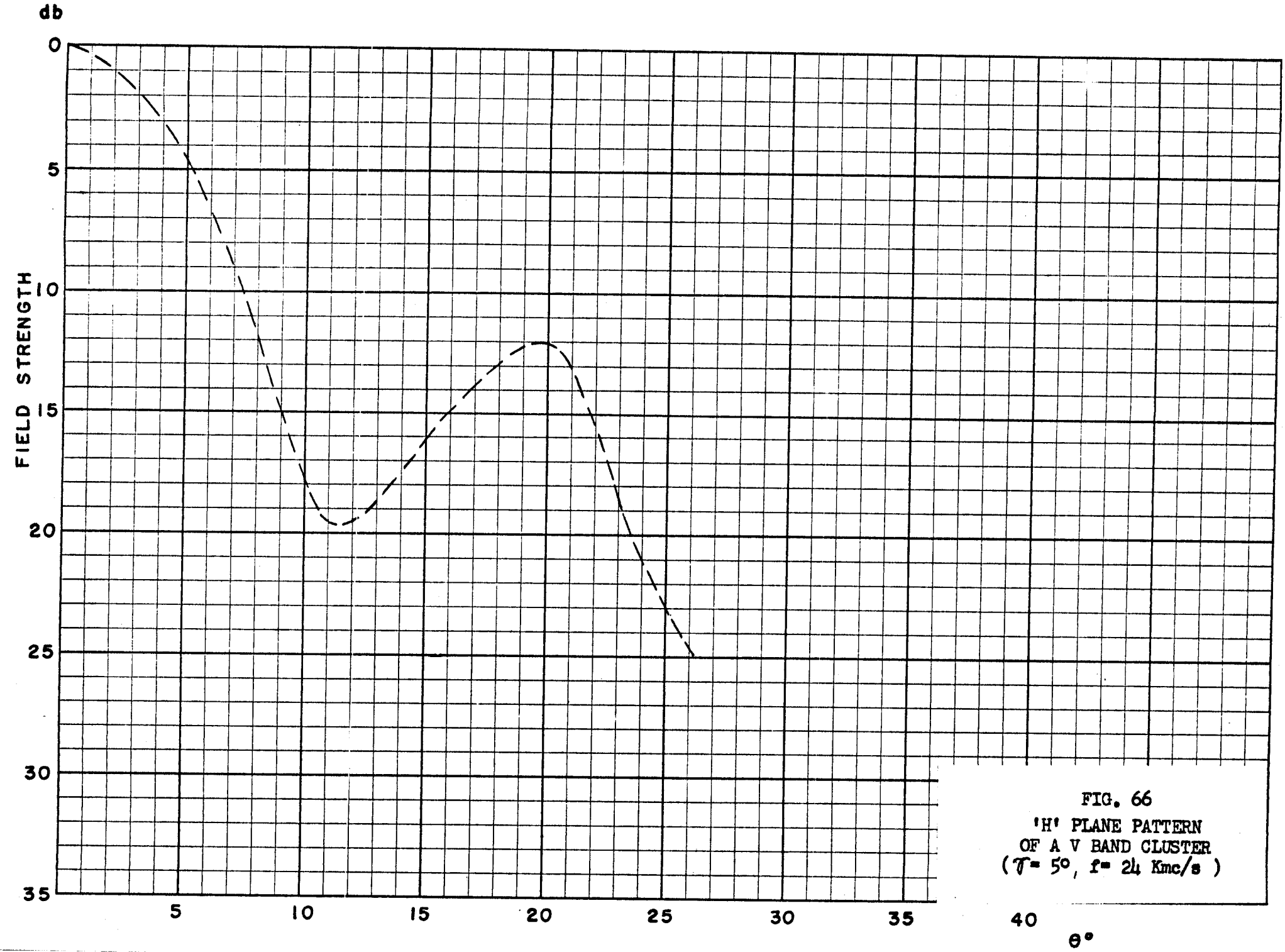

FIG. 66
'H' PLANE PATTERN
OF A V BAND CLUSTER
(τ = 5°, f = 24 Kmc/s)

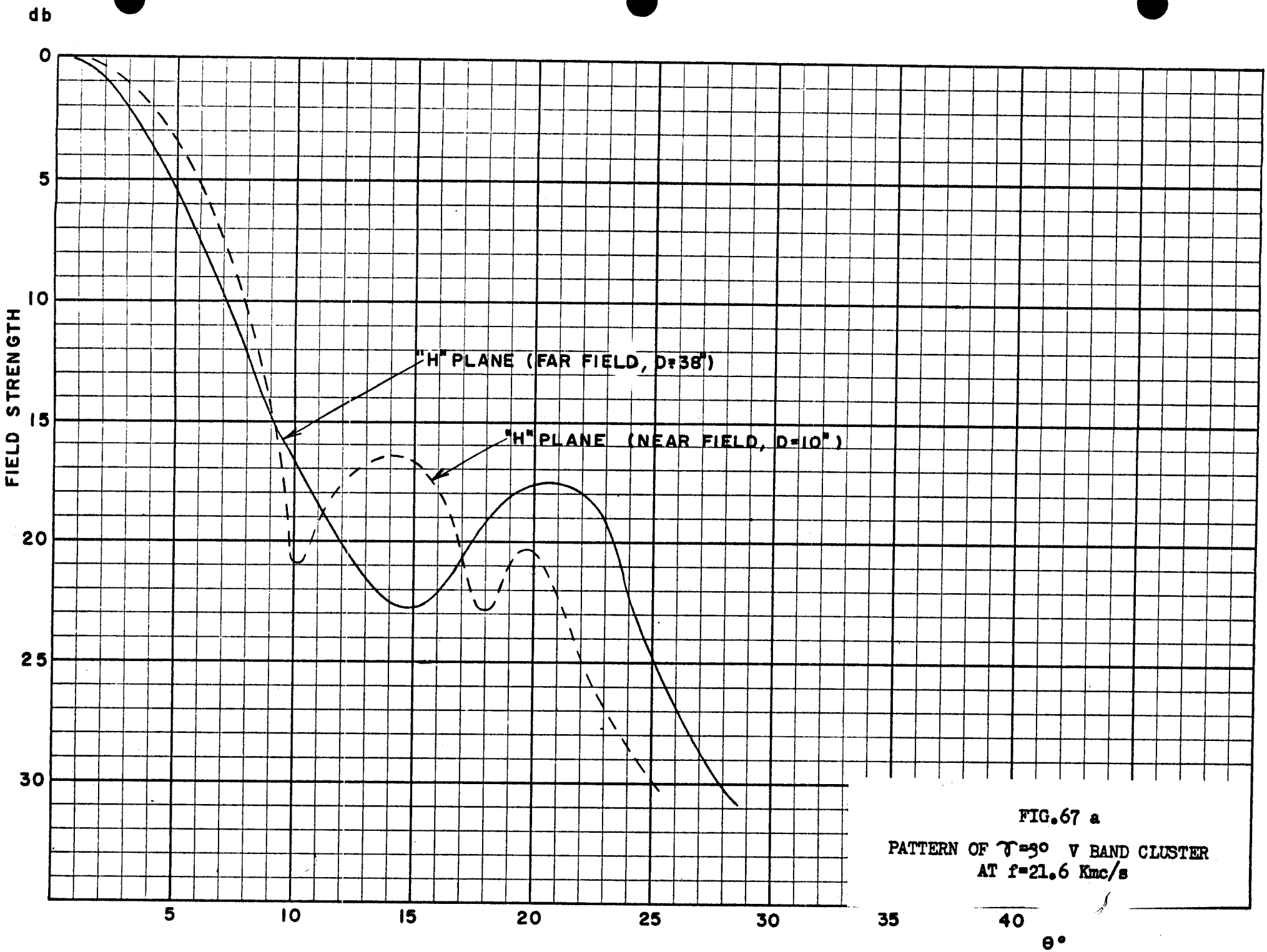

FIG. 67 a

PATTERN OF τ=3° V BAND CLUSTER
AT f=21.6 Kmc/s

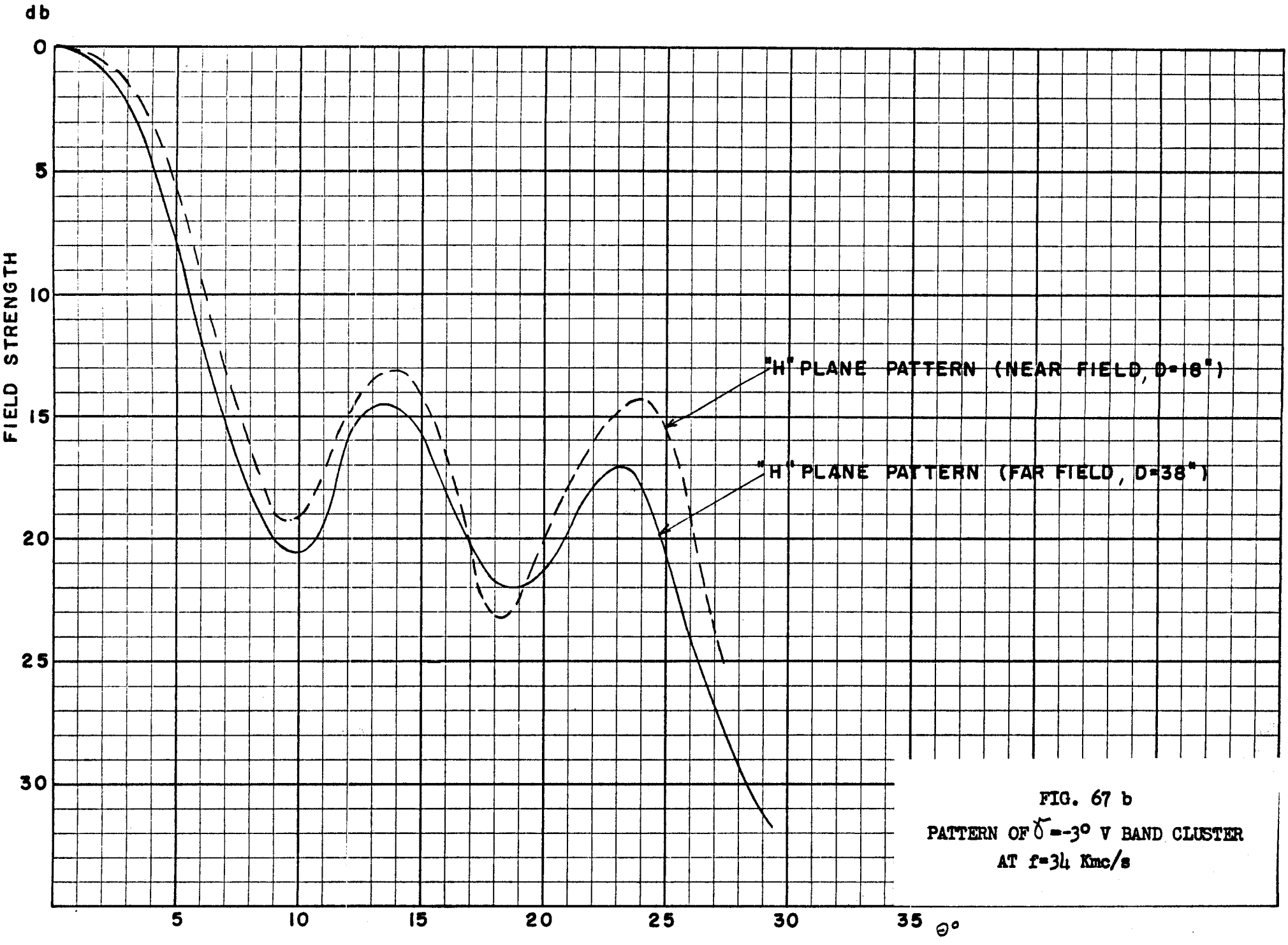

FIG. 67 b

PATTERN OF δ=-3° V BAND CLUSTER

AT f=34 Kmc/s

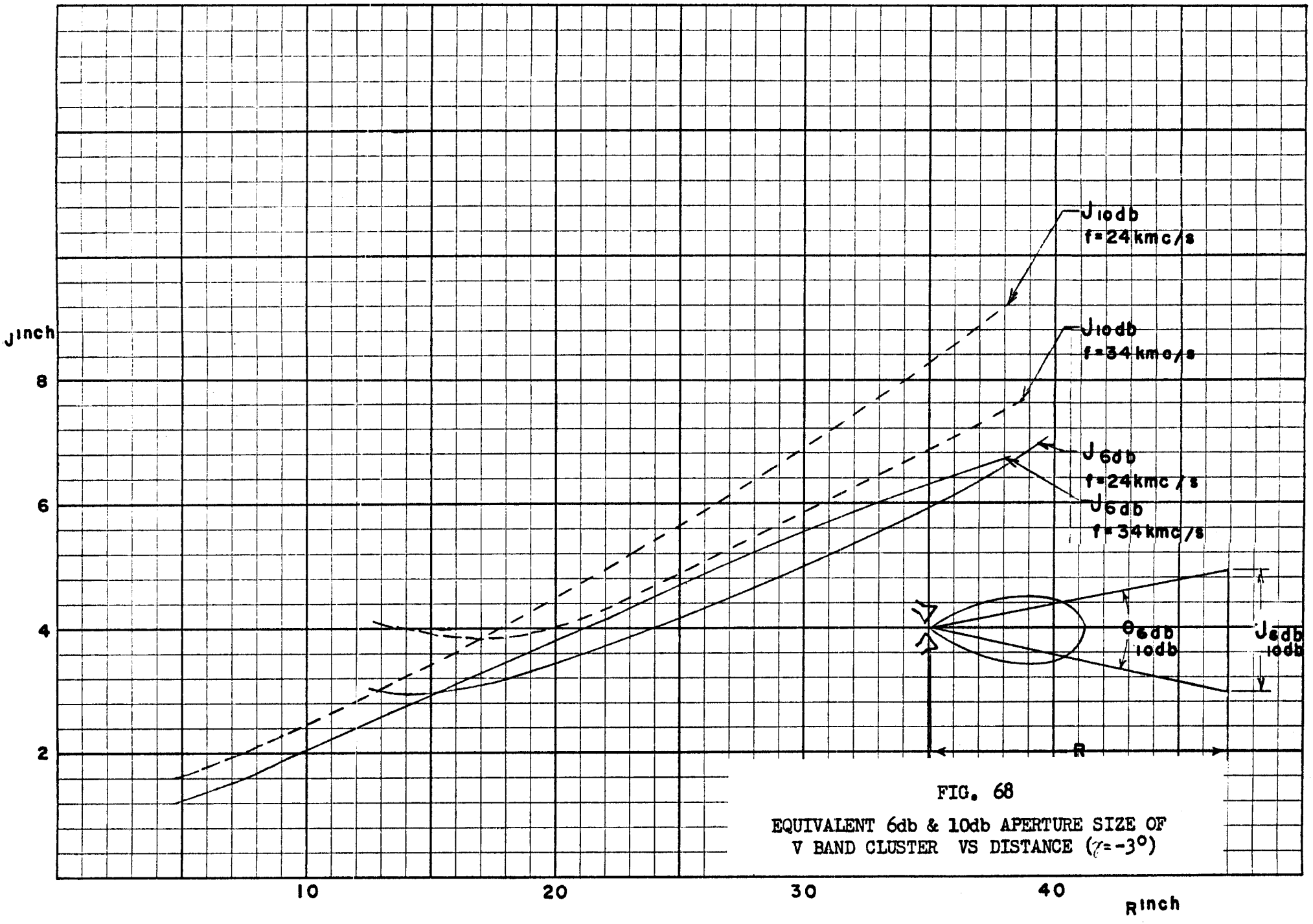

FIG. 68

EQUIVALENT 6db & 10db APERTURE SIZE OF V BAND CLUSTER VS DISTANCE ($\gamma = -3^{\circ}$)

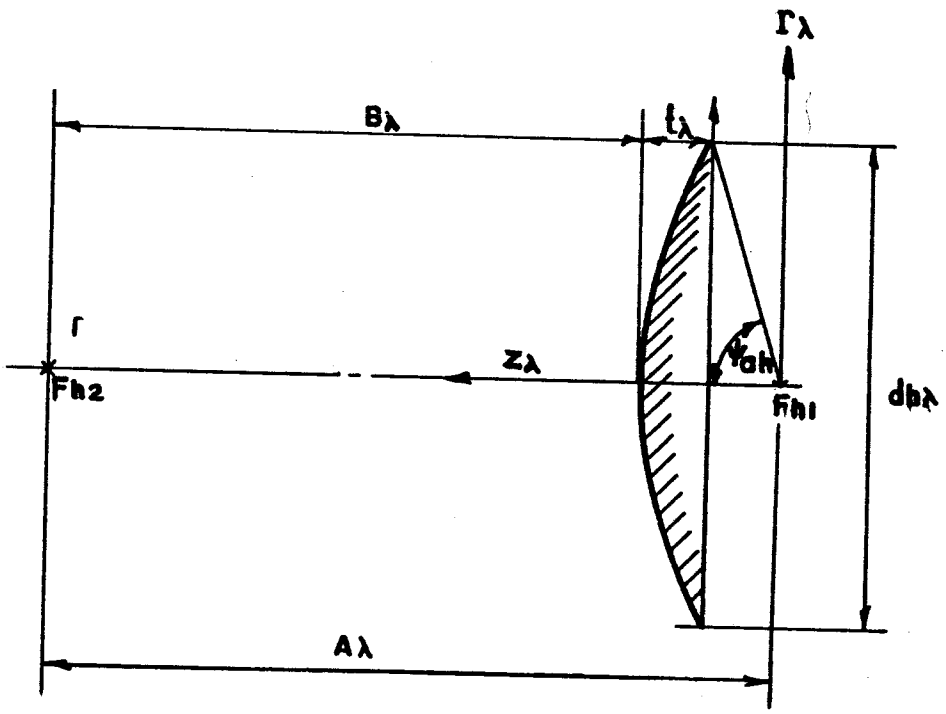

FIG. 69

DEFINITION OF HYPERBOLOID COORDINATES

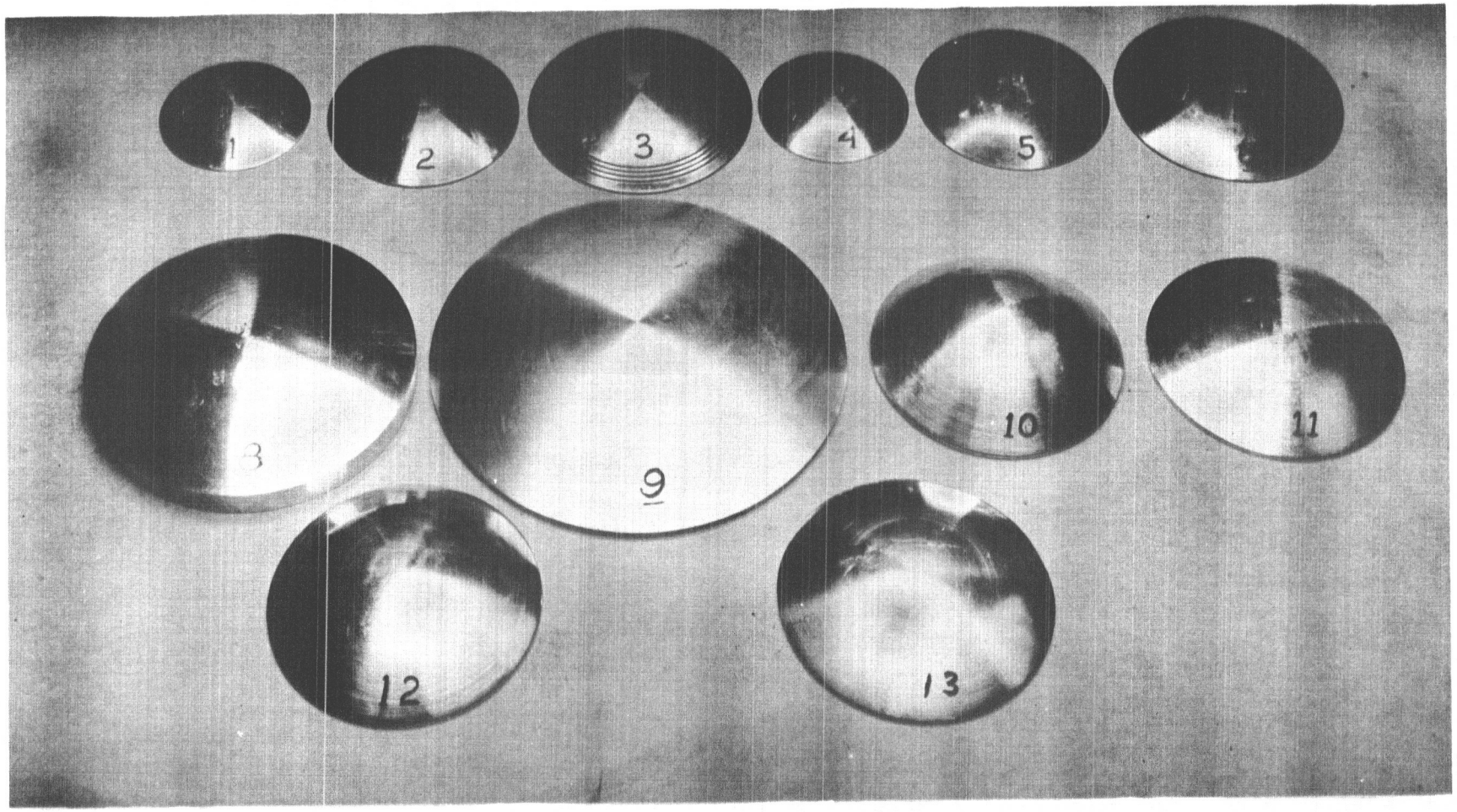

FIG. 70 PHOTOGRAPH OF REFLECTORS

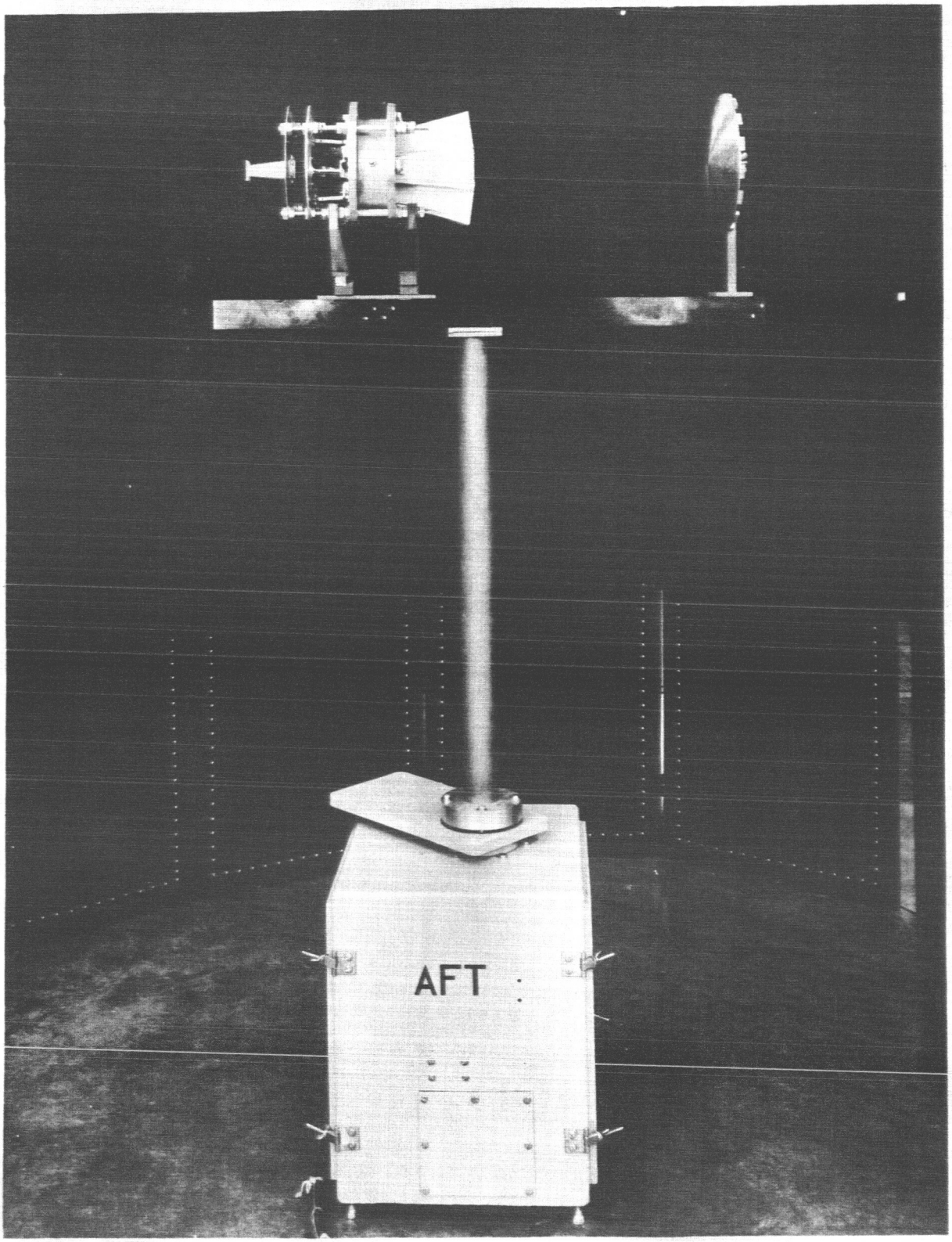

FIG. 71
ARRANGEMENT FOR EDGE CURRENT CONTROL

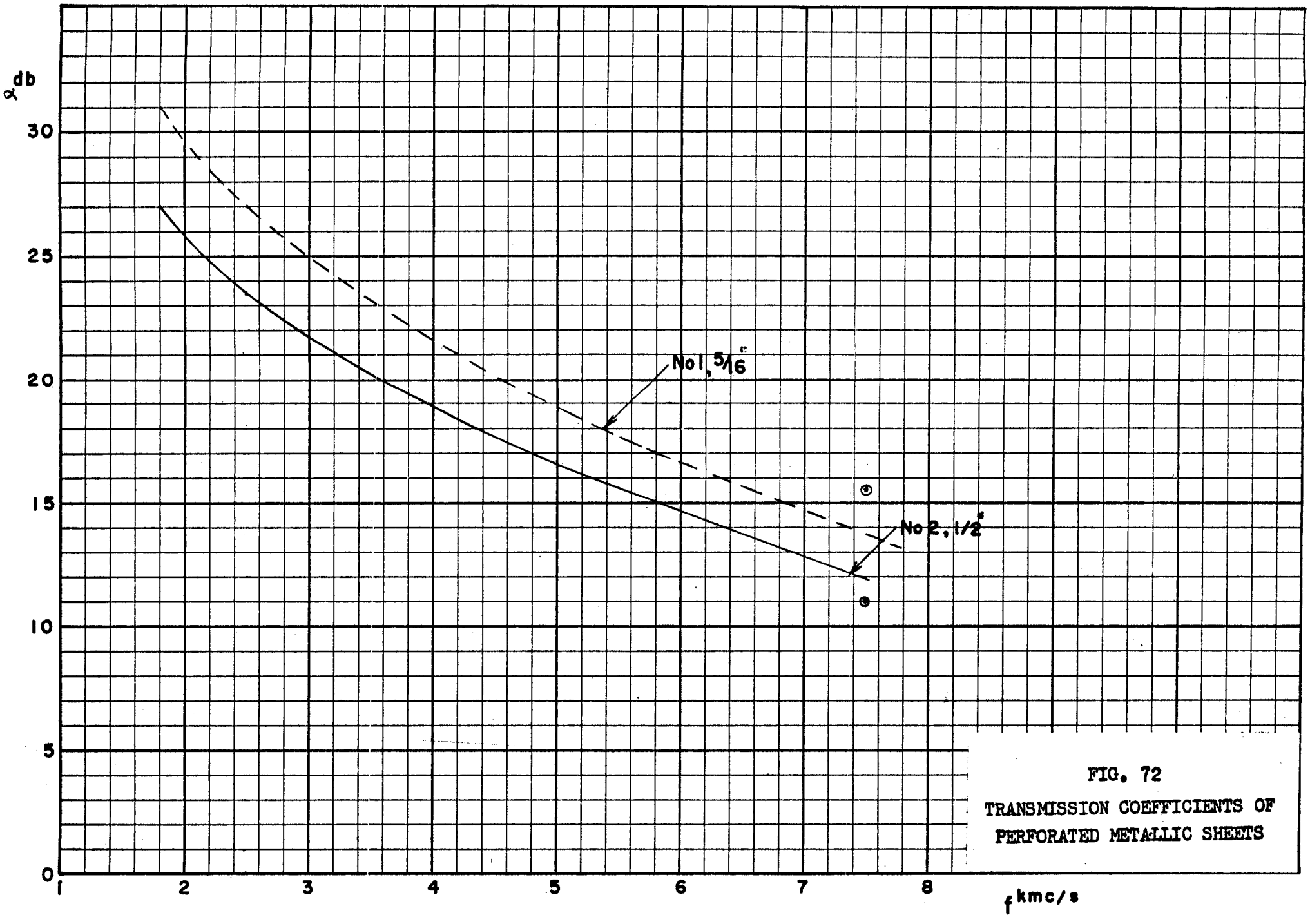

FIG. 72

TRANSMISSION COEFFICIENTS OF PERFORATED METALLIC SHEETS

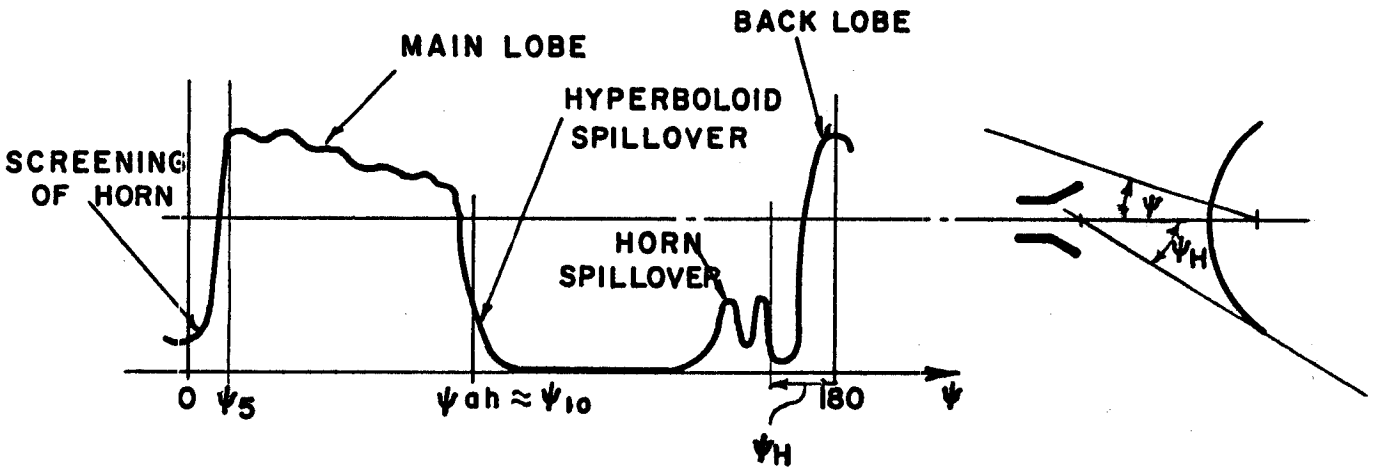

FIG. 73

CHARACTERISTIC REGIONS OF FEED SYSTEM PATTERNS

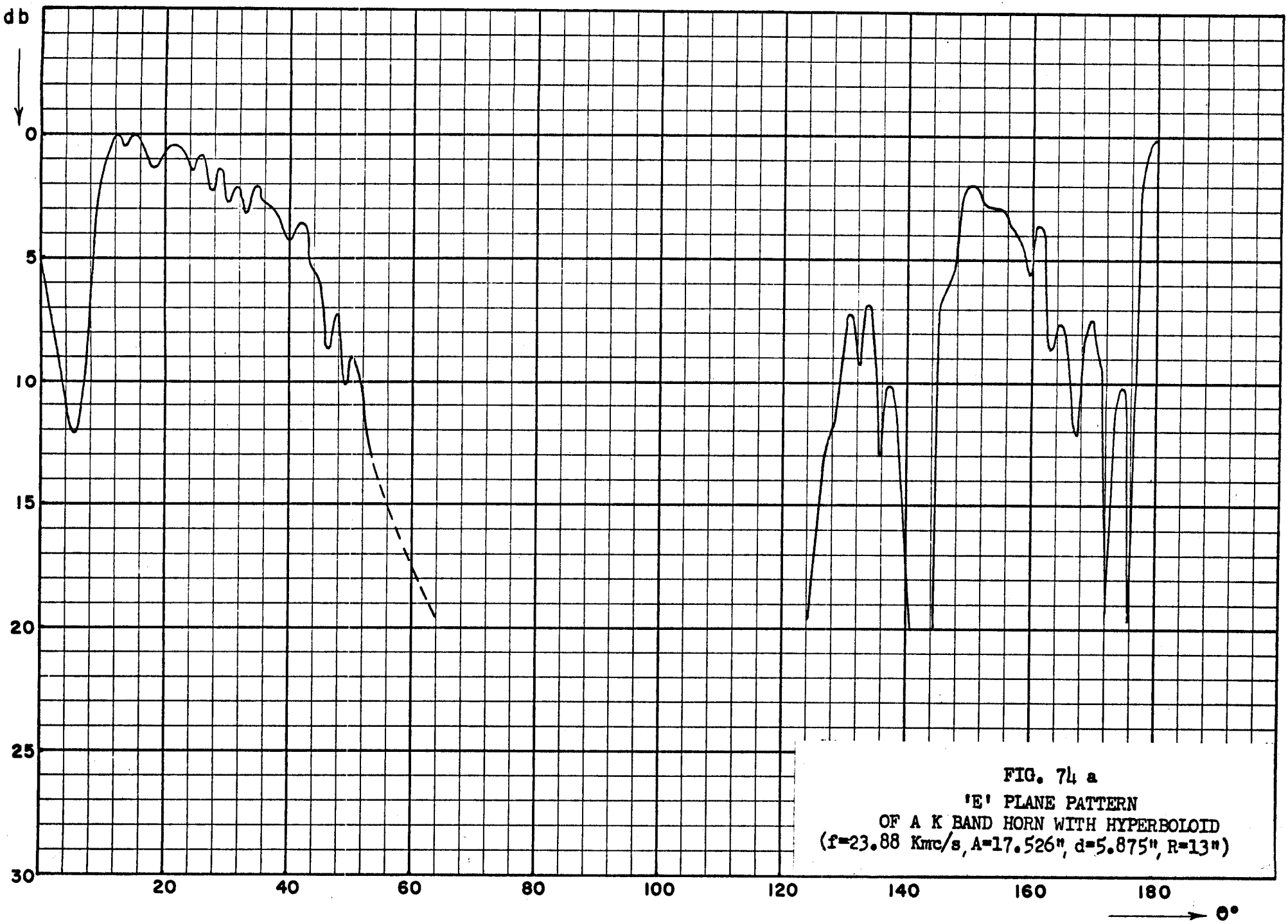

FIG. 74 a
'E' PLANE PATTERN
OF A K BAND HORN WITH HYPERBOLOID
(f=23.88 Kmc/s, A=17.526", d=5.875", R=13")

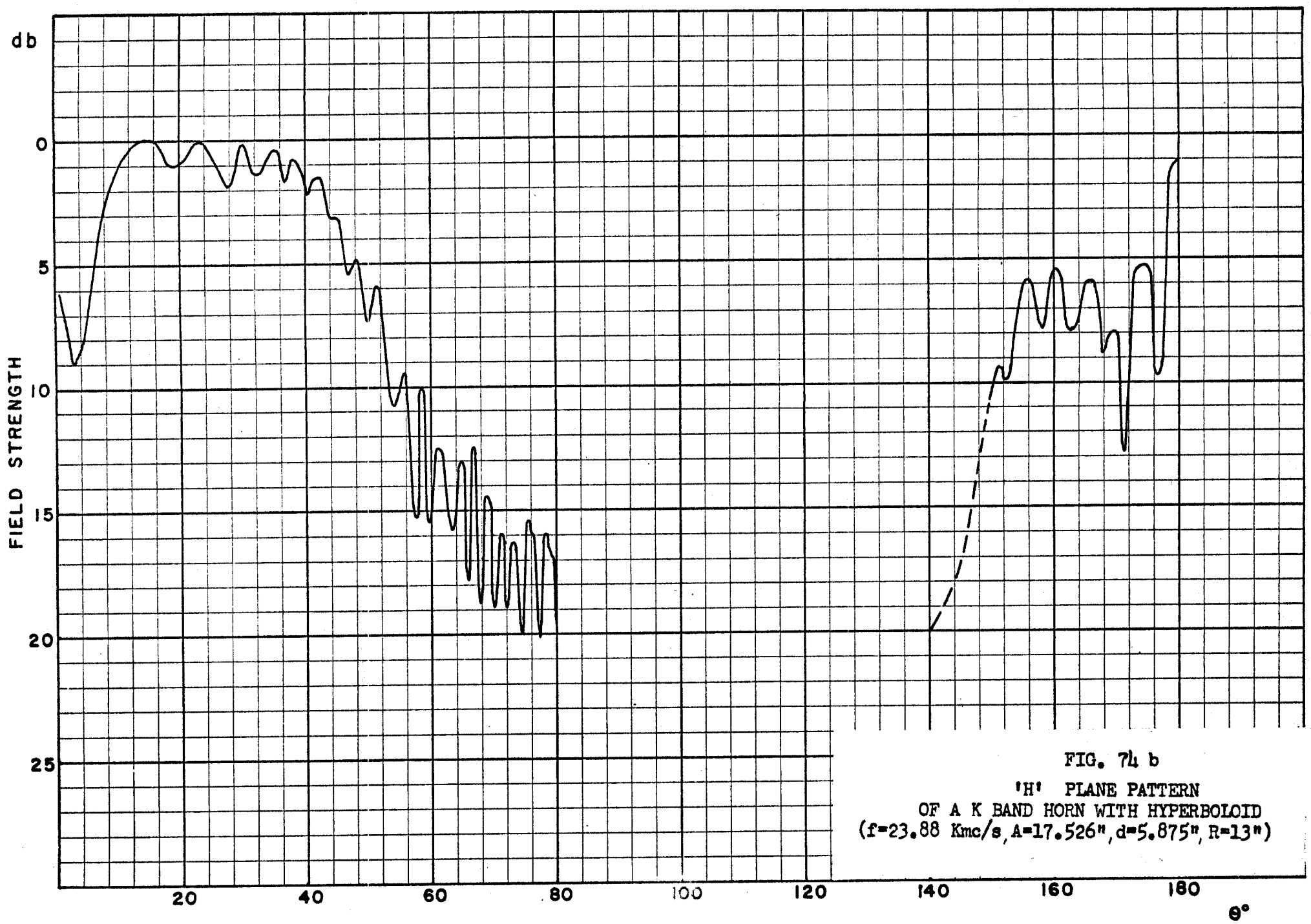

FIG. 74 b

'H' PLANE PATTERN
OF A K BAND HORN WITH HYPERBOLOID
(f=23.88 Kmc/s, A=17.526", d=5.875", R=13")

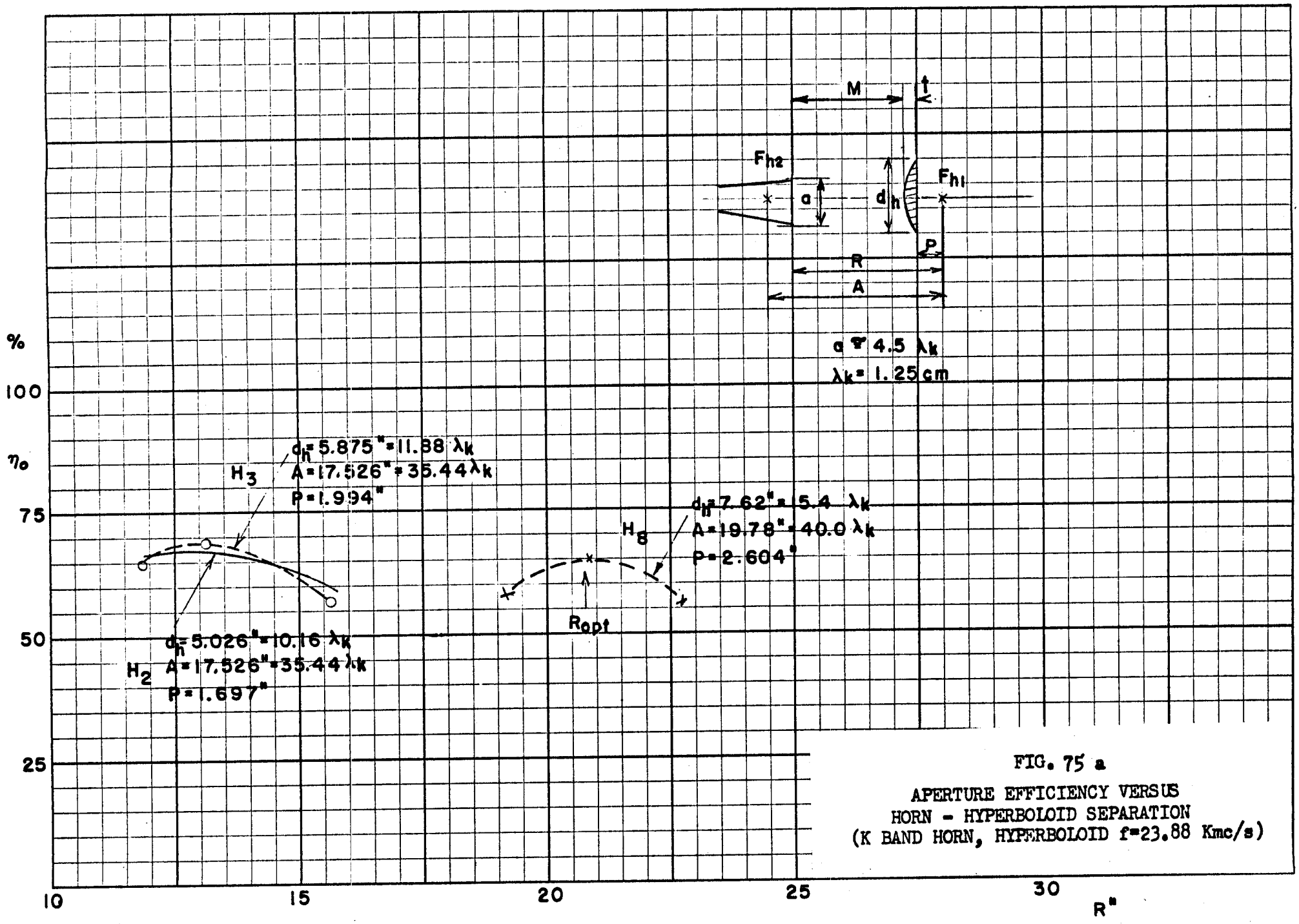

FIG. 75 a

APERTURE EFFICIENCY VERSUS
HORN - HYPERBOLOID SEPARATION
(K BAND HORN, HYPERBOLOID f=23.88 Kmc/s)

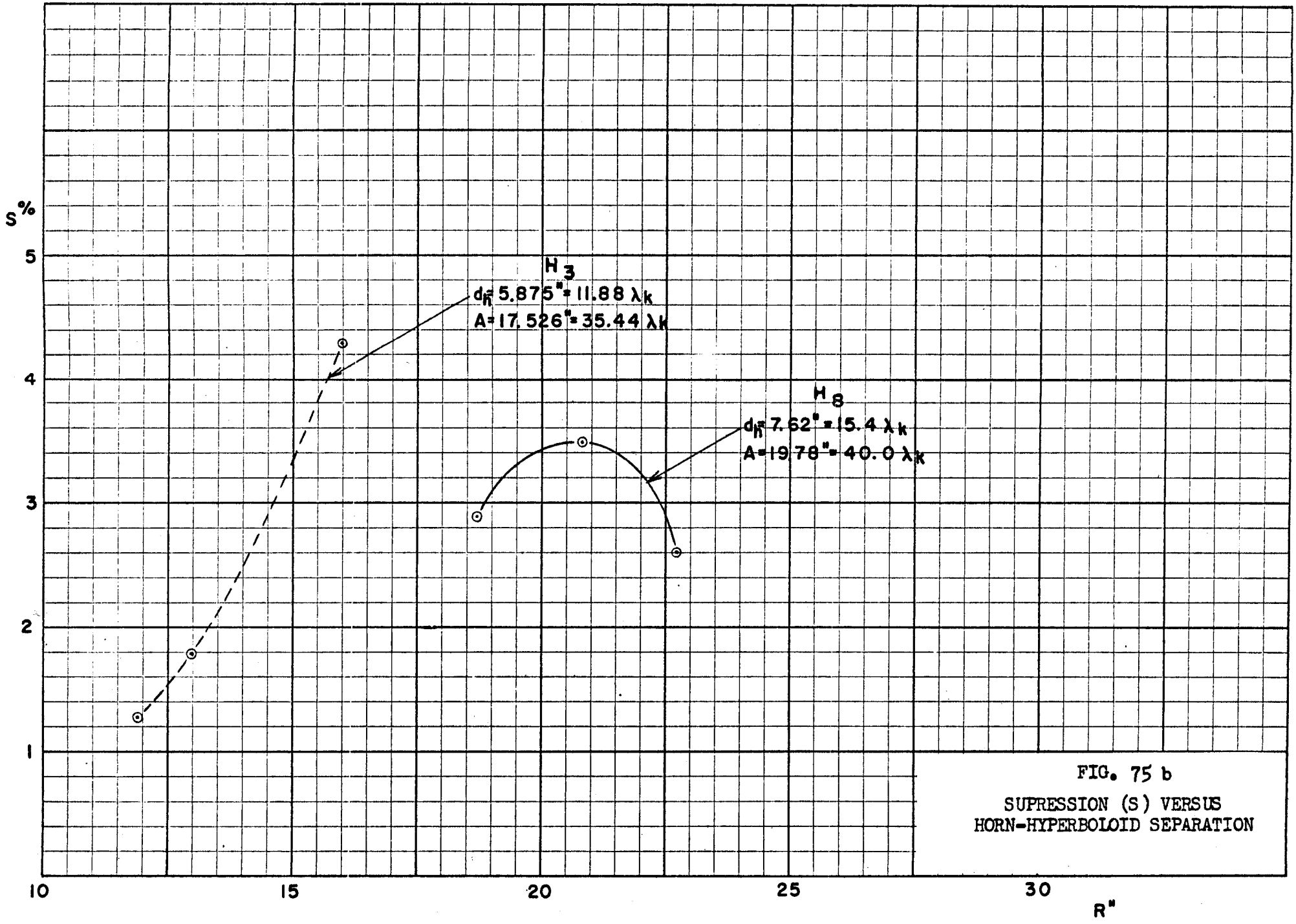

FIG. 75 b

SUPRESSION (S) VERSUS
HORN-HYPERBOLOID SEPARATION

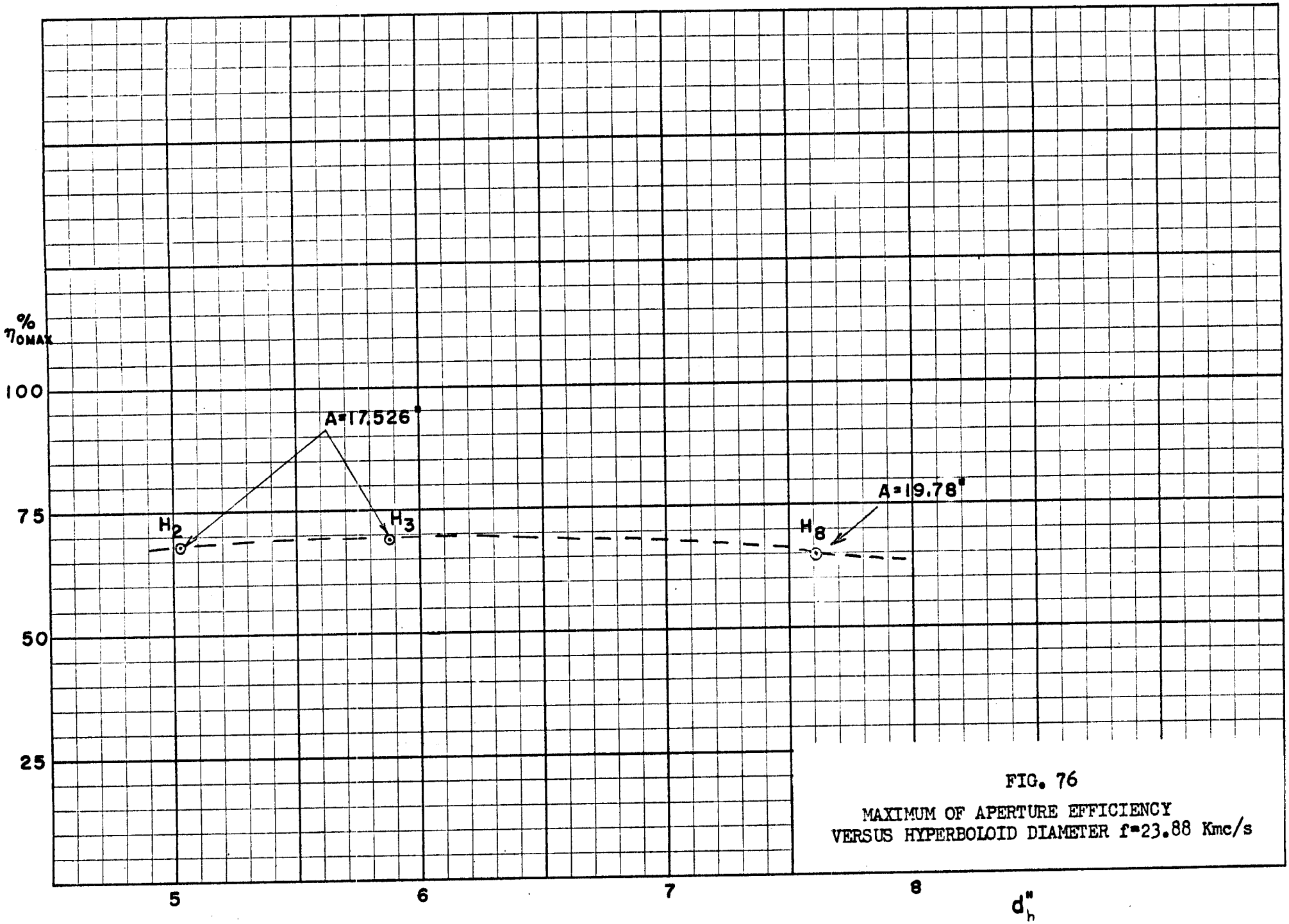

FIG. 76

MAXIMUM OF APERTURE EFFICIENCY
VERSUS HYPERBOLOID DIAMETER f=23.88 Kmc/s

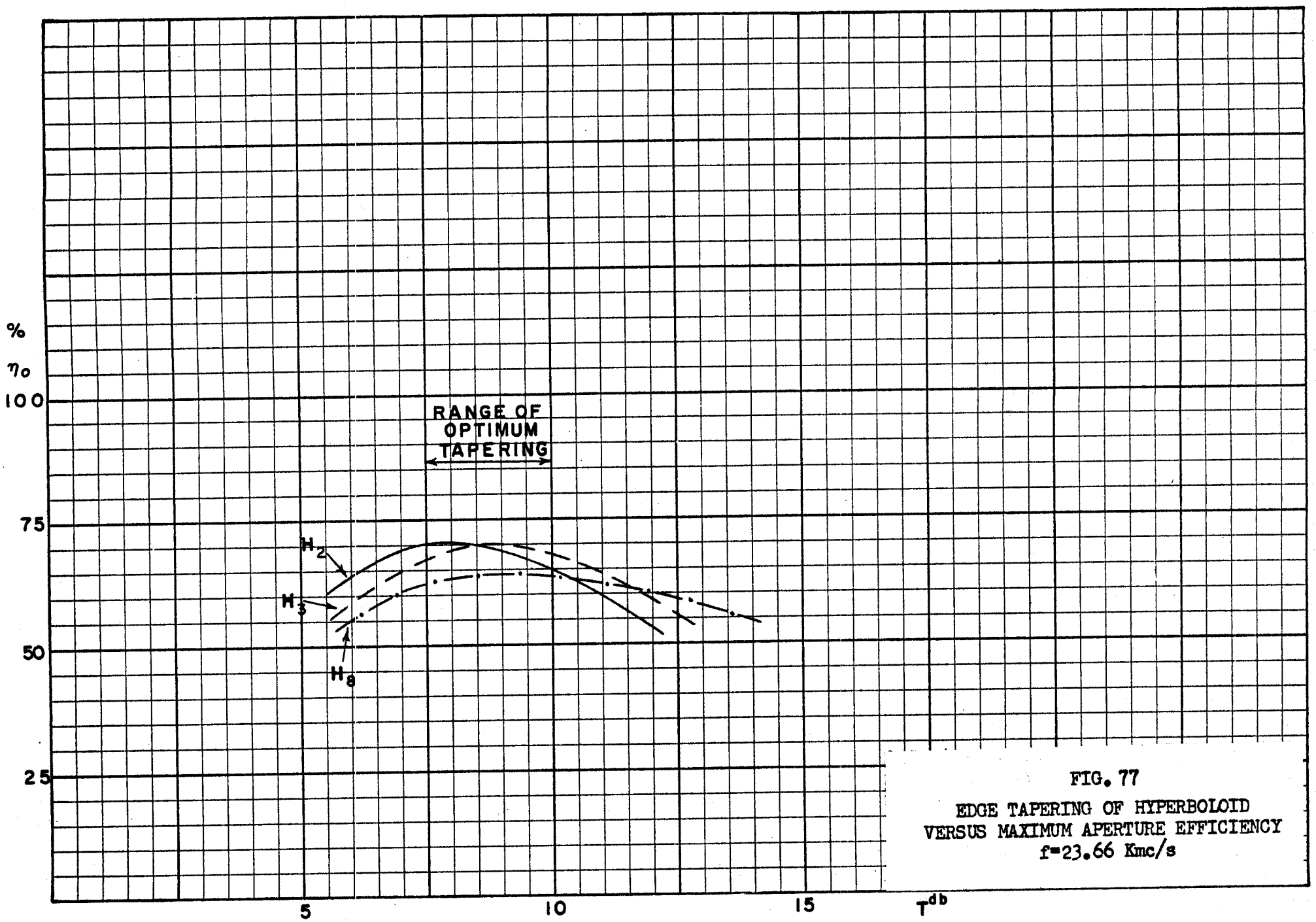

FIG. 77

EDGE TAPERING OF HYPERBOLOID
VERSUS MAXIMUM APERTURE EFFICIENCY
f=23.66 Kmc/s

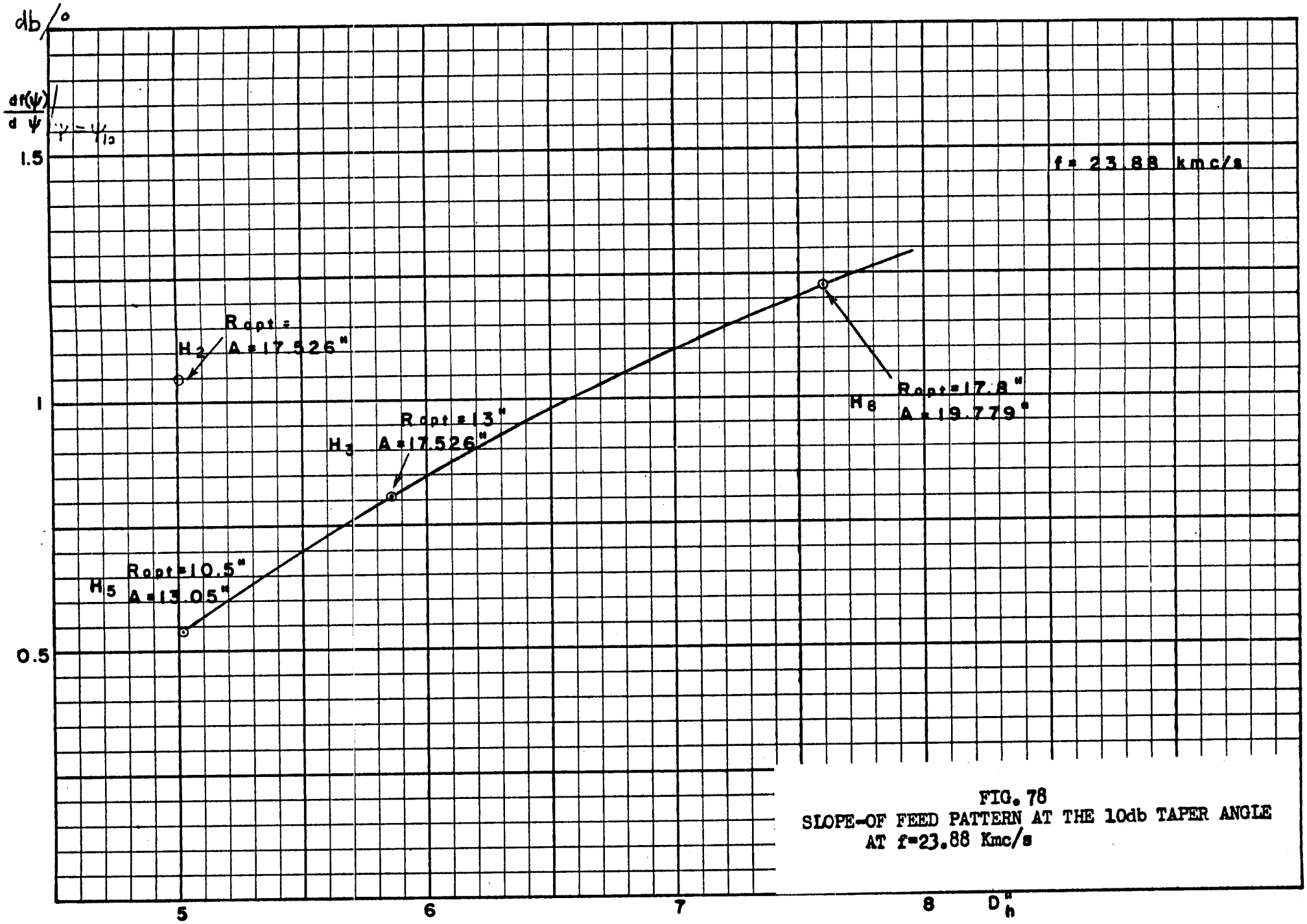

FIG. 78
SLOPE-OF FEED PATTERN AT THE 10db TAPER ANGLE
AT f=23.88 Kmc/s

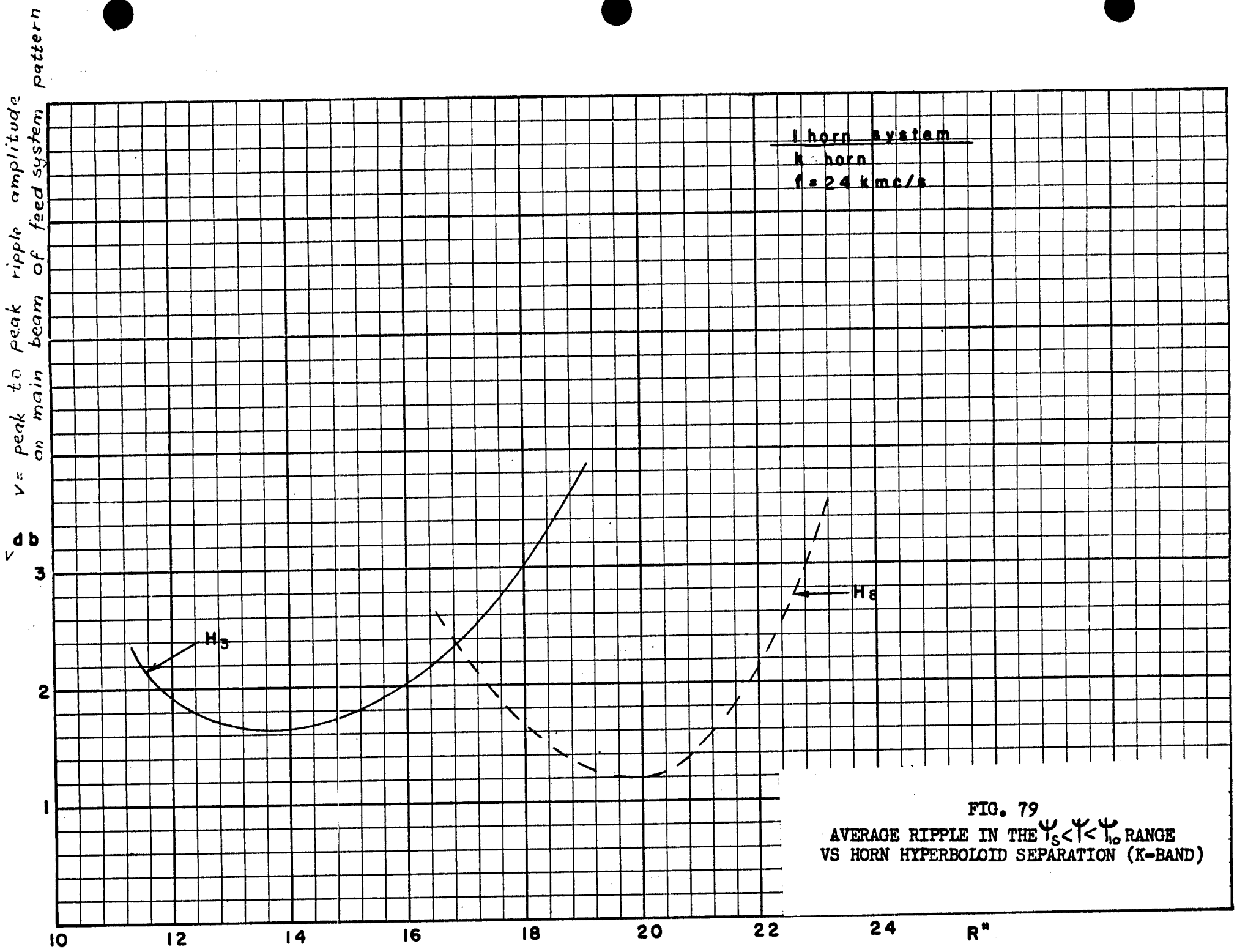

FIG. 79
AVERAGE RIPPLE IN THE $\Psi_S < \Psi < \Psi_{10}$ RANGE
VS HORN HYPERBOLOID SEPARATION (K-BAND)

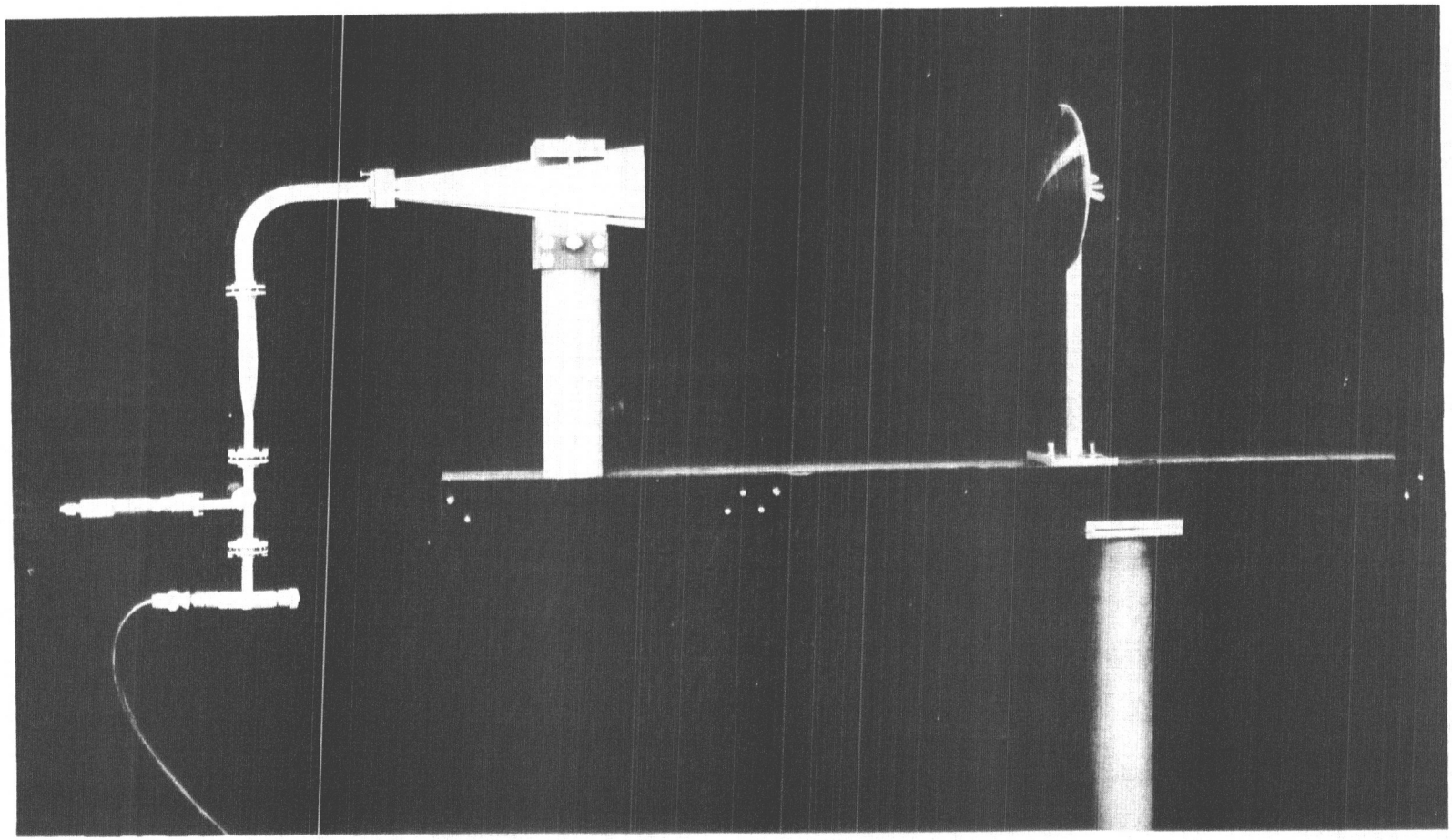

FIG. 80
PHOTOGRAPH OF A TYPICAL K-BAND FEED SYSTEM

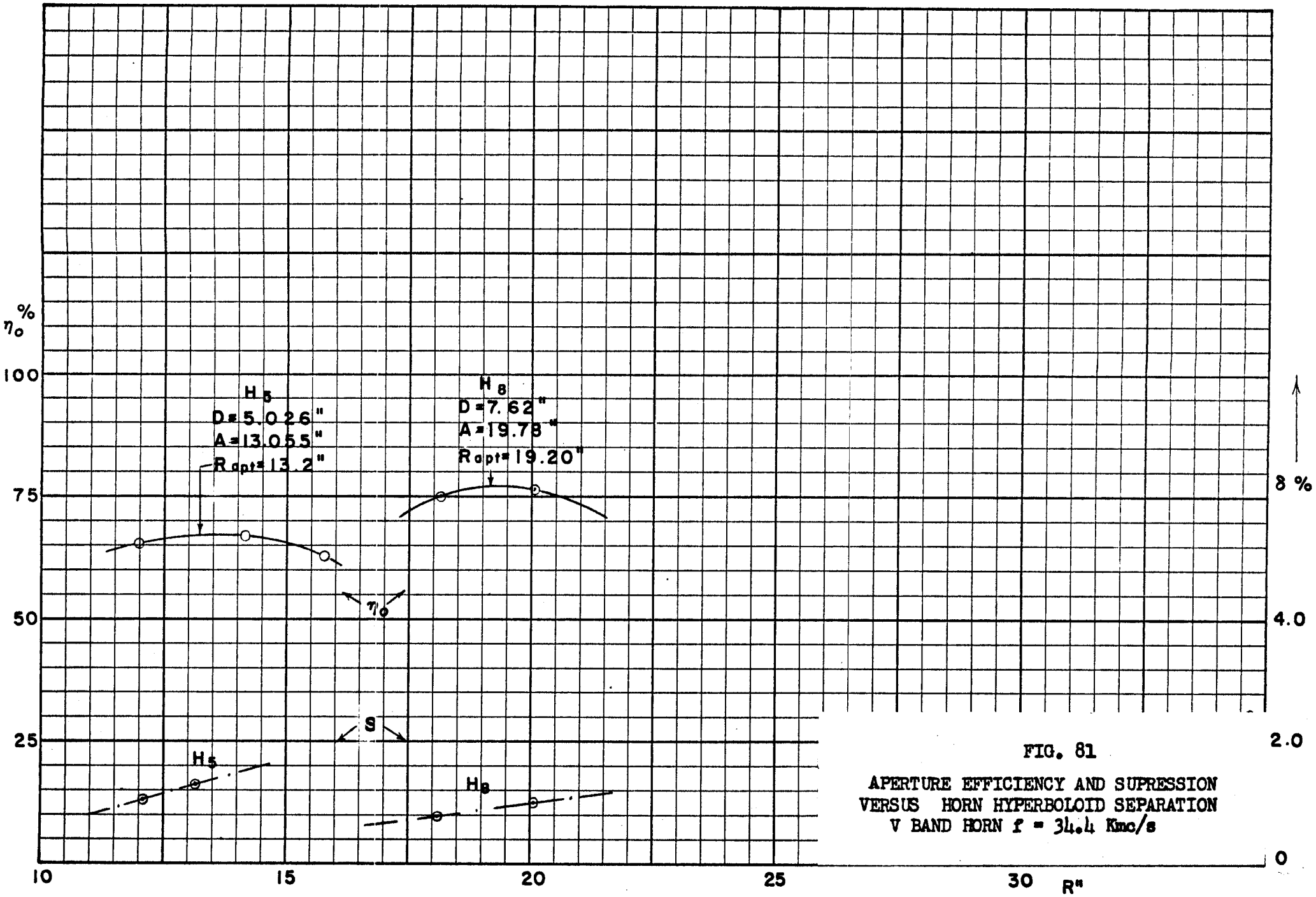

FIG. 81

APERTURE EFFICIENCY AND SUPRESSION VERSUS HORN HYPERBOLOID SEPARATION
V BAND HORN f = 34.4 Kmc/s

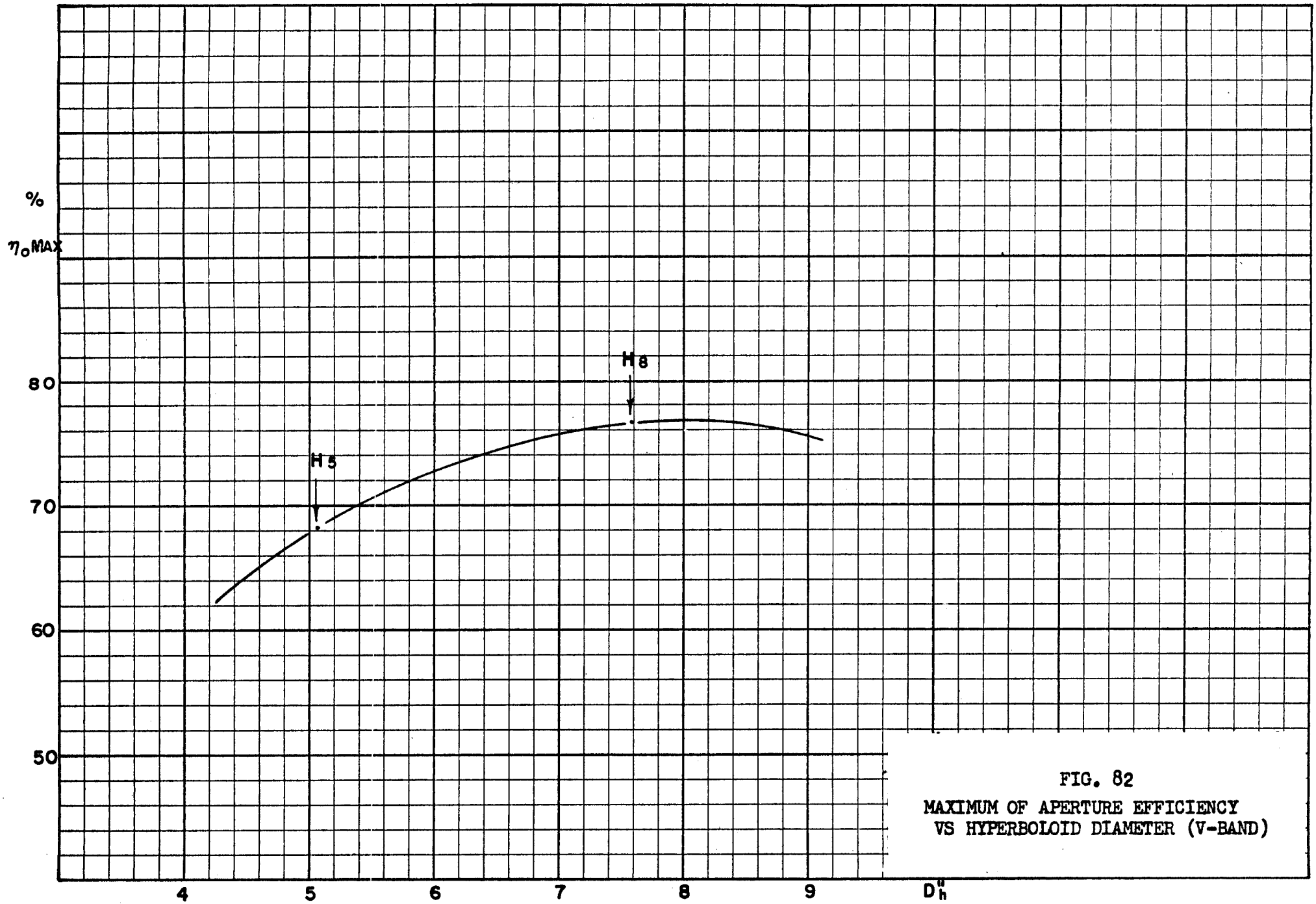

FIG. 82
MAXIMUM OF APERTURE EFFICIENCY
VS HYPERBOLOID DIAMETER (V-BAND)

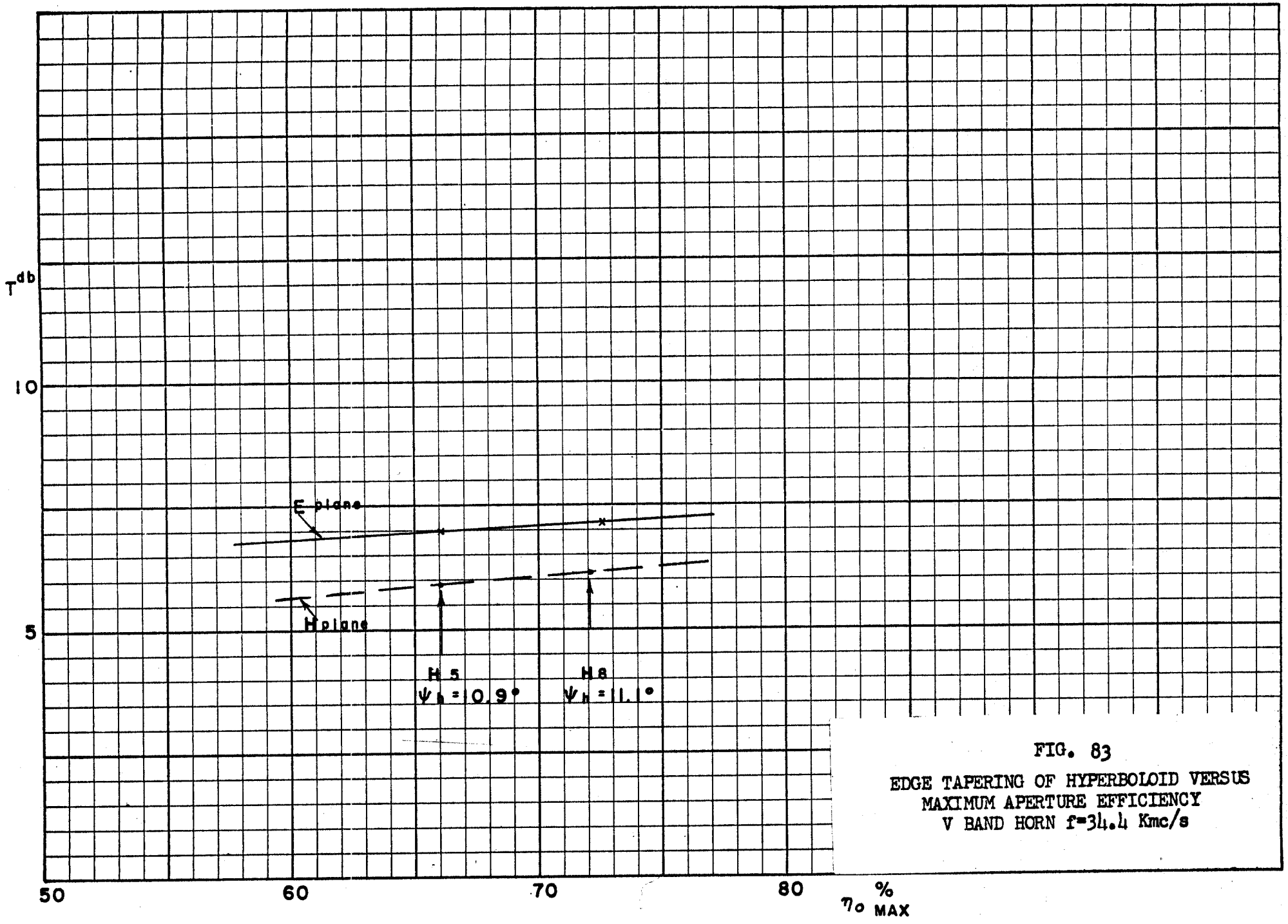

FIG. 83

EDGE TAPERING OF HYPERBOLOID VERSUS MAXIMUM APERTURE EFFICIENCY V BAND HORN f=34.4 Kmc/s

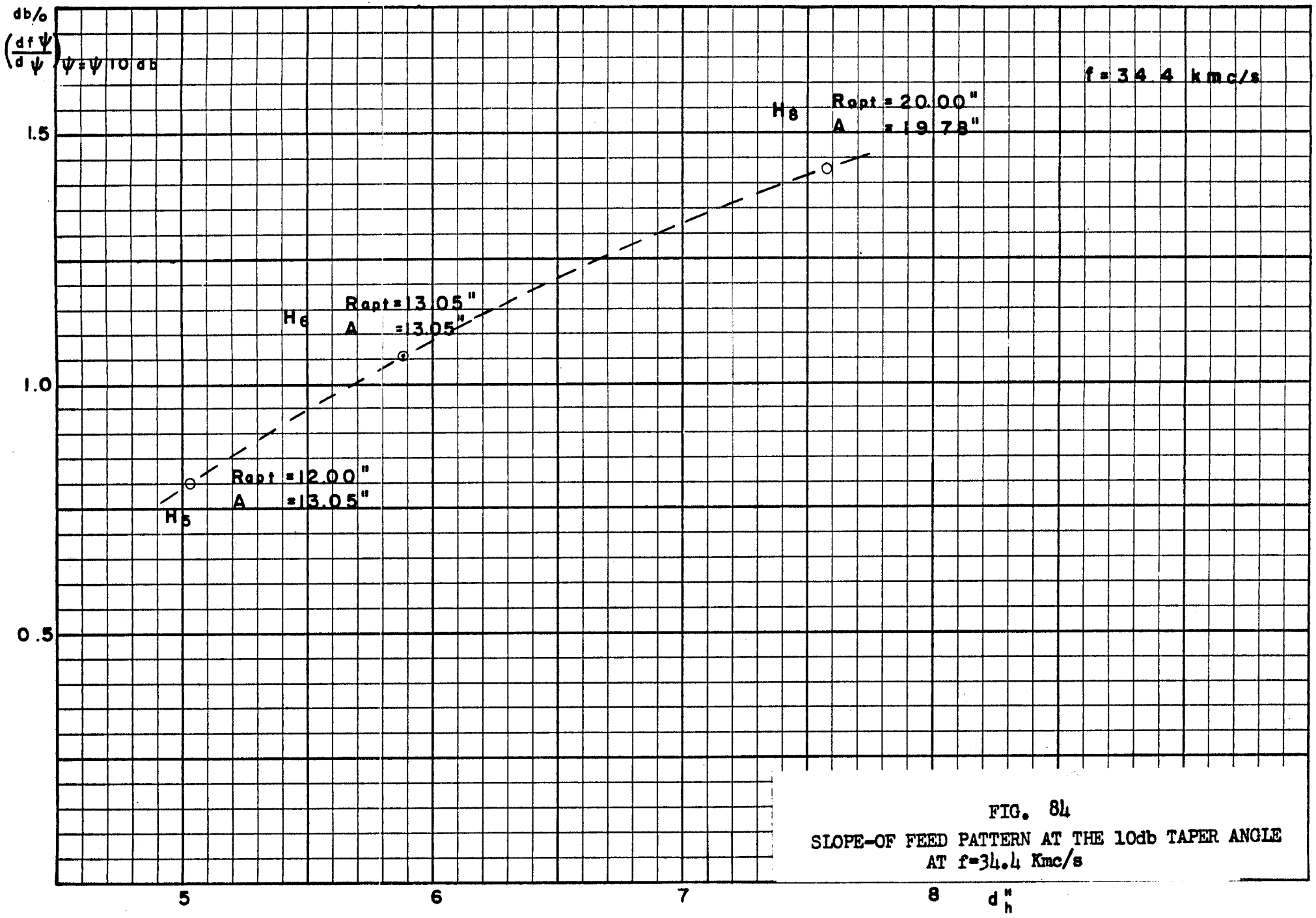

FIG. 84

SLOPE-OF FEED PATTERN AT THE 10db TAPER ANGLE AT f=34.4 Kmc/s

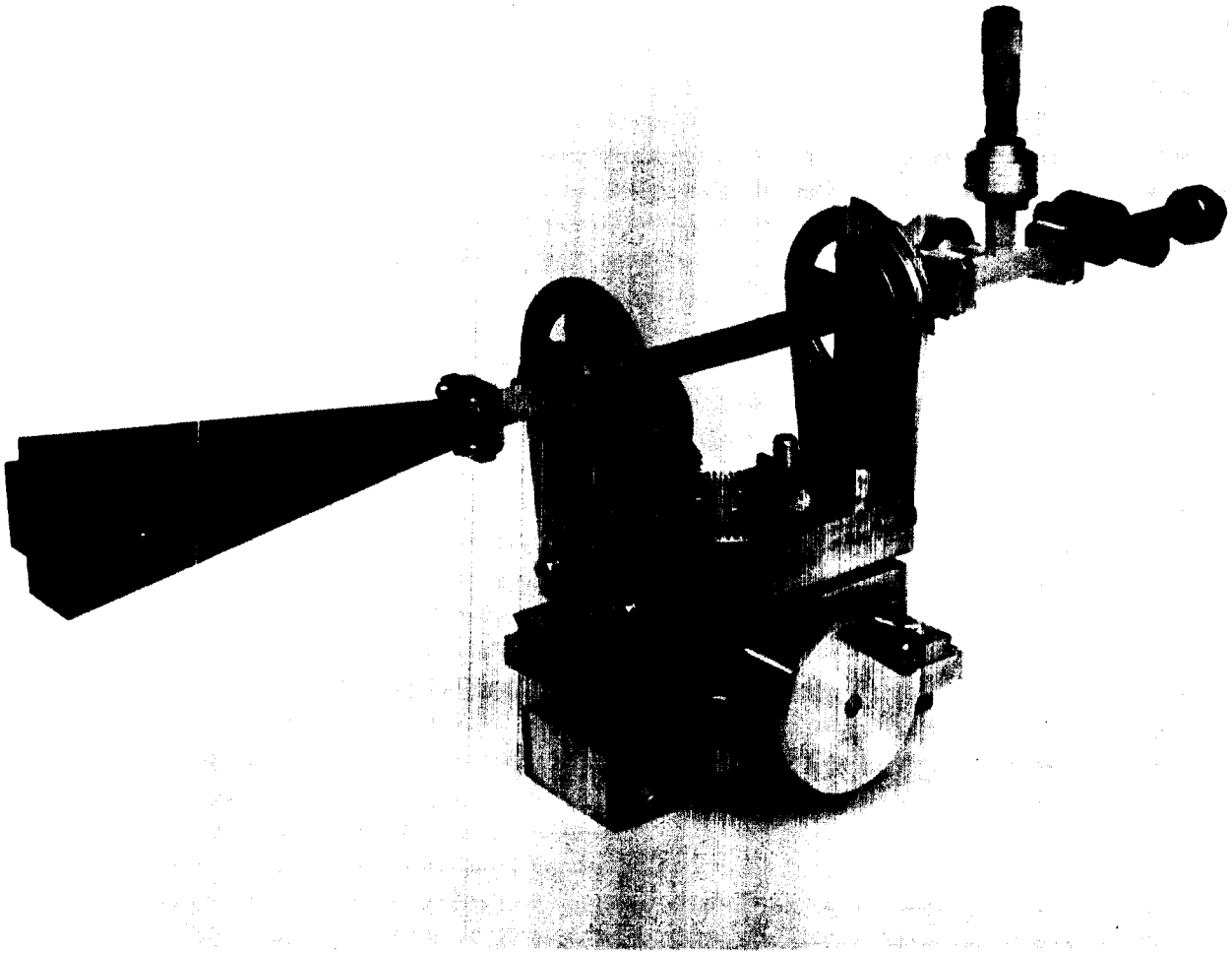

FIG. 85 PHOTOGRAPH OF A TYPICAL V-BAND FEED.

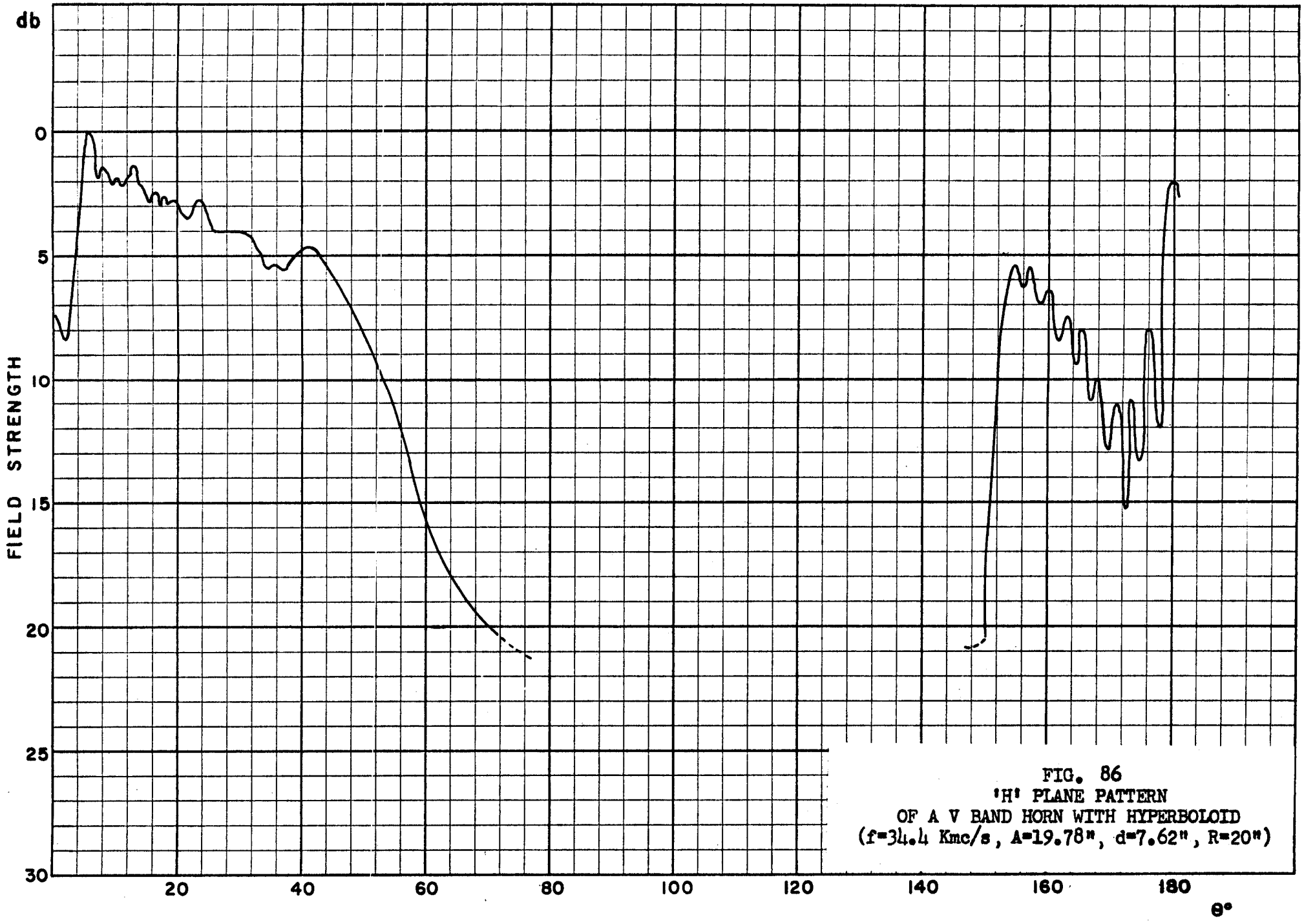

FIG. 86
'H' PLANE PATTERN
OF A V BAND HORN WITH HYPERBOLOID
(f=34.4 Kmc/s, A=19.78", d=7.62", R=20")

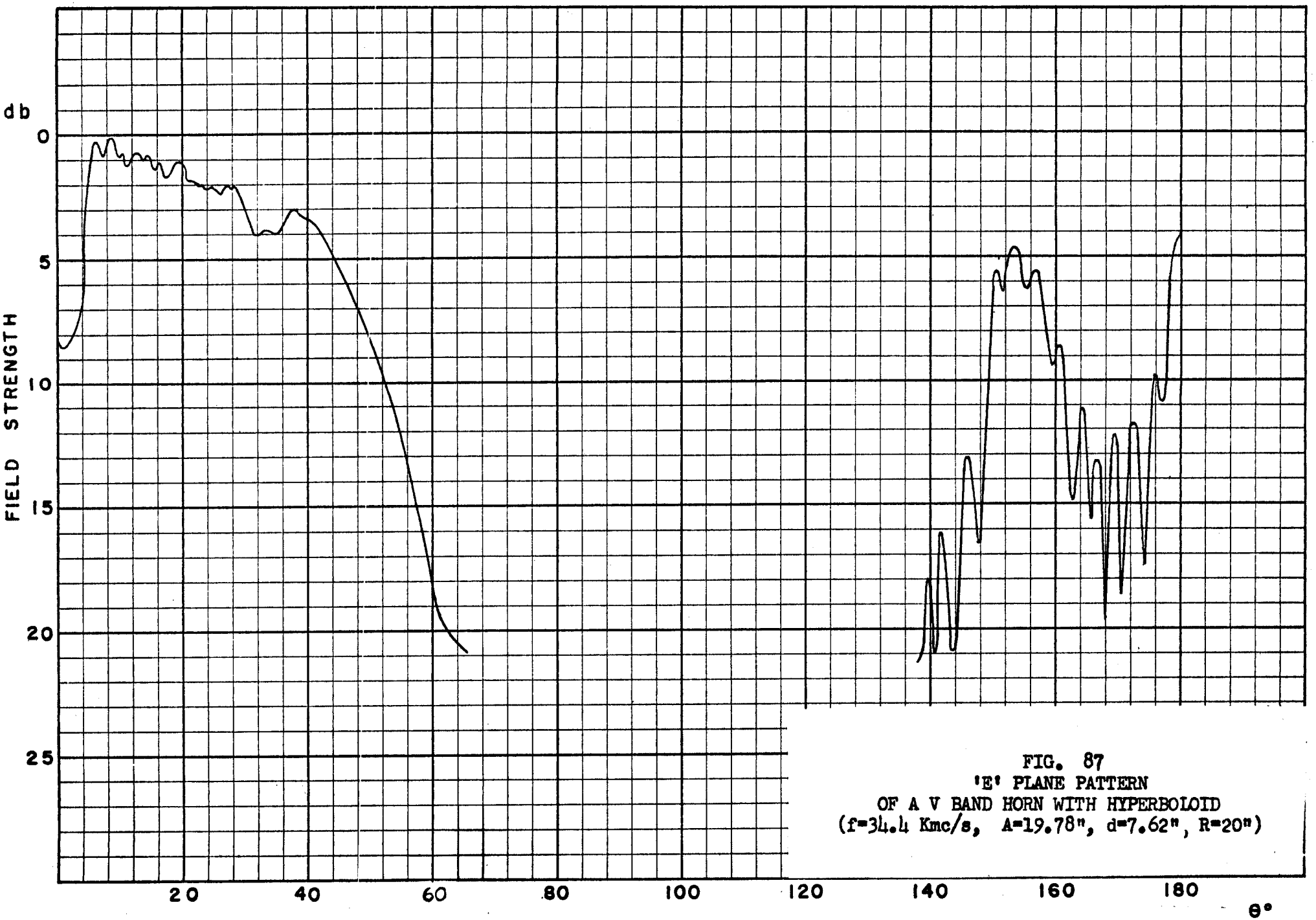

FIG. 87
'E' PLANE PATTERN
OF A V BAND HORN WITH HYPERBOLOID
(f=34.4 Kmc/s, A=19.78", d=7.62", R=20")

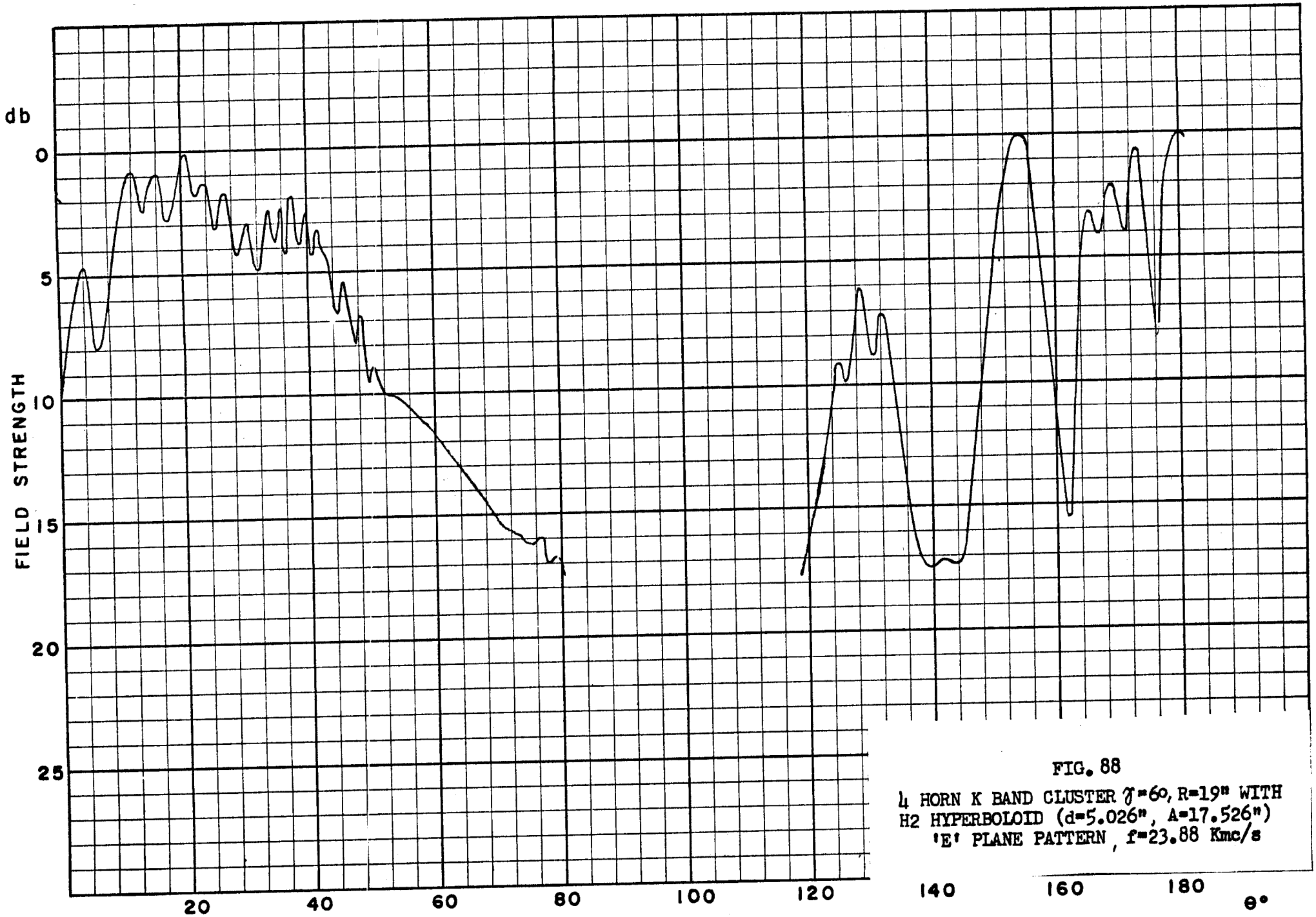

FIG. 88

4 HORN K BAND CLUSTER γ=60, R=19" WITH H2 HYPERBOLOID (d=5.026", A=17.526")
'E' PLANE PATTERN, f=23.88 Kmc/s

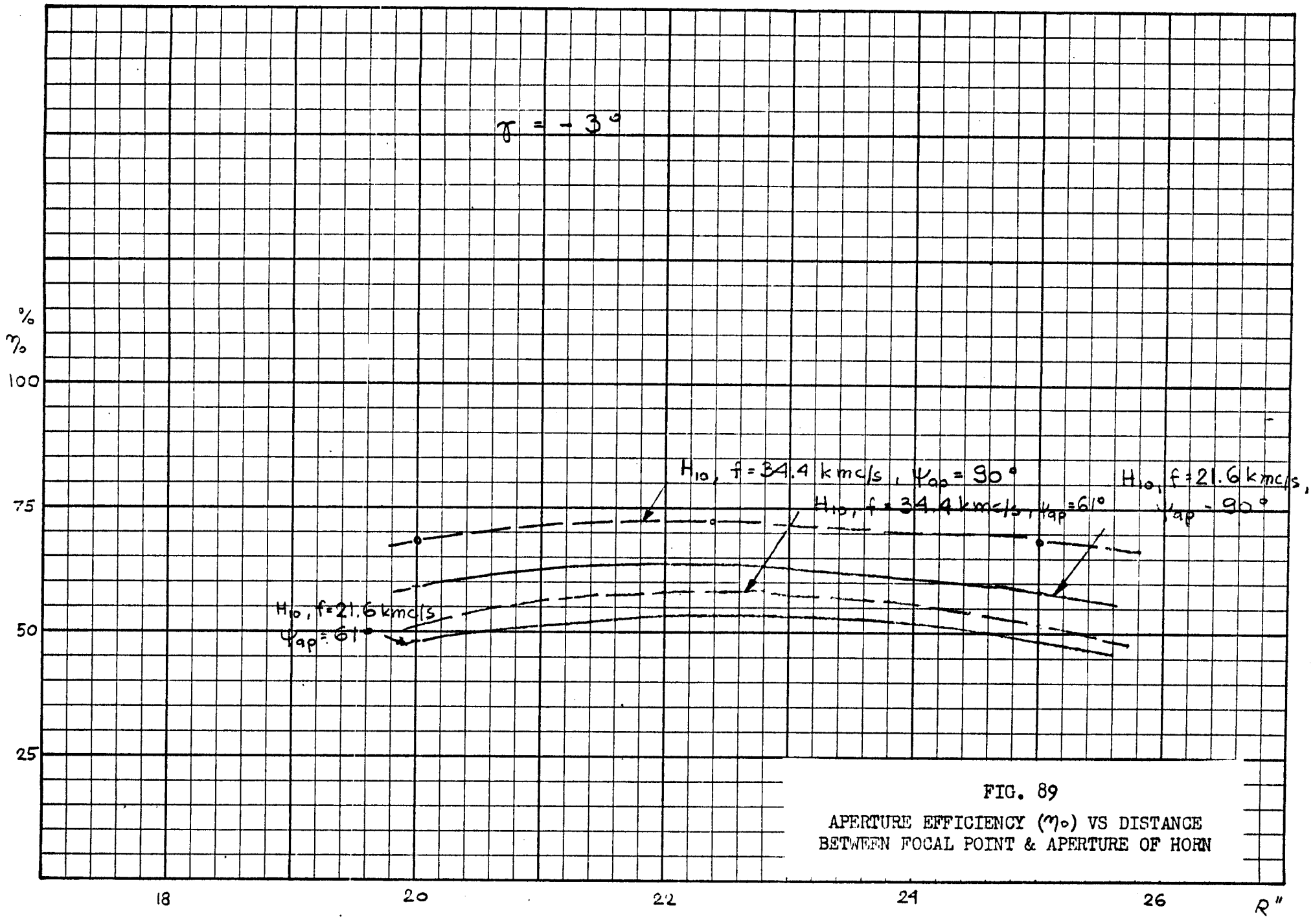

FIG. 89

APERTURE EFFICIENCY (η_0) VS DISTANCE BETWEEN FOCAL POINT & APERTURE OF HORN

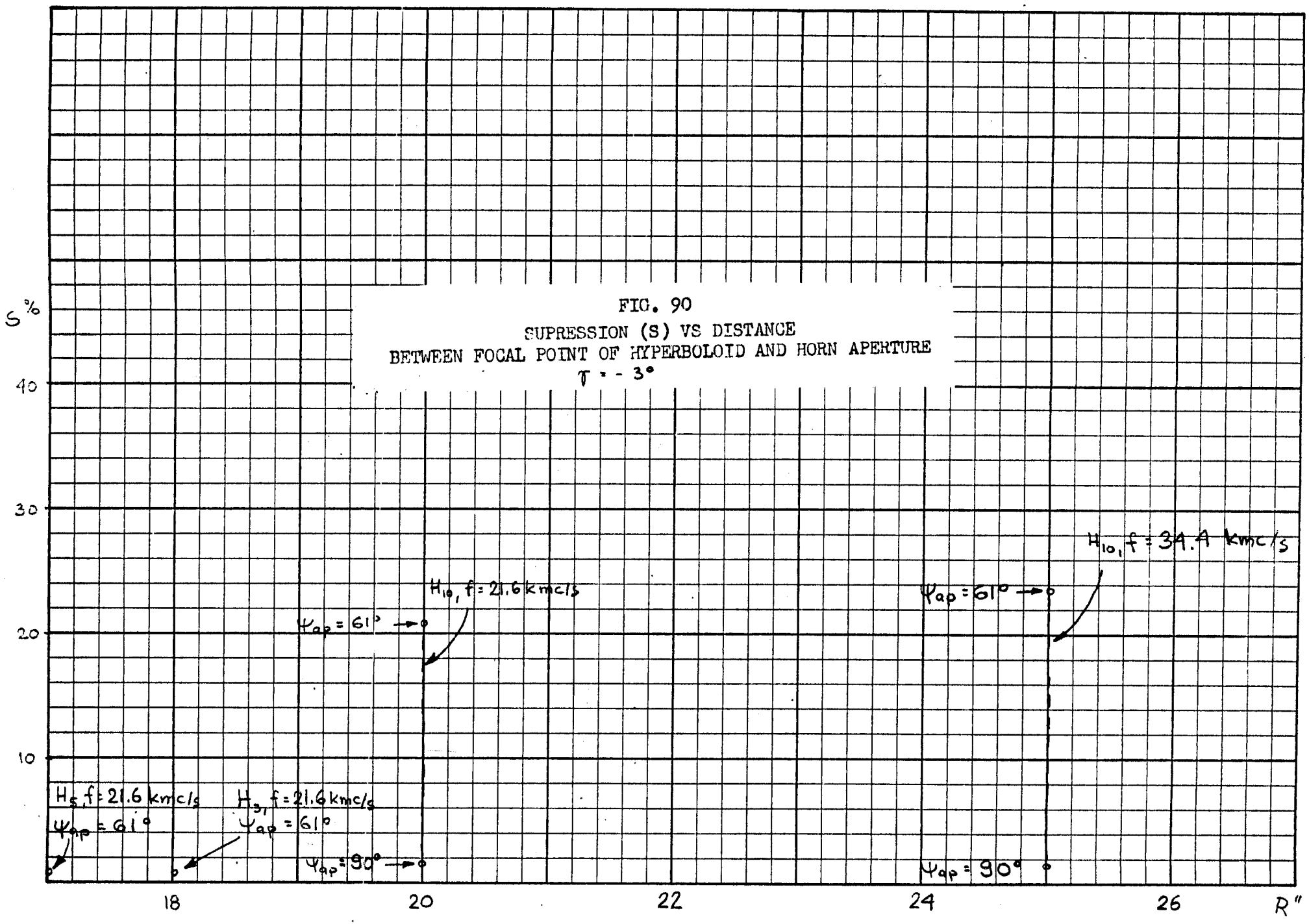

FIG. 90
SUPRESSION (S) VS DISTANCE
BETWEEN FOCAL POINT OF HYPERBOLOID AND HORN APERTURE
τ = - 3°

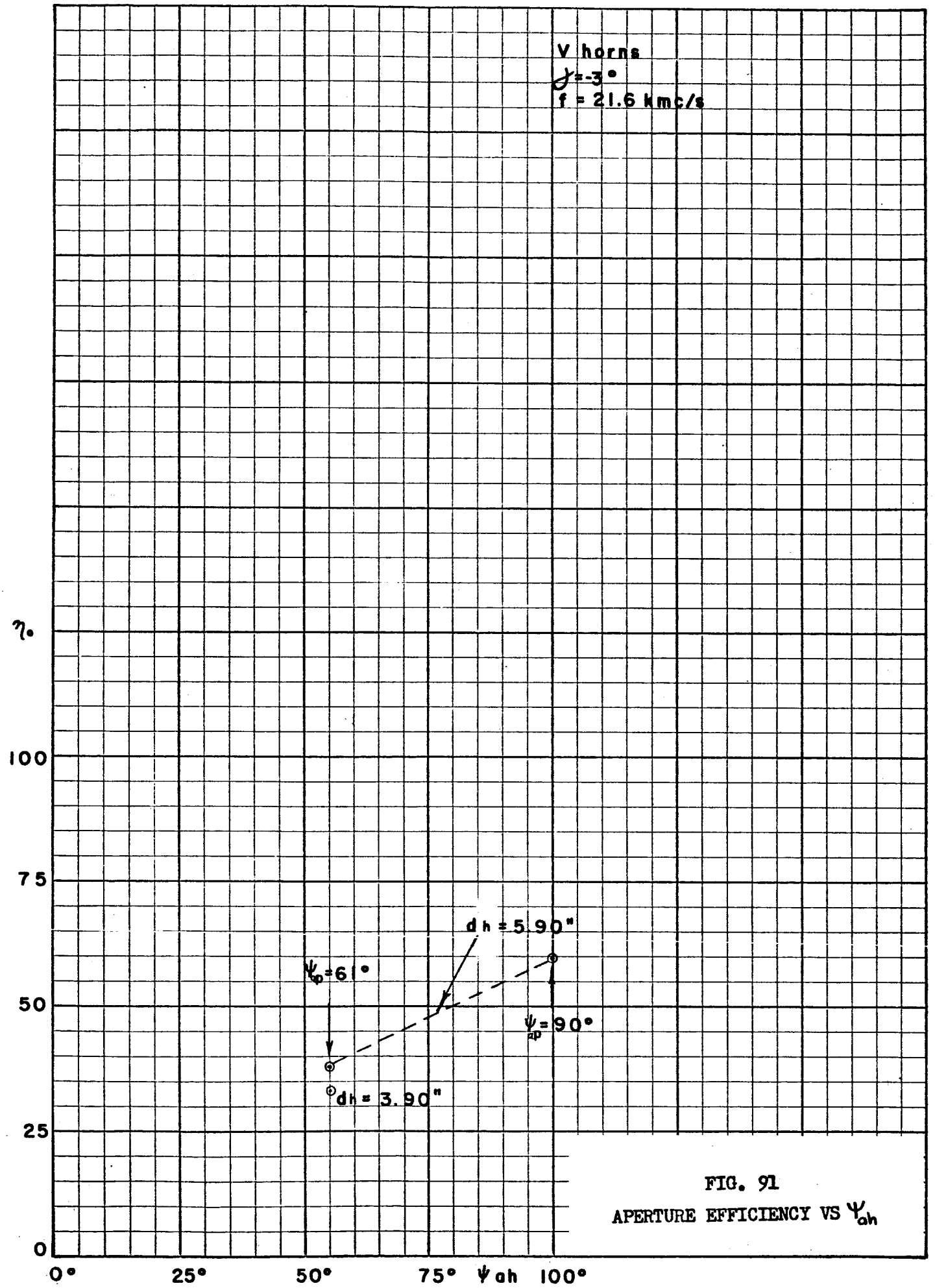

FIG. 91

APERTURE EFFICIENCY VS ψ_{ah}

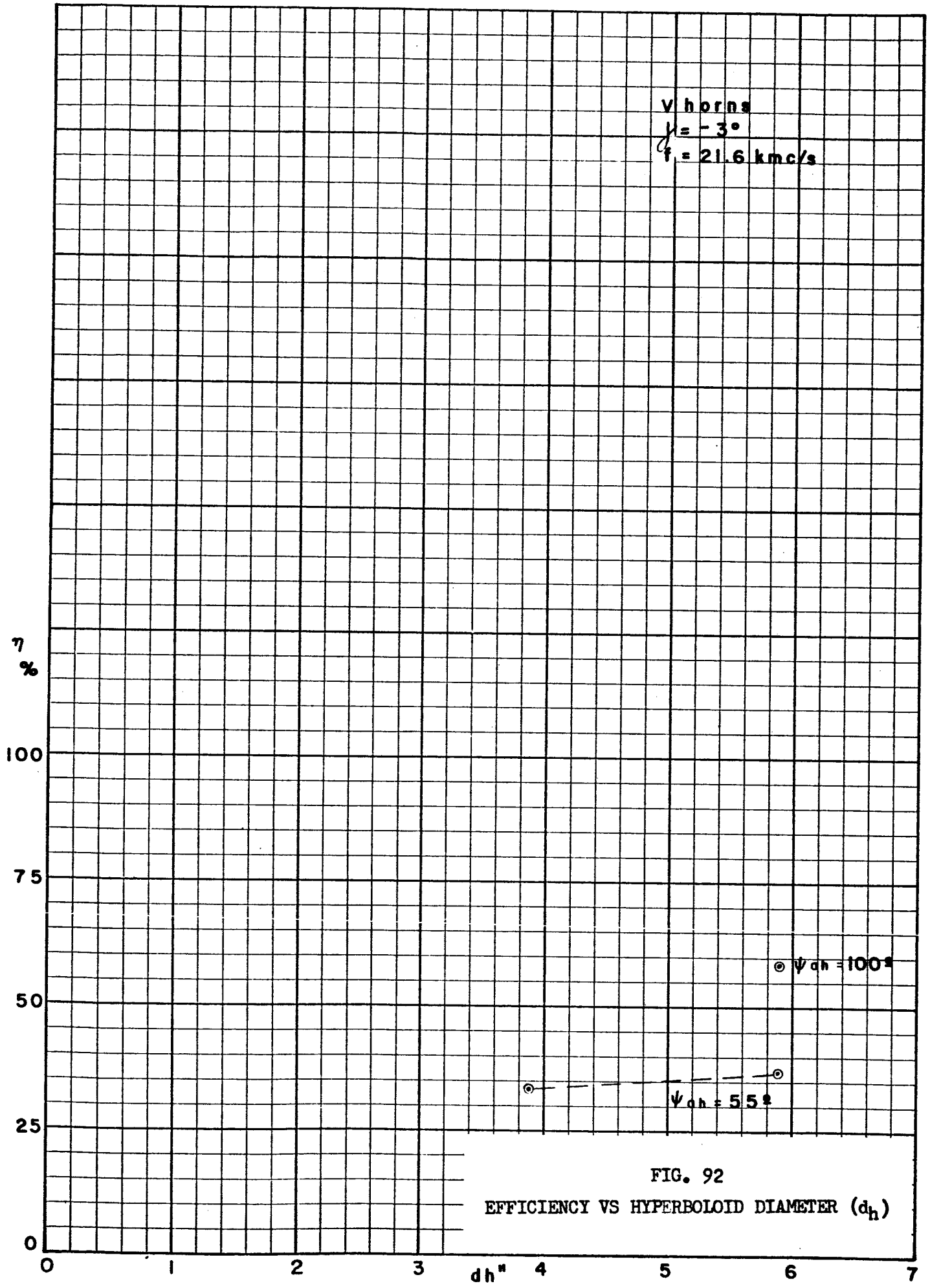

FIG. 92

EFFICIENCY VS HYPERBOLOID DIAMETER (d_h)

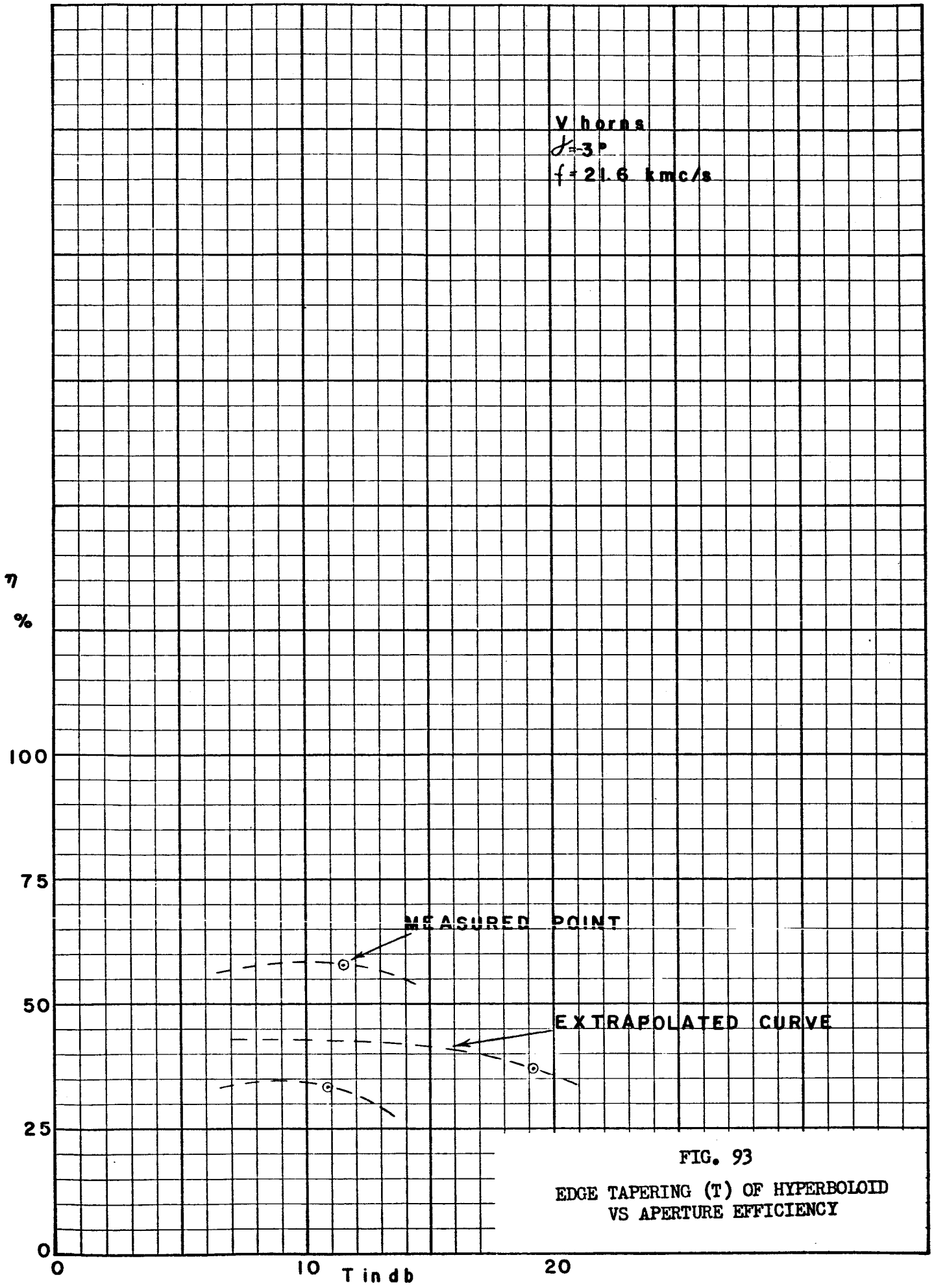

FIG. 93

EDGE TAPERING (T) OF HYPERBOLOID
VS APERTURE EFFICIENCY

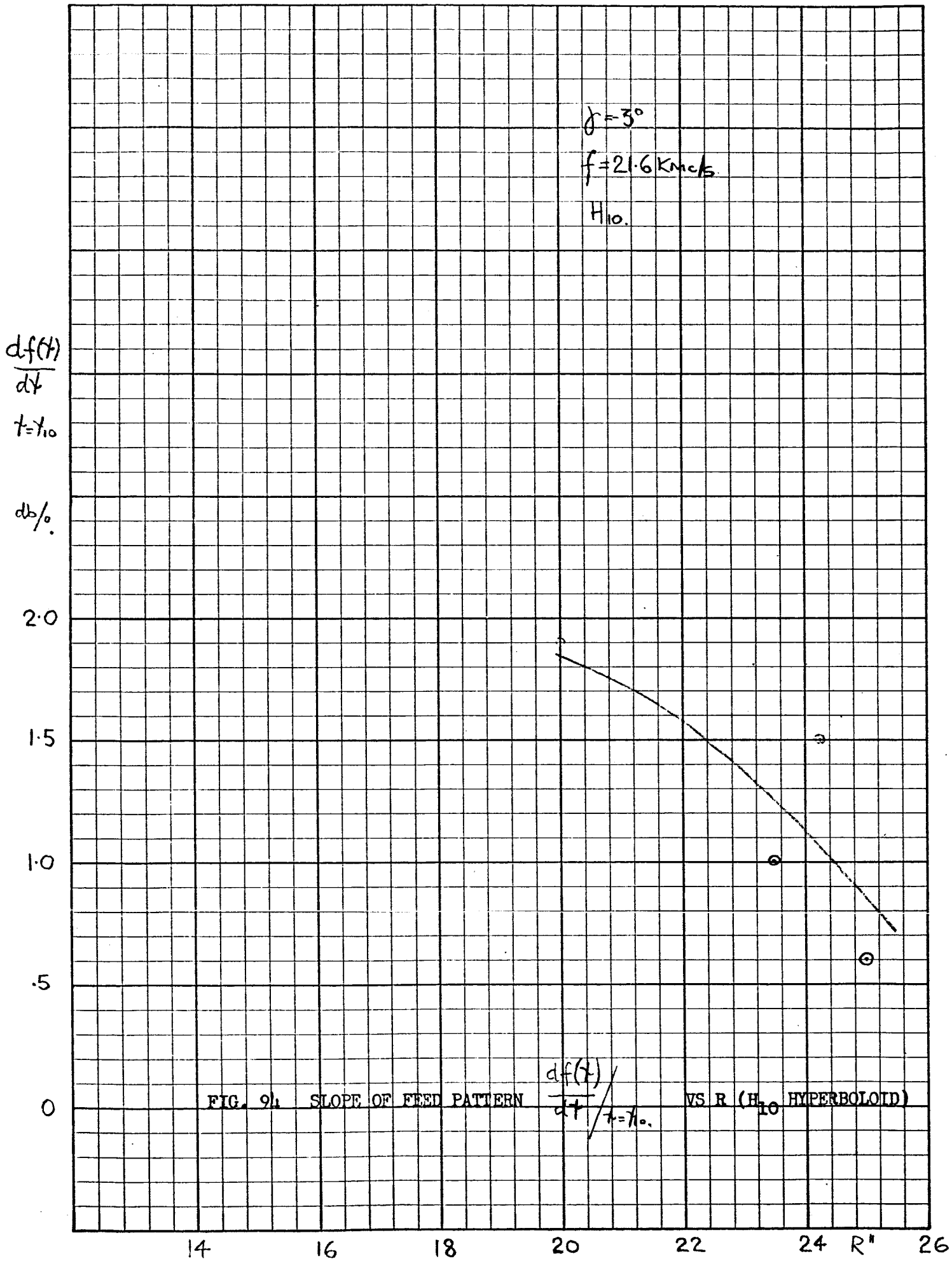

FIG. 94 SLOPE OF FEED PATTERN $\left.\frac{df(\gamma)}{d\gamma}\right/_{\gamma=\gamma_{10}}$ VS R (H_{10} HYPERBOLOID)

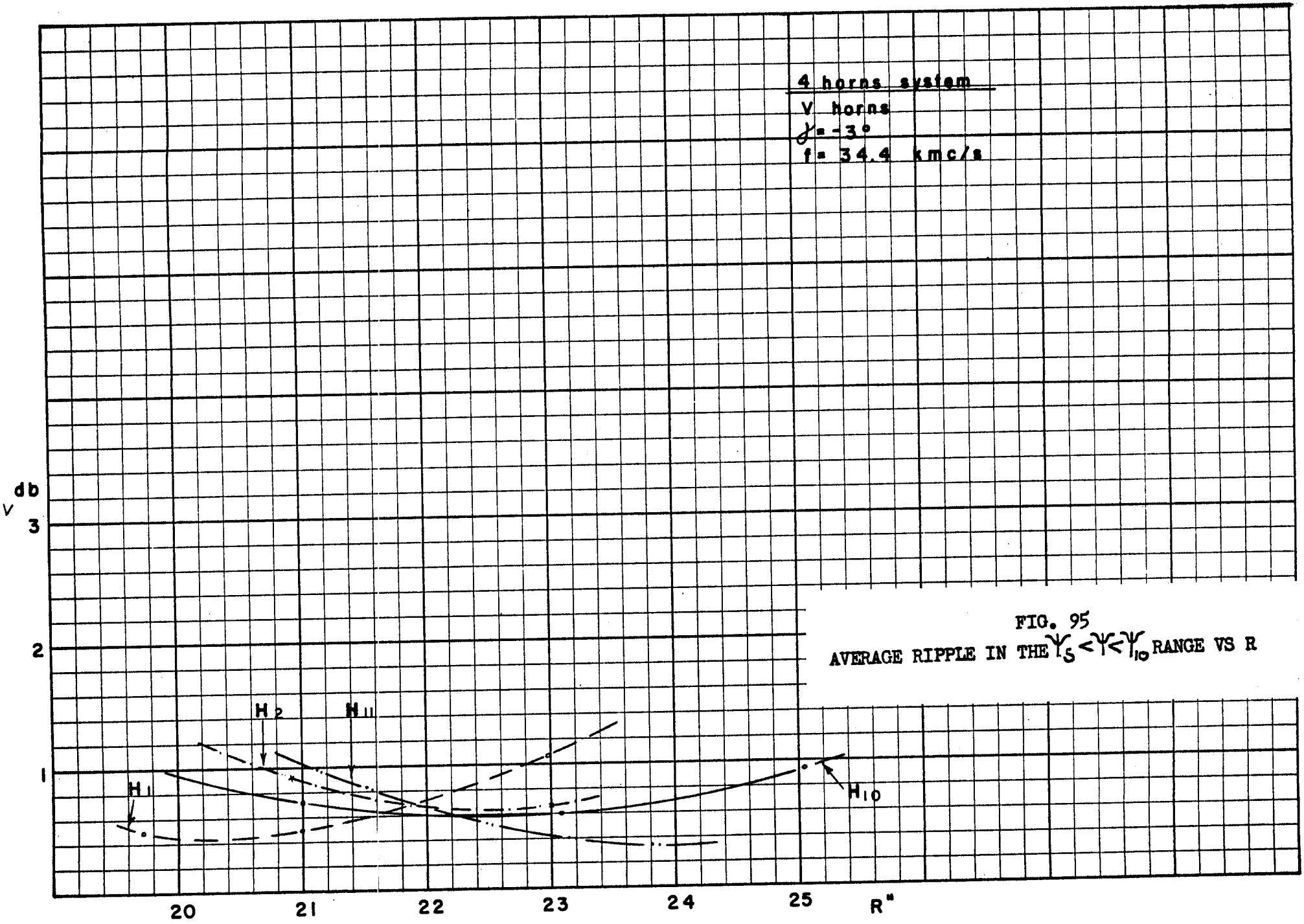

FIG. 95

AVERAGE RIPPLE IN THE $\Psi_5 < \Psi < \Psi_{10}$ RANGE VS R

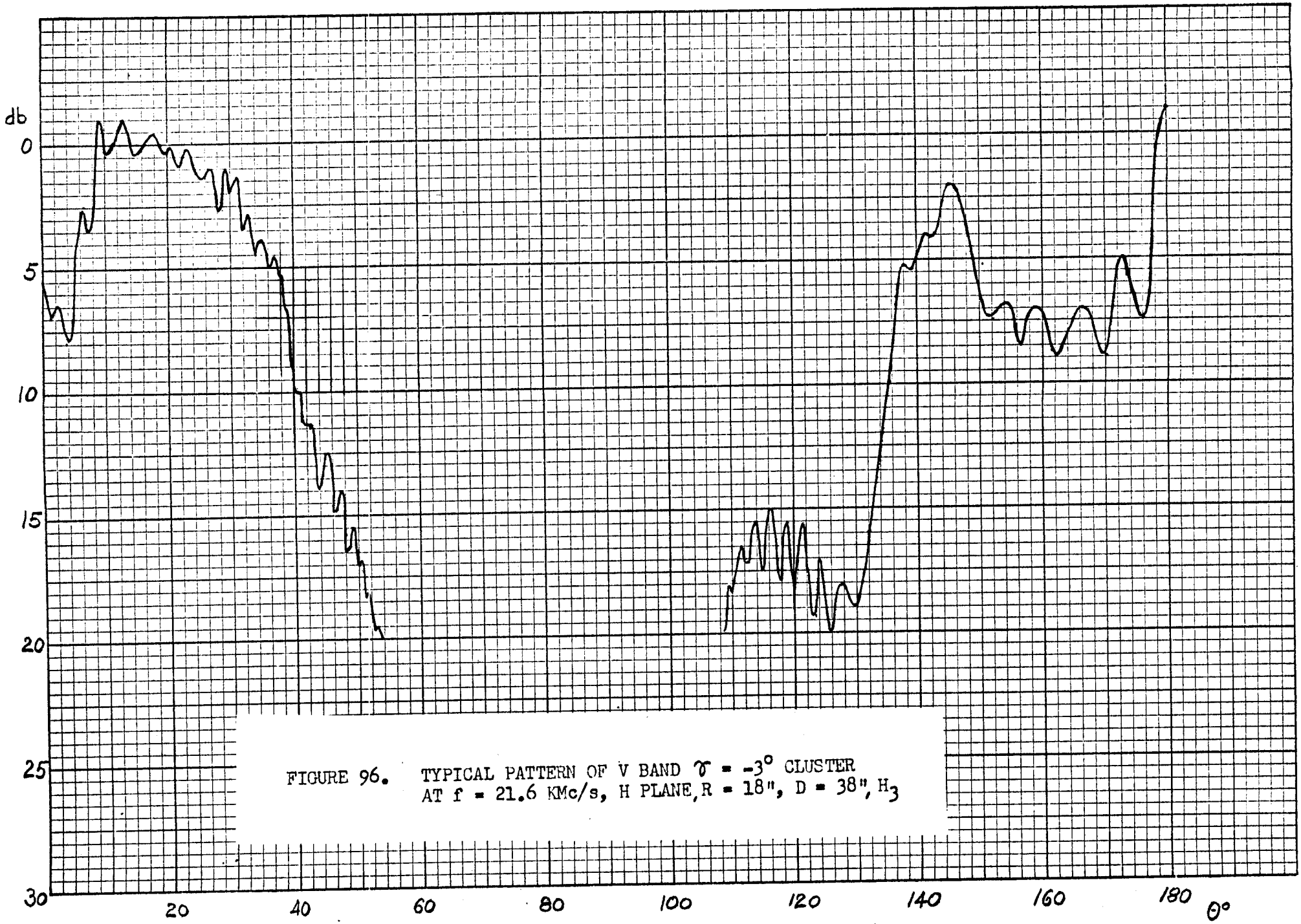

FIGURE 96. TYPICAL PATTERN OF V BAND $\gamma = -3^{\circ}$ CLUSTER AT f = 21.6 KMc/s, H PLANE, R = 18", D = 38", H_3

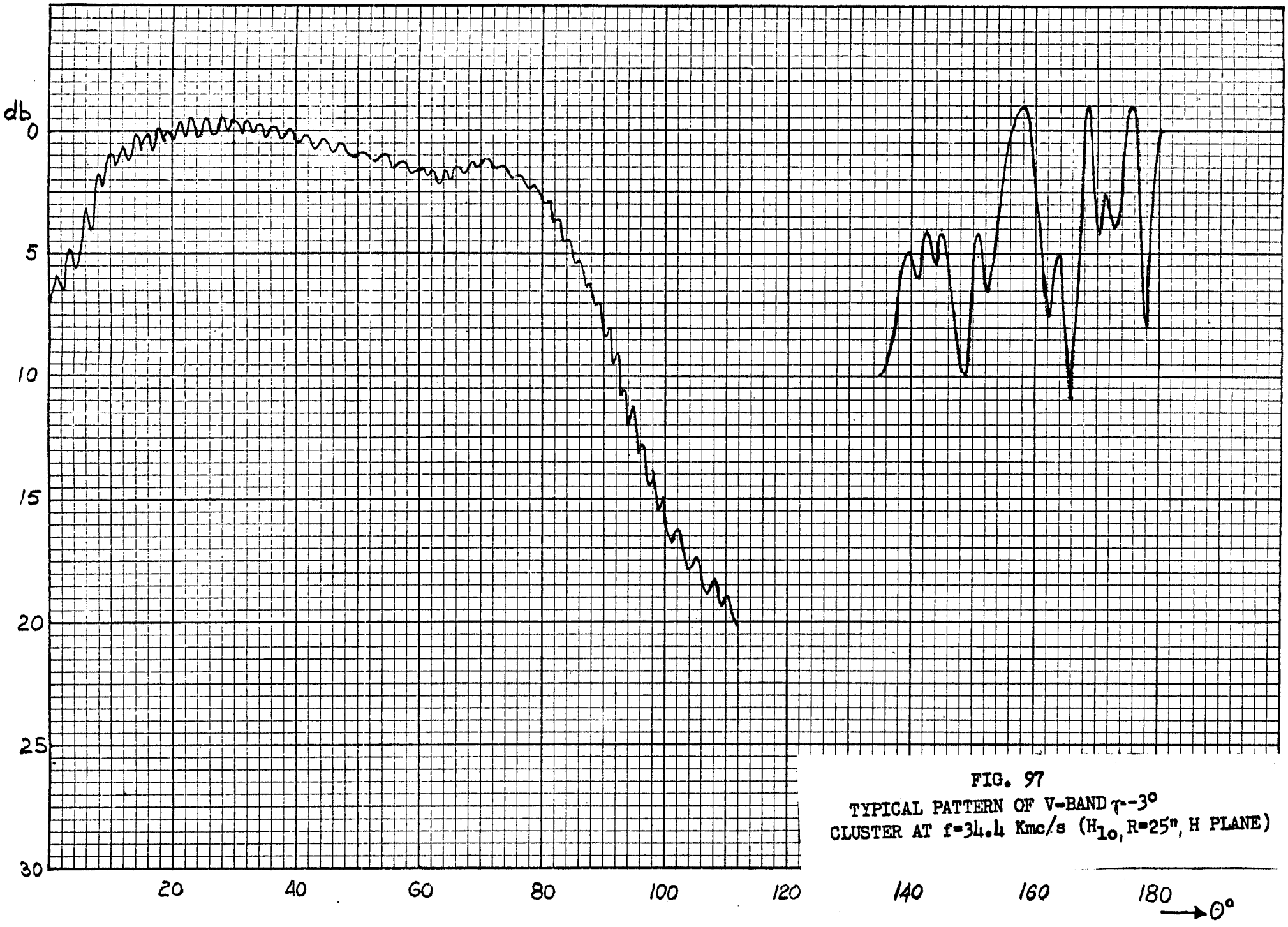

FIG. 97
TYPICAL PATTERN OF V-BAND τ-3°
CLUSTER AT f=34.4 Kmc/s (H_{10}, R=25", H PLANE)

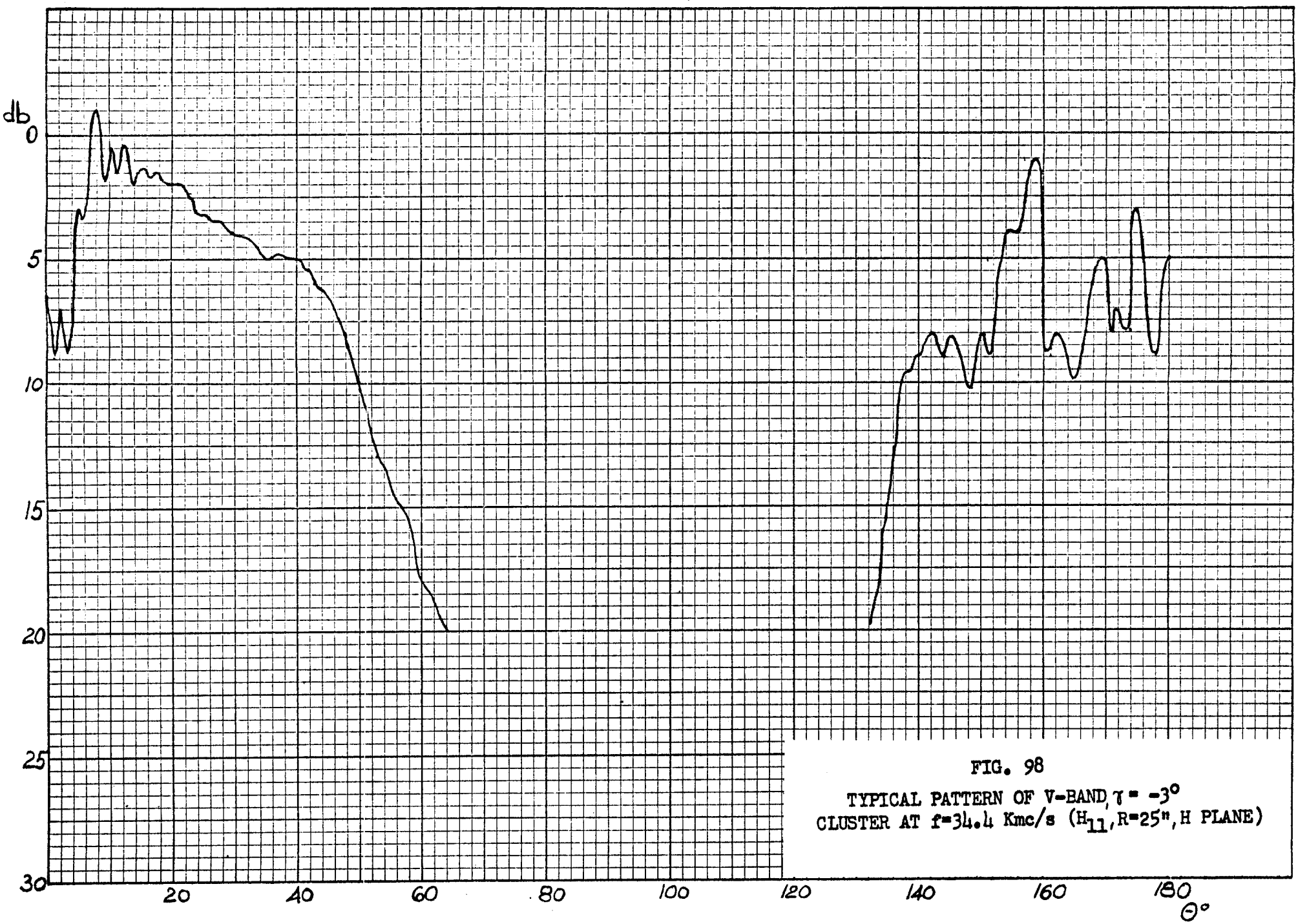

FIG. 98

TYPICAL PATTERN OF V-BAND, $\gamma = -3^\circ$
CLUSTER AT f=34.4 Kmc/s (H_{11}, R=25", H PLANE)

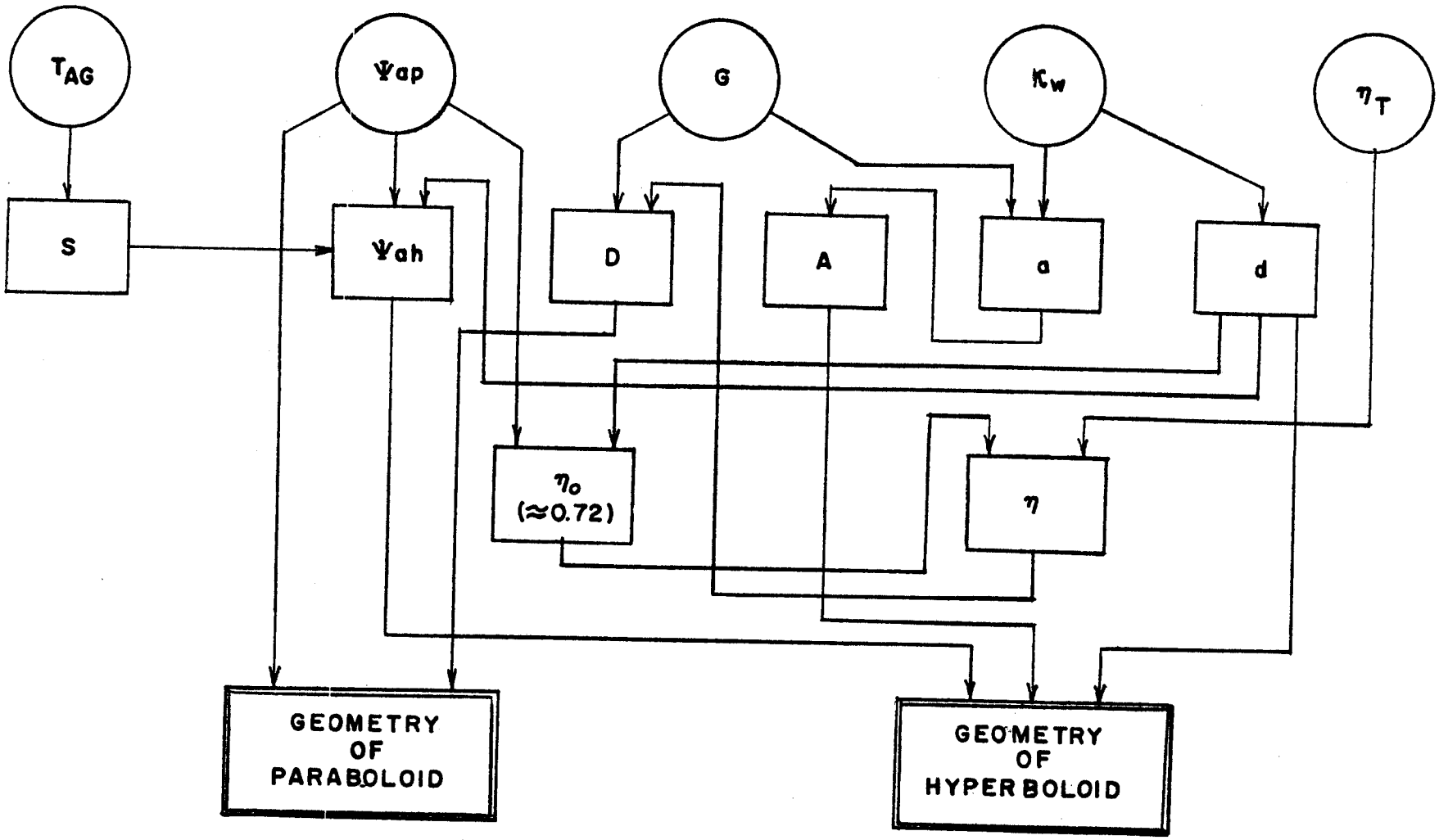

FIG. 99
DESIGN FLOW DIAGRAM OF
A LOW NOISE CASSAGRAIN ANTENNA

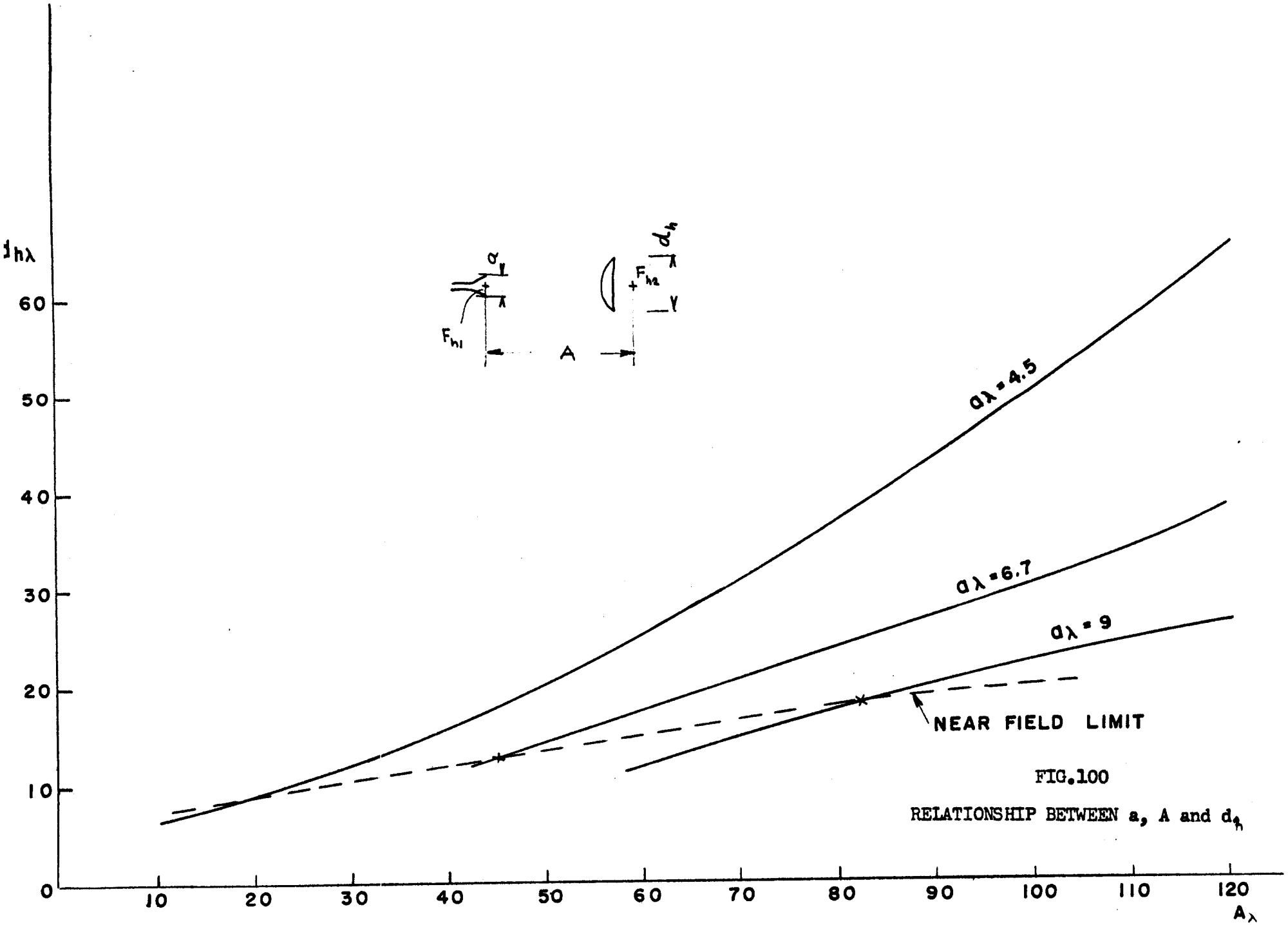

FIG.100

RELATIONSHIP BETWEEN a, A and d_h

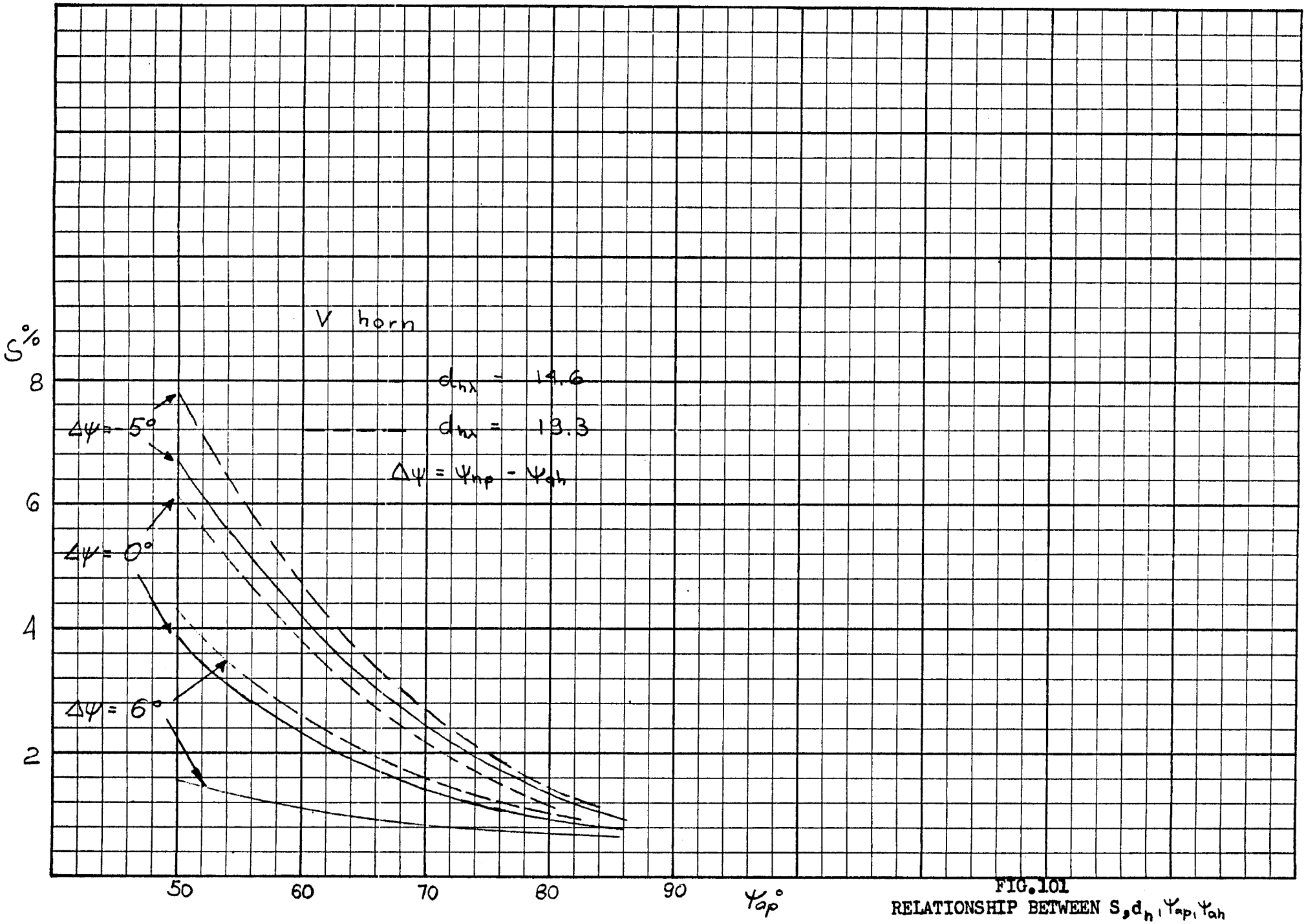

FIG. 101
RELATIONSHIP BETWEEN $S, d_h, \psi_{ap}, \psi_{ah}$

FIG. 102 a

MEASURED FEED PATTERN OF H_3 HYPERBOLOID

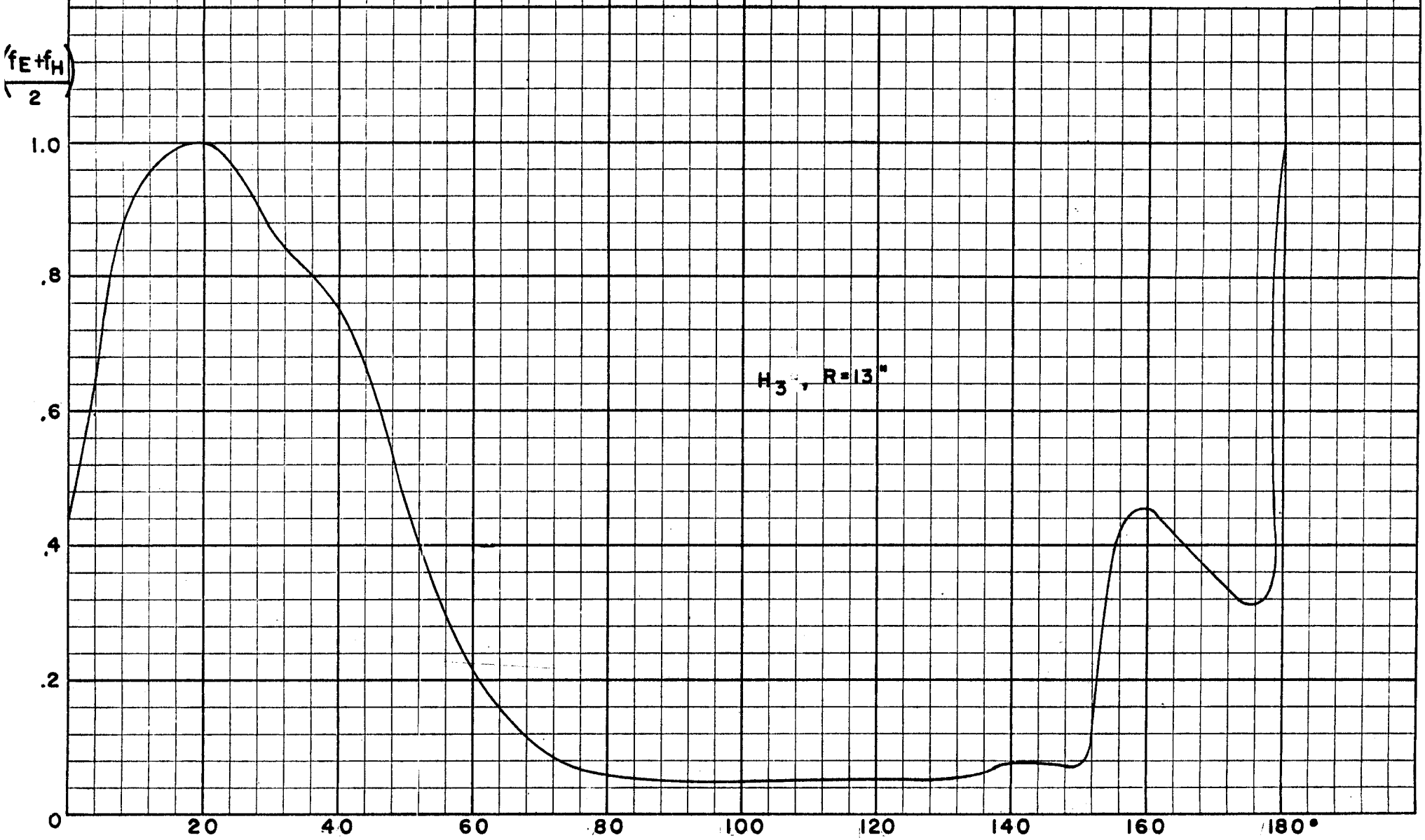

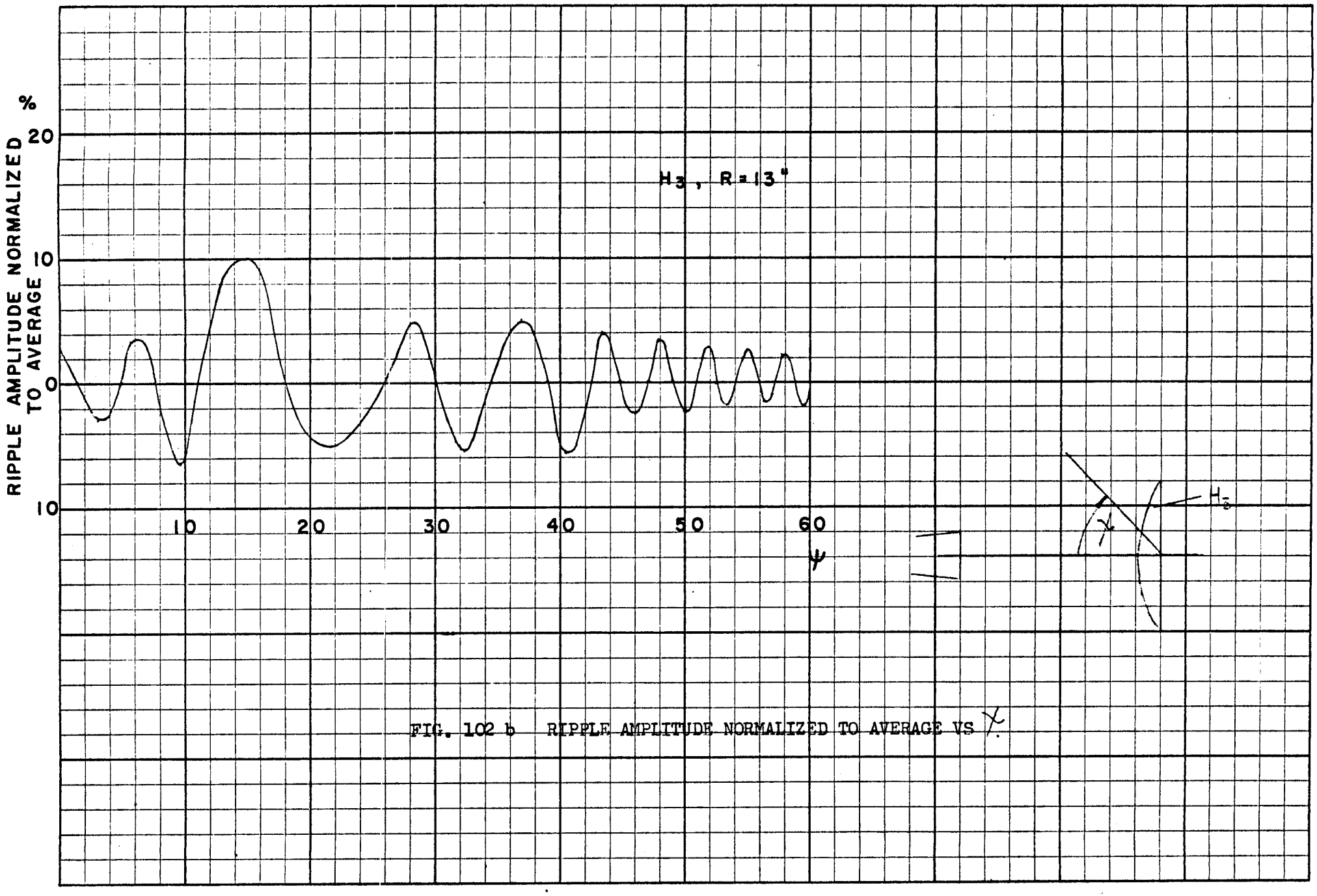

FIG. 102 b RIPPLE AMPLITUDE NORMALIZED TO AVERAGE VS χ.

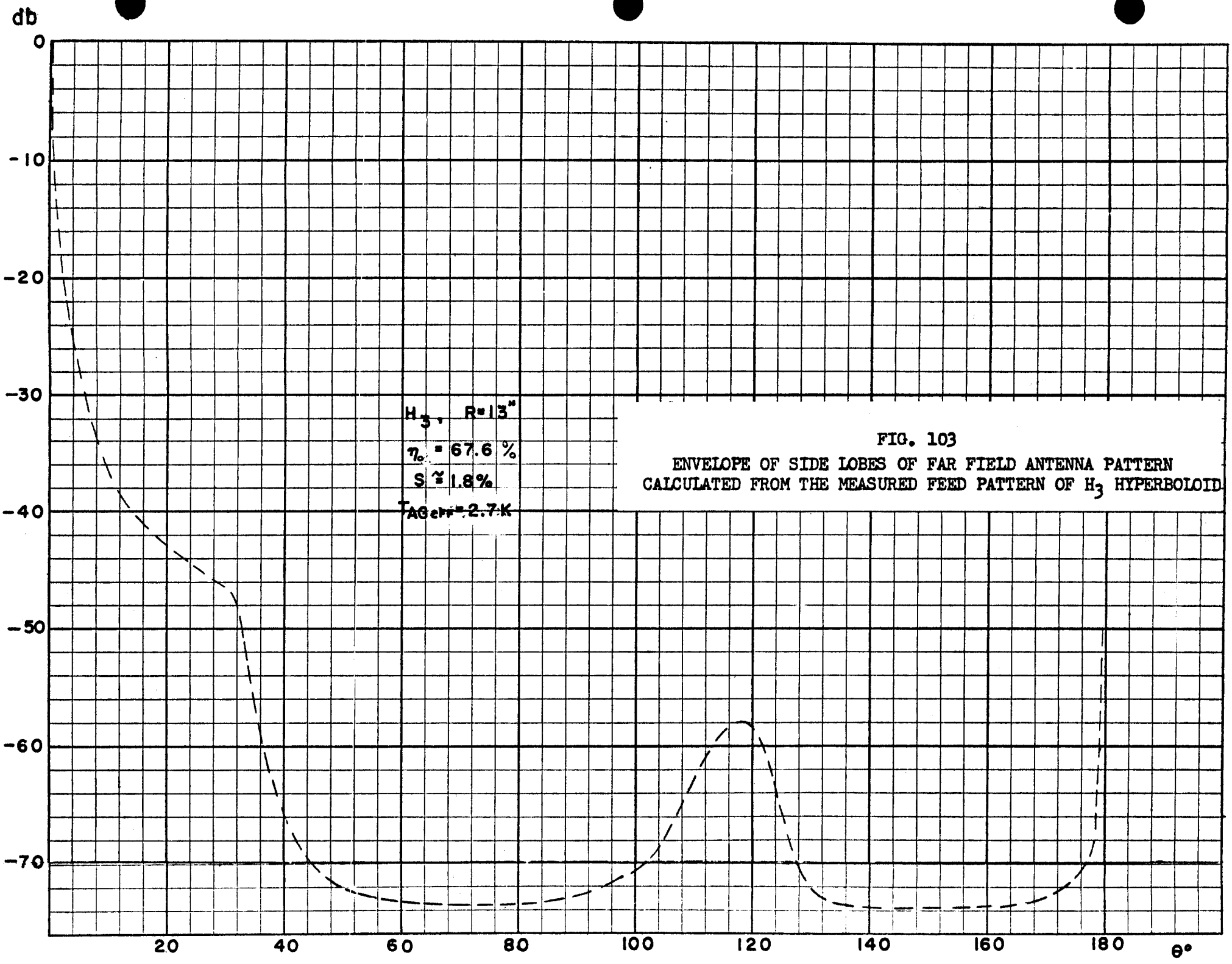

FIG. 103

ENVELOPE OF SIDE LOBES OF FAR FIELD ANTENNA PATTERN CALCULATED FROM THE MEASURED FEED PATTERN OF H_3 HYPERBOLOID

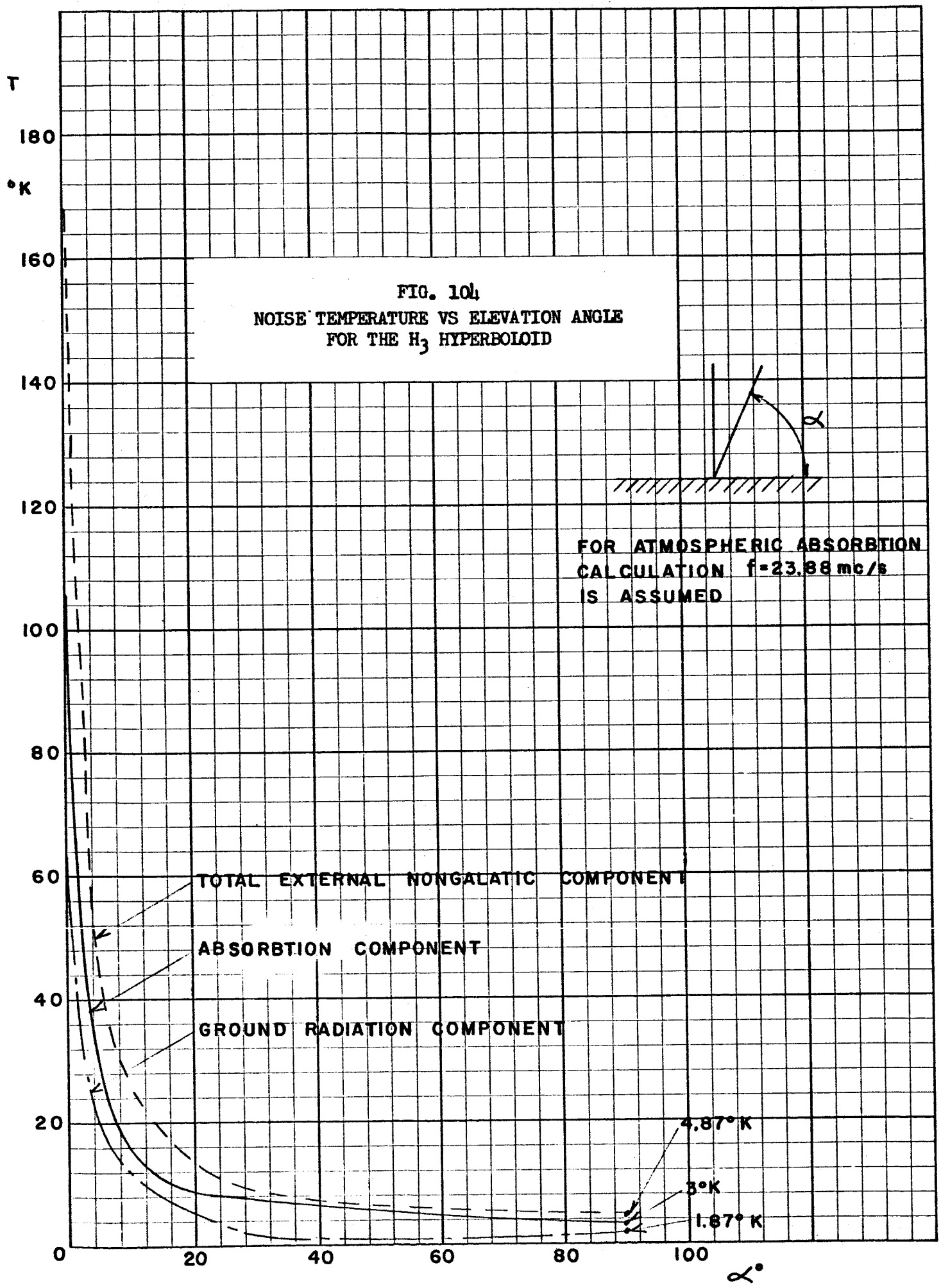

FIG. 104
NOISE TEMPERATURE VS ELEVATION ANGLE
FOR THE H_3 HYPERBOLOID

$$\eta_t = \frac{\eta}{\eta_o} = e^{-16\pi^2\left(\frac{\sigma_T}{D_p}\right)^2 D_p^2 \lambda}$$

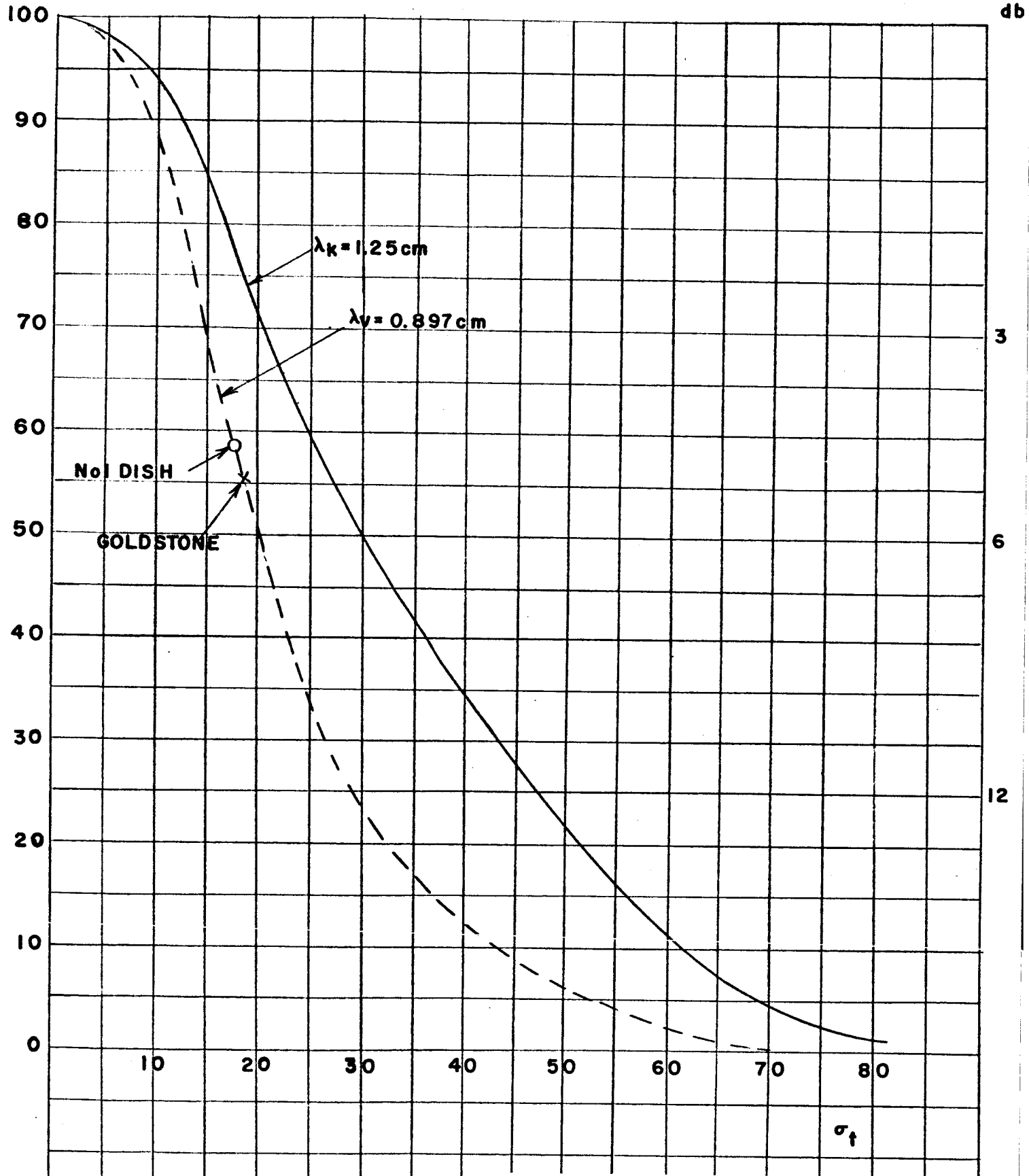

FIG. 105

SURFACE QUALITY TOLERANCE FACTOR (η_A)
VS TOTAL RMS DEVIATION OF SURFACE (t)

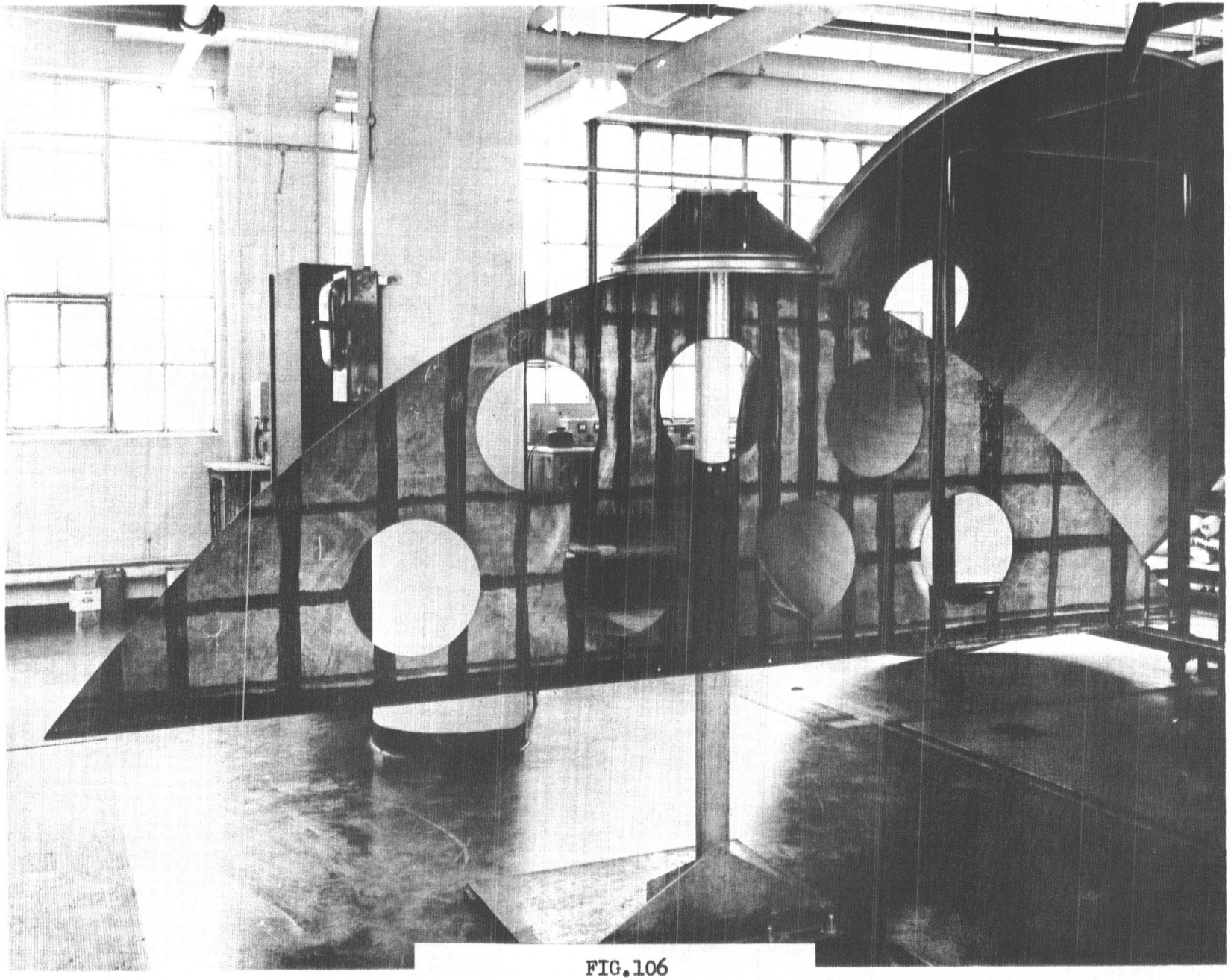

FIG. 106

TEMPLATE FOR PARABOLOID REFLECTOR
SURFACE MEASUREMENT

FIG. 107

DISH MOUNTED ON MEASURING JIG

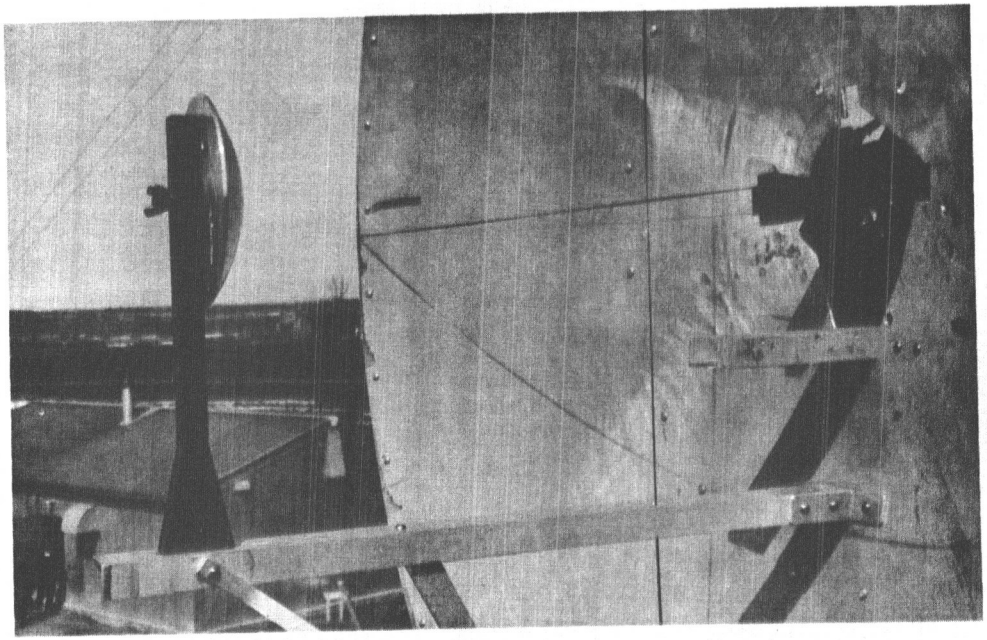

FIG. 108 ANTENNA SYSTEM UNDER TEST.

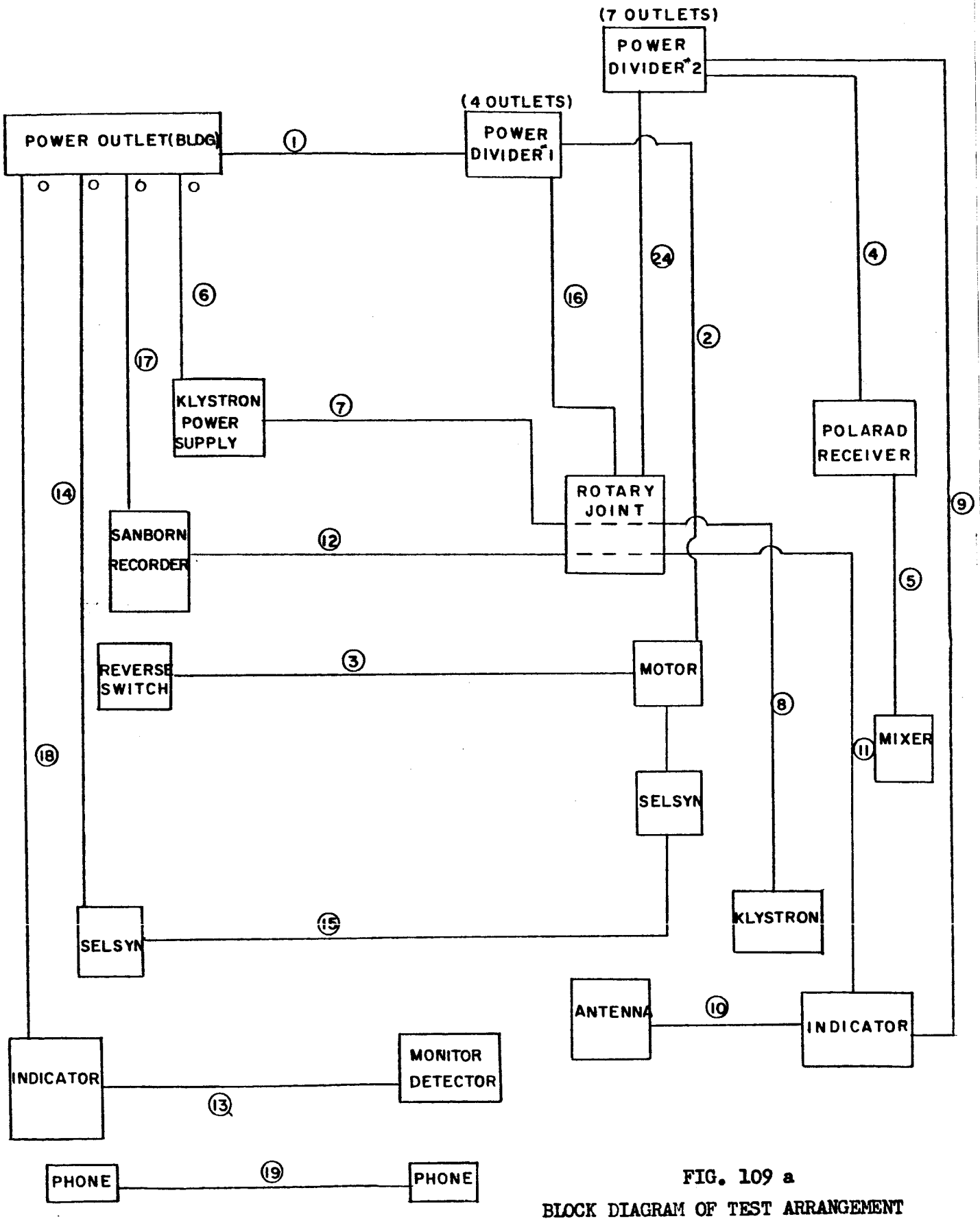

FIG. 109 a

BLOCK DIAGRAM OF TEST ARRANGEMENT FOR FAR FIELD TEST

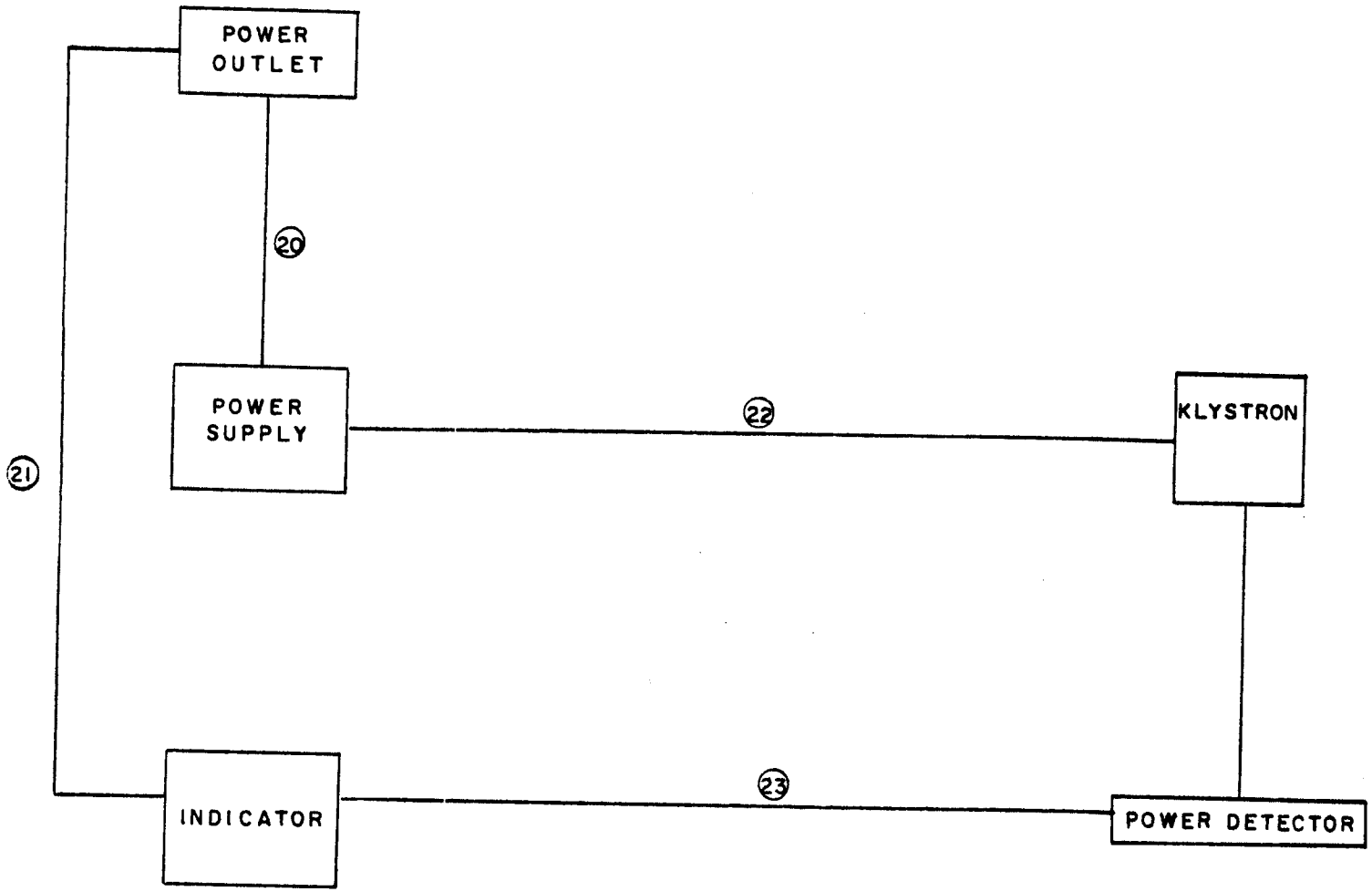

FIG. 109 b
BLOCK DIAGRAM OF TEST ARRANGEMENT
FOR FAR FIELD TEST

FIG. 110 ANTENNA UNDER TEST ON TURNTABLE.

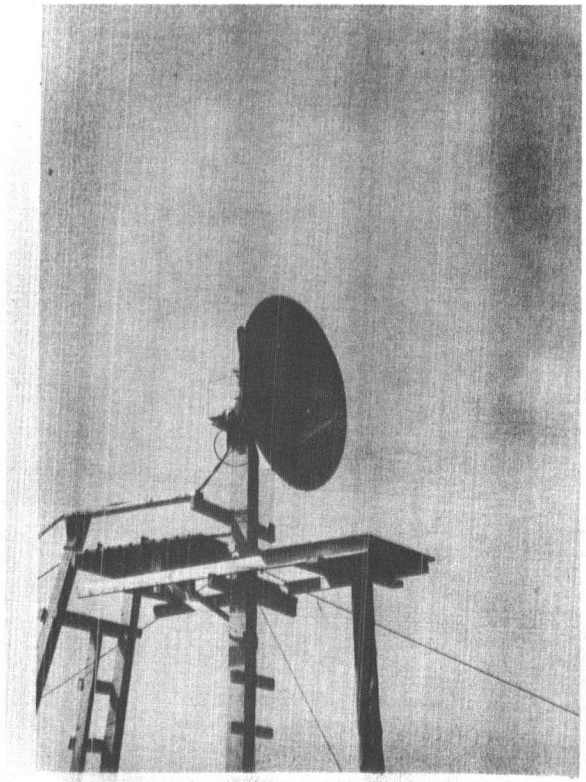

FIG. 111 TRANSMITTING ANTENNA.

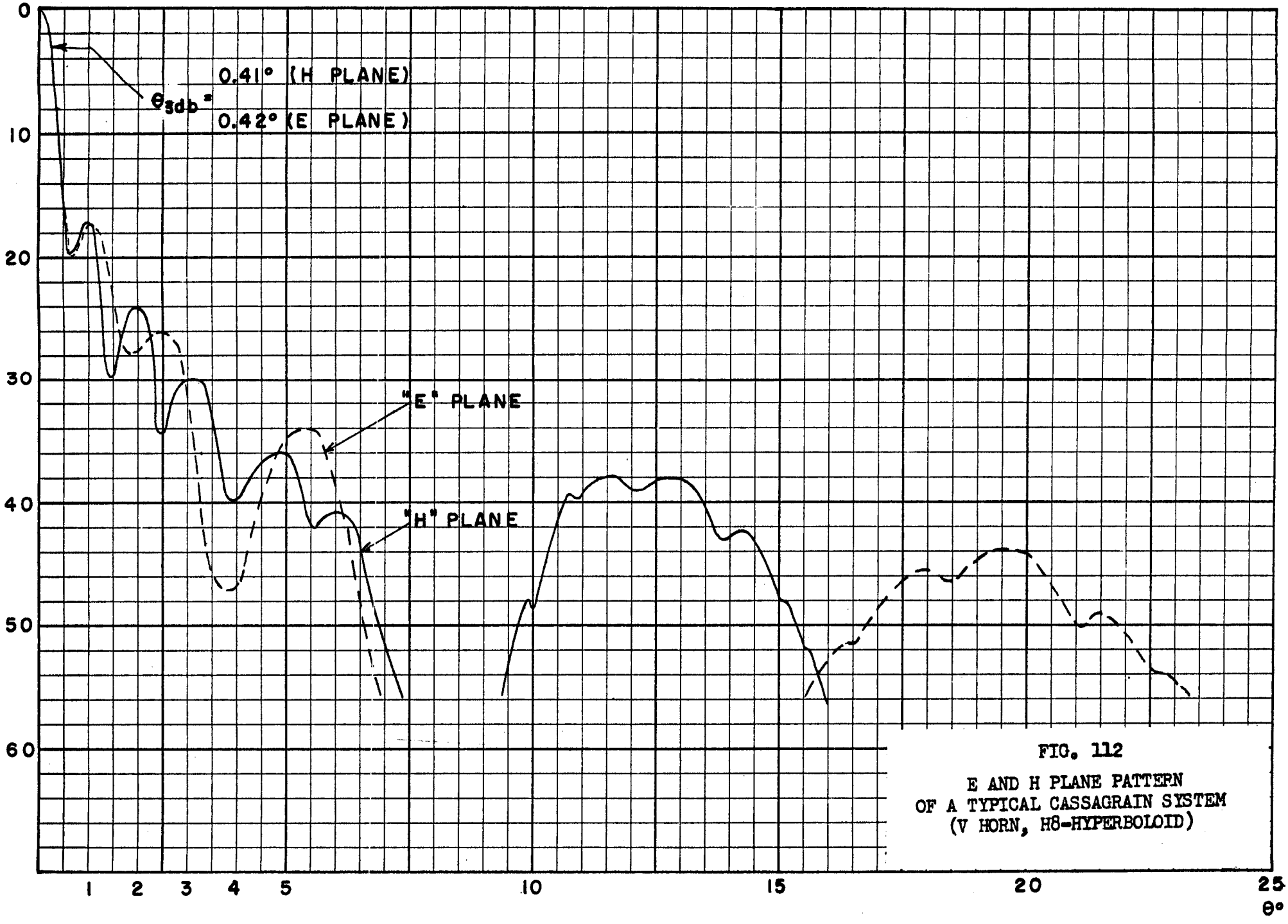

FIG. 112

E AND H PLANE PATTERN
OF A TYPICAL CASSAGRAIN SYSTEM
(V HORN, H8-HYPERBOLOID)

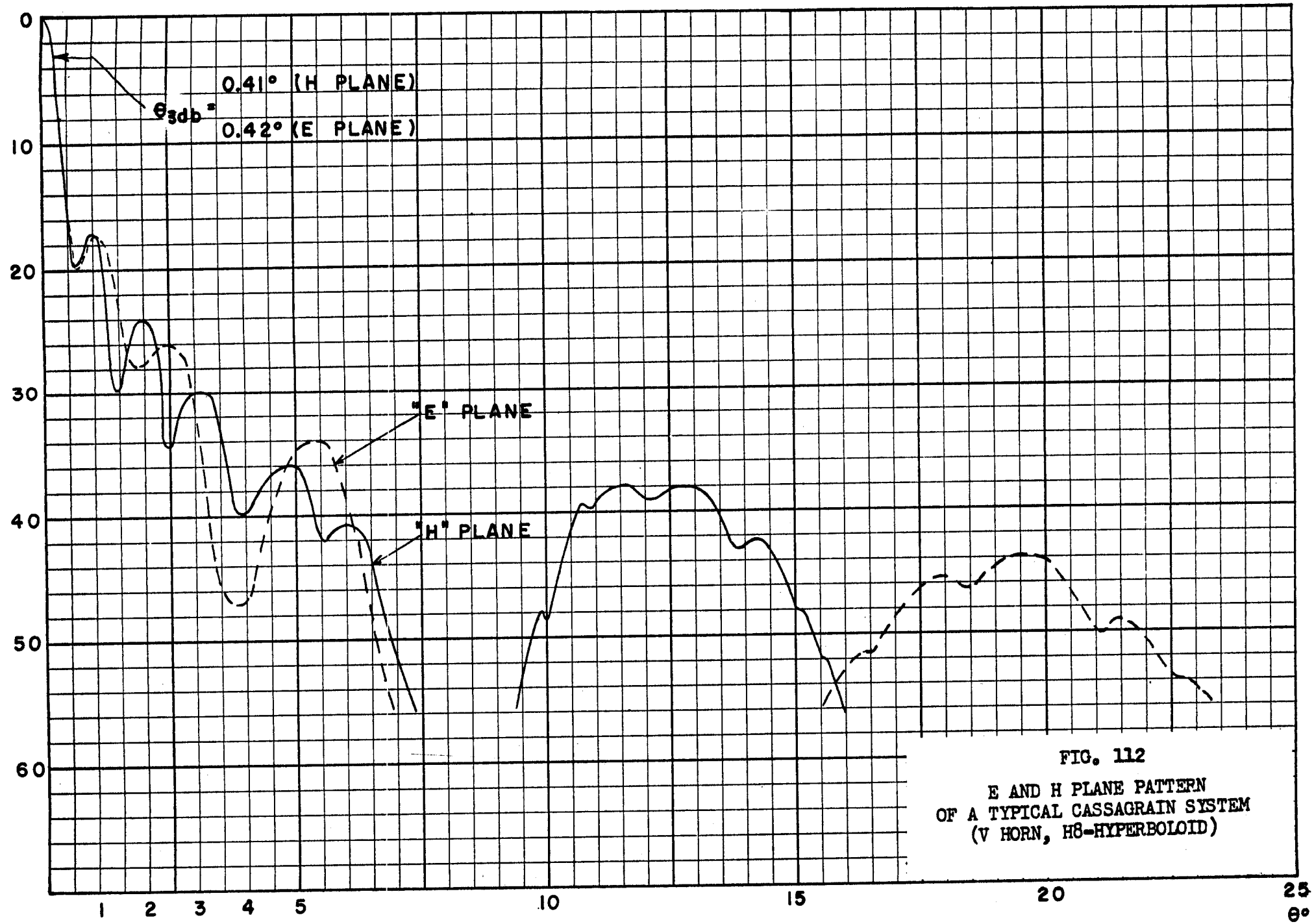

FIG. 112

E AND H PLANE PATTERN
OF A TYPICAL CASSAGRAIN SYSTEM
(V HORN, H8-HYPERBOLOID)

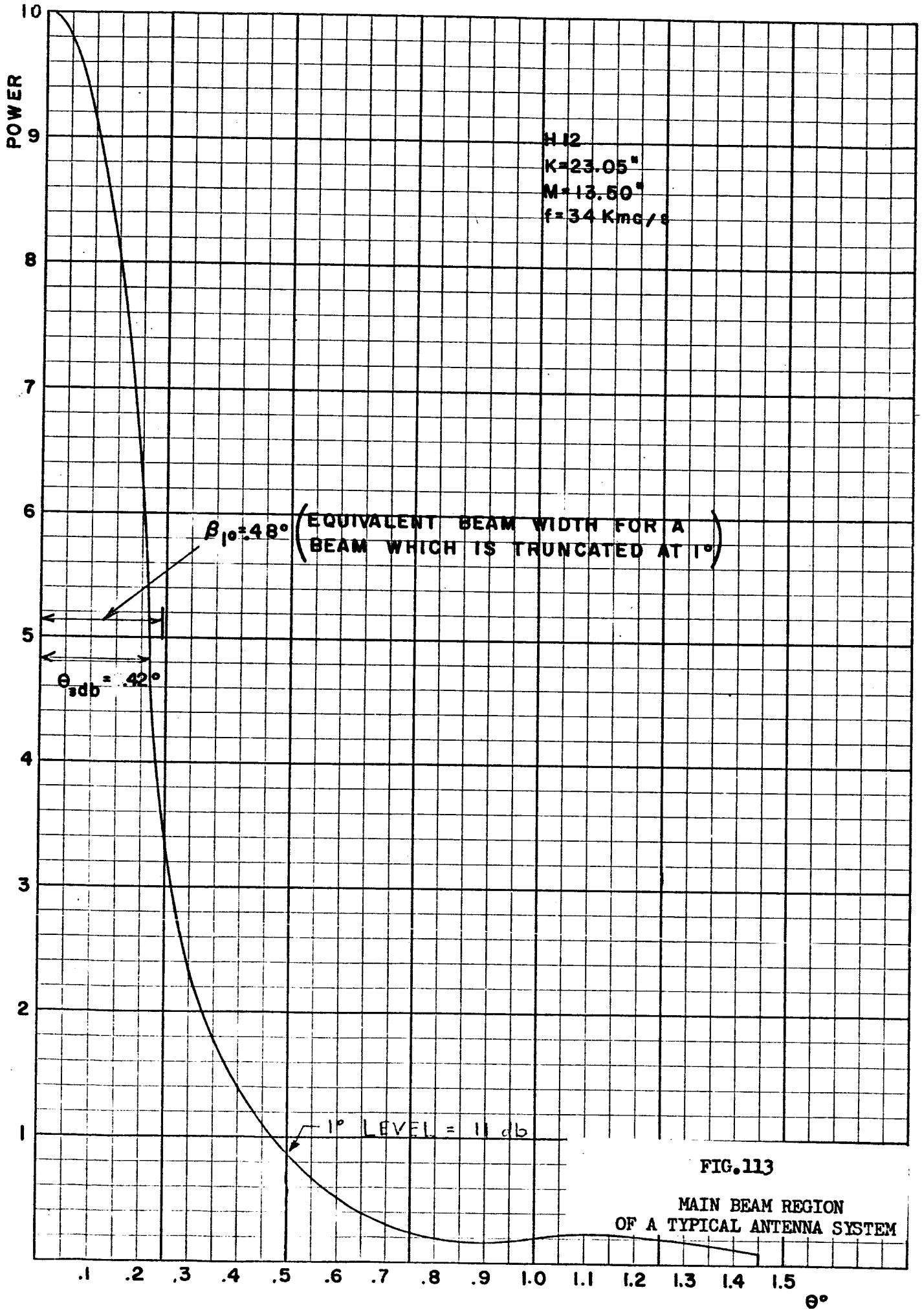

FIG. 113

MAIN BEAM REGION
OF A TYPICAL ANTENNA SYSTEM

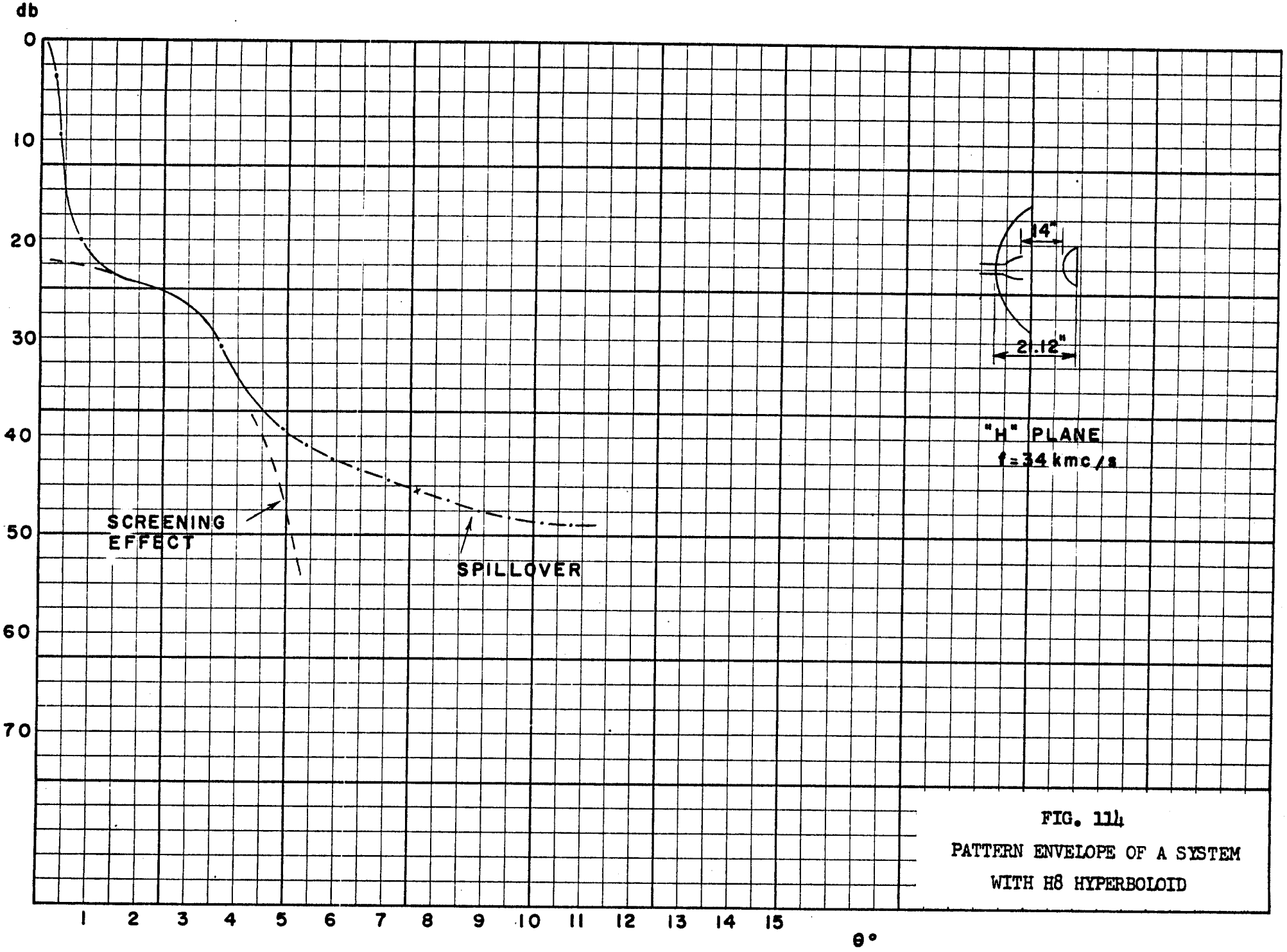

FIG. 114

PATTERN ENVELOPE OF A SYSTEM WITH H8 HYPERBOLOID

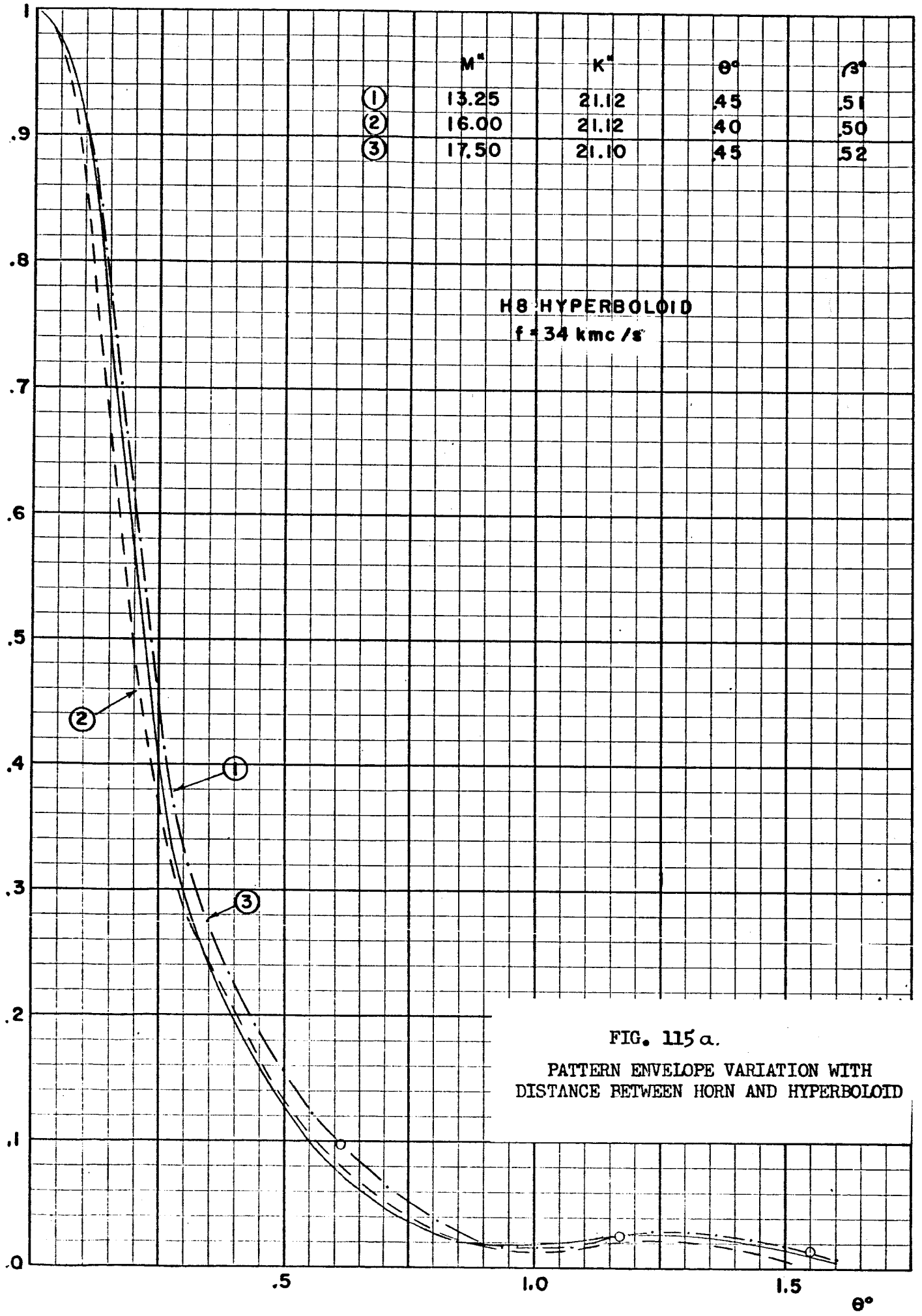

FIG. 115 a.

PATTERN ENVELOPE VARIATION WITH DISTANCE BETWEEN HORN AND HYPERBOLOID

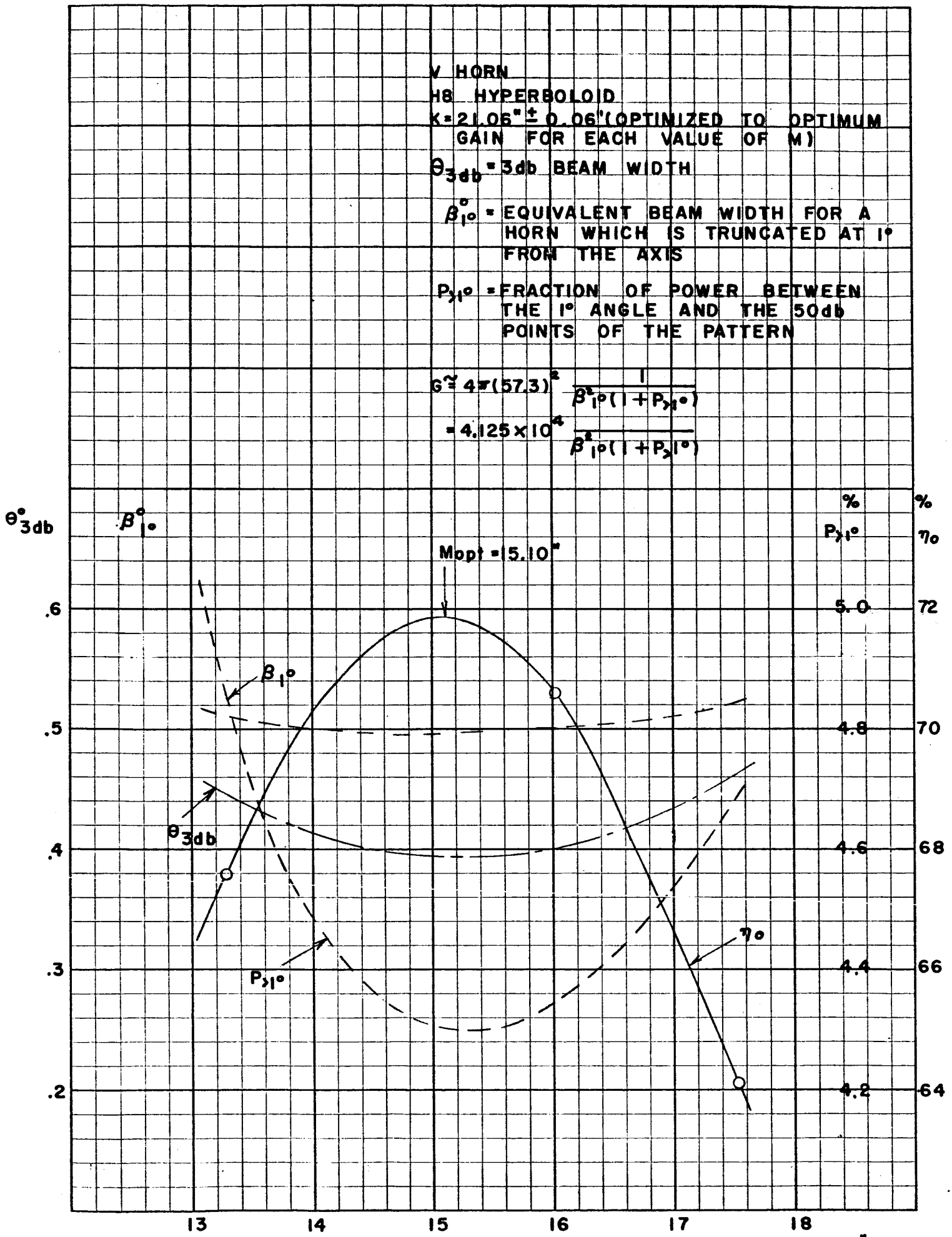

FIG. 115b. EFFECT OF AXIAL MISALIGNEMENT OF HORN TO THE 3 DB BEAMWIDTH.

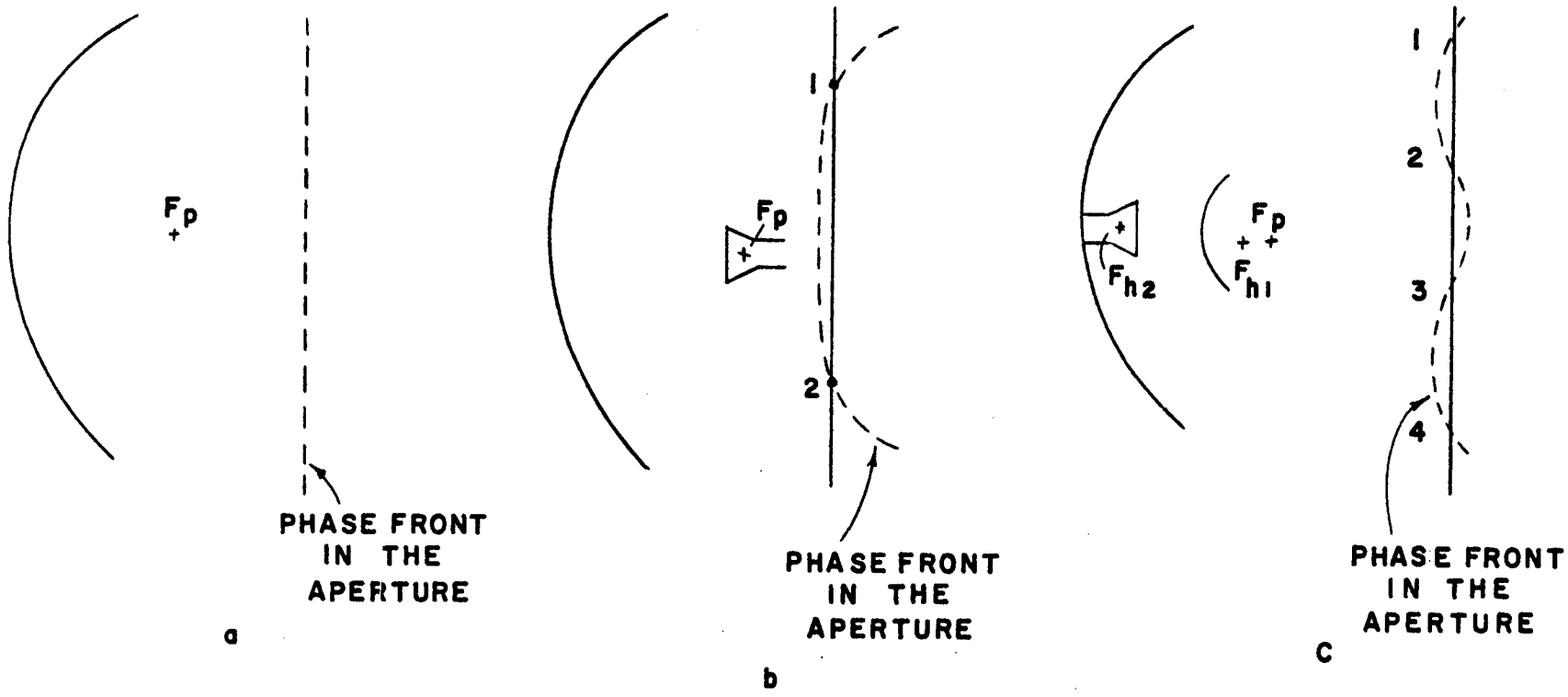

FIG. 116 POSSIBILITY OF PHASE ERROR COMPENSATION.

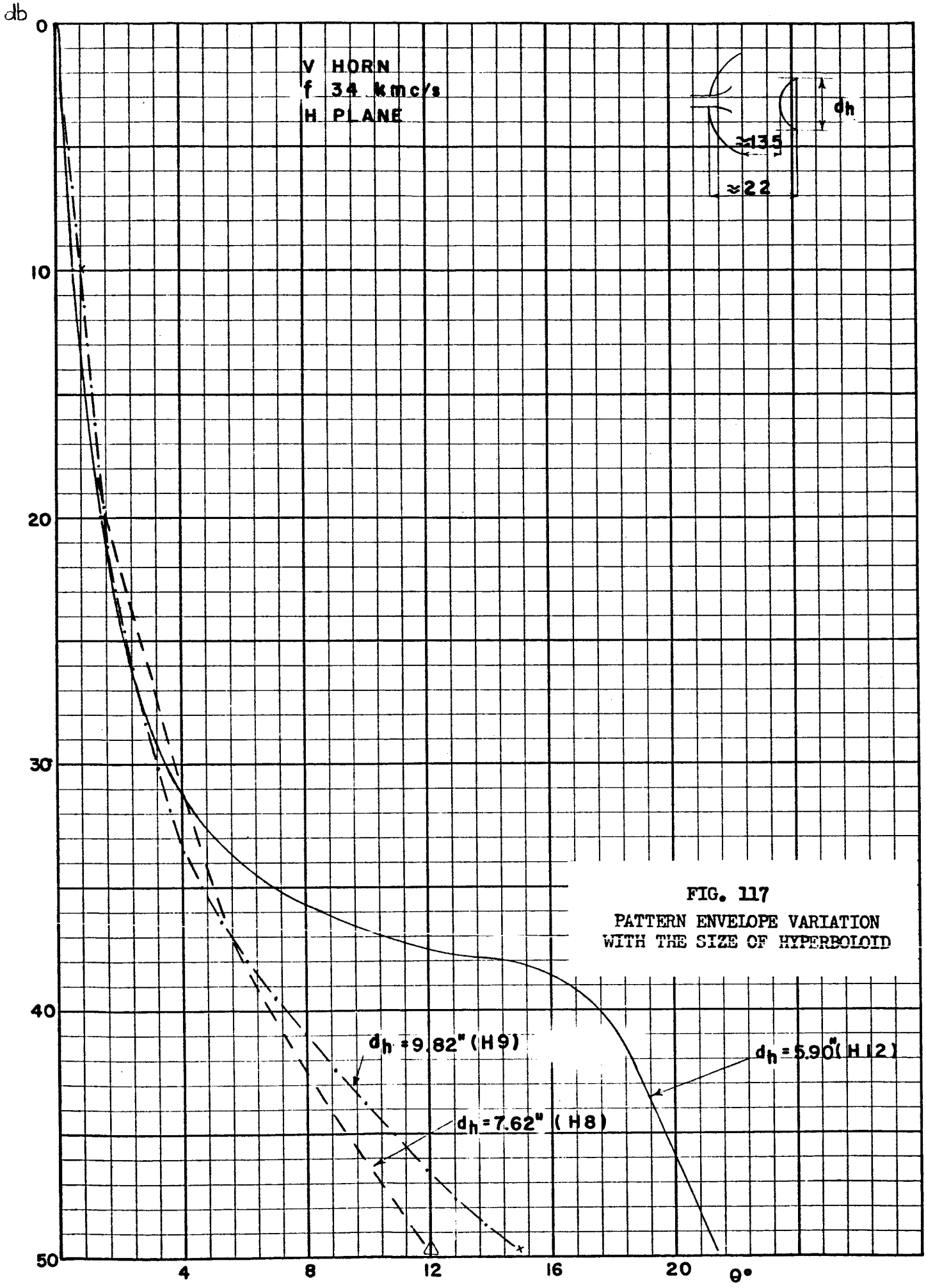

FIG. 117
PATTERN ENVELOPE VARIATION
WITH THE SIZE OF HYPERBOLOID

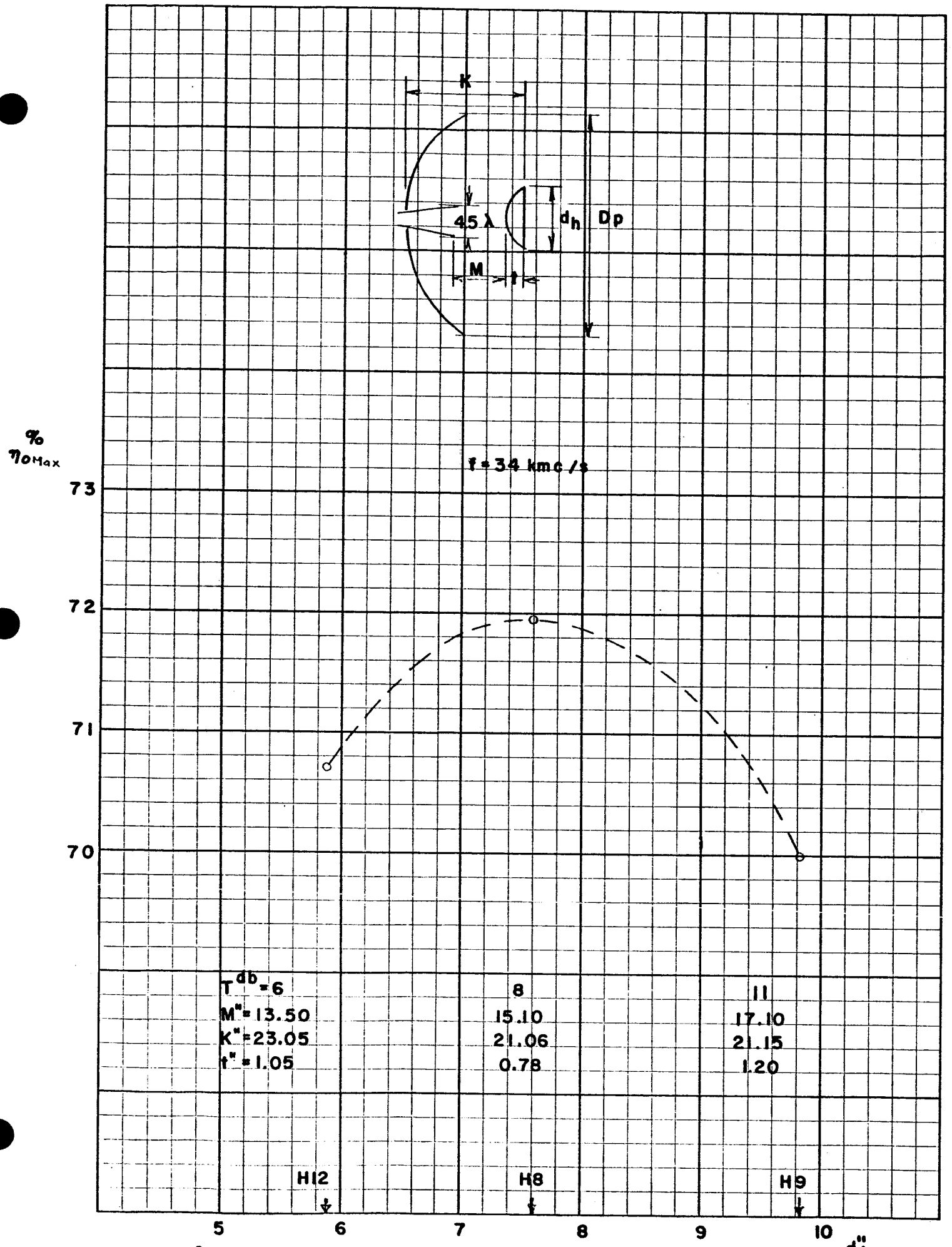

FIG. 118 VARIATION OF MAXIMUM APERTURE EFFICIENCY VS d_h

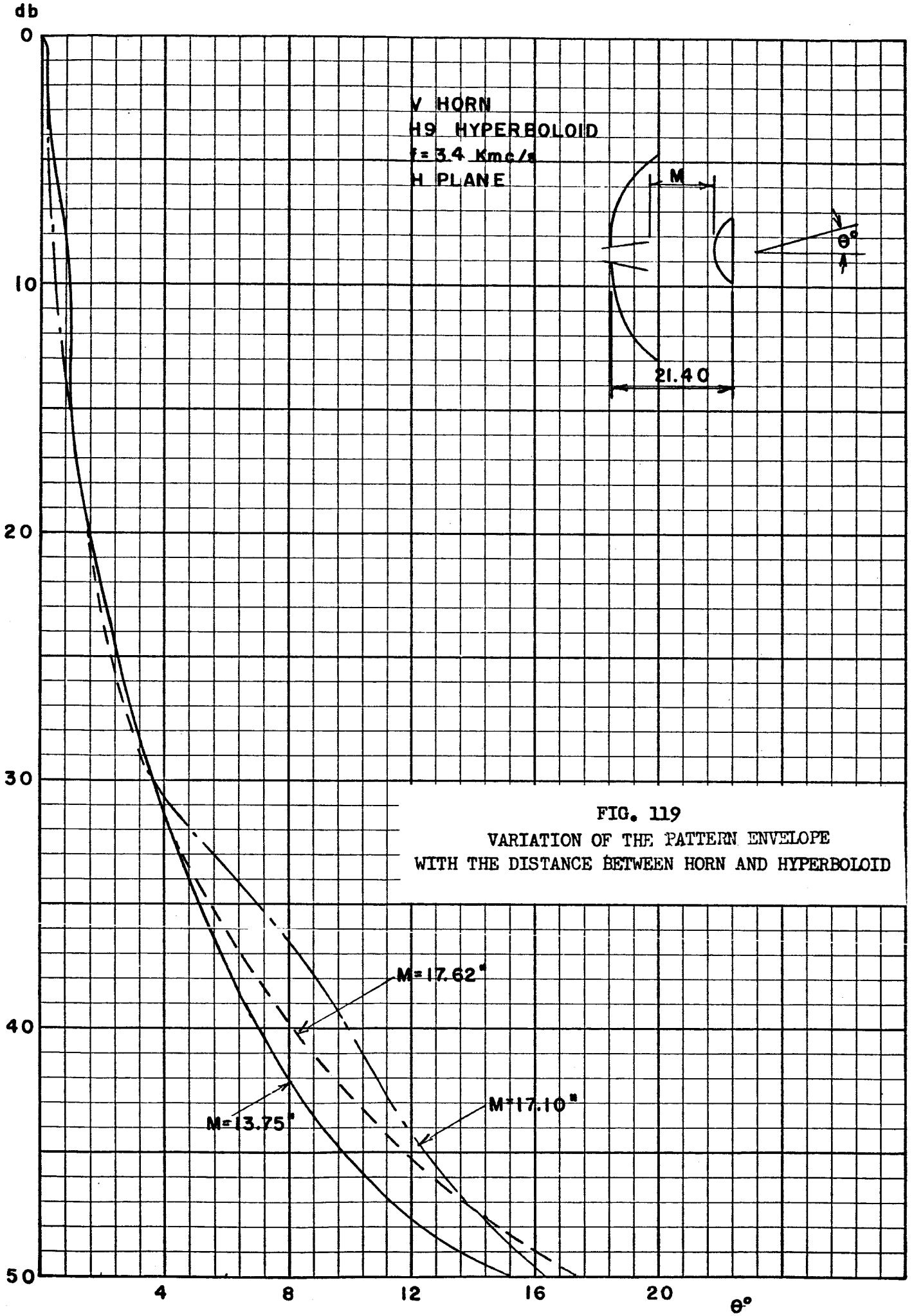

FIG. 119
VARIATION OF THE PATTERN ENVELOPE
WITH THE DISTANCE BETWEEN HORN AND HYPERBOLOID

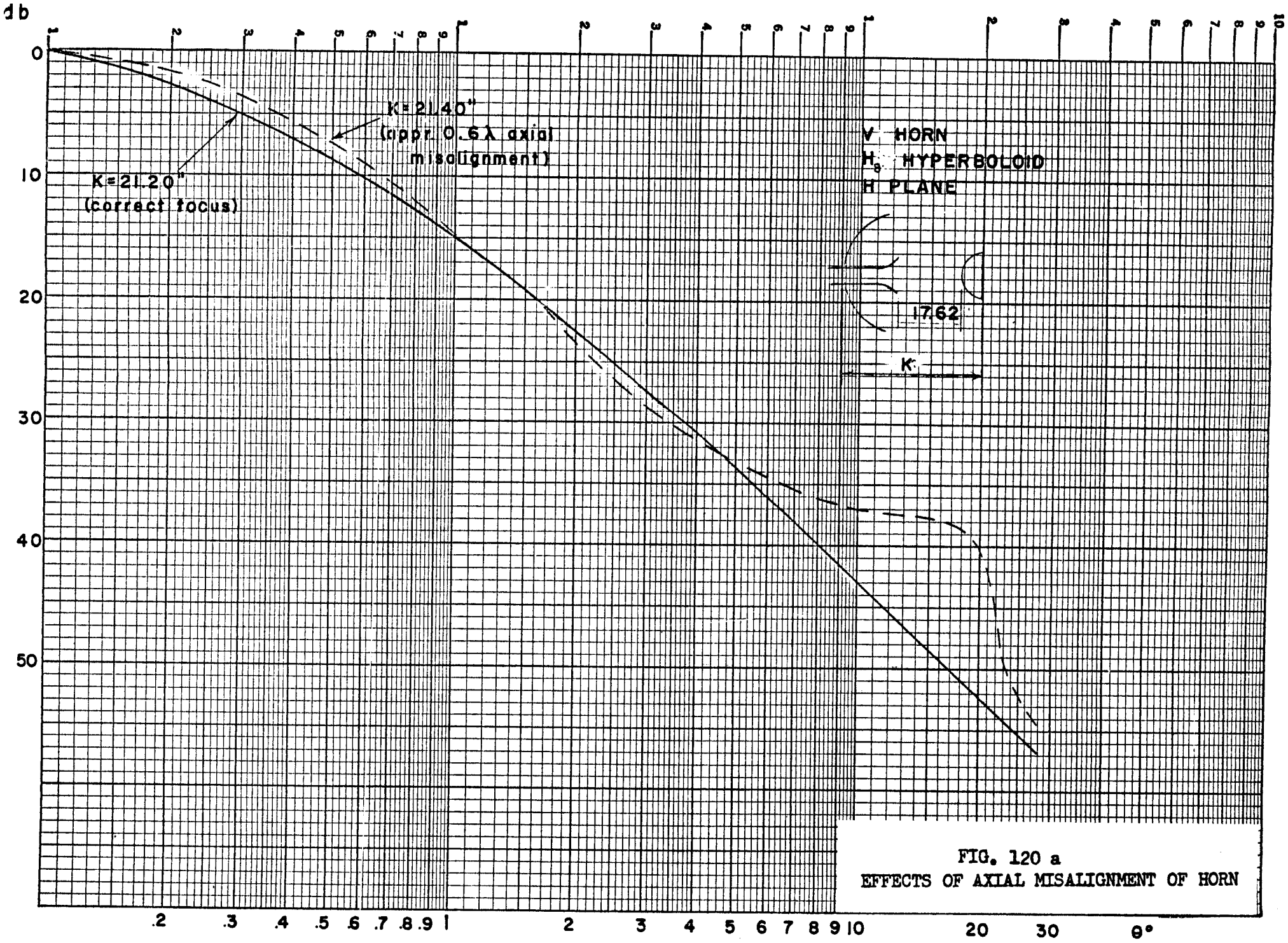

FIG. 120 a
EFFECTS OF AXIAL MISALIGNMENT OF HORN

FIG. 120 b EFFECT OF AXIAL MISALIGNEMENT OF HYPERBOLOID.

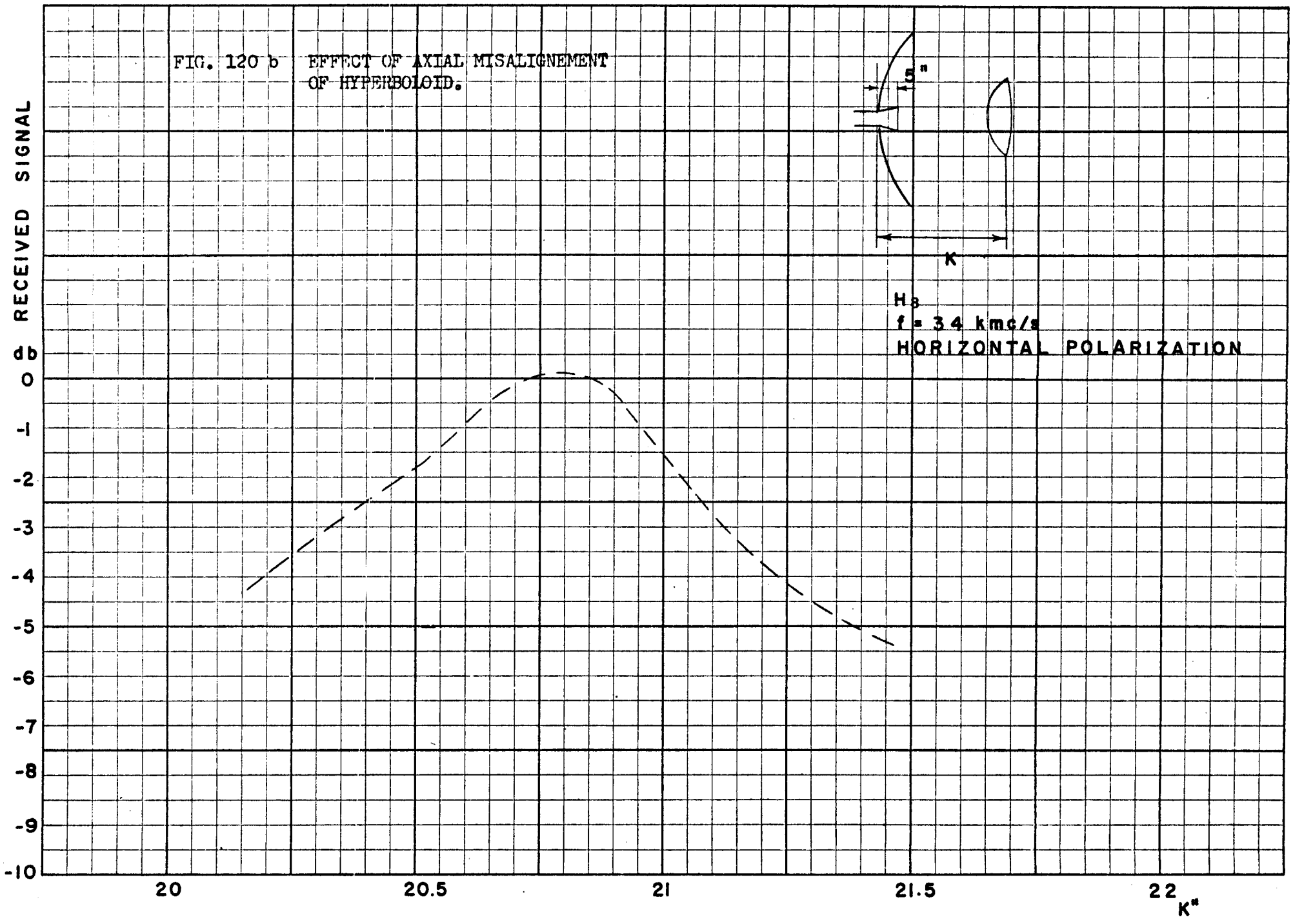

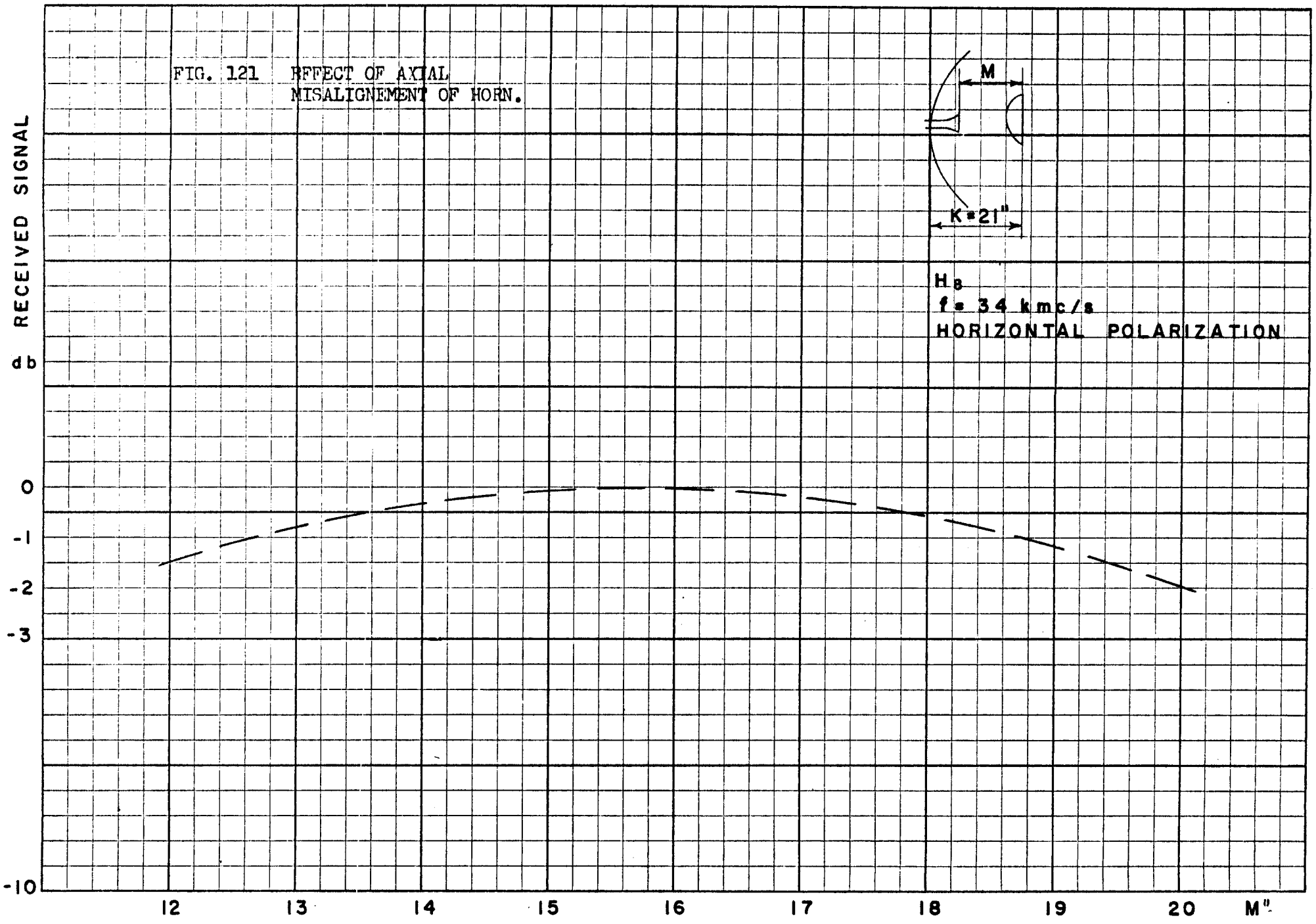

FIG. 121 EFFECT OF AXIAL MISALIGNEMENT OF HORN.

FIG. 122 EFFECT OF THE OFF-AXIS MISALIGNEMENT OF HORN.

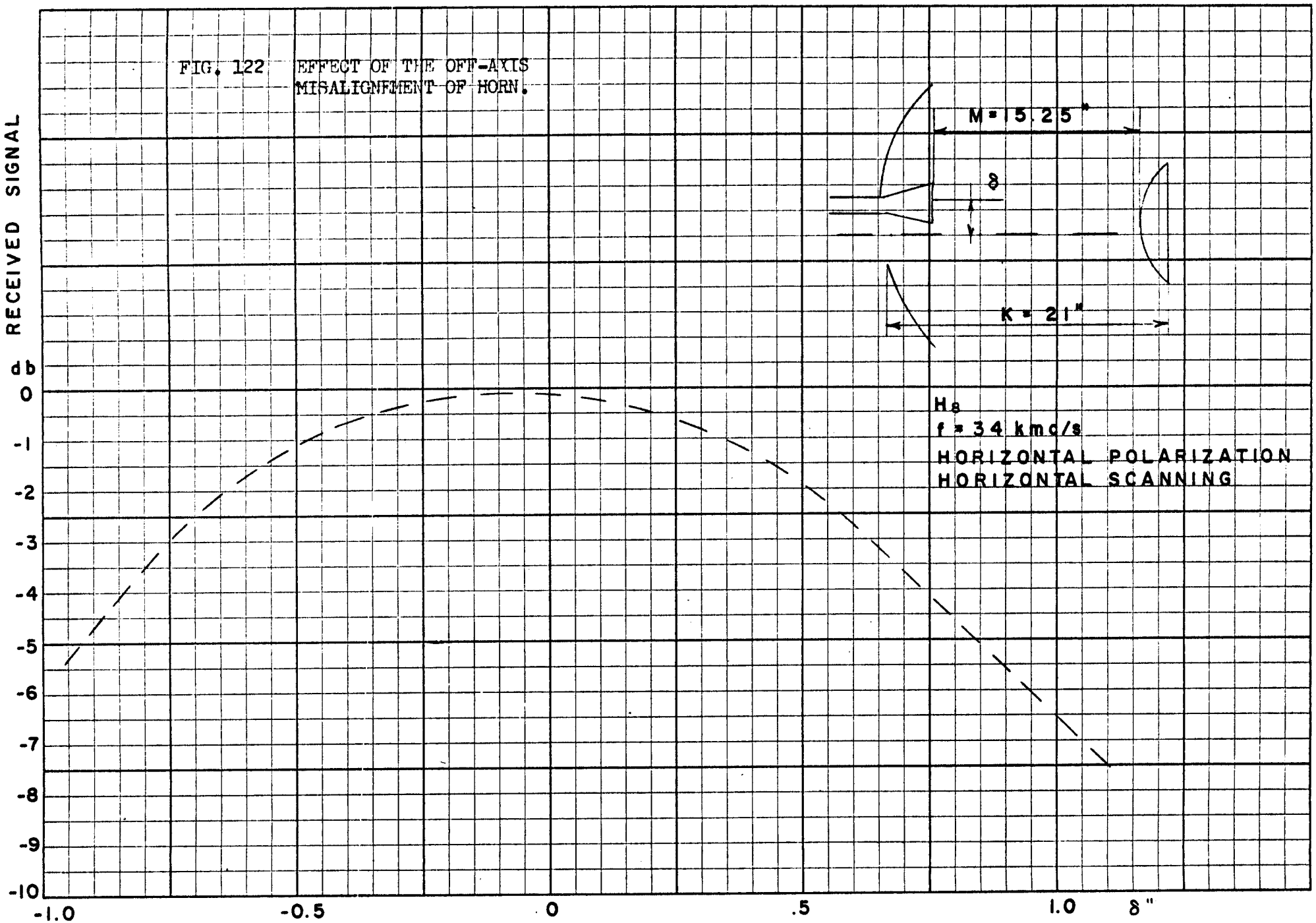

FIG. 123 EFFECT OF ROTATION OF HYPERBOLOID.

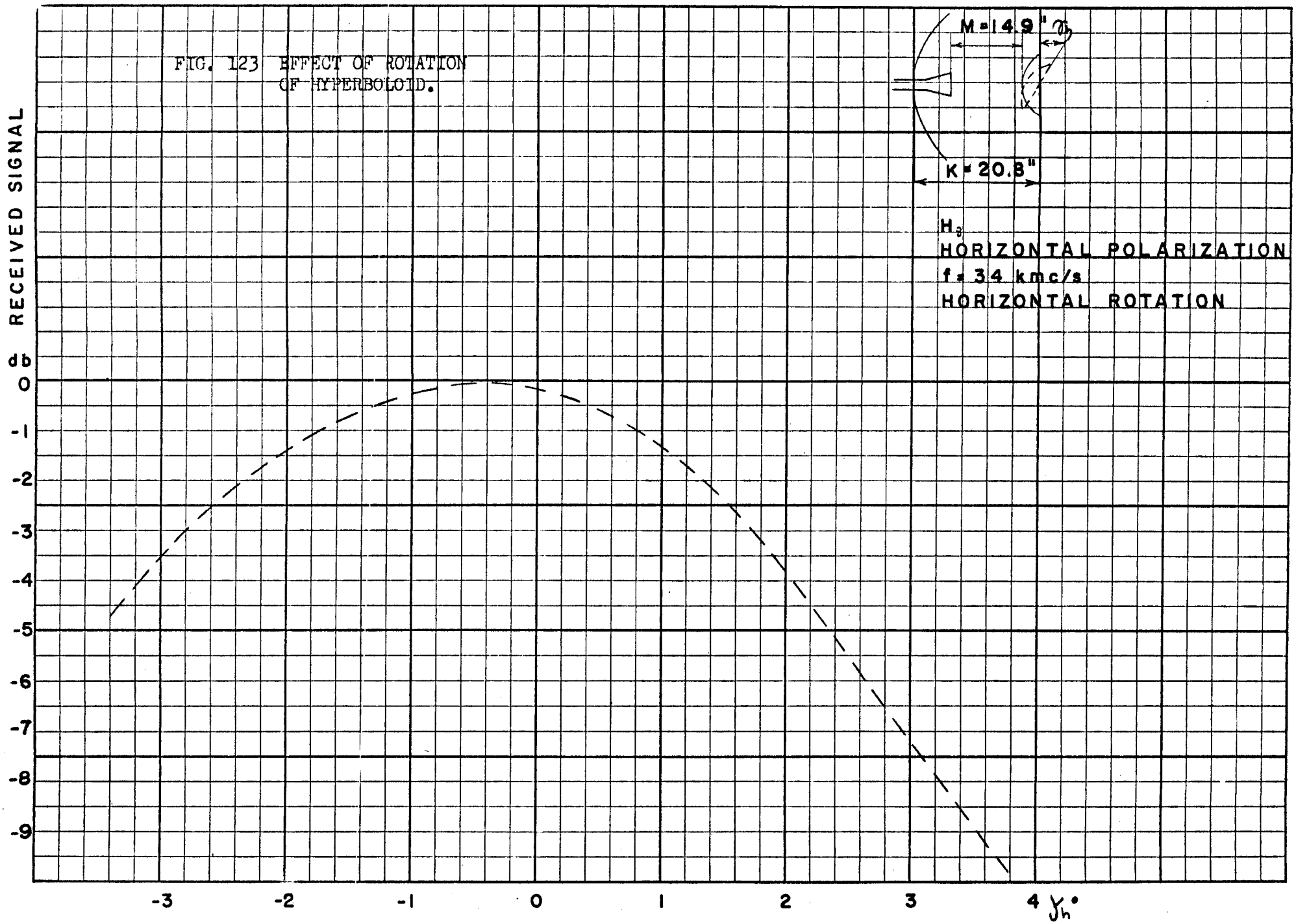

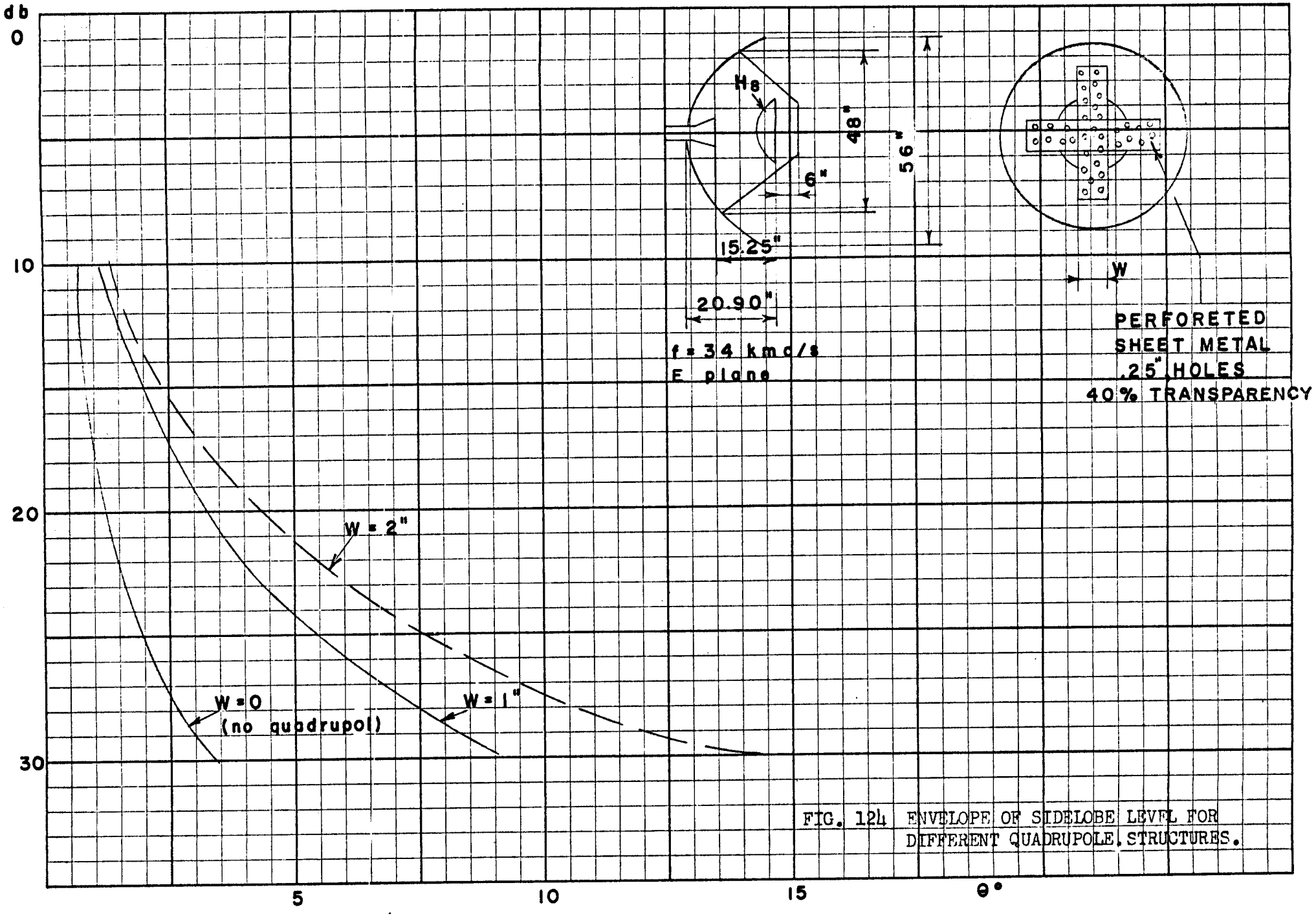

FIG. 124 ENVELOPE OF SIDELOBE LEVEL FOR DIFFERENT QUADRUPOLE STRUCTURES.